



Paterson, Sarah (2024) *Searching for impulsive hard x-ray emission from the quiet sun*. PhD thesis.

<https://theses.gla.ac.uk/84081/>

Copyright and moral rights for this work are retained by the author

A copy can be downloaded for personal non-commercial research or study, without prior permission or charge

This work cannot be reproduced or quoted extensively from without first obtaining permission from the author

The content must not be changed in any way or sold commercially in any format or medium without the formal permission of the author

When referring to this work, full bibliographic details including the author, title, awarding institution and date of the thesis must be given

Enlighten: Theses

<https://theses.gla.ac.uk/>  
[research-enlighten@glasgow.ac.uk](mailto:research-enlighten@glasgow.ac.uk)

# Searching For Impulsive Hard X-Ray Emission from the Quiet Sun

Sarah Paterson

Submitted in fulfilment of the requirements for the  
degree of Doctor of Philosophy

Astronomy and Astrophysics Group  
School of Physics and Astronomy  
University of Glasgow



University  
of Glasgow

---

This thesis is my own composition except where indicated in the text.  
No part of this thesis has been submitted elsewhere for any other degree  
or qualification.

**Copyright © 2024 Sarah Paterson**

25th January 2024

---

# Abstract

The temperature of the solar corona is orders of magnitude hotter than that of the surface of the Sun. This is referred to as the coronal heating problem, and one of the leading theories to solve this is that a multitude of very small-scale energy release events called nanoflares, too small to resolve individually, could together sustain the high temperature of the corona. Nanoflare heating models predict a high temperature ( $> 5$  MK) component and, if operating through similar mechanisms to large flares, they would also produce non-thermal emission due to accelerated electrons. Searching for these signatures in small-scale phenomena requires the investigation of their hard X-ray (HXR) emission.

In this thesis, we analyse HXR observations of small-scale sources in the quiet Sun. In Chapter 1, we introduce the coronal heating problem, as well as the types of small-scale phenomena that are typically found in the quiet Sun. We also give a brief overview of the mechanisms which produce solar HXR emission, and the models used to describe it. In Chapter 2, we introduce the instruments whose data is used in this thesis. This includes the Nuclear Spectroscopic Telescope Array (NuSTAR), a sensitive HXR focusing telescope which, though designed as an astrophysics mission, has observed the Sun at  $\sim 2\text{--}79$  keV.

During the recent solar minimum (2018–2020), NuSTAR observed the quiet Sun a number of times, and these campaigns are summarised in Chapter 3. The absence of bright sources on the disk at this point provided the unique opportunity to observe their faint HXR emission for the first time with a sensitive HXR imaging spectrometer, allowing a search for high temperature and non-thermal components. In Chapter 3, we also introduce the data analysis methods used throughout this thesis, including NuSTAR HXR spectroscopy, differential emission measure (DEM) analysis, and calculating NuSTAR non-thermal upper limits.

In Chapter 4, we analyse a variety of quiet Sun HXR sources which were captured in the NuSTAR full-disk mosaics from 28 September 2018. Among these are several X-ray bright points, an emerging flux region, and a jet. By fitting their NuSTAR spectra, we find that they all have temperatures lying in the narrow range between 2–3.2 MK. DEM analysis

## *Abstract*

confirms the presence of no significant emission at temperatures  $> 4$  MK. We find no evidence of high temperature or non-thermal components, though we obtain upper limits on the non-thermal emission consistent with a null detection.

The full-disk mosaic observations are limited by their short  $\sim 100$  s pointings, which result in noisy spectra and are not ideal for studying time evolution of HXR sources. In Chapter 5, we instead focus on two X-ray bright points observed over several hours during NuSTAR quiet Sun dwell observations, one on 21 February 2020 and another on 12–13 September 2020. We study their time evolution, finding that both show significant HXR variability over the observations. We find that the February 2020 bright point produces “flares”, observed as spikes in the HXR emission. During flaring times, this bright point reaches temperatures  $> 4$  MK, hotter than previous temperatures found for X-ray bright points. Conversely, fitting the NuSTAR spectra of the September bright point during times of X-rays spikes reveals no hotter component during these times, only an increase in emission measure of material at  $\sim 2.6$  MK. DEM analysis confirms that there are no significant temperature increases.

In this chapter, we also fit the two bright points’ spectra integrated over several hours. We find that these spectra are dominated by a thermal component with a temperature of 2.6–3.2 MK at energies  $< 4$  keV. At energies higher than this, the NuSTAR instrumental background dominates. No significant hot or non-thermal component is detected.

In addition to capturing the time evolution of persisting sources, NuSTAR’s dwell observation mode also increases the chance of detecting transients. In Chapter 6, we identify seven small-scale impulsive quiet Sun events captured in the 21 February and 12–13 September 2020 observing campaigns, one of which is a mini-filament eruption. From fitting their NuSTAR HXR spectra, we find that their temperatures range from 3.3–4.0 MK. In general, no hot or non-thermal components are detected in these short-duration events. However, through NuSTAR spectral analysis for the mini-filament eruption, we find evidence of emission up to temperatures of  $\sim 5$  MK. DEM analysis confirms that this event had more material heated to temperatures  $> 2$  MK than the other events. Again, as no non-thermal component is directly observed, we obtain upper limits on the non-thermal emission consistent with a null detection. We find that the non-thermal distribution would have to be very steep between 3–4 keV to produce the observed heating.

# Contents

<b>Abstract</b>	<b>ii</b>
<b>List of Tables</b>	<b>viii</b>
<b>List of Figures</b>	<b>ix</b>
<b>Acknowledgements</b>	<b>xii</b>
<b>1 Introduction</b>	<b>1</b>
1.1 The Solar Atmosphere . . . . .	1
1.1.1 Impulsive Energy Release in the Solar Atmosphere . . . . .	2
1.2 The Coronal Heating Problem . . . . .	4
1.2.1 Parker’s Nanoflares . . . . .	4
1.2.2 Modelling . . . . .	5
1.3 The Quiet Sun . . . . .	6
1.3.1 Coronal Bright Points . . . . .	7
1.3.2 Emerging Flux Regions . . . . .	12
1.3.3 Quiet Sun Flares . . . . .	13
1.3.4 Mini-Filament Eruptions . . . . .	15
1.3.5 Jets . . . . .	15
1.3.6 Full-Disk Quiet Sun Emission . . . . .	16
1.4 Hard X-ray Observations of the Quiet Sun . . . . .	17
1.5 X-Ray Emission From the Sun . . . . .	19
1.5.1 Spectral Lines . . . . .	19
1.5.2 Bremsstrahlung . . . . .	20
1.5.3 Thermal Bremsstrahlung . . . . .	21
1.5.4 Non-Thermal Bremsstrahlung . . . . .	23
<b>2 Instrumentation</b>	<b>25</b>
2.1 The Nuclear Spectroscopic Telescope Array . . . . .	25
2.1.1 Detectors and Optics . . . . .	26

Contents

2.1.2	Data Processing . . . . .	31
2.1.3	Solar Observing Modes . . . . .	32
2.1.4	NuSTAR Temperature Responses . . . . .	35
2.1.5	Instrumental Background . . . . .	36
2.2	The Solar Dynamics Observatory . . . . .	38
2.2.1	The Atmospheric Imaging Assembly . . . . .	38
2.2.2	The Helioseismic and Magnetic Imager . . . . .	41
2.3	The Hinode X-Ray Telescope . . . . .	41
<b>3</b>	<b>NuSTAR Quiet Sun Data and Analysis Methods</b>	<b>43</b>
3.1	An Overview of the NuSTAR Quiet Sun Data . . . . .	43
3.1.1	28 September 2018 . . . . .	45
3.1.2	12 January 2019 . . . . .	47
3.1.3	25 April 2019 . . . . .	50
3.1.4	02 July 2019 . . . . .	51
3.1.5	21 February 2020 . . . . .	53
3.1.6	12–13 September 2020 . . . . .	54
3.2	Analysis Methods for NuSTAR Quiet Sun Data . . . . .	57
3.2.1	Images and Lightcurves . . . . .	57
3.2.2	NuSTAR HXR Spectral Fitting . . . . .	59
3.2.3	Differential Emission Measure Analysis . . . . .	62
3.2.4	Non-Thermal Upper Limits . . . . .	65
3.3	Summary . . . . .	70
<b>4</b>	<b>A Survey of Quiet Sun Features Captured in NuSTAR Full-Disk Mosaics</b>	<b>71</b>
4.1	Emerging Flux Region . . . . .	72
4.1.1	NuSTAR Spectral Analysis . . . . .	76
4.1.2	Differential Emission Measures . . . . .	78
4.1.3	Non-Thermal Upper Limits . . . . .	81
4.2	X-ray Bright Points . . . . .	82
4.2.1	NuSTAR Spectral Analysis . . . . .	85
4.2.2	Differential Emission Measures . . . . .	87
4.2.3	Non-Thermal Upper Limits . . . . .	88
4.3	Jet . . . . .	90
4.3.1	NuSTAR Spectral Analysis . . . . .	93
4.3.2	Non-Thermal Upper Limits . . . . .	94

Contents

4.4	Decayed Active Region . . . . .	95
4.4.1	NuSTAR Spectral Analysis . . . . .	96
4.5	A Comparison of the Thermal Properties . . . . .	96
4.6	Summary and Conclusions . . . . .	100
<b>5</b>	<b>Time Evolution of X-Ray Bright Points from the NuSTAR Quiet Sun Dwell Observations</b>	<b>102</b>
5.1	Overview . . . . .	103
5.2	A Bright Point in the 21 February 2020 Observation . . . . .	106
5.2.1	Flare 1 . . . . .	106
5.2.2	Flare 2 . . . . .	114
5.3	A Bright Point in the 12–13 September 2020 Observation . . . . .	118
5.3.1	NuSTAR Spectral Analysis . . . . .	118
5.3.2	DEM Analysis . . . . .	123
5.3.3	Non-Thermal Upper Limits . . . . .	125
5.4	Integrated Spectra . . . . .	126
5.5	Summary and Conclusions . . . . .	131
<b>6</b>	<b>Impulsive Events Observed in the NuSTAR Quiet Sun Dwell Observations</b>	<b>135</b>
6.1	Overview of Events . . . . .	136
6.2	Event Summaries . . . . .	137
6.2.1	Event 1 . . . . .	137
6.2.2	Event 2 . . . . .	137
6.2.3	Event 3 . . . . .	140
6.2.4	Event 4 . . . . .	143
6.2.5	Event 5 . . . . .	143
6.2.6	Event 6 . . . . .	145
6.2.7	Event 7 . . . . .	145
6.3	NuSTAR Spectral Analysis . . . . .	148
6.3.1	Event 1 . . . . .	148
6.3.2	Event 2 . . . . .	148
6.3.3	Event 3 . . . . .	151
6.3.4	Event 4 . . . . .	152
6.3.5	Event 5 . . . . .	153
6.3.6	Event 6 . . . . .	154
6.3.7	Event 7 . . . . .	154
6.4	DEM Analysis . . . . .	155

*Contents*

6.5	Correlation Between AIA and NuSTAR . . . . .	158
6.6	Non-Thermal Upper Limits . . . . .	159
6.7	Summary and Conclusions . . . . .	165
<b>7</b>	<b>Conclusions and Future Work</b>	<b>169</b>
7.1	Conclusions . . . . .	169
7.2	Future Work . . . . .	173
	<b>Bibliography</b>	<b>176</b>

# List of Tables

3.1	Overview of NuSTAR quiet Sun observing campaigns . . . . .	44
3.2	A summary of the NuSTAR orbits from 28 September 2018 observation. . .	45
3.3	A summary of the NuSTAR orbits from 12 January 2019 observation. . . .	47
3.4	A summary of the NuSTAR orbits from 25–26 April 2019 observation. . . .	50
3.5	A summary of the NuSTAR orbits from 02 July 2019 observation. . . . .	51
3.6	A summary of the NuSTAR orbits from 21 February 2020 observation. . . .	53
3.7	A summary of the NuSTAR orbits from 12–13 September 2020 observation. .	56
4.1	Spectral fitting results for the 28 September 2018 mosaic features . . . . .	98
5.1	An overview of the orbits used for the bright point integrated spectra . . .	128
6.1	A summary of the small-scale impulsive events from 21 February and 12–13 September 2020 . . . . .	136
6.2	A summary of the spectral fitting results for the small-scale impulsive events from 21 February and 12–13 September 2020 . . . . .	162

# List of Figures

1.1	Standard model for solar flares from Benz (2017) . . . . .	3
1.2	High- and low-frequency heating from Klimchuk (2015) . . . . .	5
1.3	Sunspot number against time . . . . .	7
1.4	The full solar disk during solar minimum, observed in soft X-rays . . . . .	8
1.5	DEMs of a CBP from Doschek et al. (2010) . . . . .	11
1.6	Flare frequency distribution from Hannah et al. (2008) . . . . .	14
1.7	Quiet Sun hard X-ray upper limits from Hannah et al. (2010) and Buitrago-Casas et al. (2022). . . . .	18
1.8	Diagram of X-ray bremsstrahlung . . . . .	21
2.1	NuSTAR instrument from Harrison et al. (2013) . . . . .	26
2.2	NuSTAR detectors . . . . .	27
2.3	An example of a NuSTAR ghost ray pattern . . . . .	29
2.4	NuSTAR solar observing modes . . . . .	33
2.5	NuSTAR individual mosaic tiles . . . . .	34
2.6	NuSTAR temperature responses . . . . .	35
2.7	NuSTAR instrument background from Wik et al. (2014) . . . . .	37
2.8	AIA temperature responses . . . . .	39
2.9	XRT temperature responses . . . . .	42
3.1	28 September 2018 NuSTAR QS Mosaics Overview . . . . .	46
3.2	12 January 2019 NuSTAR QS dwells overview . . . . .	48
3.3	12 January 2019 NuSTAR QS mosaics overview . . . . .	49
3.4	25–26 April 2019 NuSTAR QS mosaics overview . . . . .	51
3.5	02 July 2019 NuSTAR QS mosaics overview . . . . .	52
3.6	21 February 2020 NuSTAR QS dwells overview . . . . .	55
3.7	21 February and 12–13 September 2020 NuSTAR QS mosaics overview . . . . .	56
3.8	12–13 September 2020 NuSTAR QS dwells overview . . . . .	58
3.9	An example of simultaneously fitting mosaic pointings . . . . .	61
3.10	Simulated spectra using Sunxspex models . . . . .	67

*List of Figures*

4.1	28 September 2018 NuSTAR QS Mosaics Overview . . . . .	72
4.2	AIA 211 Å and HMI images showing the evolution of the EFR . . . . .	73
4.3	AIA and XRT images of the EFR . . . . .	74
4.4	AIA and XRT time profiles for the EFR . . . . .	75
4.5	NuSTAR spectral fitting for the EFR . . . . .	77
4.6	Temperature and emission measure vs. time for the EFR . . . . .	78
4.7	Examples of DEMs calculated with and without X-ray data . . . . .	79
4.8	DEMs for the EFR . . . . .	80
4.9	Non-thermal upper limits for the EFR . . . . .	82
4.10	AIA 211 Å and XRT Be-thin images of the three X-ray bright points . . . . .	83
4.11	AIA 211 Å and XRT Be-thin time profiles for the three X-ray bright points . . . . .	84
4.12	NuSTAR spectral fitting for the three X-ray bright points . . . . .	86
4.13	NuSTAR spectral fitting for the quiet Sun loops . . . . .	87
4.14	DEMs for the three X-ray bright points . . . . .	89
4.15	Non-thermal upper limits for BP1 and BP2 . . . . .	91
4.16	AIA and XRT images of the jet . . . . .	92
4.17	AIA, XRT, and NuSTAR time profiles for the jet . . . . .	93
4.18	NuSTAR spectral fitting for the jet . . . . .	94
4.19	Non-thermal upper limits for the jet . . . . .	95
4.20	NuSTAR and XRT images of the decayed active region . . . . .	97
4.21	NuSTAR spectral fitting for the decayed active region . . . . .	98
4.22	A comparison of DEMs of features from the 28 September 2018 mosaics . . . . .	99
5.1	21 February 2020 bright point overview . . . . .	104
5.2	12–13 September 2020 bright point overview . . . . .	105
5.3	February 2020 bright point, Flare 1 overview . . . . .	107
5.4	NuSTAR spectral fitting for Flare 1 . . . . .	109
5.5	DEMs for Flare 1 . . . . .	111
5.6	Non-thermal upper limits for Flare 1 . . . . .	113
5.7	February 2020 bright point, Flare 2 overview . . . . .	114
5.8	NuSTAR spectral fitting for Flare 2 . . . . .	116
5.9	Non-thermal upper limits for Flare 2 . . . . .	117
5.10	12–13 September 2020 bright point overview . . . . .	119
5.11	NuSTAR spectral fitting for the September 2020 bright point . . . . .	121
5.12	Temperature and emission measure vs. time for the September 2020 bright point . . . . .	122
5.13	DEMs for the September 2020 bright point . . . . .	124

*List of Figures*

5.14	Non-thermal upper limits for the September 2020 bright point . . . . .	125
5.15	Integrated NuSTAR spectra for the February and September 2020 bright points, single orbit . . . . .	127
5.16	Integrated NuSTAR spectra for the February 2020 bright point, multiple orbits	129
5.17	Integrated NuSTAR Spectra for the September 2020 bright point, multiple orbits . . . . .	130
6.1	21 February 2020, impulsive Event 1 overview . . . . .	138
6.2	21 February 2020, impulsive Event 2 overview . . . . .	139
6.3	21 February 2020, impulsive Event 3 overview . . . . .	141
6.4	12–13 September 2020, impulsive Event 4 overview . . . . .	142
6.5	12–13 September 2020, impulsive Event 5 overview . . . . .	144
6.6	12–13 September 2020, impulsive Event 6 overview . . . . .	146
6.7	12–13 September 2020, impulsive Event 7 overview . . . . .	147
6.8	NuSTAR spectral fitting for Event 1 . . . . .	149
6.9	NuSTAR spectral fitting for Event 2 . . . . .	150
6.10	NuSTAR spectral fitting for Event 3 . . . . .	152
6.11	NuSTAR spectral fitting for Event 4 . . . . .	153
6.12	NuSTAR spectral fitting for Event 5 . . . . .	154
6.13	NuSTAR spectral fitting for Event 6 . . . . .	155
6.14	NuSTAR spectral fitting for Event 7 . . . . .	156
6.15	DEMs for Events 1–7 . . . . .	157
6.16	AIA versus NuSTAR 2.2–3.2 keV flux for Events 1–7 . . . . .	160
6.17	AIA versus NuSTAR 3.2–5.0 keV flux for Events 1–7 . . . . .	161
6.18	Non-thermal upper limits Events 1–3 . . . . .	163
6.19	Non-thermal upper limits for Events 4–7 . . . . .	164
6.20	T-EM comparison plot for flares/microflares and quiet Sun events . . . . .	166

# Acknowledgements

First and foremost, this thesis would not have been possible without the support of my supervisor, Iain Hannah. Thank you so much for all of your help, guidance, and insightful feedback over the last four years, and for helping me figure out the right direction to take with the NuSTAR quiet Sun data.

I'd also like to thank everyone in the Astronomy and Astrophysics group for making the sixth floor of the Kelvin Building such a friendly working environment. Particular thanks to my second supervisor, Lyndsay Fletcher, whose enthusiasm for solar physics is inspirational.

Thanks must also go to everyone on the NuSTAR heliophysics team. The fortnightly telecons were always interesting, and the opportunity to receive your feedback on my work has been invaluable.

A huge thanks to all of the residents (past and present) of Room 604 for making the commute through rush hour traffic worthwhile. It's been great to see the office become more lively again after the pandemic, and I'm very grateful for all of your support and encouragement—especially during my thesis write-up and on the lead up to my viva. I'd like to give a special thanks to Kris and Natalia for the many helpful discussions about working with NuSTAR data.

Finally, I could not have undertaken this journey without the encouragement of my family. I am eternally grateful to my Mum and Dad for their unwavering support. Thank you to David and Hannah for distracting me with games of Mario Kart during my thesis write-up (even if I hardly ever won). Thanks to Merlin and Louie for all of the cuddles and emotional support. I'm also grateful to my grandparents for always encouraging a love of learning. Lastly, I'd like to thank my great aunt, Janette, whose unfailing love for life and positive attitude I've tried my best to emulate throughout my PhD.

# 1

## Introduction

For centuries, solar physics has been an exciting area of research, as the Sun's proximity to us allows the study of its behaviour in greater detail than is possible for any other star. While decades of solar research has given us insight into many dynamic processes that occur in the Sun, one question that remains unanswered is that of the high temperature of the Sun's corona compared to its surface. This is called the coronal heating problem, and the solution to this may lie in tiny heating events, which cannot be individually resolved. Ever-evolving instrumentation has provided the opportunity to observe the Sun with greater sensitivity and higher resolution, both spatial and temporal. This has enabled observations of increasingly small-scale phenomena, which could be key in understanding the mechanism that sustains the high temperature of the corona.

We begin this chapter by introducing the different layers of the solar atmosphere in Section 1.1, and discuss the coronal heating problem and its possible solutions in Section 1.2. Section 1.3 introduces the quiet Sun and gives a brief overview of the types of small-scale phenomena that can be found within it, with a focus on coronal bright points. In Section 1.5, we discuss solar X-ray emission mechanisms and analysis.

### 1.1 The Solar Atmosphere

The Sun's atmosphere is comprised of the following layers, in order of increasing height: the photosphere, the chromosphere, and the corona (Carroll & Ostlie 2007, pages 332–358). These layers are classified based on their respective temperatures and densities.

The innermost layer of the solar atmosphere is named the *photosphere*, which has a temperature of 5800 K and is  $\sim 500$  km thick. This is the layer that is the visible surface of

## 1.1 The Solar Atmosphere

the Sun. Dark regions can be seen on the photosphere, which are named *sunspots*, and are regions of strong magnetic field. The *chromosphere* is the next layer moving outwards, with the temperature increasing up to 10000 K. This layer extends to a height of  $\sim 2100$  km. The outermost layer in the solar atmosphere is the *corona*, which has an extremely hot temperature of  $\sim 10^6$  K, and a much lower density compared to the lower layers. Between the chromosphere and the corona, there is a thin *transition region*, throughout which the temperature and density change drastically. This sharp increase in temperature is an unsolved mystery in solar physics, termed the coronal heating problem (see Section 1.2).

In the corona, the plasma- $\beta$  (the ratio of the gas pressure to the magnetic pressure) is  $< 1$ . This means that the magnetic field dominates, and large loop structures can be observed in the corona as a consequence of this. When the Sun is magnetically active, active regions (regions of strong magnetic activity, which are associated with sunspots in the photosphere) can be observed in the corona. These regions can produce solar flares, intense brightenings that can be observed across a wide range of wavelengths. The Sun in the absence of active regions is referred to as the *quiet Sun*, which will be further discussed in Section 1.3.

### 1.1.1 Impulsive Energy Release in the Solar Atmosphere

Large-scale impulsive energy release in the Sun's atmosphere occurs during solar flares. These are intense brightenings in emission across a wide range of wavelengths, and these typically occur in active regions. During flares, the energy previously stored in the magnetic field is released due to magnetic reconnection, a reconfiguring of the magnetic field to a lower energy state. This magnetic energy is converted to particle acceleration and plasma heating (Benz 2017).

The “standard” picture of solar flares is shown in Figure 1.1. In this model, electrons are accelerated from the reconnection site down to the chromosphere, hence transferring energy from the corona to the chromosphere. When these electrons hit the dense plasma in the lower atmosphere, they produce hard X-rays (HXR) through non-thermal bremsstrahlung (see Section 1.5.4). These are referred to as HXR *footpoints*. The electrons also heat the chromosphere, causing material to “evaporate”, and expand up into the loop. This creates structures called flare loops, which are observed at soft X-ray (SXR) wavelengths.

Flares are often classified by their SXR flux in the 1–8 Å band detected by the Geostationary Operational Environmental Satellite (GOES). They are split into five different bands, which

## 1.1 The Solar Atmosphere

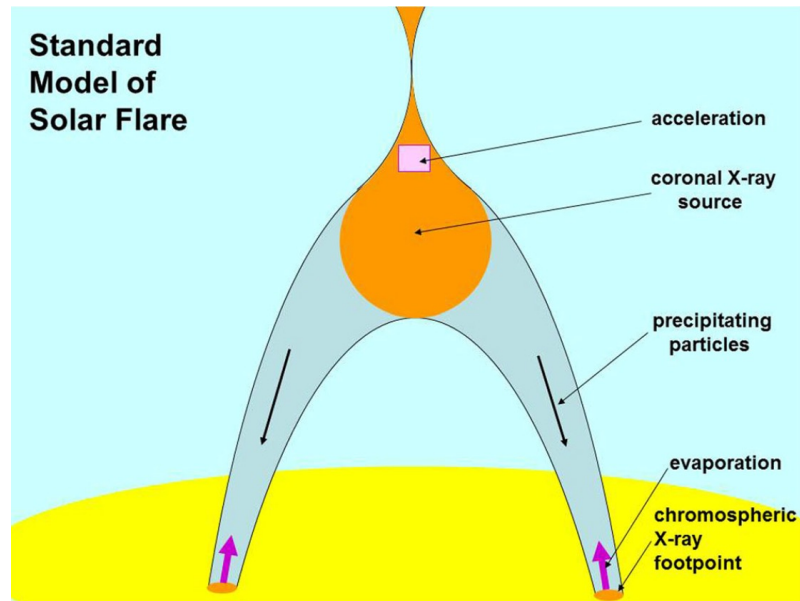


**Figure 1.1:** A schematic diagram showing the standard picture of solar flares. This figure is taken from [Benz \(2017\)](#).

are (from strongest to weakest SXR flux): X, M, C, B, A. The SXR flux decreases by an order of magnitude between each of these classes. A and B class flares are typically referred to as *microflares*.

Flares have a frequency distribution which takes the form of a negative power law ([Hudson 1991](#)), with smaller flares occurring much more frequently than large ones. As stated by [Hudson \(1991\)](#), this negative power law can be written as:

$$dN/dW \sim W^{-\alpha} \quad (1.1)$$

where  $N$  is the number of events,  $W$  is the energy of the flare, and  $\alpha$  is the power law index. As flares release energy that heats the surrounding atmosphere, their role in heating the corona has been investigated. [Hudson \(1991\)](#) found that, for flares to be the mechanism by which the corona is heated, this would require  $\alpha > 2$ , which would mean that small-scale events would dominate the distribution. Otherwise, large flares—which do not produce the energy required to sustain the high temperature of the corona, particularly during solar minimum—would dominate. One possible solution to the coronal heating is nanoflares, very small-scale energy release events (which will be discussed further in Section 1.2).

## 1.2 The Coronal Heating Problem

The outermost layer of the solar atmosphere, the corona, is orders of magnitude hotter than the surface of the Sun ( $\sim 10^6$  K, compared to  $\sim 6000$  K). While many studies have aimed to investigate the heating mechanism responsible for maintaining these high temperatures, the coronal heating problem remains yet unsolved. However, it is generally agreed upon that the source of the energy required to heat the corona must be stored in magnetic fields which become stressed due to photospheric motions (e.g. Klimchuk 2006). The heating source would also have to operate even in the absence of active regions, as the corona's high temperature is sustained even during solar minimum when there are no active regions on the disk. Solving the coronal heating problem requires identifying a source of heating which balances the losses due to thermal conduction and radiation, which are observed in both the quiet Sun and active regions (Withbroe & Noyes 1977).

The majority of coronal heating models involve either wave heating or magnetic reconnection. In wave heating models, upwards propagating waves carry energy from the photosphere through to the corona. Many of these models use Alfvén waves (which are traveling oscillations of ions and magnetic fields) as the mechanism which transports the energy (e.g. Tomczyk et al. 2007; McIntosh et al. 2011).

### 1.2.1 Parker's Nanoflares

Another leading theory was put forth by Parker (1988), who was motivated by observations of localised X-ray brightenings with energies down to  $10^{24}$  erg reported on by Lin et al. (1984). He suggested that the corona could be heated to the observed high temperatures by a multitude of small-scale impulsive energy release events, too small to be individually resolved. Parker termed such events *nanoflares*, and predicted that they would have energies of  $\sim 10^{24}$  erg or less, which is several orders of magnitude smaller than the energy released by large flares. He proposed that these nanoflares could occur as a result of the coronal magnetic field becoming gradually stressed and “braided” as a result of photospheric motions. This would lead to energy release via magnetic reconnection.

When solar flares occur, they release large amounts of energy into the the atmosphere, heating the surrounding plasma to temperatures up to 30 MK (e.g. Benz 2017). It is possible that nanoflares could heat the solar atmosphere through similar mechanisms to large flares, though on a much smaller scale. If this were the case, nanoflares would produce

## 1.2 The Coronal Heating Problem

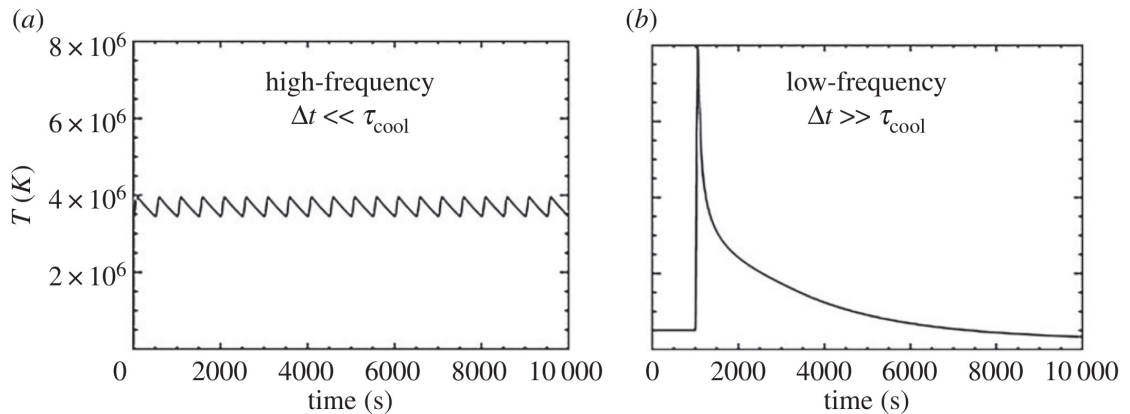


**Figure 1.2:** The temperature evolution of a magnetic strand when heated by high-frequency (left) and low-frequency (right) nanoflares. This figure is taken from Klimchuk (2015).

a weak non-thermal signature due to accelerated electrons. Detecting this component would require observations of higher energy X-rays.

### 1.2.2 Modelling

Nanoflares have been modelled using zero-dimensional (0-D) and one-dimensional (1-D) hydrodynamics codes, an example of which is the Enthalpy-Based Thermal Evolution of Loops (EBTEL) (Klimchuk et al. 2008; Cargill et al. 2012). This allows the time evolution of plasma parameters—such as temperature, density, and pressure—averaged along a loop in response to a heating pulse to be investigated.

The heating by nanoflares is considered to be impulsive. One important aspect when modelling coronal heating is the frequency at which loops are heated (e.g. Klimchuk 2015). The temperature evolution of a magnetic strand heated by high and low-frequency nanoflares is shown in Figure 1.2. In the high-frequency scenario, the time between heating events is much shorter than the cooling time of the strand. The strand does not have time to cool between heating events, and the temperature therefore fluctuates around some mean value. This results in a plasma with a very narrow (almost isothermal) temperature distribution. A sufficiently high frequency will produce a similar effect to steady heating.

Conversely, for low-frequency heating, each strand has sufficient time to cool before being re-heated. In this case, the plasma would have a much broader temperature distribution, with a significant amount of plasma at lower temperatures. A consequence

### 1.3 The Quiet Sun

of low-frequency nanoflare heating is the presence of very hot ( $> 5$  MK) plasma (e.g. Klimchuk 2017). This is because the heating rate would need to be extremely high to maintain the temperature of the corona in this scenario. However, this hot component would be expected to be very faint, and therefore difficult to detect.

HXR observations would allow a search for this hot component, as well as the non-thermal component that would be consistent with flare-like heating, as this emission would be dominated by bremsstrahlung continuum emission from a thermal and/or non-thermal population of electrons (see Section 1.5). In Chapters 4, 5, and 6, we search for these components in the faint HXR emission from small-scale sources observed with the Nuclear Spectroscopic Telescope Array (NuSTAR; Harrison et al. (2013)) in the quiet Sun during the recent solar minimum.

### 1.3 The Quiet Sun

It is well-known that the Sun's magnetic activity follows an 11 year cycle. At the height of this cycle, referred to as solar maximum, the Sun is very active, with a number of sunspots, active regions, and large flares. Conversely, during solar minimum, there are almost no sunspots, active regions or large flares. The term *quiet Sun* refers to a region of the Sun where there are no active regions or sunspots. During solar minimum, the entire solar disk is generally very quiet. Figure 1.3 plots the monthly number of sunspots on the solar disk over recent years. It can be seen in this plot that the most recent solar minimum occurred over 2018–2020, and that the Sun is currently in a much more active state. This plot also indicates the times of the NuSTAR quiet Sun observations which are studied in detail throughout this thesis.

While no large-scale activity occurs in the quiet Sun during solar minimum, numerous smaller features are observed on the disk, such as coronal bright points and emerging flux regions. Many small-scale impulsive events also occur, such as quiet Sun jets and mini-filament eruptions, which produce emission across a range of wavelengths. Throughout this section, the types of phenomena that can be found in the quiet Sun during solar minimum are described. During the recent solar minimum, NuSTAR observed these phenomena for the first time at HXR energies (which are analysed throughout Chapters 4, 5, and 6).

### 1.3 The Quiet Sun

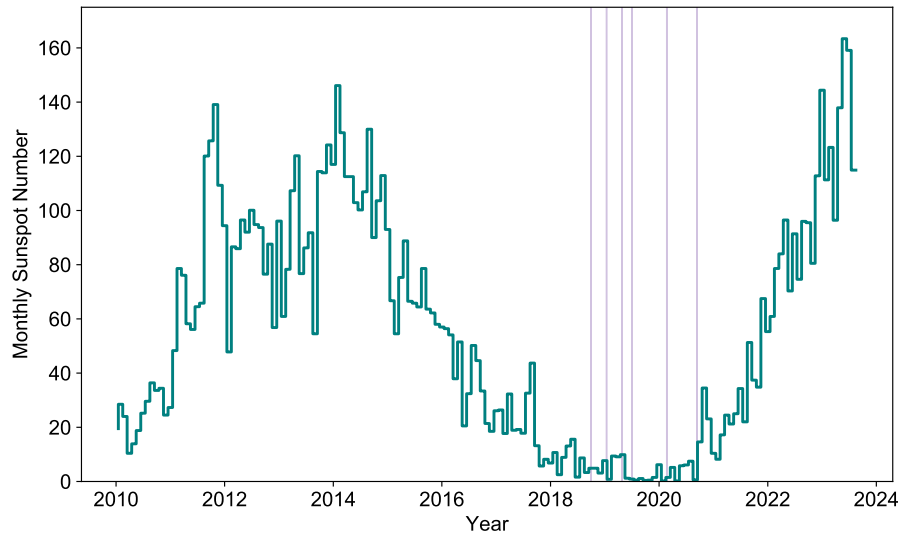


**Figure 1.3:** The monthly number of sunspots on the solar disk against time (blue), demonstrating the Sun’s 11-year activity cycle. The times of the NuSTAR solar minimum quiet Sun observing campaigns, which are summarised later in Chapter 3, are also highlighted on this plot (purple).

#### 1.3.1 Coronal Bright Points

When the quiet Sun is viewed in extreme ultraviolet (EUV) and soft X-rays (SXR), many *coronal bright points* (CBPs)—often referred to as X-ray bright points (XBPs) when viewed in X-rays—can be observed, distributed over the entire solar disk. An example of this is shown in Figure 1.4. CBPs are defined as small-scale bipolar loop structures in the lower corona which show enhanced emission in EUV and SXR. Their characteristics indicate that they are essentially smaller-scale counterparts to active regions (Madjarska 2019).

CBPs were first observed in SXR as point-like features with the Apollo Telescope Mount onboard SkyLab, an Earth-orbiting laboratory, in 1973 (Vaiana et al. 1973). Since then, much work has been done on understanding these features based on observations at EUV and SXR wavelengths, which is summarised throughout the rest of this section.

As they are ubiquitous in the quiet Sun, the role of CBPs in heating the corona is of interest. However, the opportunity to investigate their contribution to coronal heating has been limited by the lack of a solar HXR telescope with the required sensitivity to search for the weak hot ( $> 5$  MK) and/or non-thermal components in their emission that are predicted by coronal heating models. In Chapters 4 and 5, we search for these components in the

### 1.3 The Quiet Sun

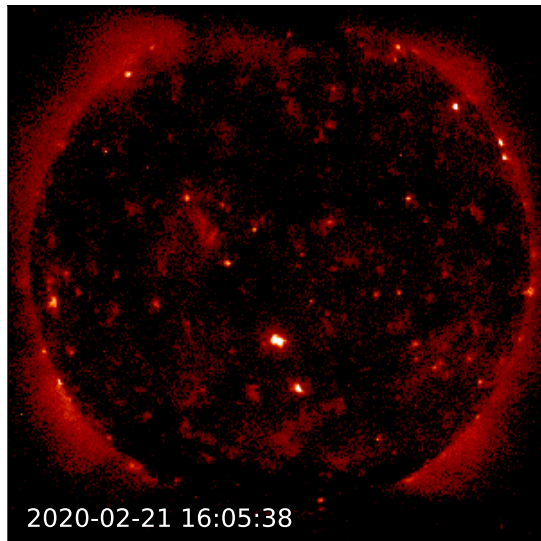


**Figure 1.4:** A full disk image of the Sun in soft X-rays from the X-Ray Telescope on board Hinode. Many small X-ray bright points can be seen distributed across the disk.

HXR emission from X-ray bright points observed for the first time with NuSTAR, which is an astrophysics mission, during solar minimum.

#### General Characteristics

Observations of CBPs in both X-rays and EUV have confirmed that they can reach diameters up to  $\sim 60''$ , and are generally located on boundaries of the magnetic network (where magnetic fields encircle convective supergranulation cells) (Golub et al. 1974; Mou et al. 2018). Statistical studies of CBP lifetimes in SXR found that they exist on average in X-rays for  $\sim 10$  hours (Golub et al. 1974; Harvey et al. 1993). In EUV, these features are longer lived, generally persisting for up to  $\sim 20$  hours (Alipour & Safari 2015).

CBPs consist of several loops, with heights averaging at  $\sim 5000$  km at coronal temperatures (Tian et al. 2007). Studies have found that these loops have different temperatures, with the hotter loops overlying the cooler ones (Doschek et al. 2010; Kwon et al. 2012).

SXR observations have suggested that the number of CBPs on the disk is anti-correlated with the solar cycle (Golub et al. 1979). However, it has been shown that this is purely an effect of the lower background at solar minimum compared to solar maximum (Nakakubo & Hara 2000). The lower background intensity allows the detection of fainter CBPs, thus

### 1.3 The Quiet Sun

creating the impression of increased numbers. On average, the number of CBPs that appear on the solar disk each day is  $\sim 600$  (Alipour & Safari 2015).

#### Previous Work on CBPs Observed in EUV and Soft X-Rays

When observed at EUV and SXR wavelengths, the emission from CBPs has been shown to exhibit variability on short timescales (down to a few minutes) throughout their lifetimes (Habbal & Withbroe 1981; Alexander et al. 2011).

EUV and SXR observations of CBPs have also been used to investigate their temperatures. This was done for the first time by Golub et al. (1974), who used X-ray observations from the Skylab S-054 X-ray telescope, and determined the temperatures of several CBPs from the ratios between the observed intensities in two X-ray filters. This study found temperatures of 1.3–1.7 MK. A further study by Kariyappa et al. (2011) used the same technique with observations from the X-ray Telescope (XRT) on board Hinode to find temperatures lying between 1.1–3.4 MK. Of the seven CBPs studied, six had temperatures  $\leq 2.3$  MK, with the 3.4 MK being an atypical case. They investigated the evolution of the intensity ratios, and found that they showed significant variability, indicating changes in temperature. However, using intensity ratios to obtain a temperature assumes isothermal plasma, which is not necessarily the case for CBPs.

Another study by Alexander et al. (2011) studied a single CBP over its lifetime ( $\sim 13$  hours) observed with Hinode/XRT and the Extreme-Ultraviolet Imaging Spectrometer (EIS), also on board Hinode. This study found that the X-ray emission showed significant variability over this time, and that the temperature (obtained using EM loci, which are discussed in Section 3.2.3) stayed almost isothermal, ranging between 1.2–1.7 MK.

All of the above results indicate that CBPs are heated to coronal temperatures, ranging between 1–3.4 MK. While these studies investigated CBP temperatures by assuming an isothermal plasma, other EUV and SXR studies of CBPs have investigated the multi-thermal nature of these features. This has been done via differential emission measure (DEM) analysis.

The DEM of a source (see Section 1.5.3) shows the distribution of emission over a range of temperatures, indicating the contribution from each temperature to the overall emission. The first DEM analysis of a CBP was carried out by Brosius et al. (2008), using an EUV spectrum observed with the EUNIS sounding rocket (covering a temperature range of

### 1.3 The Quiet Sun

$\log(T) \sim 5.3\text{--}6.4$ ). The resulting DEM was found to have only one peak at  $\log(T) \sim 6.15$  (and a local minimum at  $\log(T) \sim 5.35$ ).

A similar study was conducted by [Doschek et al. \(2010\)](#) using data from Hinode/EIS. Their results from calculating a DEM for several sub-regions with a CBP, as well as for a background region, are shown in Figure 1.5. It can be seen that these DEMs have three-peak structures, with peaks at  $\log(T) \sim 5.2$ , 5.8, and 6.15. The authors attributed the lowest temperature peak to the presence of O IV and He II. The middle peak is at the same level in all of the sub-regions of the CBP as it is in the background DEM, leading to the conclusion that this peak is a property of the background coronal plasma. The hottest peak at  $\log(T) \sim 6.15$  (a result also found by [Brosius et al. \(2008\)](#)) is more than an order of magnitude higher than in the DEM for the background, and so the authors concluded that this peak describes the CBP itself. This study also determined that the CBPs were composed of hotter loops lying on top of ones at lower temperatures. [Chitta et al. \(2013\)](#) calculated DEMs for CBPs using EUV imaging data from the Atmospheric Imaging Assembly (AIA) on board the Solar Dynamics Observatory, and found that the resulting DEMs showed peaks at  $\log(T) \sim 5.8$  and 6.3.

All of these DEM calculations using EUV data were well constrained up to  $\log(T) \sim 6.3$ . However, the DEMs relied on extrapolation at temperatures above this, and were therefore subject to large uncertainties. In order to obtain a more reliable result for the high temperature tail of the DEM, X-ray data would have to be included in the calculation.

#### Associated Phenomena

Just as active regions are the site of large solar flare events, coronal bright points can be associated with smaller-scale transient phenomena, such as microflares, jets, and eruptions. When CBPs were first observed with the X-ray telescope onboard Skylab, it was found that regions within the CBPs showed heightened X-ray emission for durations on the order of minutes, as reported on by [Golub et al. \(1974\)](#). This study found that 5–10 % of the CBPs investigated showed this flaring behaviour, and the authors suggested that these small flares (often termed microflares) occurring in CBPs are analogous to large solar flares occurring in active regions.

[Strong et al. \(1992\)](#) investigated the variability in the SXR emission from several CBPs observed with the Yohkoh Soft X-ray Telescope. They found that the intensity of the SXR emission from the CBPs varied over time scales ranging between a few minutes and hours. In addition to this, some CBPs were found to flare occasionally, resulting in an increase of

### 1.3 The Quiet Sun

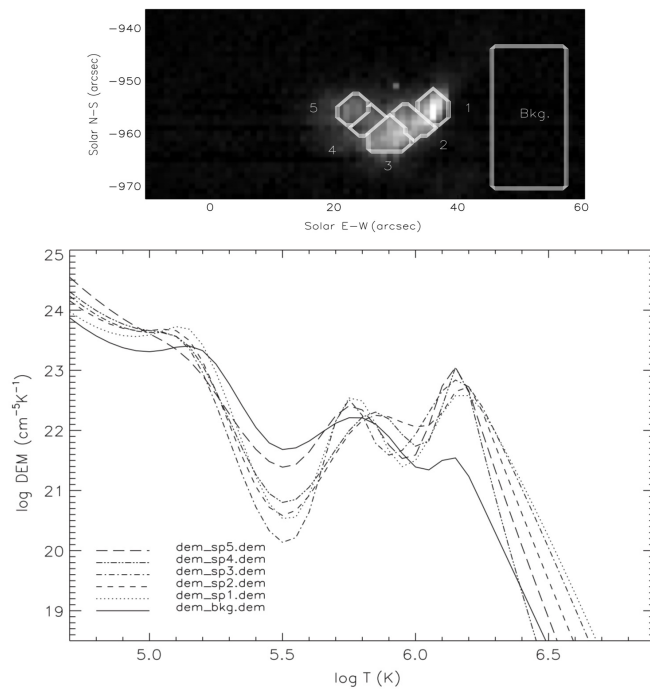


**Figure 1.5:** An example of CBP DEMs obtained in [Doschek et al. \(2010\)](#), using EUV data from Hinode/EIS. (Top) An image of the CBP, split into several sub-regions (as well as a background region) for the DEM calculation. (Bottom) The DEMs calculated for each of the sub-regions. This figure is taken from [Doschek et al. \(2010\)](#).

### 1.3 The Quiet Sun

SXR emission of more than an order of magnitude. This work also reported the observation of X-ray jets from CBPs. Brightenings were observed extending along loops, originating from the CBPs. A study of over 500 CBPs observed in SXR, also with Yohkoh, was later conducted by [Harvey et al. \(1993\)](#). This study similarly found that the SXR emission from CBPs was highly variable, and that they generally produced a flare several hours after their emergence, with some of the observed CBPs flaring more than once. In some cases, mini-eruptions were observed in the CBPs, with larger loop structures connected to the flaring region of the CBPs being found to brighten.

Microflares have also been observed in CBPs with Hinode/XRT. [Kamio et al. \(2011\)](#) investigated microflares observed in CBPs with Hinode/XRT (defining these microflares as transient brightenings of durations of a few minutes), in both quiet Sun regions and coronal holes. They found that the SXR intensity increased over timescales of a few minutes, creating spikes in the XRT time profiles. XRT's Be-thin filter is more sensitive to higher temperature emission than Al-Poly (see Section 2.3), and the flares were detected more strongly in Be-thin, suggesting that the flares take place at high coronal temperatures. These impulsive peaks in the XRT time profiles were found to coincide with peaks in the Fe XV and Fe XVI lines (observed with Hinode/EIS), which form at high temperatures of  $\sim 2$  MK. The peak in the hotter lines was followed by another peak that was only observed in cooler lines (He II and O V), suggesting plasma cooling. This cooling behaviour is commonly observed in active region flares, and so the authors concluded that these CBP microflares are similar to these events but on a smaller scale.

#### 1.3.2 Emerging Flux Regions

Emerging Flux Regions (EFRs) are formed when new concentrations of magnetic flux form on the solar surface. When the new flux emerges, it interacts with the pre-existing magnetic field, leading to the formation of new magnetic structures. The flux emergence can follow one of two paths. It may continue to grow and evolve until it becomes a large-scale active region (e.g. [van Driel-Gesztelyi & Green 2015](#)), which can remain on the solar surface for days or weeks. However, the growth of the EFR may not be sufficient to produce an active region, and instead a small-scale, shorter-lived CBP is formed (e.g. [Kontogiannis et al. 2020](#)).

[Kontogiannis et al. \(2020\)](#) investigated the DEM of an EFR that went on to become a CBP using data from the Extreme-Ultraviolet Imaging Telescope (EIT) on the Solar and Heliospheric Observatory (SOHO). They found that, similar to bright point DEM analyses

### 1.3 The Quiet Sun

(Brosius et al. 2008; Doschek et al. 2010), the DEM showed a peak at  $\log(T) \sim 6.1$ . In Section 4.1 of Chapter 4, we study an EFR (which went on to become an active region) observed in HXRs with NuSTAR during solar minimum, including recovering its DEM.

#### 1.3.3 Quiet Sun Flares

Small-scale transient soft X-ray and EUV brightenings can be observed in the quiet Sun. While these may be associated with CBPs (as discussed in Section 1.3.1), these brightenings can also occur where there are no resolvable pre-existing magnetic structures (Krucker et al. 1997; Krucker & Benz 1998; Aschwanden et al. 2000; Parnell & Jupp 2000). The nanoflare coronal heating theory of Parker (1988) prompted a number of analyses of these small-scale impulsive brightenings which aimed to determine whether they could occur at a high enough frequency to sustain the high temperature of the corona, and whether they operate through similar mechanisms to large flares.

Several different names have been used for these types of events. Small-scale impulsive SXR brightenings observed in the quiet Sun with the Yohkoh Soft X-ray telescope were reported on by Krucker et al. (1997). This study detected several brightenings—which the authors referred to as *network flares*—and determined an extrapolated occurrence rate of one event on the whole disk per 3 s. They also found that the total energy of these network flares ranged from  $10^{25}$ – $10^{26}$  erg, which is several orders of magnitude smaller than typical active region microflares (e.g. Hannah et al. 2008). These events showed a number of similarities to large flares, including evidence of chromospheric evaporation and similar ratios of energies radiated in SXRs and radio waves. However, they did note that these events had much cooler temperatures ( $\sim 1$  MK) and shorter durations ( $\sim 10$  minutes) compared to larger flares.

Other early works on small-scale impulsive quiet Sun events referred to them as *nanoflares*. Several of these studies investigated the power law index,  $\alpha$ , of the flare frequency distribution (see Section 1.1.1). These have generally found values of  $\alpha \sim 2$ , as shown in Figure 1.6. The first EUV nanoflare frequency distribution was obtained by Krucker & Benz (1998), who studied a number of heating events with energies between  $8 \times 10^{24}$ – $1.6 \times 10^{26}$  erg observed with the SOHO/EIT, finding  $\alpha = 2.3$ – $2.6$ . A further study of EUV nanoflares observed with SOHO/EIT (Benz & Krucker 2002) yielded  $\alpha = 2.1$ – $2.3$ . The events analysed in this study, which each had energies lying in the range  $5 \times 10^{24}$ – $5 \times 10^{26}$  erg, were found to have contribute 12% of the energy radiated by the corona in the quiet Sun region from which the nanoflares originated.

### 1.3 The Quiet Sun

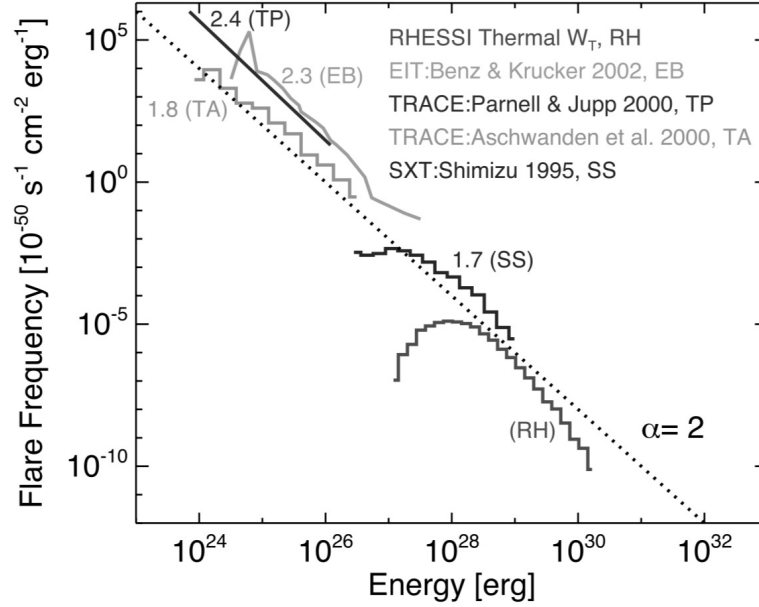


**Figure 1.6:** A flare frequency distribution, combining studies on EUV nanoflares (at smaller energies) and active region microflares observed in HXRs with the Reuven Ramaty High Energy Solar Spectroscopic Imager (RHESSI) (at larger energies). The dotted line shows the slope of  $\alpha = 2$ . This figure is taken from [Hannah et al. \(2008\)](#).

[Parnell & Jupp \(2000\)](#) analysed thousands of impulsive increases in EUV emission observed with the Transition Region and Coronal Explorer (TRACE). They found that, assuming a constant line-of-sight depth,  $\alpha$  lay between 2.4–2.6. When a constant line-of-sight depth was not assumed, this value decreased to 2.0–2.1. This study found events with energies down to  $10^{23}$  erg. [Aschwanden et al. \(2000\)](#) studied 281 EUV nanoflares also observed with TRACE. They found that their events had energies ranging from  $10^{24}$ – $10^{26}$  erg, and behaved in similar ways to large flares, but with lower temperatures of  $< 2$  MK. They found  $\alpha = 1.8$ , and attributed the discrepancy compared to [Krucker & Benz \(1998\)](#) and [Parnell & Jupp \(2000\)](#) to different nanoflare selection criteria and model assumptions.

A more recent work by [Kuhar et al. \(2018\)](#) investigated HXR spectroscopic observations of three impulsive quiet Sun brightenings, captured with NuSTAR between 2016–2017. This gave the opportunity to search for hot and non-thermal components in the events' HXR emission. The quiet Sun flares were found to have higher temperatures, of 3.2–4.1 MK, compared to the EUV nanoflares and the SXR network flares. However, no high temperature ( $> 5$  MK) or non-thermal component was found in their NuSTAR HXR spectra.

In Chapter 6, we investigate a number of quiet Sun flares also observed with NuSTAR.

### 1.3 The Quiet Sun

These events were observed during the recent solar minimum, and the lower background level at this time compared to when the events from [Kuhar et al. \(2018\)](#) were observed allowed even fainter events to be detected.

#### 1.3.4 Mini-Filament Eruptions

Filaments are long structures on the solar surface which are cool and dense compared to the surrounding plasma. Coronal mass ejections (CMEs) are large-scale eruptions of material from the solar atmosphere. It has been observed that the majority of CMEs are associated with erupting filaments ([Munro et al. 1979](#)). Several mechanisms have been suggested to trigger filament eruptions, including flux emergence ([Chen & Shibata 2000](#)), flux cancellation ([Zhang et al. 2001](#)), and magnetohydrodynamic (MHD) instabilities ([Török & Kliem 2005](#)). Models of these events involve a rising filament, which stretches the overlying field lines and initiates magnetic reconnection beneath the filament. This can then eject plasma into space, forming a CME.

However, smaller-scale eruptive events have been observed in the quiet Sun, as shown by [Hermans & Martin \(1986\)](#). This work investigated a number of small-scale eruptive filaments (later referred to as mini-filament eruptions), and found that these events were a smaller version (averaging a length of 15'') of large-scale filament eruptions. They estimated that these events would have an occurrence rate of > 600 eruptions per day over the whole disk, which is a much greater occurrence rate compared to large filament eruptions. Mini-filament eruptions can be associated with CBPs (e.g. [Hong et al. 2014](#)). In Chapter 6, we investigate the time evolution and thermal properties of a mini-filament eruption observed in HXRs with NuSTAR.

#### 1.3.5 Jets

Solar jets are the ejection of plasma in a collimated beam along straight magnetic field lines (e.g. [Shen 2021](#)). Jets have been observed and studied extensively at EUV and SXR wavelengths. They can originate from several different environments, and are observed all through the solar cycle. Jets can occur in the quiet Sun ([Panesar et al. 2016](#)), or in coronal hole regions ([Panesar et al. 2018](#)), with observations suggesting that the jets from these regions are triggered by magnetic flux cancellation (where a mini-filament forms over the magnetic neutral line between positive and negative-polarity magnetic fluxes,

### 1.3 The Quiet Sun

and cancellation of these fluxes causes it to become unstable, which forms a jet). They can also originate from active regions (Mulay et al. 2017).

As discussed in Section 1.3.1, jets (particularly those observed in coronal holes) are often rooted in coronal bright points (Moore et al. 1977). A number of studies have found that jets can also occur together with mini-filament eruptions (Adams et al. 2014; Hong et al. 2016). Jets typically have an inverted-Y shape, which are named “anemone jets” (Shibata et al. 1994). In Section 4.3 of Chapter 4, we perform HXR spectroscopy on a quiet Sun jet observed with NuSTAR.

#### 1.3.6 Full-Disk Quiet Sun Emission

Some previous studies have investigated the SXR emission from the whole Sun. During the solar minimum of 2009, the SphinX (Solar PHotometer IN X-rays) mission provided sensitive spectroscopic SXR observations of the Sun at an energy range of 1–15 keV. Sylwester et al. (2012) analysed data from the quietest time periods from this data through spectral fitting. They fitted the X-ray spectra for 27 time intervals, and found temperatures that ranged from 1.7–1.9 MK, and emission measures (see Section 1.5.3) between  $4 \times 10^{47}$  and  $1.1 \times 10^{48} \text{ cm}^{-3}$ . The authors compared their results to imaging observations from Hinode/XRT, from which they deduced that the three brightest X-ray bright points contributed only 1.6% of the full-disk X-ray emission that SphinX observed, with emission from general coronal structures dominating.

A follow-up to this study was presented by Sylwester et al. (2019), which analysed data from hundreds of quiet time intervals. They fitted the quiet Sun X-ray spectra for times where there was no activity, X-ray brightenings, or GOES sub-A class microflares. They found that the temperatures obtained from the spectral fitting ranged from 1.69–1.86 MK. However, they found that their spectra were not well-described by isothermal models at energies  $> 2.5 \text{ keV}$ , and therefore also calculated differential emission measures (DEMs), showing the distribution of the emission over temperature (see Section 1.5.3). They found that the resulting DEMs had a cool component at 1.6 MK, but also a hot component which varied between 2.5–3.5 MK depending on whether the time interval contained no activity, or an X-ray brightening or microflare. However, they found no evidence in their data of the hot ( $> 5 \text{ MK}$ ) component that is implied by the nanoflare theory for coronal heating (Cargill 1994). They concluded that they found no components at temperatures  $> \sim 3 \text{ MK}$ .

The Solar X-ray Monitor (XSM; Vadawale et al. (2014)) on board the Chandrayaan-2 Orbiter observed the quiet Sun during the recent solar minimum from September 2019–May 2020

#### 1.4 Hard X-ray Observations of the Quiet Sun

(Vadawale et al. 2021). The aim of the Chandrayaan-2 mission—which is in a lunar orbit—is to study the elemental composition of the Moon’s surface through X-ray fluorescence spectroscopy, wherein the characteristic X-ray lines emitted by different elements upon excitation by solar X-rays are measured. This requires two X-ray detectors: one to measure the X-ray fluorescence spectrum from the lunar surface, the other to measure the incident solar X-ray spectrum. The latter is XSM, which can also be used for solar physics. XSM measures the X-ray spectrum from the full solar disk at energies from 1–15 keV. A recent study by Mondal et al. (2023) used the disk-integrated SXR data obtained by XSM during solar minimum, combined with EUV data from the Solar Dynamic Observatory’s Atmospheric Imaging Assembly to calculate differential emission measures (see Section 3.2.3) of the quiet Sun and X-ray bright points. Their full-Sun DEM showed two peaks, the strongest around 1 MK, and a smaller (by  $\sim 2$ –3 orders of magnitude) at  $\log(T) \sim 6.1$ –6.4. The authors concluded that the lower temperature peak likely represented the diffuse corona, and they found that the smaller peak at higher temperatures was dominated by X-ray bright points. This result is in line with the result found by Sylwester et al. (2012) from SphinX data that general coronal structures dominated their observed SXR emission over coronal bright points.

The integrated quiet Sun emission from the full disk has also been investigated through HXR observations. Details of these studies are discussed in the next section.

#### 1.4 Hard X-ray Observations of the Quiet Sun

As discussed in Section 1.2.1, nanoflare models predict a high temperature ( $> 5$  MK) component. If they were heating the atmosphere through similar mechanisms to large flares, they would also be expected to produce a weak non-thermal component. Both cases would result in a weak HXR signature. However, the lack of a dedicated solar HXR instrument with the required sensitivity has limited the opportunity to search for these signatures in faint quiet Sun X-ray sources. Solar HXR telescopes, such as the Reuven-Ramaty High Energy Solar Spectroscopic Imager (RHESSI; Lin et al. (2002))—which observed from 2002–2018—have been optimised for the observation of bright sources, such as large solar flares. RHESSI therefore did not have the sensitivity required to individually resolve faint HXR sources in the quiet Sun, such as X-ray bright points.

While RHESSI could not be used to study individual features, upper limits could be obtained from the whole Sun in the absence of flares and active regions. Hannah et al. (2007, 2010)

## 1.4 Hard X-ray Observations of the Quiet Sun

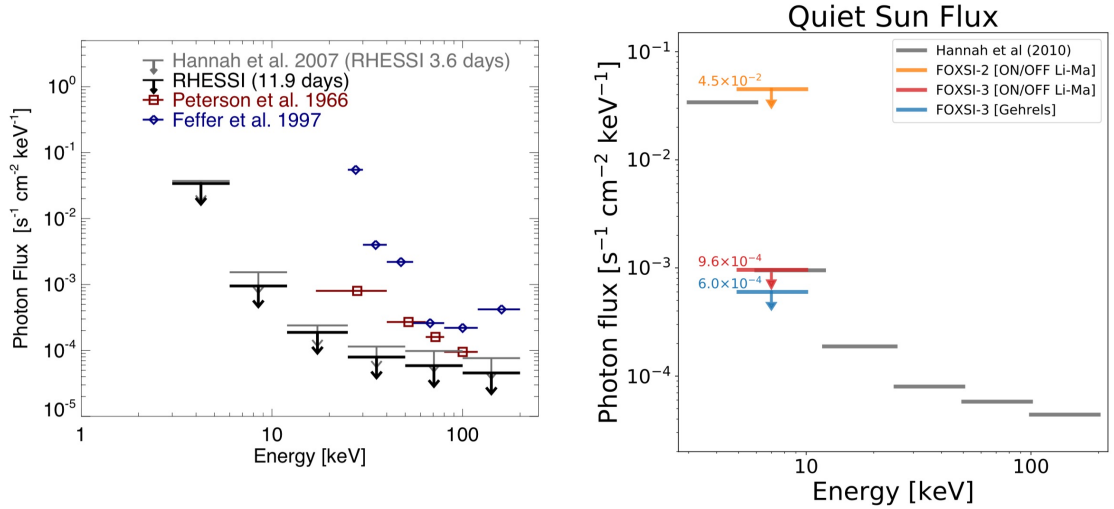


**Figure 1.7:** (Left) Upper limits on the HXR emission from the quiet Sun obtained using RHESSI data, taken from Hannah et al. (2010). (Right) Upper limits obtained using FOXSI data, taken from Buitrago-Casas et al. (2022). This plot includes a comparison to the earlier RHESSI work of Hannah et al. (2010).

determined upper limits on the HXR emission in the 3–200 keV energy range from the quiet Sun using RHESSI data. This was achieved using an off-pointing mode of observation called fan-beam modulation, which allowed the weak HXR emission from the full disk to be studied. To obtain these upper limits, Hannah et al. (2010) combined a total of 11.9 days of data from 19 different observations. The resulting upper limits from this study are shown in Figure 1.7 (left panel).

The RHESSI upper limits were compared to nanoflare models (e.g. Klimchuk et al. 2008). When constrained in terms of non-thermal emission, it was found that a very steep non-thermal distribution of electrons (see Section 1.5.4) with a spectral index  $> 5$ , extending down to very low energies ( $\sim 1$  keV) would be consistent with the observed upper limits. As this result assumed that the observed upper limits were purely non-thermal, and any additional thermal component would reduce the amount of non-thermal emission further, it was concluded that it was unlikely that nanoflares could heat the corona through similar mechanisms to large flares.

Another hard X-ray instrument which has recently observed the Sun is the Focusing Optics X-ray Solar Imager (FOXSI; Glesener et al. (2016)) sounding rocket. FOXSI, which has completed three observing campaigns, observes hard X-rays in the energy range 5–20 keV. FOXSI uses focusing optics, and has a sensitivity  $\sim 10$  times greater than RHESSI (Athiray et al. 2020). Buitrago-Casas et al. (2022) also determined upper limits on the HXR emission

## 1.5 X-Ray Emission From the Sun

from the quiet Sun, using  $\sim 6.5$  minutes of data from FOXSI-3. The results from this work, including a comparison with [Hannah et al. \(2010\)](#), are shown in Figure 1.7 (right panel). This figure demonstrates that the FOXSI upper limits are similar to those found using RHESSI data in [Hannah et al. \(2010\)](#), though required only  $\sim 1/2600$  of the observing time in comparison due to FOXSI's superior sensitivity.

The Nuclear Spectroscopic Telescope Array (NuSTAR; [Harrison et al. \(2013\)](#)) is a HXR astrophysics telescope, but is capable of observing the Sun ([Grefenstette et al. 2016](#)). A detailed overview of the NuSTAR instrument is presented in Section 2.1. During the recent solar minimum, six NuSTAR quiet Sun observing campaigns were carried out, summarised in Section 3.1. NuSTAR uses focusing optics, allowing it to have a much higher sensitivity than RHESSI ([Grefenstette et al. 2016](#)). Additionally, it can observe lower energies, down to  $\sim 2$  keV, compared to FOXSI. NuSTAR can be used to obtain HXR spectra for individual quiet Sun features, like X-ray bright points.

## 1.5 X-Ray Emission From the Sun

The work presented throughout Chapters 4, 5, and 6 involves the analysis of X-ray observations of quiet Sun phenomena. These X-ray observations can be used to diagnose the thermal and non-thermal properties of the emitting plasma. In this section, we introduce the mechanisms which produce solar X-ray emission.

At lower X-ray energies, the solar spectrum is dominated by a thermal bremsstrahlung continuum (free-free emission). In Section 1.5.2, we discuss both thermal and non-thermal bremsstrahlung, also introducing the concept of *emission measure*. There is also a contribution to the solar X-ray spectrum from atomic spectral lines (bound-bound emission), which is briefly discussed in Section 1.5.1.

### 1.5.1 Spectral Lines

One diagnostic which is often used when investigating processes occurring in the solar atmosphere is X-ray emission lines, which are produced by bound-bound processes. Measuring these lines with a spectrometer can provide insight into various plasma properties, such as temperature, density, magnetic field strength, and doppler velocities.

## 1.5 X-Ray Emission From the Sun

CHIANTI (Dere et al. 1997) is a comprehensive atomic database which contains all of the information on the properties of emission lines that is required when analysing X-ray spectra. In later chapters, we use CHIANTI—assuming coronal abundances (Feldman 1992)—to generate temperature responses for various EUV and X-ray instruments (see Sections 2.1.4, 2.2.1, and 2.3).

In Chapters 4–6, we analyse X-ray spectra of quiet Sun phenomena from NuSTAR. There are a number of X-ray spectral lines which lie within the range of NuSTAR’s temperature sensitivity. These are produced by many different elements, including ionised Fe, Ca, Ni, S, K, and Ar (Del Zanna & Mason 2018). However, while many lines form at energies and temperatures that NuSTAR is sensitive to, NuSTAR’s spectral resolution is not sufficient for most of these lines to be identified in NuSTAR solar spectra. This means that we must obtain information about the emitting plasma’s properties from the bremsstrahlung continuum.

A line from Ca XIX, and an iron line complex at 6.7 keV (formed from the Fe XXV and several Fe XXIV satellites) can be identified in some NuSTAR microflare spectra (Duncan et al. 2021). These lines are characteristics of hot flaring plasma (Phillips 2004). However, these form at higher temperatures ( $> 10$  MK) than are present in the quiet Sun.

### 1.5.2 Bremsstrahlung

The thermal bremsstrahlung continuum dominates solar X-ray spectra at low energies. Bremsstrahlung, also known as “braking radiation”, is the process through which an electron is deflected and therefore decelerated by a nearby charged particle (typically a proton). The electron’s lost kinetic energy is converted to a photon, resulting in an X-ray being emitted. This emission mechanism is illustrated in Figure 1.8.

The simplified form of the bremsstrahlung photon flux spectrum  $I(\epsilon)$  can be written as:

$$I(\epsilon) = \frac{1}{4\pi R^2} \int_V \int_{\epsilon}^{\infty} n(\mathbf{r}) F(E, \mathbf{r}) Q(\epsilon, E) dE dV \quad (1.2)$$

where  $V$  is the volume of the emitting source,  $\mathbf{r}$  is the position on the Sun,  $n(\mathbf{r})$  is the plasma number density,  $F(E, \mathbf{r})$  is the electron flux spectrum in electron energy  $E$ , and  $Q(\epsilon, E)$  is the bremsstrahlung cross section (Holman et al. 2011).  $R$  is the distance between the source and the X-ray detector, and the division by  $4\pi R^2$  is on the assumption that the source emits isotropically. The integration over electron energies in this equation is only

## 1.5 X-Ray Emission From the Sun

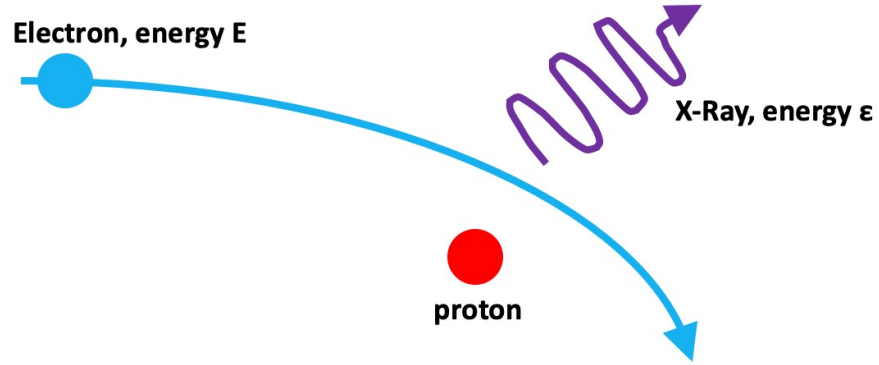


**Figure 1.8:** A diagram showing the process of X-ray bremsstrahlung, a free-free process wherein a electrons is deflected by a charged particle, and an X-ray is emitted.

performed over  $E > \epsilon$ . This is because electrons with energies of  $E < \epsilon$  cannot radiate a photon with energy  $\epsilon$ .

### 1.5.3 Thermal Bremsstrahlung

When the energy distribution of the electrons is a Maxwell-Boltzmann distribution, X-rays are produced via thermal bremsstrahlung. The electron flux density in a Maxwellian distribution for an isothermal plasma is given by:

$$F(E) = \frac{2^{3/2}}{(\pi m_e)^{1/2}} \frac{n(\mathbf{r})E}{(kT(\mathbf{r}))^{3/2}} \exp\left(\frac{-E}{kT(\mathbf{r})}\right) \quad (1.3)$$

where  $E$  is the electron energy,  $k$  is the Boltzmann constant,  $m_e$  is the electron mass, and  $T$  is the temperature of the plasma (Brown & Emslie 1988).

For an isothermal plasma, the photon spectrum due to thermal bremsstrahlung takes the form:

$$I(\epsilon) \propto \frac{n^2(\mathbf{r})V(\mathbf{r})}{\epsilon T^{1/2}(\mathbf{r})} \exp\left(\frac{-\epsilon}{kT(\mathbf{r})}\right) \quad (1.4)$$

## 1.5 X-Ray Emission From the Sun

where  $\epsilon$  is photon energy and  $V(\mathbf{r})$  is the volume of the emitting source. The  $n^2(\mathbf{r})V(\mathbf{r})$  term is an important plasma parameter, called the *emission measure*, which will be discussed later in this section.

The total thermal emission from an isothermal and homogeneous plasma is a combination of the thermal bremsstrahlung continuum and X-ray emission lines. Therefore, a thermal model for a source can be obtained by summing the photon spectrum due to the continuum and the photon spectrum due to spectral lines:

$$I_{\text{total}}(\epsilon) = I_{\text{thermal bremsstrahlung}}(\epsilon) + I_{\text{emission lines}}(\epsilon) \quad (1.5)$$

The resulting model photon spectrum, which depends on plasma parameters such as temperature and emission measure, can be used when fitting the observed X-ray spectrum. In Chapters 4, 5, and 6, we fit NuSTAR HXR spectra using an X-ray spectral fitting program called XSPEC (Arnaud et al. 1999). XSPEC contains the “APEC” (Astrophysical Plasma Emission Code) thermal model. Rather than the CHIANTI database (see Section 1.5.1), the APEC model uses the Astrophysical Plasma Emission Database<sup>1</sup> (APED).

However, XSPEC has no non-thermal model for solar analysis. Therefore, when finding non-thermal upper limits in Chapters 4, 5, and 6, we instead use Sunxspex<sup>2</sup>, a new X-ray spectral fitting program. As this analysis (method detailed in Section 3.2.4) requires the use of a thermal model, we use Sunxspex’s `f_vth` model (which is calculated using CHIANTI) rather than APEC.

### Emission Measure

The emission measure is an important parameter in solar X-ray analysis. This value is related to the electron number density  $n_e$  and the volume of the source  $V$ , and can be written as (Phillips et al. 2008, page 94):

$$EM = \int_V n_e^2 dV = n_e^2 V \quad [\text{photons cm}^{-3}] \quad (1.6)$$

---

<sup>1</sup><http://www.atomdb.org/faq.php>

<sup>2</sup><https://github.com/sunpy/sunxspex>

## 1.5 X-Ray Emission From the Sun

The first of the above expressions is for a general case, with the second assuming an isothermal and homogeneous plasma. The emission measure is equal to the number of photons emitted per unit volume.

For a plasma that is *not* isothermal and homogeneous, the concept of a *differential emission measure* (DEM) must be introduced. The DEM,  $\xi(T)$ , is a measure of how much plasma is emitting at each temperature. For a multi-thermal plasma, the emission measure is the DEM integrated over all temperatures, and can therefore be re-expressed as:

$$EM = \int_V n_e^2 dV = \int_T \xi(T) dT \quad [\text{photons cm}^{-3}] \quad (1.7)$$

The recovery of a source's DEM is an ill-posed inverse problem (Jefferies et al. 1972; Craig & Brown 1977), and therefore cannot be done directly. In Section 3.2.3, we detail the inverse regularisation method of Hannah & Kontar (2012) for DEM analysis. This method is used a number of times throughout Chapters 4, 5, and 6 to reconstruct the DEMs for quiet Sun features, in order to investigate their multi-thermal emission.

An estimate of the instantaneous thermal energy of a source can be obtained using the emission measure, along with other plasma parameters. We discuss this further in Section 3.2.4.

### 1.5.4 Non-Thermal Bremsstrahlung

When a population of electrons is accelerated out of the Maxwellian distribution (as in solar flares), it is said to be *non-thermal*, and X-rays are emitted through non-thermal bremsstrahlung. This emission mechanism dominates at energies  $> 10$  keV.

The non-thermal distribution of electrons takes the form of a power law (Kontar et al. 2011):

$$F(E > E_C) = AE^{-\delta} \quad (1.8)$$

where  $A$  is a normalisation constant and  $\delta$  is the power-law index, which is the slope of the electron distribution.  $E_C$  is the low-energy cutoff, which is the lowest possible energy in the electron distribution.

## 1.5 X-Ray Emission From the Sun

The total electron flux,  $N_{TOT}$ , in this distribution can then be obtained by integrating the distribution over all energies above the low-energy cutoff:

$$N_{TOT} = \int_{E_C}^{\infty} F(E) dE \quad (1.9)$$

An expression for the normalisation constant  $A$  can be obtained by substituting Equation 1.8 into Equation 1.9:

$$N_{TOT} = \int_{E_C}^{\infty} AE^{-\delta} dE = \frac{AE_C^{1-\delta}}{\delta - 1} \quad (1.10)$$

The above equation can then be rearranged to obtain an expression for  $A$ . An expression for the power in the non-thermal distribution can then be found via:

$$P(> E_C) = \int_{E_C}^{\infty} F(E)E dE = \int_{E_C}^{\infty} AE^{-\delta+1} dE = \frac{AE_C^{2-\delta}}{\delta - 2} = N_{TOT}E_C \frac{\delta - 1}{\delta - 2} \quad (1.11)$$

Non-thermal X-rays are often considered using one of two scenarios, *thin target* and *thick target*. For the thin target scenario, the plasma that the electrons are interacting with has a low density, as is the case in the solar corona. As the density is low, the energy losses experienced by the electrons while propagating through this plasma are not significant. In the case of a thick target, the plasma density is high, an example of which is the solar chromosphere. The electrons will interact much more frequently with the plasma, and will therefore lose all of their energy. This is the scenario that produces the HXR footpoints which are observed in large flares (see Section 1.1.1).

In Section 3.2.4, we discuss a method to determine upper limits on non-thermal emission from HXR spectra of quiet Sun sources, which involves calculating non-thermal powers using Equation 1.11. This method requires the use of a thick target non-thermal model. The X-ray spectral fitting program XSPEC (Arnaud et al. 1999) is used extensively in this thesis to fit NuSTAR HXR spectra. While XSPEC contains the APEC thermal model (see Section 1.5.3), it is limited in that it has no non-thermal model for solar analysis. When calculating the non-thermal upper limits, we instead use the non-thermal thick target model in Sunxspex.

# 2

## Instrumentation

This thesis makes use of data from several instruments, an overview of which will be given in this chapter. The work presented in later chapters is focused around quiet Sun data from the Nuclear Spectroscopic Telescope Array (NuSTAR), a hard X-ray imaging spectrometer which is discussed in Section 2.1. We also make use of data from two instruments on board the Solar Dynamics Observatory (SDO, Section 2.2): the Atmospheric Imaging Assembly (AIA, Section 2.2.1) and the Helioseismic and Magnetic Imager (HMI, Section 2.2.2). Finally, we give a brief overview of the X-Ray Telescope (XRT) on board Hinode in Section 2.3.

### 2.1 The Nuclear Spectroscopic Telescope Array

The Nuclear Spectroscopic Telescope Array (NuSTAR; [Harrison et al. \(2013\)](#)) is a hard X-ray (HXR) telescope, which uses focusing optics and observes over an energy range of  $\sim 2\text{--}79$  keV. The NuSTAR satellite was launched on 13 June 2012, and was the first HXR focusing telescope to be in orbit. It was designed by NASA to observe the HXR emission from far off astrophysical sources, such as active galaxies and supernova remnants.

While NuSTAR was designed as an astrophysics mission, it can also observe the Sun without damaging the optics ([Grefenstette et al. 2016](#)). Since NuSTAR was first pointed at the Sun in September 2014, there have been a number of NuSTAR solar observing campaigns<sup>1</sup>.

---

<sup>1</sup>An overview of all of the NuSTAR solar observations can be found at [https://ianan.github.io/nsigh\\_all/](https://ianan.github.io/nsigh_all/)

## 2.1 The Nuclear Spectroscopic Telescope Array

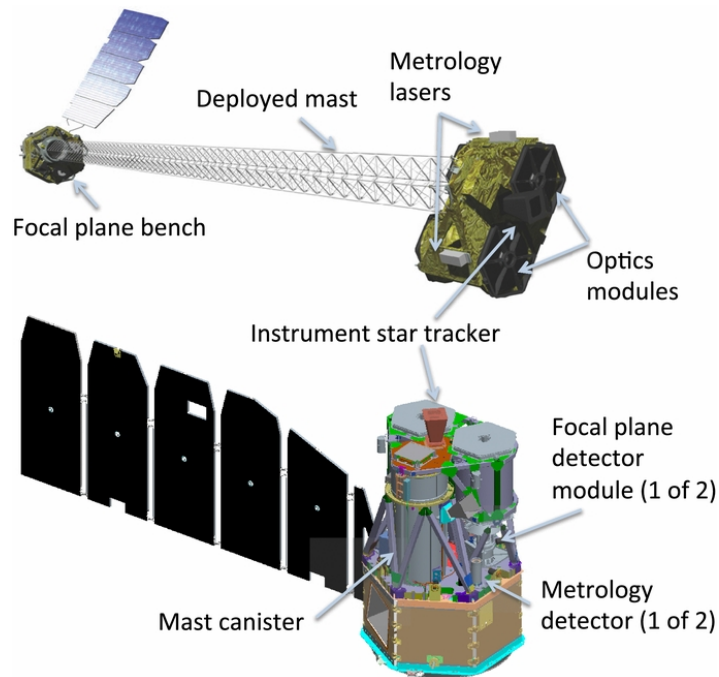


**Figure 2.1:** Diagram of NuSTAR, showing the deployed (top) and stowed (bottom) configurations. This figure was taken from [Harrison et al. \(2013\)](#).

### 2.1.1 Detectors and Optics

A diagram of the NuSTAR instrument is shown in Figure 2.1. NuSTAR has two co-aligned telescopes, each with their own focal plane module: FPMA and FPMB. These are located in the focal plane bench ([Harrison et al. 2013](#)), which can be seen in the diagram of NuSTAR's deployed configuration in the top panel of Figure 2.1. Incoming HXRs are focused by two Wolter-I conical approximation optics, consisting of 133 nested grazing incidence shells, onto the focal plane modules. The two focal plane modules, which are mounted on a 10 m mast, are comprised of four CdZnTe pixel detectors in a  $2 \times 2$  array, labelled DET0–3. This configuration is illustrated in Figure 2.2. These four detectors are separated by chip-gaps, and any photons incident on these gaps will not be detected. It is therefore desirable for a source to be positioned far away from any detector gaps. Both FPMs have a field-of-view (FOV) of  $12' \times 12'$  (which does not cover the entire solar disk). NuSTAR's point spread function (PSF) has a full-width half maximum (FWHM) of  $18''$  and a half-power diameter of  $60''$  ([Madsen et al. 2015](#)). NuSTAR was previously calibrated at energies down to 2.5 keV ([Grefenstette et al. 2016](#)), though a recent calibration update has extended this even further down to 2.2 keV ([Madsen et al. 2021](#)).

## 2.1 The Nuclear Spectroscopic Telescope Array

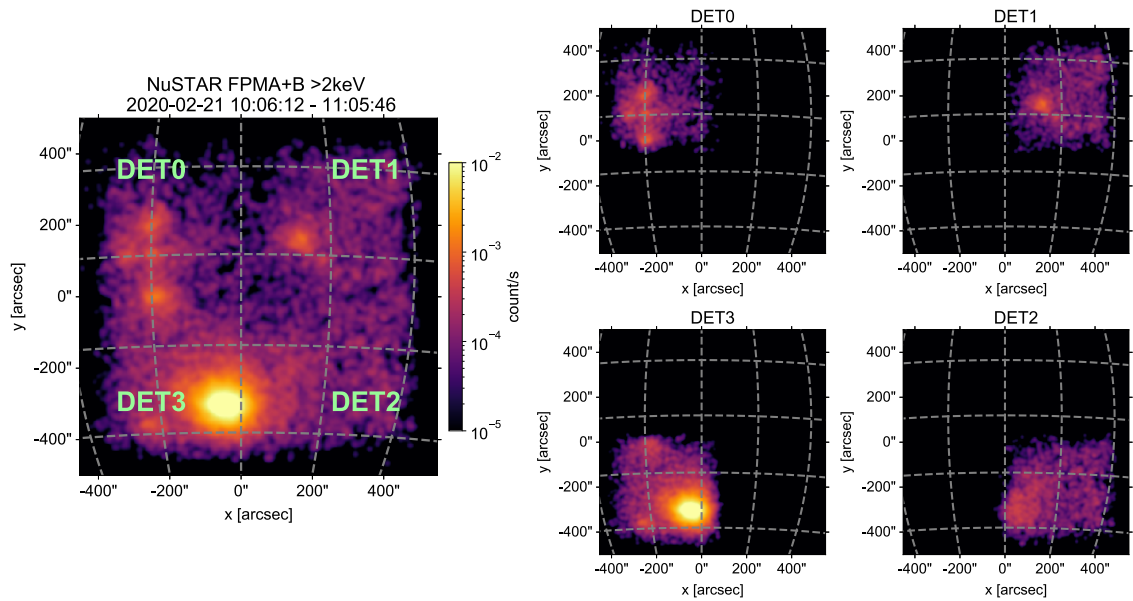


**Figure 2.2:** An example NuSTAR image (where NuSTAR was pointed at disk centre), illustrating the detector configuration. (Left) An image including counts from all detectors (DET0–3), which have gaps between them. (Right) NuSTAR images showing the counts in the four detectors separately.

Due to its use of focusing optics, NuSTAR has a much greater sensitivity compared to previous solar HXR instruments, such as the Reuven Ramaty Solar Spectroscopic Imager (RHESSI; [Lin et al. \(2002\)](#)). RHESSI was a HXR imaging spectrometer which was designed to study flares, using indirect imaging methods. NuSTAR’s effective area is more than ten times larger and its detector background (see Section 2.1.5) is more than four orders of magnitude smaller compared to RHESSI ([Grefenstette et al. 2016](#)). This results in NuSTAR having a significantly higher sensitivity, which is required to observe faint emission from quiet Sun HXR sources.

### Pointing

NuSTAR’s pointing is determined using star trackers ([Harrison et al. 2013](#)), also referred to as Camera Head Units (CHUs). NuSTAR has four of these CHUs, pointing in approximately orthogonal directions. In solar observations, three of the CHUs (CHU1–3), which are pointing perpendicular from the detector plane in different directions, are used to determine NuSTAR’s pointing. Throughout an orbit, the CHU combination being used generally changes multiple times, for example when one or more of the star trackers is blocked by the Earth. These changes in CHU combination result in pointing changes. If

## 2.1 The Nuclear Spectroscopic Telescope Array

a source lies close to a detector gap (or the edge of the FOV), any pointing changes can in turn cause the source to move in and out of these gaps. This can therefore result in significant changes to the detected HXR emission. Consequently, pointing shifts must be carefully monitored when analysing NuSTAR solar data. There can be long intervals between any changes in CHU combination (as long as  $\sim 30$  minutes in the data analysed in this thesis), but NuSTAR's pointing can remain unstable for up to a few minutes during a change. It is desirable for an event to be captured during a time period with no CHU changes.

As the fourth star tracker is pointed in the same direction as the detectors (towards the Sun), it is blinded and therefore unusable during solar observations. This results in NuSTAR having a pointing uncertainty of  $\sim 1.5'$  (e.g. Glesener et al. 2017). This means that NuSTAR's pointing must be corrected for by aligning the NuSTAR data with data from an instrument with a greater pointing accuracy, such as AIA. This is achieved manually by shifting the NuSTAR images so that bright sources in the FOV overlies the corresponding sources in AIA (a good example of convincing agreement between NuSTAR and AIA images with multiple sources can be found later in this thesis, in Figure 5.1, top left panel).

### Throughput and Livetime

NuSTAR is a photon counting device, and NuSTAR records a photon's energy, time of detection, and location on the detector when an event is triggered. When an incoming photon is detected, NuSTAR has a deadtime of 2.5 ms (Harrison et al. 2013), during which time NuSTAR cannot detect any other incoming photons. This deadtime is a result of NuSTAR having a limited throughput of 400 counts  $\text{s}^{-1}$ . This throughput is adequate for astrophysical sources, but can prove challenging when NuSTAR is observing the Sun. If there is a bright source in NuSTAR's FOV, this will dominate the throughput, meaning that the majority of incoming photons will not be detected and it will therefore be difficult to detect the HXR emission from any fainter sources present (Grefenstette et al. 2016).

We define the *livetime* as the fraction of time during which NuSTAR is open to detecting incoming photons. When observing bright sources, NuSTAR's limited throughput can result in significantly reduced livetime (for example,  $< 1\%$  for an active region microflare with GOES class A5.7 reported on by Glesener et al. (2020)). Fortunately, this issue is also not significant for the quiet Sun observations; the lack of extremely bright sources on the disk allows livetimes up to  $\sim 90\%$ , as seen later in Section 3.1. For microflares with GOES classes of high B and above, the livetime is so low that the NuSTAR electronics begin

## 2.1 The Nuclear Spectroscopic Telescope Array

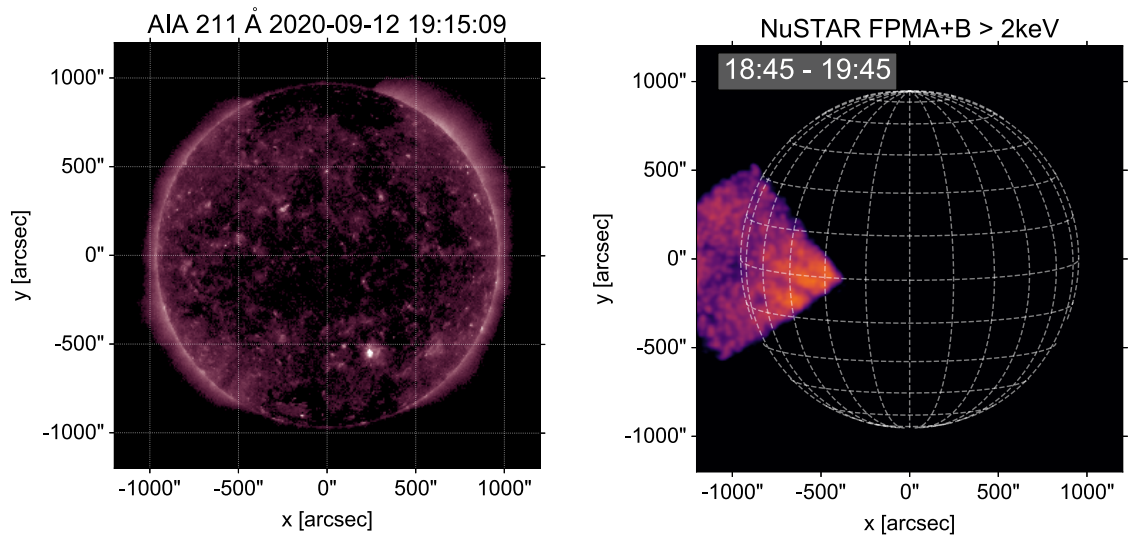


**Figure 2.3:** A NuSTAR image (right) showing an example of the distinctive ghost ray pattern, as well as the corresponding EUV image from AIA 211 Å (left). The NuSTAR ghost rays originate from the bright source in AIA 211 Å which is located at  $\sim (250'', -550'')$ .

to reject photons. The rejection of events by the electronics means that the accepted count rate is even lower than the maximum throughput of  $400 \text{ counts s}^{-1}$ . During bright microflares, the accepted count rate can fall to an order of magnitude below the maximum throughput.

### Ghost Rays

In addition to the limited throughput, using NuSTAR as a solar observer presents another challenge in the form of “ghost rays” (Grefenstette et al. 2016). The NuSTAR optics are a set of grazing incidence mirrors, and a photon that is correctly focused will be reflected twice off of these mirrors before detection. However, it is possible for a photon to be reflected only once off of the optics (either off of the primary or the secondary mirror, depending on the angle of incidence of the photon), which means that sources outside of the double-bounce FOV can be detected. These improperly focused photons are referred to as ghost rays (Madsen et al. 2015). These become an issue when there is a very bright source on the disk (for example an active region or a flare) which is outside of the FOV. In this scenario, NuSTAR will detect some ghost rays from the bright source even though it is not pointed at it.

Ghost rays produce a distinctive radial pattern that can be traced back to the source, an

## 2.1 The Nuclear Spectroscopic Telescope Array

example of which is shown in Figure 2.3. The direction of the ghost ray pattern suggests that they originated from the bright source in the EUV image from AIA 211 Å located at  $\sim (250'', -550'')$ . The ghost ray flux is reduced by a factor of 20–100 (if the source is  $0.1\text{--}0.5^\circ$  away) compared to if the source were in the FOV. If the source were more than  $0.5^\circ$  away, the ghost ray rate would be considerably smaller (see Figure 7, Appendix B in Grefenstette et al. (2016)). Fortunately, as the work presented in this thesis deals with quiet Sun observations from solar minimum (when there were few bright active regions or flares on this disk), their effect on this analysis is minimal.

### Grade

All events detected by NuSTAR are assigned a “grade”, an integer between 0–31 which is based on how the incoming photon interacts with the pixels in a  $3 \times 3$  grid surrounding the triggered pixel. Every 2.5 ms, the first pixel to be triggered is readout, and during the 2.5 ms readout time, what is happening in the neighbouring pixels is recorded via grade. Events where only one pixel (the central pixel) is above the trigger threshold are called grade-0 events. However, when an event is detected in more than one neighbouring pixels, this results in grades  $> 0$ . The mapping between the number and orientation of pixels that are above the trigger threshold in the  $3 \times 3$  grid around the central pixel and grade is detailed in Figure 2 of the NuSTAR Data Analysis Software Guide<sup>2</sup>.

In low-lifetime NuSTAR microflare observations, pileup can be an issue. The high count rates from these bright sources can lead to pileup through two different scenarios: two photons hitting the same pixel may be registered by the on-board electronics as the same event, or two photons hitting two adjacent pixels may be classified as a single grade  $> 0$  event. Due to the latter scenario, it is typically recommended to remove all events with grades  $> 0$  for solar analysis (Grefenstette et al. 2016). However, the lifetime is significantly higher in the NuSTAR quiet Sun observations compared to microflare observations, meaning the the above issue is much less severe. As a result, it is not necessary to remove events with grade  $> 0$  from the quiet Sun data, since few exist.

---

<sup>2</sup>[https://heasarc.gsfc.nasa.gov/docs/nustar/analysis/nustar\\_swguide.pdf](https://heasarc.gsfc.nasa.gov/docs/nustar/analysis/nustar_swguide.pdf)

## 2.1 The Nuclear Spectroscopic Telescope Array

### 2.1.2 Data Processing

NuSTAR data downloaded from the archive (HEASARC<sup>3</sup>) must first be processed before use. This is done via the NuSTAR Data Analysis Software (NuSTARDAS<sup>4</sup>), which is a part of HEASoft<sup>5</sup> and is detailed in the NuSTAR Data Analysis Guide<sup>6</sup>. The routine which is used to process Level 1 data, `nupipeline`, is comprised of three stages and produces Level 3 files which are properly calibrated.

The first of the three stages is data calibration, where the the event files are calibrated using the calibration database (CALDB<sup>7</sup>). In this stage, the thermal motions of the mast are corrected for using the laser meteorology system. The attitude data from the CHU combinations is then processed, bad and hot pixels are identified, and each event is allocated a grade. Gain corrections are also applied to convert the data from electronic units (the charge from each detected photon) to energy units (keV), and the position of each event on the NuSTAR detector is converted to sky co-ordinates. These data calibration steps together produce a Level 1a event file, which is a list of all of the detected events, each with an energy, grade, position, and time of detection.

The data from the Level 1a files can then be screened according to orbital and instrument parameters and event properties. During this stage, which produces level 2 event files, bad pixels and non-grade 0 events can be removed. Data from times during which NuSTAR was moving through the South Atlantic Anomaly (SAA) or was occulted by the Earth can also be removed. The data can also be filtered to include events from only a specific time interval or spatial region, using Good Time Interval (GTI) and Region (REG) files, respectively. It is generally recommended to remove all non-grade 0 events for NuSTAR solar observations at this stage (Grefenstette et al. 2016). However, as discussed in the previous section, filtering out the non-grade 0 events is not required for the high livetime quiet Sun observations.

During the third and final stage of data processing, high-level products (Level 3) are obtained, such as images, energy spectra, response files and lightcurves. It is from this stage that the necessary files for NuSTAR spectral analysis (method detailed in Section 3.2.2) are produced. These are the Pulse Height Amplitude, Ancillary Response, and Redistribution Matrix files (PHA, ARF, and RMF, respectively). The PHA file contains the energy spectrum

---

<sup>3</sup><https://heasarc.gsfc.nasa.gov>

<sup>4</sup><https://heasarc.gsfc.nasa.gov/docs/nustar/analysis/>

<sup>5</sup><https://heasarc.gsfc.nasa.gov/docs/software/lheasoft/>

<sup>6</sup>[https://heasarc.gsfc.nasa.gov/docs/nustar/analysis/nustar\\_swguide.pdf](https://heasarc.gsfc.nasa.gov/docs/nustar/analysis/nustar_swguide.pdf)

<sup>7</sup>[https://heasarc.gsfc.nasa.gov/docs/heasarc/caldb/caldb\\_intro.html](https://heasarc.gsfc.nasa.gov/docs/heasarc/caldb/caldb_intro.html)

## 2.1 The Nuclear Spectroscopic Telescope Array

obtained from the data which has been filtered for a particular region of the detector, time range, and grade. The ARF file contains information about the effective area of the telescope, while the RMF file contains information about the conversion between photons and counts. Together, the ARF and RMF files are used to determine how the incoming photons were converted to a count spectrum, information which is required for spectral analysis (see Section 3.2.2). These files are also required to obtain the spectral response matrix (SRM), which is needed to calculate the NuSTAR temperature responses discussed in Section 2.1.4.

There is an additional step of data processing which is specific to the NuSTAR solar observations. The above stages result in data with spatial co-ordinates in units of right ascension and declination (R.A./Dec). These can be converted to solar helioprojective co-ordinates using code from the NuSTAR solar Python repository<sup>8</sup>. This means that NuSTAR images can be produced by spatially binning the solar co-ordinate event list, which can then be compared to data from other instruments, such as AIA and XRT (Grefenstette et al. 2016). This allows the NuSTAR data to be aligned with data from these instruments, meaning that NuSTAR's pointing can be corrected.

### 2.1.3 Solar Observing Modes

NuSTAR's FOV is  $12' \times 12'$ , which means that it can only cover a fraction of the solar disk. Over the course of NuSTAR's  $\sim 97$  minute Earth orbit, it spends  $\sim$  an hour in sunlight. When NuSTAR's pointing is kept constant (meaning a constant right ascension and declination; the pointing can drift across the solar disk slightly) for a whole orbit, it therefore provides  $\sim$  an hour of data on a region or feature of interest. This observing mode is referred to as a *dwelt*, an example of which is shown in Figure 2.4 (left panel). Dwells are ideal for tracking the time evolution of interesting features or events.

However, NuSTAR also has the capability to observe the entire solar disk over the course of an orbit when it is used in *full-disk mosaic* mode. NuSTAR's pointing is regularly shifted over the course of the orbit in order to build up an image of the full disk, an example of which is shown in Figure 2.4 (right panel). This mosaic example contains a particularly bright source on the East limb, and the NuSTAR detector gaps can be seen cutting through this feature.

---

<sup>8</sup>[https://github.com/NuSTAR/nustar\\_pysolar](https://github.com/NuSTAR/nustar_pysolar)

## 2.1 The Nuclear Spectroscopic Telescope Array

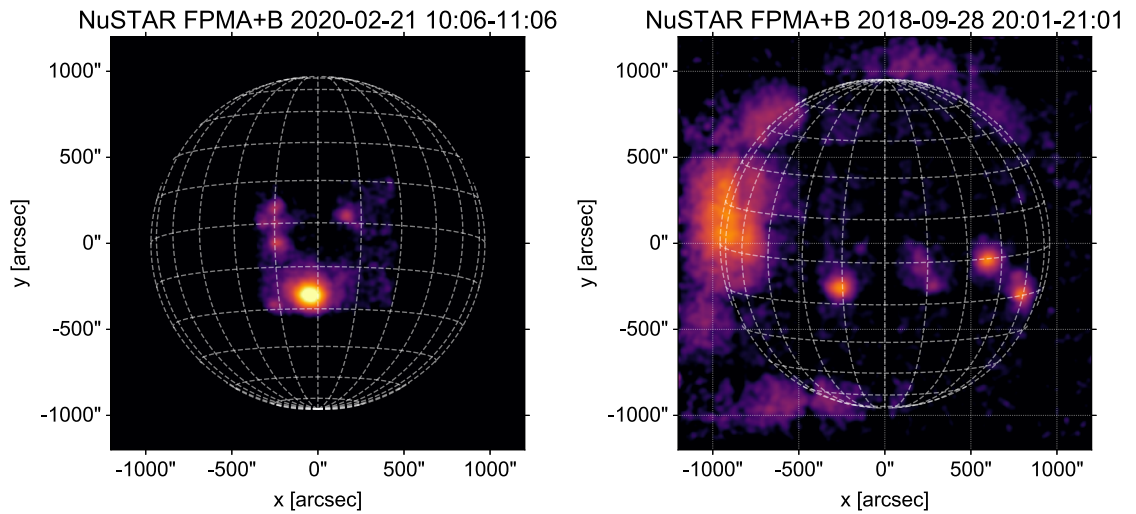


**Figure 2.4:** An example of each of NuSTAR’s solar observing modes. (Left) An example of a dwell orbit, where NuSTAR’s pointing remained fixed for  $\sim 1$  hour. (Right) An example of a full-disk mosaic orbit, where NuSTAR’s pointing was shifted throughout to build up an image of the full Sun. NuSTAR’s detector gaps can clearly be seen in this mosaic cutting through the bright feature on the East limb. The 25 individual mosaic tiles (each observed for  $\sim 100$  s, and arranged in a  $5 \times 5$  pattern) that make up this mosaic are shown in Figure 2.5.

During the first ever NuSTAR solar observation (on 29 April 2015), NuSTAR spent one of the orbits in full-disk mosaic mode, and the resulting mosaic had 16 tiles in a  $4 \times 4$  pattern. However, all of the quiet Sun mosaics from solar minimum (detailed later in Section 3.1) contain 25 tiles (pointings labelled P1–25), in a  $5 \times 5$  pattern. Each tile has an observing time of  $\sim 100$  s. Unlike dwells, this observing mode is therefore not suitable for a thorough investigation of the time evolution of features or events. However, this mode was used several times during the recent solar minimum in order to obtain information about many sources on the disk at the same time. These mosaics (and also dwells from solar minimum) are summarised in Section 3.1.

The NuSTAR quiet Sun mosaics were taken such that sources on the disk could be sampled multiple times, increasing the amount of data for each feature, and allowing a limited investigation of their time evolution. The 25 individual tiles of the mosaic in Figure 2.4 are shown separately in Figure 2.5. It can be seen that the first tile is in the top right corner, and NuSTAR then rastered over the entire solar disk. When NuSTAR’s pointing shifted between mosaic tiles, it shifted by  $\sim$  half of the FOV. Consequently, areas on the disk are sampled four times. However, this shifting pattern also means that regions at the limb are sampled only twice, or once in each of the four corners. This is illustrated in Figure 2.5. Therefore, when making the mosaic images, a correction must be applied to account for

## 2.1 The Nuclear Spectroscopic Telescope Array

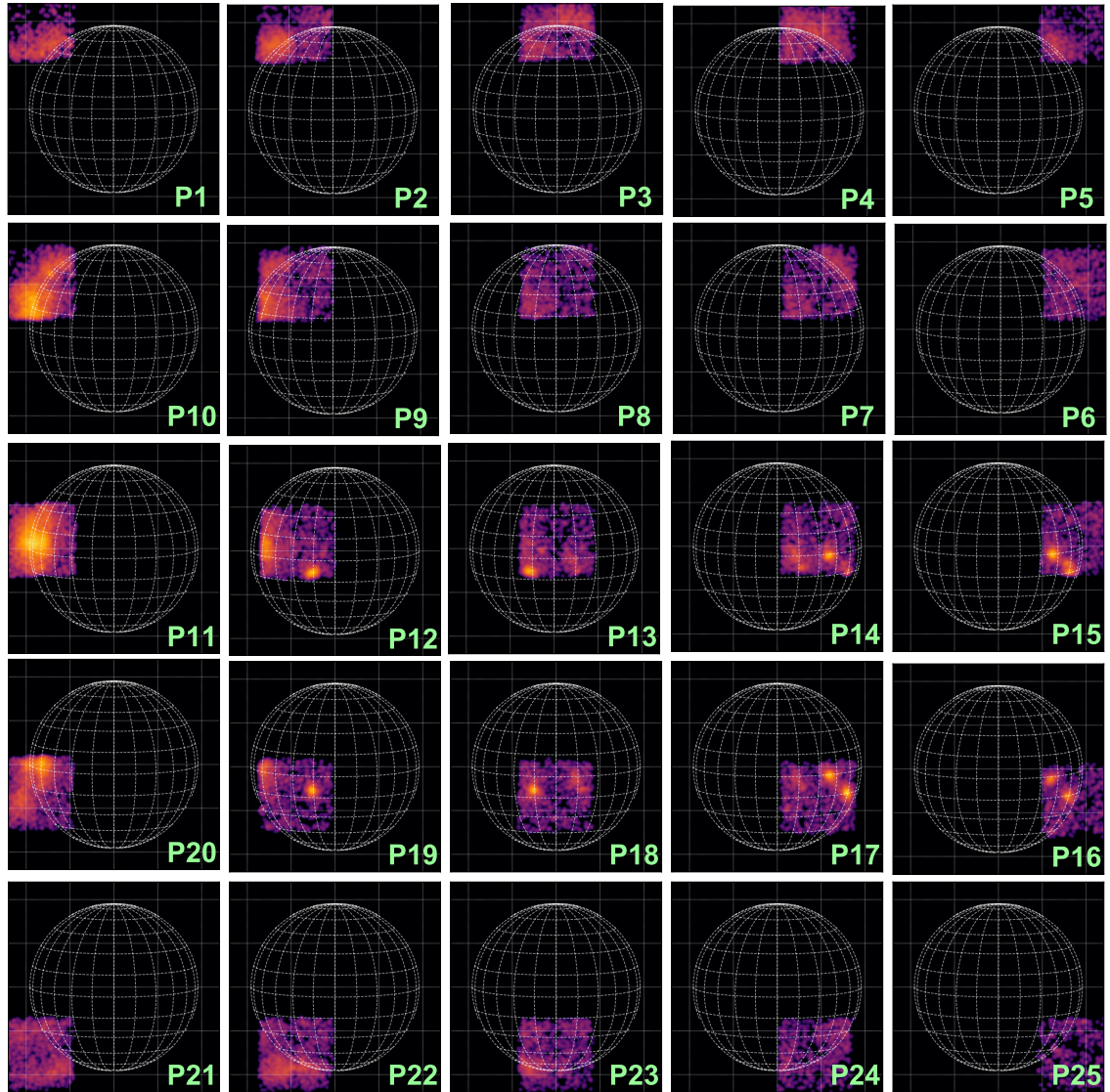


**Figure 2.5:** An example of the individual pointings making up a NuSTAR quiet Sun mosaic. These have 25 pointings (P1–25) in a  $5 \times 5$  pattern. When combined, these tiles make up the mosaic shown in Figure 2.4 (right panel)

## 2.1 The Nuclear Spectroscopic Telescope Array

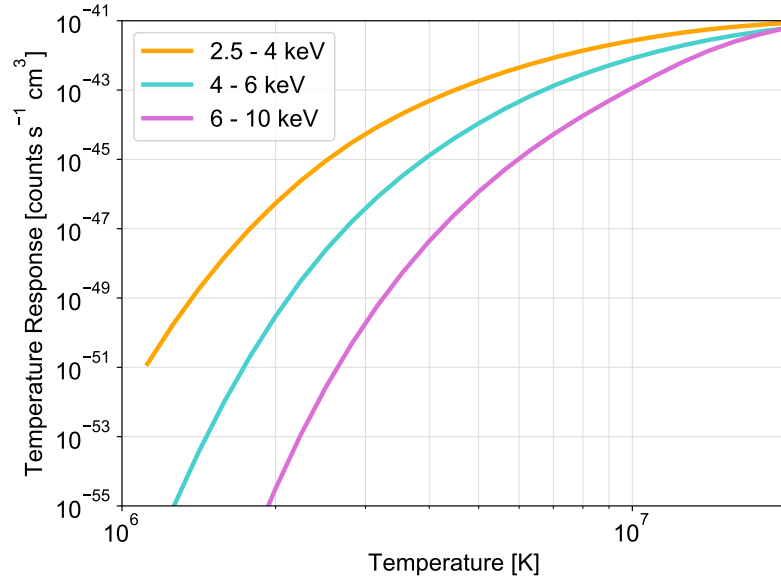


**Figure 2.6:** Temperature responses (labelled TR(T) in Equation 2.1) for NuSTAR for three different energy bands: 2.5–4 keV (orange), 4–6 keV (blue), and 6–10 keV (purple).

this (as discussed in Section 3.2.1).

The overlapping nature of the tiles can also increase the limited usefulness of the mosaic mode in tracking the HXR evolution of short-lived events. For example, in Section 4.3, we investigate a jet captured by NuSTAR in a full-disk mosaic. This event had a short duration of a few minutes, and the overlapping tiles meant that it could be captured in four consecutive pointings.

### 2.1.4 NuSTAR Temperature Responses

The temperature response function for an instrument gives the emission that would be expected from an isothermal source at a range of temperatures, integrated over a unit volume. NuSTAR temperature responses for three different energy bands (2.5–4, 4–6, and 6–10 keV) are plotted in Figure 2.6. It can be seen from this figure that NuSTAR’s response sharply increases across several orders of magnitude beginning around  $T \sim 10^6$  MK. The NuSTAR responses shown were calculated in Python<sup>9</sup> from the instrument spectral response matrix (SRM), with units counts photon<sup>-1</sup> cm<sup>2</sup>, which is obtained from the RMF and ARF files and determines how the incident photon spectrum is converted to the observed count spectrum. As each observation has a different SRM, the NuSTAR

<sup>9</sup>[https://github.com/ianan/nustar\\_sac/blob/master/python/ns\\_tresp.py](https://github.com/ianan/nustar_sac/blob/master/python/ns_tresp.py)

## 2.1 The Nuclear Spectroscopic Telescope Array

responses must be calculated separately each time. The temperature response,  $TR(T)$  can be calculated for any chosen energy band via:

$$TR(T) = \int_{E_{\text{low}}}^{E_{\text{high}}} \frac{I(T, EM)SRM(E)}{EM} dE \quad [\text{counts s}^{-1} \text{ cm}^3] \quad (2.1)$$

where  $E_{\text{low}}$  and  $E_{\text{high}}$  are the lower and upper boundaries of the chosen energy range,  $I(T, EM)$  is the thermal photon model spectrum, and  $EM$  is the emission measure. The thermal model (see Section 1.5.3) contains both bremsstrahlung continuum and emission lines (though the former dominates), and was calculated using the CHIANTI atomic database (Dere et al. 1997) with coronal abundances (Feldman 1992). We used CHIANTI version 9 (Dere et al. 2019). Note that CHIANTI version 10 is now available (Del Zanna et al. 2021), though this has minimal differences compared to version 9 at this energy range and NuSTAR’s energy resolution. The above calculation is performed over a range of temperatures to produce the response curves plotted in Figure 2.6. It can be seen in the plot of the calculated temperature responses (Figure 2.6) that the higher energy bands have less sensitivity to emission at lower temperatures compared to the lower energy bands.

### 2.1.5 Instrumental Background

Compared to RHESSI—which used larger, unshielded germanium detectors (Lin et al. 2002)—NuSTAR’s instrumental background is significantly smaller (Grefenstette et al. 2016). In fact, when observing the bright emission from solar sources (compared to the astrophysical sources that NuSTAR was designed for), the background can be considered negligible due to short exposures, low instrument background, and low throughput. However, the background can still be observed in a solar observation with a sufficiently long integration time.

Figure 2.7 plots the contribution to the NuSTAR background from multiple sources, described in Wik et al. (2014). The internal background is a result of the radiation conditions of NuSTAR’s orbit, with a continuum which is produced predominantly by high energy gamma rays which scatter in the detector, and some instrumental lines (due to instrumental fluorescence and activation caused by interactions between radiation and the NuSTAR detectors) dominating the background at energies of 22–32 keV. The dominant background component at low energies  $< 20$  keV is aperture stray light, which results from X-rays (mainly from the cosmic X-ray background) being detected through an unbaffled

## 2.1 The Nuclear Spectroscopic Telescope Array

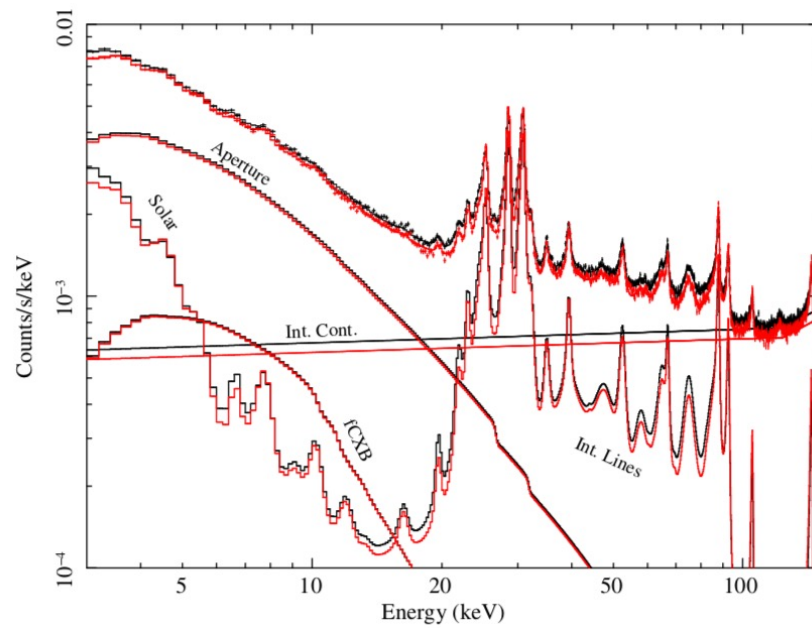


**Figure 2.7:** A plot of the NuSTAR instrumental background from Wik et al. (2014) for FPMA (black) and FPMB (red), showing the separate background components. These include the aperture background, which dominates at energies  $< 20$  keV, and the instrumental lines, which dominate at energies of 22–32 keV. This background was observed over a total integration time of 2500 ks (Wik et al. 2014).

## 2.2 The Solar Dynamics Observatory

part of the instrument. These photons pass directly into the detector aperture rather than going through the focusing optics. The background component from the Sun is relevant only for astrophysical observations, since in solar observations the Sun is being directly focused.

This background is sufficiently small compared to the bright emission from the Sun (which dominates the throughput) that it is typically ignored in solar observations. However, in Section 5.4, we illustrate that the NuSTAR background can be sampled when the quiet Sun observations are integrated over several hours.

## 2.2 The Solar Dynamics Observatory

The Solar Dynamics Observatory (SDO; [Pesnell et al. \(2012\)](#)), which was launched on 11 February 2010, carries three instruments: the Atmospheric Imaging Assembly (AIA; [Lemen et al. \(2012\)](#)), the Extreme Ultraviolet Variability Experiment (EVE; [Woods et al. \(2012\)](#)), and the Helioseismic and Magnetic Imager (HMI; [Schou et al. \(2012\)](#)). SDO has been providing high resolution (both spatial and temporal) UV and EUV solar data since its launch in 2010, and it has been immensely useful in providing a comparison to other observations from instruments observing at different wavelengths.

In this thesis, we use data from only two of the three instruments on board SDO: AIA and HMI. Brief overviews of these instruments are given in Sections 2.2.1 and 2.2.2, respectively.

### 2.2.1 The Atmospheric Imaging Assembly

AIA has been providing continuous observations of the full Sun since 2010, with seven channels observing at EUV wavelengths and two at UV wavelengths. AIA has a pixel size of  $0.6''$  and a high spatial resolution of  $1.5''$ , and observes at a cadence of down to 12 s ([Lemen et al. 2012](#)), allowing the evolution of dynamic phenomena to be captured. Six of the EUV channels observe optically-thin plasma at coronal temperatures, and these are the 94, 131, 171, 193, 211, and 335 Å channels. The remaining EUV channel, 304 Å, observes emission at chromospheric temperatures. The coronal temperature channels are all centred on Fe lines, whereas 304 Å emission comes from a He II line. The two UV channels, 1600 and 1700 Å, observe continuum emission around these wavelengths.

## 2.2 The Solar Dynamics Observatory

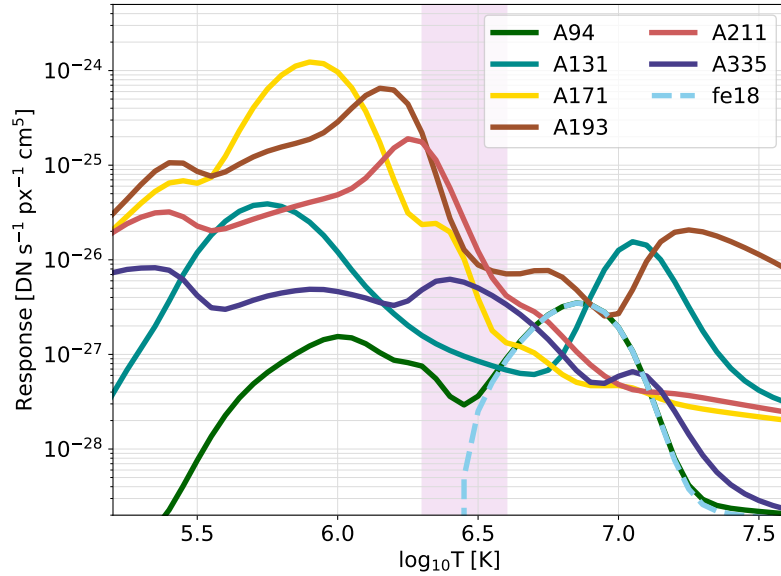


**Figure 2.8:** Temperature responses for the six coronal temperature EUV channels of AIA. The shaded region indicates the temperature range of 2–4 MK, within which lie the temperatures of majority of the quiet Sun features investigated throughout this thesis.

AIA data is used extensively in this thesis throughout Chapters 4, 5, and 6. AIA’s high resolution images are used to put the NuSTAR images into better spatial context and to correct NuSTAR’s pointing. We also use AIA data in these chapters in differential emission measure (DEM) analysis (as described in Section 3.2.3). Calculating DEMs requires the use of instrumental temperature responses.

The AIA channels each have a different temperature response function. The temperature responses of the six EUV channels that are centred on Fe lines (and observe at coronal temperatures), in units of  $\text{DN s}^{-1} \text{px}^{-1} \text{cm}^5$ , are plotted in Figure 2.8. For AIA, DN (*data number*) values are the raw detector output which have not been converted to units that are physically meaningful. The AIA temperature responses were calculated using the standard SolarSoft IDL routine from the AIA instrument team, `aia_get_response.pro`<sup>10</sup>. As for the NuSTAR responses in Figure 2.6, we used CHIANTI version 9 with coronal abundances (Feldman 1992). Figure 2.8 demonstrates that all six of the channels observe multi-thermal emission, with contributions across a wide range of temperatures (Boerner et al. 2012, 2014). The responses of several of the channels peak at around 1–2 MK (193, 211 Å), whereas the 335 Å channel has a broader response. It can be seen that there is a gap in AIA’s sensitivity between 2–4 MK, where none of the channels have a strong peak

<sup>10</sup>[https://hesperia.gsfc.nasa.gov/ssw/sdo/aia/idl/response/aia\\_get\\_response.pro](https://hesperia.gsfc.nasa.gov/ssw/sdo/aia/idl/response/aia_get_response.pro)

in sensitivity.

For differential emission measure (DEM) analysis, we use EM-loci curves to constrain the DEM solutions. These are obtained by dividing the observed flux in each channel by the corresponding temperature response curve. This gives the maximum possible emission as a function of temperature. Further discussion of this can be found in Section 3.2.3.

### Fe XVIII Channel

In the temperature response plot in Figure 2.8, there is a seventh curve that is not attributed to any of the AIA filters. This is the response of the Fe XVIII proxy channel of [Del Zanna \(2013\)](#). It can be seen in this figure that the temperature response of the 94 Å channel has a two-peaked structure. From this, it is clear that, while this channel has significant response at high temperatures ( $\sim 4\text{--}10$  MK), there is also a significant contribution from temperatures at around 1 MK.

In NuSTAR microflare analysis, NuSTAR has typically observed emission at temperatures  $> 5$  MK ([Cooper et al. 2020](#); [Duncan et al. 2021](#); [Cooper et al. 2021](#)). These analyses have made use of the Fe XVIII proxy channel, which isolates the high temperature sensitivity peak of the 94 Å channel (as shown in Figure 2.8), and therefore is sensitive to plasma at similar temperatures to the NuSTAR microflare emission. This proxy channel removes any contribution from the lower temperature peak of the 94 Å channel's response, thus removing ambiguity about what temperature range the emission that the 94 Å channel observed lies within.

The Fe XVIII channel is a linear combination of the 94, 171, and 211 Å channels, and is empirically given by:

$$I_{\text{Fe XVIII}} = I_{94\text{\AA}} - \frac{I_{211\text{\AA}}}{120} - \frac{I_{171\text{\AA}}}{450} \quad (2.2)$$

where  $I_{\text{Fe XVIII}}$  is the intensity in the Fe XVIII channel, and  $I_{94\text{\AA}}$ ,  $I_{171\text{\AA}}$ ,  $I_{211\text{\AA}}$  are the intensities (with a correction applied to account for instrument degradation) in the 94, 171, and 211 Å channels ([Del Zanna 2013](#)).

While most of the quiet Sun HXR sources studied in this thesis are not heated to high enough temperatures to produce Fe XVIII emission, there is a mini-filament eruption which was detected in this channel, analysed in Chapter 6.

### 2.2.2 The Helioseismic and Magnetic Imager

The other SDO instrument that we use data from in this thesis is the Helioseismic and Magnetic Imager (HMI). HMI continuously observes the full disk at  $6173 \text{ \AA}$  with a cadence of 45 s and a resolution of  $\sim 1'$  (Schou et al. 2012), providing dopplergrams and magnetograms (both vector and line-of-sight) of the photosphere.

In this work, we use HMI data to relate the underlying photospheric magnetic field to the processes occurring in the corona, as observed with AIA and NuSTAR. In Chapter 4, we use HMI magnetograms to investigate the evolution of a region of emerging flux. Later, in Chapter 6, we again use HMI magnetograms to put into context the behaviour of small-scale impulsive events in the quiet Sun.

## 2.3 The Hinode X-Ray Telescope

The X-Ray Telescope on board Hinode (XRT; Kosugi et al. (2007); Golub et al. (2007)) was designed to observe soft X-ray emission from the corona, at a broad temperature range of  $6.1 < \log(T) < 7.5$ , using grazing incidence optics. XRT has a FOV of  $35'$  square, meaning that it is capable of taking full disk images when pointed at disk centre. However, it also has the capability to take images with a reduced FOV, allowing cadences of down to 2 s, with a resolution of  $2''$ .

XRT has nine filters, all with distinct temperature sensitivities. A specific Hinode Operation Plan (HOP) was run to give optimal coverage during NuSTAR quiet Sun campaigns. For the NuSTAR observations studied in this thesis, full-disk XRT images with low spatial resolution, but high cadence, were obtained in two suitable filters—the Beryllium (Be)-thin and Aluminium (Al)-poly filters. The temperature responses for these two filters are plotted in Figure 2.9. As for NuSTAR and AIA (see Figures 2.6 and 2.8), we generated these responses using CHIANTI version 9 with coronal abundances (Feldman 1992). These responses were calculated using the standard IDL routine from the instrument team, `make_xrt_temp_resp.pro` (Narukage et al. 2011; Narukage et al. 2014).

It can be seen that, of the two, Al-poly has a broader temperature response, having more sensitivity to temperatures  $< 1 \text{ MK}$  compared to Be-thin. As Be-thin has less sensitivity to lower temperature emission, we generally use data from this filter in our analysis, as it makes a better comparison with NuSTAR, which is only sensitive to higher temperatures (see Figure 2.6).

### 2.3 The Hinode X-Ray Telescope

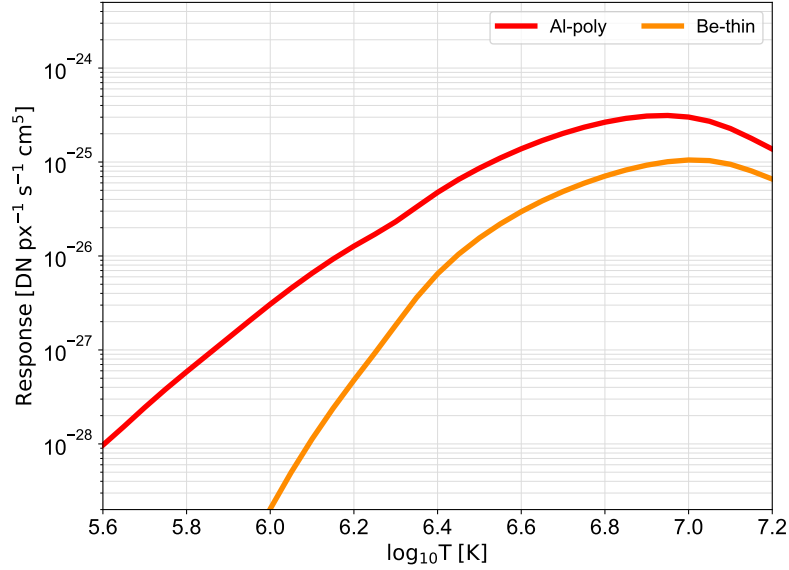


**Figure 2.9:** Temperature responses for the Beryllium-thin (orange) and Aluminium-poly (red) filters of XRT.

There can be issues when working with XRT data, one of which is that there are contamination spots on the CCD. Another is that XRT can become saturated when observing bright features. As Al-poly has a broader temperature response with more sensitivity to lower temperatures, it is more prone to saturation than Be-thin. This is another reason why we use Be-thin data more extensively than Al-poly in this analysis.

Throughout Chapters 4–6, the SXR observations from XRT provide a useful comparison with NuSTAR. We also use the temperature responses shown in Figure 2.9 in DEM calculations. There is a suggestion that the XRT temperature response functions are too small by a factor of 2 (e.g. Schmelz et al. 2015). This will be further discussed in Section 3.2.3 in regards to DEM analysis.

# 3

## NuSTAR Quiet Sun Data and Analysis Methods

In this chapter, we summarise the NuSTAR quiet Sun data, and the techniques used to analyse it. In Section 3.1, we present a brief overview of each of the six NuSTAR quiet Sun observing campaigns from the recent solar minimum between 2018–2020, including those from 28 September 2018 (analysed in Chapter 4), and 21 February and 12–13 September 2020 (both analysed in Chapters 5 and 6).

In Section 3.2, we detail the methods used to analyse the NuSTAR quiet Sun data, including making NuSTAR images and lightcurves, fitting NuSTAR spectra, differential emission measure analysis, and the calculation of non-thermal upper limits.

### 3.1 An Overview of the NuSTAR Quiet Sun Data

NuSTAR was used to observe the Sun on a number of occasions between 2018–2020, when the Sun was in the minimum of its 11 year activity cycle. Observing the Sun during this period, when there were no active regions or bright flares, allowed the observation of the faint HXR emission from small-scale phenomena in the quiet Sun. NuSTAR’s high sensitivity meant that many of these types of sources could be observed for the first time at HXR energies, providing the opportunity to search for the high temperature ( $> 5$  MK) and non-thermal components that are predicted by coronal heating models (see Section 1.2.1) in their emission.

A summary of the NuSTAR quiet Sun observing campaigns is detailed in Table 3.1. This table summarises the six observations, including the number of orbits which NuSTAR observed the Sun over and the livetime (see Section 2.1) of the observations. It also gives details on what observing modes were used for each of the campaigns. NuSTAR

### 3.1 An Overview of the NuSTAR Quiet Sun Data

**Table 3.1:** An overview of the NuSTAR quiet Sun observing campaigns. The highlighted data sets are those which are analysed in detail later in this thesis.

Start Date	Number of Orbits	Livetime (%)	Observing Mode
28 Sep 2018*	2	63–91	Mosaics
12 Jan 2019	4	58–93	2 Mosaics, 2 Dwells
25 Apr 2019	4	43–93	Mosaics
02 Jul 2019	2	50–94	Mosaics
21 Feb 2020 <sup>+</sup>	11	50–94	2 Mosaics, 9 Dwells
12 Sep 2020 <sup>+</sup>	10	88–92	1 Mosaic, 9 Dwells

\* = analysed in Chapter 4

+ = analysed in Chapters 5 and 6

performed some of these observations in full-disk (FD) mosaic mode for all orbits, and other campaigns included some orbits during which NuSTAR observed in dwell mode (see Section 2.1.3 for details on observing modes). All of the campaigns had at least one full-disk mosaic.

The first of the NuSTAR quiet Sun observations was carried out on 28 September 2018 over two orbits, with three more short campaigns being conducted throughout the following year. These were mainly done in mosaic mode, allowing surveys of all of the features appearing on the solar disk at the time. In 2020, NuSTAR observed the quiet Sun twice, for much longer periods (11 orbits in February, 10 orbits in September). These longer campaigns were predominantly done in dwell mode, meaning that NuSTAR captured the features present over many hours of their evolution. The livetimes for almost all of these quiet Sun observations are  $> 50\%$ , which is much higher than for NuSTAR active regions and microflares (e.g.  $0.1\%$  for a microflare analysed in Glesener et al. (2020)). The only observation for which the livetime dropped below  $50\%$  is 25–26 April 2019, as a result of a bright mini-filament eruption (see Section 3.1.3 for more details).

In the following sections, we present an overview of the six NuSTAR quiet Sun observations, including NuSTAR and AIA images, and discussions of all of the sources present. Note that all of the NuSTAR mosaic images from different dates are plotted on the same scale in order to convey the relative brightness of the features between the observations.

### 3.1 An Overview of the NuSTAR Quiet Sun Data

**Table 3.2:** A summary of the NuSTAR orbits from 28 September 2018 observation.

Orbit	Time	Observing Mode
1	18:24:58–19:24:28	FD Mosaic
2	20:02:24–21:01:08	FD Mosaic

#### 3.1.1 28 September 2018

NuSTAR first observed the quiet Sun over two orbits during the solar minimum on 28 September 2018. This observation was done in full-disk mosaic mode and therefore two mosaics (timings summarised in Table 3.2), each with 25 tiles (duration  $\sim 100$  s) in a  $5 \times 5$  pattern, were obtained. As discussed in Section 2.1.3 (and shown in Figure 2.5), the first pointing (P1) of the NuSTAR quiet Sun mosaics is in the top left corner. The following pointings are shifted to the right until P5, and then P6 is shifted down. This pattern continues until P25 in the bottom right corner. The overlapping tiles result in the features on the disk being captured in more than one pointing.

EUV and SXR data is also available for the time of this NuSTAR observation from AIA and XRT, respectively (though no XRT images were taken between 19:13–19:38 UT). An overview of this observation is shown in Figure 3.1. In the NuSTAR mosaics, it can be seen that there are several HXR sources present, with counterparts also appearing in EUV and SXRs. A detailed analysis of this observation is presented in Chapter 4 (based on the work from Paterson et al. (2023)), but the features captured by NuSTAR can be briefly summarised as follows:

- An emerging flux region (EFR) is present, and is captured by NuSTAR in both orbits. This region evolved to become the NOAA active region 12723 $\beta$  in the days following this NuSTAR observation. Detailed analysis of this feature can be found in Section 4.1.
- Three X-ray bright points were also present on the disk at this time, appearing in both NuSTAR orbits, which we label these BP1–3. BP3 (the faintest of the bright points) lies close to a set of quiet Sun loops. The results for these sources are presented in Section 4.2.

### 3.1 An Overview of the NuSTAR Quiet Sun Data

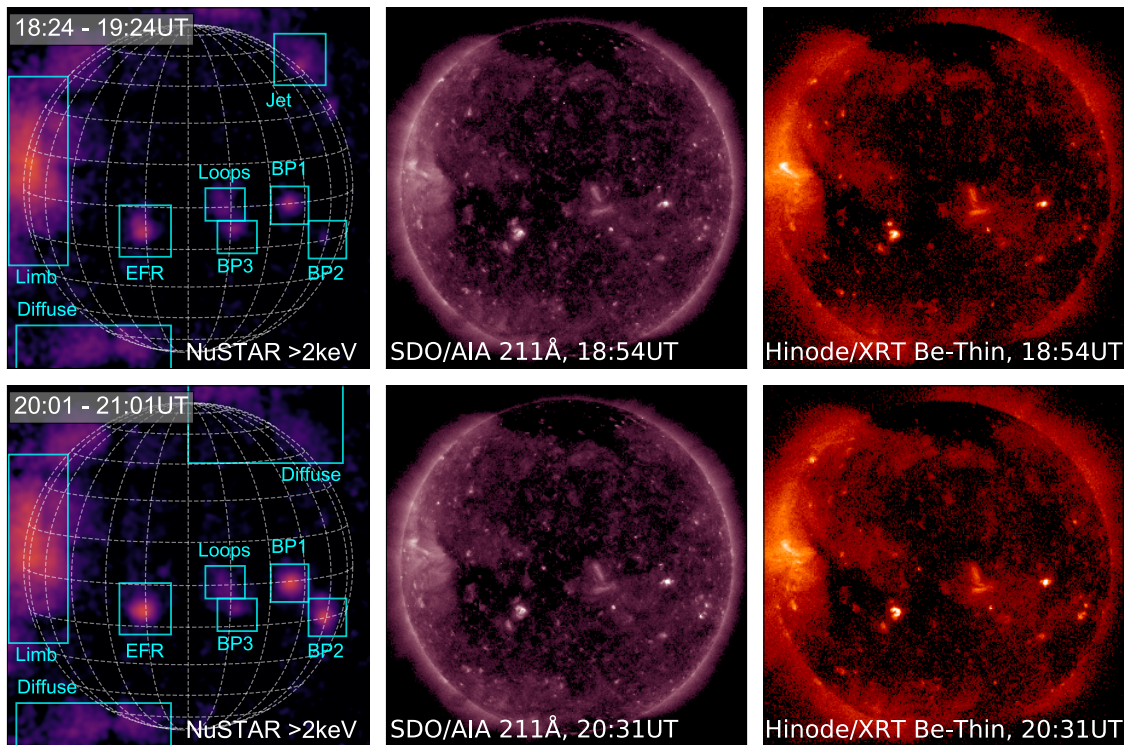


**Figure 3.1:** An overview of the NuSTAR QS observation on 28 September 2018 (taken from Paterson et al. (2023)), where NuSTAR observed in mosaic mode for two orbits. Full-disk images are from NuSTAR (left), AIA 211 Å (middle), and XRT Be-thin (right), with the top row showing images from the first NuSTAR orbit and the bottom row showing images from the second. The boxes marked on the NuSTAR images highlight the different features observed, and the AIA and XRT images are from the mid-time of the two NuSTAR orbits.

### 3.1 An Overview of the NuSTAR Quiet Sun Data

**Table 3.3:** A summary of the NuSTAR orbits from 12 January 2019 observation.

Orbit	Time	Observing Mode
1	16:34:22–17:34:41	Dwell
2	18:11:01–19:11:20	Dwell
3	19:47:48–20:30:09	FD Mosaic
4	21:24:27–22:13:09	FD Mosaic

- A source appears in the top right corner of the first NuSTAR mosaic, but not the second, suggesting that this is a transient event. AIA images confirm that this event is a small jet, the details of which are discussed in Section 4.3.
- The most obvious source is the bright region of NuSTAR emission at the East limb. This region is large in comparison to the other NuSTAR features, and is extended enough that the detector gaps can be seen cutting through it. AIA and XRT images also show a bright loop with surrounding bright emission at this location, and confirm that this source lies at a site where there was an active region two solar rotations previous to this observation. It is therefore the remnants of this active region, and we label it a decayed active region (DAR). Analysis of this source can be found in Section 4.4.
- Finally, off the edge of the solar disk, there are regions of diffuse HXR emission detected by NuSTAR.

These mosaics were the first of the NuSTAR quiet Sun observations, and there are few very bright sources on the disk. However, there have been even quieter observations since (e.g. the February and September 2020 campaigns; see Sections 3.1.5 and 3.1.6).

#### 3.1.2 12 January 2019

The second of the NuSTAR quiet Sun observing campaigns was performed on 12 January 2019. In this campaign, NuSTAR observed the Sun in both mosaic and dwell mode, for two orbits each (as summarised in Table 3.3). The observation began with two orbits of dwells, summarised in Figure 3.2. It can be seen that NuSTAR observed several steady bright features, which were present over the whole two orbits. The NuSTAR time profile

### 3.1 An Overview of the NuSTAR Quiet Sun Data

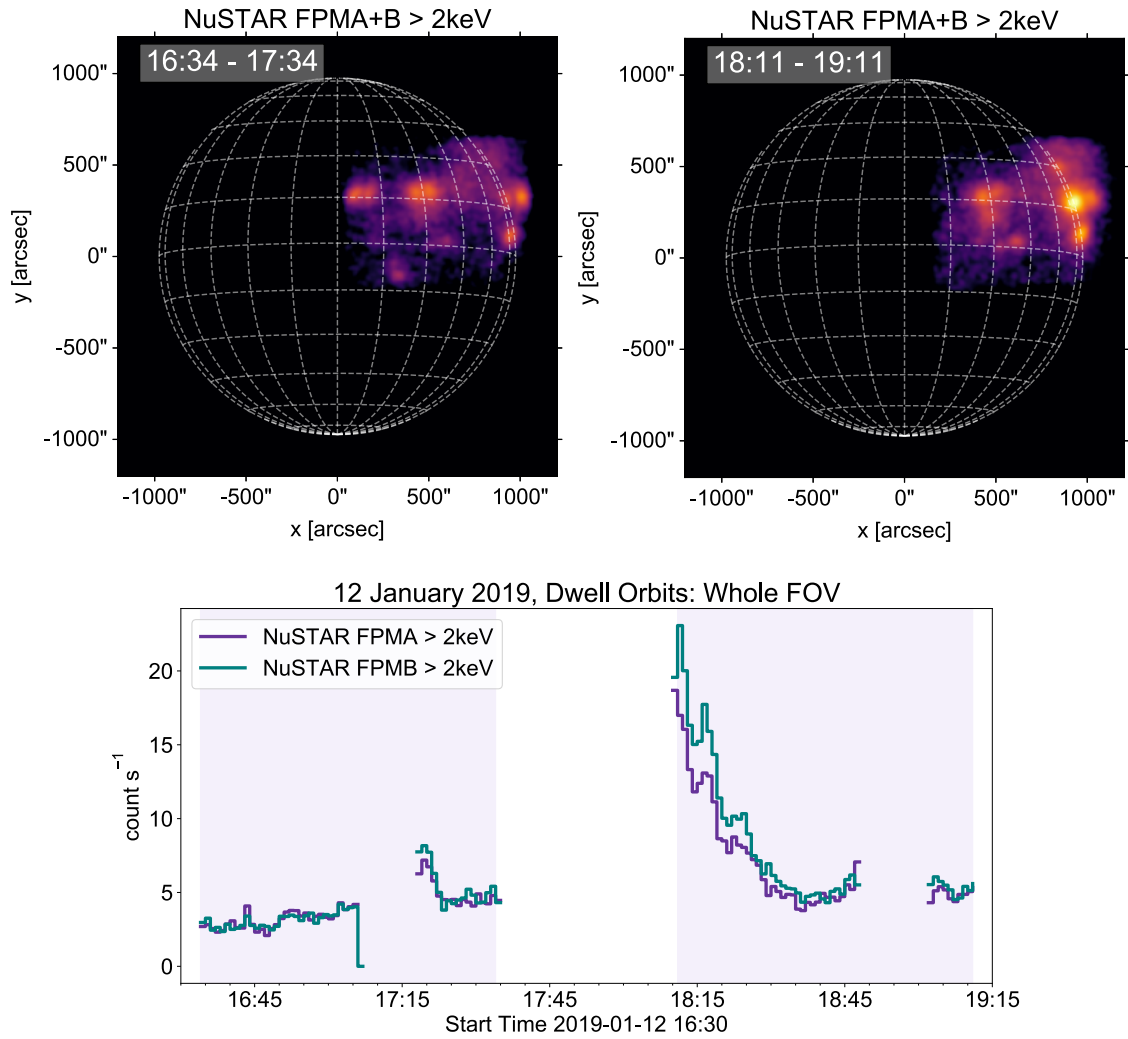


**Figure 3.2:** An overview of the NuSTAR QS dwell orbits on 12 January 2019. (Top row) NuSTAR image from the first (left) and second (right) dwell orbits. (Bottom row) NuSTAR time profiles calculated over the entire NuSTAR FOV for the two orbits. The shaded regions show the times of the first and second NuSTAR dwell orbits.

### 3.1 An Overview of the NuSTAR Quiet Sun Data

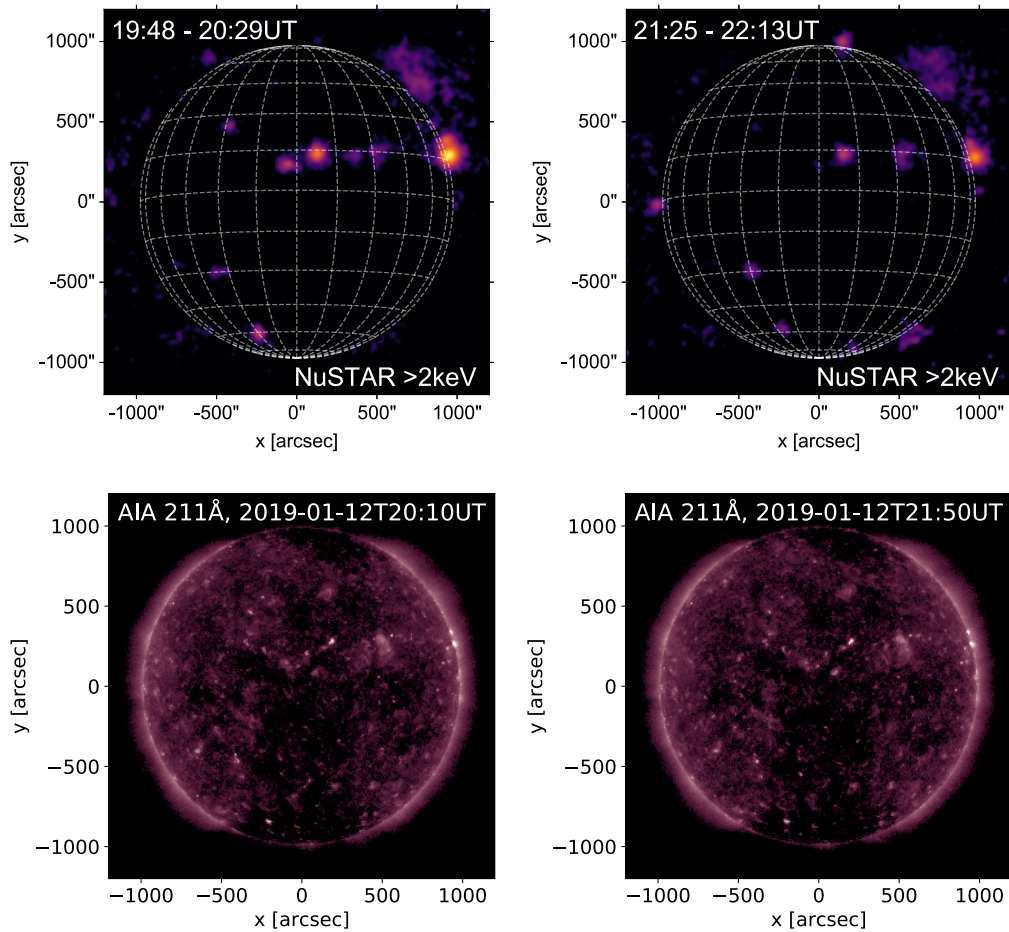


**Figure 3.3:** An overview of the two NuSTAR QS mosaics from 12 January 2019. Full-disk images are from NuSTAR (top row) and AIA 211 Å (bottom row), with the AIA images taken from the mid-times of the NuSTAR mosaics.

of this region clearly shows that the brightness varies. However, more analysis would have to be done to check whether this is genuine, or a result of sources shifting in and out of detector gaps or off of the edge of the detector. The NuSTAR time profile for this region is dominated by the brightest source, which lies on the West limb at  $\sim (950'', 250'')$ . Both the NuSTAR images and the time profiles shown in Figure 3.2 indicate that this source brightens between the two orbits, and there is a sharp peak in the NuSTAR lightcurves at the beginning of the second NuSTAR orbit. In addition to the steady bright point sources, NuSTAR also captured two small flares during these quiet Sun dwells, one around 16:48 UT, the next a little later at 17:58 UT.

The dwell orbits were followed by two mosaics which were taken between 19:48–20:30 and 21:24–22:13 UT and are summarised in Figure 3.3. Both of these mosaics are relatively

### 3.1 An Overview of the NuSTAR Quiet Sun Data

**Table 3.4:** A summary of the NuSTAR orbits from 25–26 April 2019 observation.

Orbit	Time	Observing Mode
1	22:10:47–23:10:47	FD Mosaic
2	23:47:27–00:47:26	FD Mosaic
3	01:24:06–02:24:05	FD Mosaic
4	03:00:46–04:00:44	FD Mosaic

quiet, with the same bright sources that were present in the dwell orbits appearing also in the mosaics. There are several X-ray bright points which were captured in both of these mosaics, which were also observed in EUV with AIA. As in the dwell orbits, the brightest source in NuSTAR lies on the West limb, and this also appears bright in the AIA 211 Å images. This source decreases in brightness in NuSTAR between the two orbits (though, again, more work—outside the scope of this thesis—would have to be done to check whether this is real, or just a result of the source lying near a detector gap in the second mosaic).

In addition to the X-ray bright points, there are several other interesting HXR sources which NuSTAR captured in these mosaics. For example, there is a polar source which appears at the Sun’s north pole in the second mosaic but not the first. There is also a diffuse source in the top right corner of the both mosaics.

#### 3.1.3 25 April 2019

When NuSTAR observed the Sun for four orbits in full-disk mosaics mode on 25–26 April 2019, it was very quiet, with several X-ray bright points distributed across the disk. An overview of the four orbits can be found in Table 3.4 and Figure 3.4. There are a number of bright sources that appear in the NuSTAR images, which can be identified as bright points in the AIA 211 Å images. Several of these features appear over multiple orbits, and their brightness seems to vary throughout the observation. However, more detailed analysis (including checking the position of the sources on the detector in each pointing, and investigating times where the pointing shifted, all outside the scope of this thesis) would be required in order to determine whether this brightness change is real, or just an effect of the sources moving in and out of NuSTAR’s detector gaps.

### 3.1 An Overview of the NuSTAR Quiet Sun Data

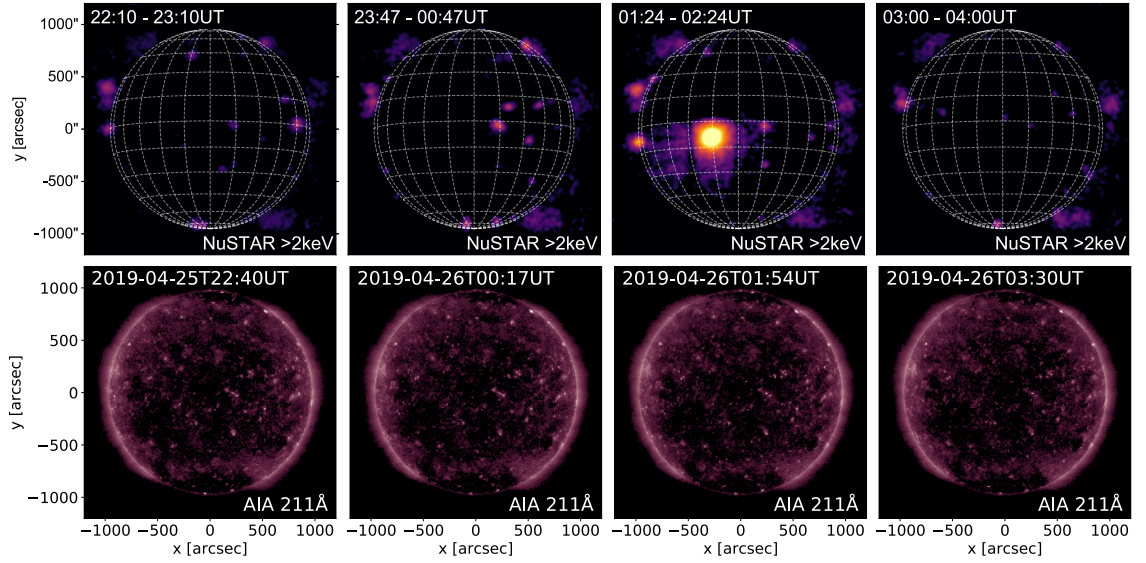


**Figure 3.4:** An overview of the NuSTAR QS observation on 25–26 April 2019, where NuSTAR observed in mosaic mode for four orbits. Full-disk images are from NuSTAR FPMA+B (top row) and AIA 211 Å (bottom row), with the AIA images taken from the mid-times of the NuSTAR mosaics.

**Table 3.5:** A summary of the NuSTAR orbits from 02 July 2019 observation.

Orbit	Time	Observing Mode
1	04:16:46–05:17:03	FD Mosaic
2	05:53:25–06:53:42	FD Mosaic

An extremely bright source appears only in the third orbit. This increase in HXR emission is due to a mini-filament eruption that occurred just after 02:00 UT on 26 April (Hannah et al., in prep). This impulsive event was captured in pointings 18 and 19 of the mosaic. Note that this event does not appear in the AIA 211 Å image from Orbit 3 because this image is from the mid-time of the orbit, prior to the eruption. Analysis of this mini-filament eruption will be presented in Hannah et al. (in prep), with NuSTAR spectroscopy indicating the presence of material either  $> 7$  MK, or possibly a non-thermal component.

#### 3.1.4 02 July 2019

### 3.1 An Overview of the NuSTAR Quiet Sun Data

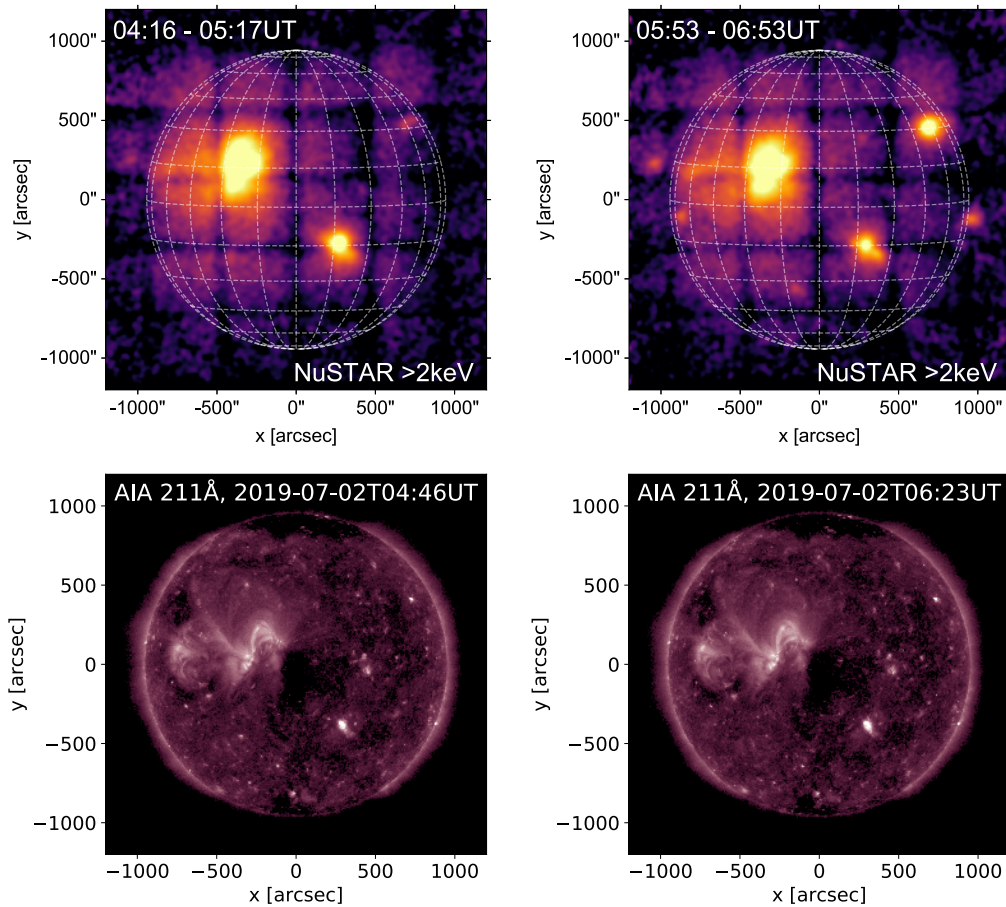


**Figure 3.5:** An overview of the NuSTAR QS observation on 02 July 2019, where NuSTAR observed in mosaic mode for two orbits. Full-disk images are from NuSTAR (top row) and AIA 211 Å (bottom row), with the AIA images taken from the mid-times of the NuSTAR mosaics.

On 02 July 2019, NuSTAR once again observed the Sun in full-disk mosaic mode for two orbits (timings summarised in Table 3.5), as shown in Figure 3.5. At this time, the Sun was less quiet than in the previous three cases, as there was a very bright diffuse region on the disk. This feature can clearly be seen in the AIA 211 Å images in Figure 3.5, and in the corresponding NuSTAR mosaics. However, in addition to this diffuse region, NuSTAR also observed several X-ray bright points, with more appearing in the second orbit than the first.

In these mosaics, which are the least quiet of the NuSTAR quiet Sun observations, the detectors gaps can clearly be seen cutting through the NuSTAR maps. Though the brightest source is obviously the diffuse region, even the bright points are brighter than those typically observed the other NuSTAR quiet Sun mosaics.

### 3.1 An Overview of the NuSTAR Quiet Sun Data

**Table 3.6:** A summary of the NuSTAR orbits from 21 February 2020 observation.

Orbit	Time	Observing Mode
1	05:16:16–06:15:51	Dwell
2	06:54:30–07:52:28	FD Mosaic
3	08:38:13–09:29:09	Dwell
4	10:06:12–11:05:47	Dwell
5	11:42:51–12:42:26	Dwell
6	13:19:29–14:19:05	Dwell
7	14:56:08–15:55:43	Dwell
8	16:32:47–17:32:22	Dwell
9	18:09:25–19:09:01	Dwell
10	19:46:06–20:46:52	FD Mosaic
11	21:22:42–22:22:18	Dwell

#### 3.1.5 21 February 2020

On 21 February 2020, NuSTAR observed the Sun for a total of eleven orbits. Of these, NuSTAR observed in dwell mode for nine orbits and in full-disk mosaic mode for two (the second and the second-to-last). The observation began just after 05:15 UT, with the final orbit concluding just after 22:20 UT. A full summary of the timings of the orbits is given in Table 3.6.

During all of the dwell orbits of this observation, NuSTAR was pointed at disk centre. Figure 3.6 shows a time profile for NuSTAR’s whole FOV over this observation (only showing the orbits with dwell data, not the mosaics). After a quiet first orbit, the HXR lightcurves show significant variability, indicating that there are many potentially interesting dynamic processes occurring during the course of this observation.

During this observation NuSTAR captured several small-scale phenomena, including both steady features and transient events. Several X-ray bright points were observed by NuSTAR over multiple orbits. The brightest feature captured by NuSTAR (whose behaviour dominates the lightcurve in Figure 3.6) is a large bright point (located at  $\sim (-50'', -300'')$ ) which began to emerge around the time of the first orbit, and persisted throughout the entire observation. This feature was detected by SPOCA (Verbeeck et al. 2014) and given

### 3.1 An Overview of the NuSTAR Quiet Sun Data

the ID number 23914. The largest spikes in the HXR time profile in Figure 3.6 are a result of this bright point flaring, and a full analysis of this feature is detailed in Chapter 5.

As well as X-ray bright points, a number of transient quiet Sun brightenings were also captured. These events are generally too faint to appear in the time profiles in Figure 3.6, which is dominated by the large bright point. However, the strongest of these impulsive events is a mini-filament eruption that occurred at  $\sim 16:45$  UT. The HXR spike from this event can be seen in the NuSTAR lightcurve for the full FOV. This small-scale eruption, as well as two other impulsive brightenings in the quiet Sun from this observation, are analysed in Chapter 6.

The two full-disk mosaics from this date were taken in the second orbit (06:54–07:53 UT) and the penultimate orbit (19:46–20:46 UT). These mosaics are shown in the left-hand panel of Figure 3.7. It can be seen that NuSTAR detected several bright features across the disk, mainly X-ray bright points. As there is a gap of  $\sim 10$  hours between the two mosaics, many of the features that are present in the first mosaic are not detected in the second. In the later mosaic, the large bright point near disk centre is again the brightest source, though there are two more bright features that do not show up strongly in the first mosaic. In the second orbit, the large bright point near disk centre is not yet sufficiently bright to be detected in the short 100 s pointings (it does show up very faintly in the first of the dwell orbits, with a  $\sim 1$  hour long observation time).

#### 3.1.6 12–13 September 2020

Later in 2020, NuSTAR again observed the quiet Sun on 12–13 September. NuSTAR began observing at 09:05 UT on the morning of 12 September, and stopped at around 00:35 UT the next day. This observation consisted of 10 NuSTAR orbits: 1 full-disk mosaic followed by 9 dwell orbits, where NuSTAR was pointed at a region on the East limb. A summary of the timings of these is shown in Table 3.7.

The full-disk mosaic, which was taken at the very start of the observation from 09:05–10:05 UT, is shown in Figure 3.7. It can be seen that the mosaic captured several bright points distributed across the disk. The brightest source is a region of diffuse emission in the top right corner of the mosaic. This region is also bright in EUV, as seen in the corresponding AIA 211 Å image. It is worth noting that there are no sources appearing

### 3.1 An Overview of the NuSTAR Quiet Sun Data

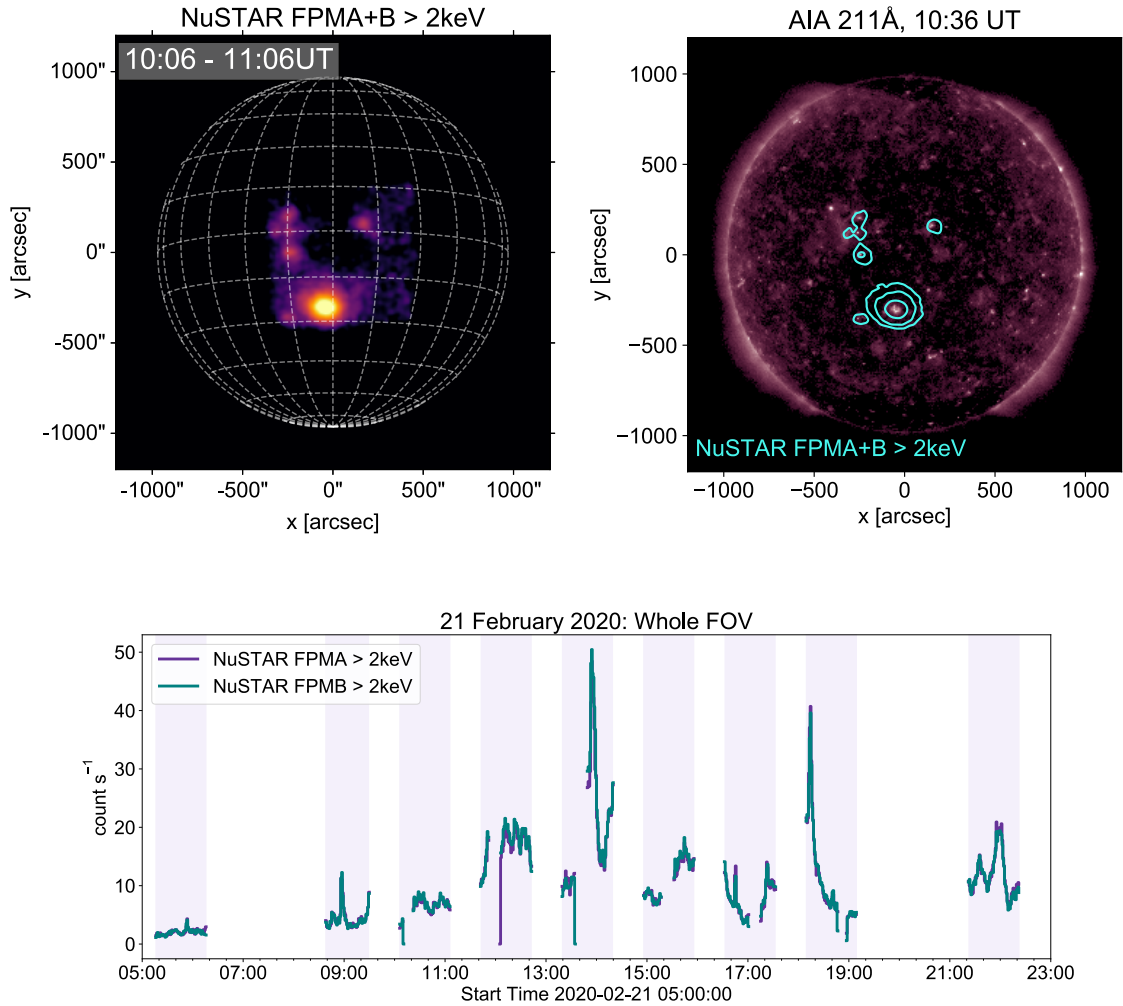


**Figure 3.6:** An overview of the dwell orbits from the 21 February 2020 observation. (Top) NuSTAR (left) and AIA 211 Å (right) images from the fourth NuSTAR orbit, showing the region which NuSTAR was pointed at and highlighting the sources which were captured. (Bottom) NuSTAR FPMA (purple) and FPMB (green) time profiles for the whole FOV. The shaded areas indicate the time ranges of each orbit (to make clearer which gaps are due to a SAA passage).

### 3.1 An Overview of the NuSTAR Quiet Sun Data

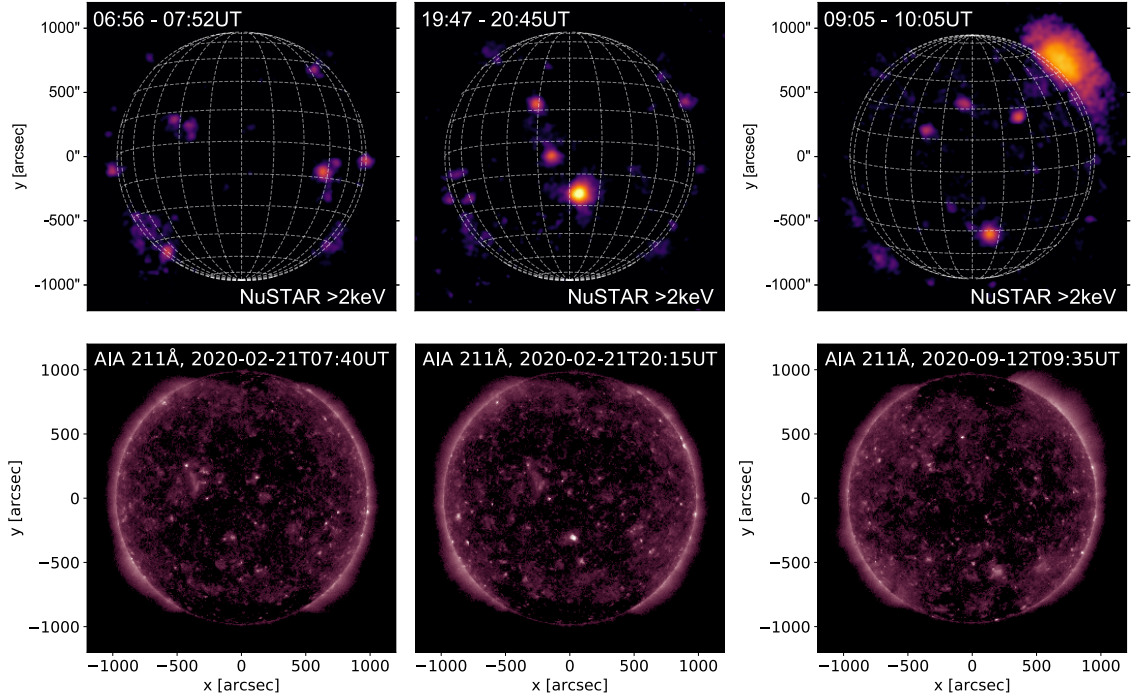


**Figure 3.7:** An overview of the NuSTAR QS mosaics taken on 21 February 2020 (left) and 12 September 2020 (right), observations that were done mainly in dwell mode. Full-disk images are from NuSTAR (top row) and AIA 211 Å (bottom row), with the AIA images taken from the mid-times of the NuSTAR mosaics.

**Table 3.7:** A summary of the NuSTAR orbits from 12–13 September 2020 observation.

Orbit	Time	Observing Mode
1	09:05:37–10:05:14	FD Mosaic
2	10:42:21–11:41:55	Dwell
3	12:18:59–13:18:12	Dwell
4	13:55:37–14:55:12	Dwell
5	15:32:16–16:31:51	Dwell
6	17:08:54–18:08:29	Dwell
7	18:45:33–19:45:07	Dwell
8	20:22:11–21:07:38	Dwell
9	21:58:49–22:50:20	Dwell
10	23:35:28–00:34:01	Dwell

## 3.2 Analysis Methods for NuSTAR Quiet Sun Data

strongly in this mosaic in the region where NuSTAR was pointed during the dwell orbits (shown in Figure 3.8, top left). This highlights how quiet the region chosen for the dwell orbits was.

Rather than disk centre, the dwells in this observation were pointed at a quiet region near the East limb. A time profile for NuSTAR for this region from Orbit 2 onwards can be found in Figure 3.8. In this time profile, there are several large short-lived spikes which are strongest in Orbits 4 and 7 (peaking at  $\sim 14:20$  and  $19:20$  UT). However, these spikes are a result of ghost rays due to activity occurring outside of NuSTAR's FOV. This is highlighted by the NuSTAR and AIA 211 Å images in the bottom row of Figure 3.8, which are from Orbit 7, during which NuSTAR observed the strongest spike. The NuSTAR image clearly shows the distinctive ghost ray pattern, and the lack of any distinct source inside the FOV confirms that this X-ray spike is a result of ghost rays. In the AIA 211 Å image, there is a bright source at  $\sim (250'', -550'')$ . It is likely that the heightened emission that NuSTAR detects during the earlier orbits is a result of this source flaring.

The observed region was mostly quiet, with very few sources appearing over multiple orbits. However, a bright point emerged later in the observation, which was captured by NuSTAR in the last three orbits. This results in a slight increase in brightness in the lightcurve in Figure 3.8 from Orbit 8 onwards. This is difficult to see clearly as the bright point is much fainter in comparison to the ghost ray spikes in the earlier orbits which dominate the NuSTAR time profile for the whole FOV. Full analysis on the evolution of this X-ray bright point is presented in Chapter 5. The bright point's emergence is much more clearly seen in the NuSTAR time profile for only a small region surrounding it, shown in Figure 5.2.

In addition to the X-ray bright point, NuSTAR also captured several small-scale impulsive phenomena over the nine dwell orbits. Analysis of four small flares in the quiet Sun observed in these dwells (as well as several from the February 2020 observation) is detailed in Chapter 6.

## 3.2 Analysis Methods for NuSTAR Quiet Sun Data

### 3.2.1 Images and Lightcurves

As discussed in Section 2.1.2, the NuSTAR data is a list of photons, each with an associated energy, time of detection, and location on the detector. When making NuSTAR images,

### 3.2 Analysis Methods for NuSTAR Quiet Sun Data

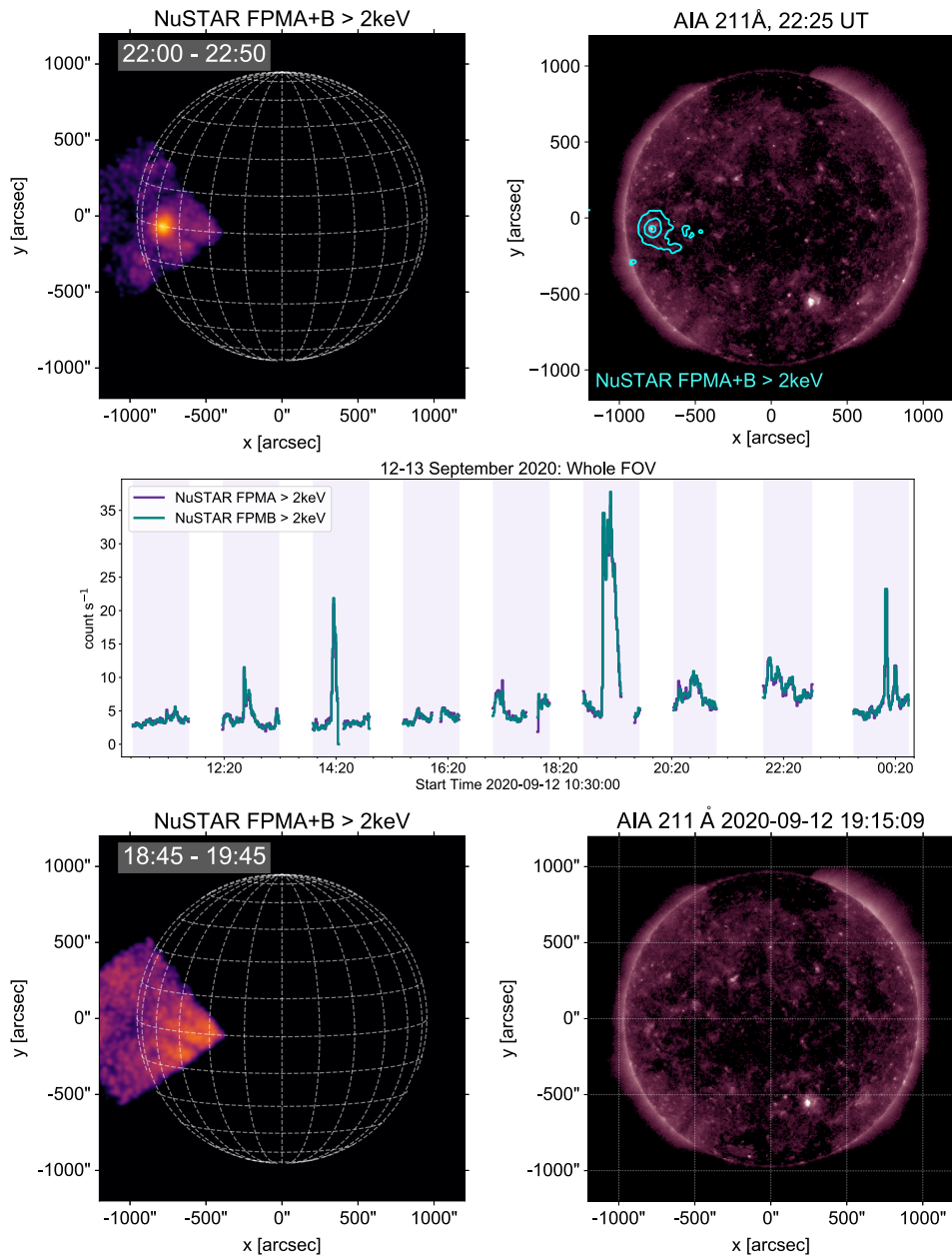


**Figure 3.8:** An overview of the dwell orbits from the 12–13 September 2020 observation. (Top row) NuSTAR (left) and AIA 211 Å (right) images from the ninth orbit, showing the region which NuSTAR was pointed at and highlighting the sources which were captured. (Middle row) NuSTAR FPMA (purple) and FPMB (green) time profiles for the whole FOV. The shaded areas indicate the time ranges of each orbit. (Bottom row) NuSTAR and AIA 211 Å images from the seventh orbit, showing the ghost ray emission.

### 3.2 Analysis Methods for NuSTAR Quiet Sun Data

the data is first filtered, for example by energy range, x-y position, time, and grade. This can either be done in the data processing stage (as discussed in Section 2.1.2) or when analysing in Python<sup>1</sup>. This results in a list of events that match the filtering criteria, which can be mapped (after being corrected for livetime to obtain count rates). For all of the NuSTAR images shown in this thesis, a gaussian blur has been applied to smooth them.

For the mosaics, as additional correction must be applied when producing the NuSTAR images. As discussed in Section 2.1.3, and illustrated in Figure 2.5, the disk is sampled more times than the limb. On-disk regions are sampled four times, limb regions twice, and the corners only once. This makes the disk appear brighter than it should relative to the limb. In order to account for that in the images, the count rate in a given region must be divided by the number of times that the region was sampled.

When making NuSTAR lightcurves (such as the one previously shown in Figure 3.8, middle row), the data must also first be filtered into the desired energy band, x-y range, and grade. Lightcurves are obtained by creating a histogram of the number of events that NuSTAR detected which matched the filtering criteria (divided by the livetime) in 1 s time bins. This histogram can then be re-binned into longer time intervals to create a NuSTAR lightcurve.

#### 3.2.2 NuSTAR HXR Spectral Fitting

As NuSTAR is an imaging spectrometer, the HXR spectrum of a source can be obtained. Fitting this spectrum allows for physical parameters, such as temperature and emission measure, of the source to be determined. The measured count spectrum,  $C$ , is related to the photon spectrum,  $I(\epsilon)$ , of a source and the SRM of the instrument by:

$$C = \int I(\epsilon) SRM d\epsilon \quad [\text{counts s}^{-1} \text{ keV}^{-1}] \quad (3.1)$$

where  $\epsilon$  is incoming photon energy. To directly extract the source's photon spectrum would require the above equation to be inverted, which is an inverse problem (discussed in more detail in Section 3.2.3). Instead, we can use the approach of *forward fitting*, wherein we choose a photon model which is dependent on several parameters (such as temperature and emission measure), and fit it to the data by generating a model count spectrum using Equation 3.1. A *fit statistic*, which is used to judge the goodness of fit, is then calculated by

---

<sup>1</sup>[https://github.com/NuSTAR/nustar\\_pysolar/blob/main/nustar\\_pysolar/filter.py](https://github.com/NuSTAR/nustar_pysolar/blob/main/nustar_pysolar/filter.py)

### 3.2 Analysis Methods for NuSTAR Quiet Sun Data

comparing the model and observed count spectra. The parameters are then changed in order to produce a model that more closely fits the data, and this process is continued until the best fit parameters are found.

The NuSTAR spectra are typically extracted over a circular region, defined by a source file created in SAOImageDS9<sup>2</sup>, an image display and visualisation tool for astronomical data. The Spectral Response Matrix for this circular region can then be obtained using the NuSTAR Data Analysis Software from the NuSTAR Response Matrix and Ancillary Response (RMF and ARF, respectively) files, as detailed in Section 2.1.2. As was mentioned in that section, there is no need to filter out non-grade 0 events as is required for other solar observations (Grefenstette et al. 2016).

In this work, all of the spectral fitting was done using XSPEC<sup>3</sup> (Arnaud 1996). XSPEC is an X-ray spectral fitting program, which is desirable to use with NuSTAR data due to its capability for simultaneous fitting (of the FPMA and FPMB spectra in this case). Due to the low numbers of counts, we use Cash statistics (Cash 1979) when fitting. This is the maximum likelihood-based statistic for data that is Poissonian (as opposed to  $\chi^2$ , which is used for Gaussian distributions). As discussed in Section 1.5.3, we use the APEC thermal model when fitting NuSTAR spectra in XSPEC, and we assume solar coronal abundances (Feldman 1992).

In the NuSTAR quiet Sun data, most of the HXR sources are faint (with livetimes up to > 90%). Although NuSTAR is highly sensitive, it is limited by its maximum throughput of 400 counts s<sup>-1</sup> FPM<sup>-1</sup>. This issue acts in combination with quiet Sun spectra that sharply fall off with increasing photon energy to cause low energy ( $\lesssim 3$  keV) counts to dominate. This is particularly problematic when fitting spectra from the full-disk mosaics, where each pointing only lasts for 100 s. Over these short observation times, the resulting spectra are often noisy, with very little counts above a few keV, and are therefore difficult to fit over such a small energy range. This is aided somewhat by a recent NuSTAR calibration update (Madsen et al. 2021), which allows spectra to be fitted down to 2.2 keV, compared to 2.5 keV, which was previously recommended for NuSTAR solar data (Grefenstette et al. 2016).

The signal-to-noise can be improved upon by making use of XSPEC's capability to simultaneously fit the FPMA and FPMB spectra, introducing a multiplicative factor to account for systematic differences between the responses of the two detectors. This factor is fixed at 1 for the FPMA spectrum, and allowed to vary for FPMB. It is one of the parameters that is determined by the fit, and is dependent on both this systematic difference and on

---

<sup>2</sup><https://sites.google.com/cfa.harvard.edu/saoimageds9>

<sup>3</sup><https://heasarc.gsfc.nasa.gov/xanadu/xspec/manual/node9.html>

### 3.2 Analysis Methods for NuSTAR Quiet Sun Data

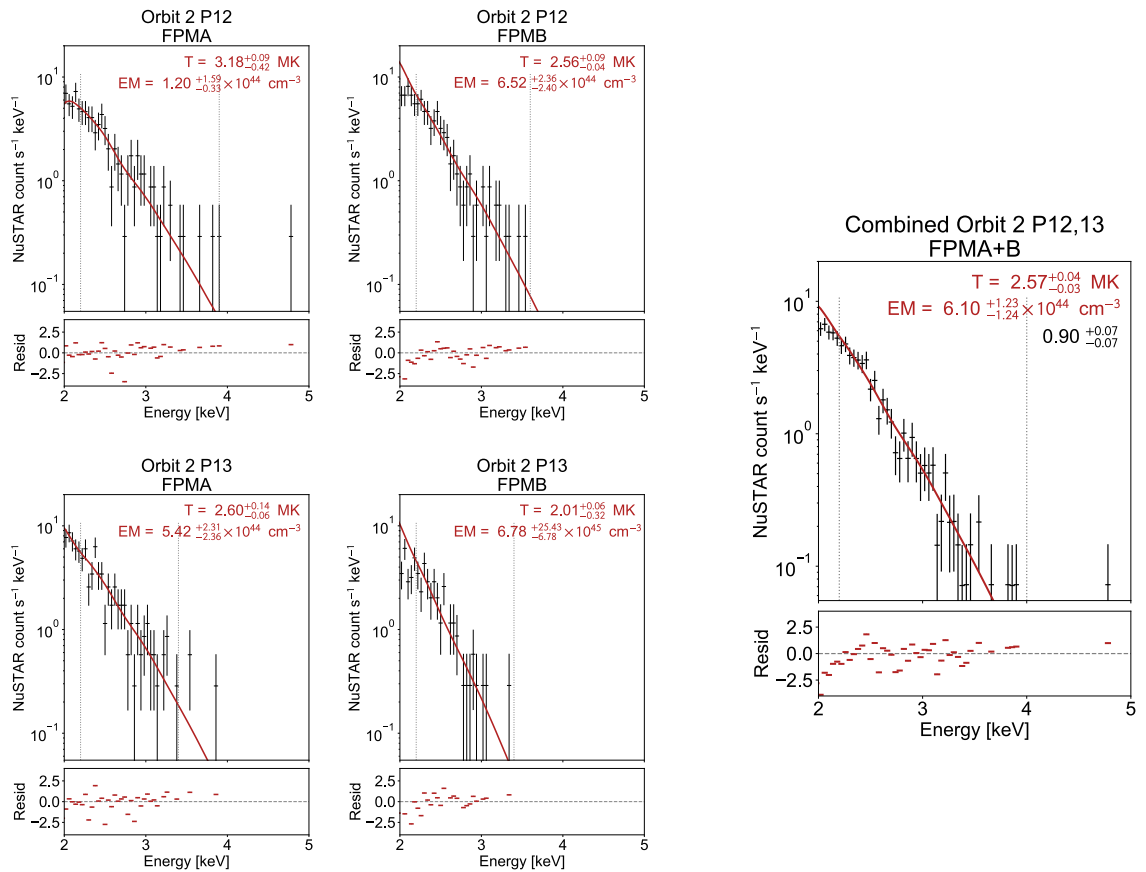


**Figure 3.9:** An example showing the benefits of fitting the spectra from multiple mosaic pointings from FPMA and FPMB simultaneously using XSPEC. These spectra are for the emerging flux region from the 28 September 2018 mosaics, from Pointings 12 and 13 from the second orbit. The spectra on the left are from individual pointings and FPMs, and the spectrum on the right was obtained by simultaneously fitting the other four.

### 3.2 Analysis Methods for NuSTAR Quiet Sun Data

what part of the detector the source was captured on. The value of this factor should be  $\lesssim 10\%$  (Madsen et al. 2015).

However, even widening the fitting range and fitting the FPMA and FPMB spectra simultaneously is not adequate to obtain reliable fits for some of the mosaic features. Fortunately, as the tiles of the mosaics overlap, the fits can further be improved by simultaneously fitting the NuSTAR spectra from multiple pointings. When using this approach, all of the FPMA spectra are grouped, with the multiplicative constant set as 1. All of the FPMB spectra are grouped together and assigned the same multiplicative constant, the value of which is decided by the fit.

The benefits of simultaneous fitting are illustrated in Figure 3.9. It can be seen that the spectra from the individual mosaic tiles (and FPMA and FPMB separately) are very noisy, with few counts above 2.2 keV. These fits do not produce reliable results, and the uncertainties on the temperatures and emission measures are large. However, when they are fitted simultaneously, the spectrum is significantly less noisy (with the number of counts being effectively increased by a factor equal to the number of pointings combined) and the resulting fit is much more reliable, with smaller uncertainties. This method can be used to improve the spectral fits for the mosaic features—though fitting spectra from different pointings simultaneously assumes that the source does not change significantly between them. It is therefore best to only use this method for pointings that are close together in time (or for a very steady source, like a quiescent X-ray bright point, over a wider time interval).

#### 3.2.3 Differential Emission Measure Analysis

NuSTAR spectra (and, in general, any X-ray spectra from an instrument of a similar energy resolution to NuSTAR) are generally dominated by an isothermal component (as shown in previously in Figure 3.9). However, there are underlying multi-thermal distributions in these sources, which can be investigated through differential emission measure (DEM) analysis.

The multi-thermal nature of a source can be investigated by recovering its differential emission measure (DEM), which was briefly discussed in Section 1.5.3. Here, we reconstruct DEMs using the regularised inversion approach of Hannah & Kontar (2012).

The line-of-sight DEM,  $\xi(T)$ , is given by:

### 3.2 Analysis Methods for NuSTAR Quiet Sun Data

$$\xi(T) = n^2 \frac{dh}{dT} \quad [\text{cm}^{-5} \text{K}^{-1}] \quad (3.2)$$

where  $n(h(T))$  is the electron density along the line-of-sight  $h$  at temperature  $T$ .

The observable,  $g$  for filter  $i$  is related to the DEM by:

$$g_i = \int_T K_i(T) \xi(T) dT + \delta g_i \quad [\text{DN s}^{-1} \text{px}^{-1}] \quad (3.3)$$

where  $K_i$  is the temperature response of the  $i^{\text{th}}$  filter and  $\delta g_i$  is the error in the observable. The temperature responses for AIA, NuSTAR, and XRT are plotted in Figures 2.8, 2.6, and 2.9, respectively.

Solving Equation 3.3 involves finding the minimum of the following problem:

$$\left\| \frac{\mathbf{K}\boldsymbol{\xi}(T) - \mathbf{g}}{\delta \mathbf{g}} \right\|^2 = \min \quad (3.4)$$

where  $\mathbf{K}$  and  $\mathbf{g}$  are arrays containing the temperature responses and observables for all of the filters. This does not have a unique solution. Recovering the DEM is an ill-posed inverse problem (Jefferies et al. 1972; Craig & Brown 1977) and so it cannot be directly obtained from observations. Any attempt to solve Equation 3.3 directly would result in the amplification of uncertainties.

Hannah & Kontar (2012) instead use linear constraints to solve the problem without the amplification of uncertainties. Equation 3.4 instead becomes:

$$\left\| \frac{\mathbf{K}\boldsymbol{\xi}(T) - \mathbf{g}}{\delta \mathbf{g}} \right\|^2 + \lambda \left\| \mathbf{L}(\boldsymbol{\xi} - \boldsymbol{\xi}_0) \right\|^2 = \min \quad (3.5)$$

where  $\mathbf{L}$  is the ‘‘constraint’’ matrix,  $\lambda$  is the ‘‘regularisation parameter’’, and  $\boldsymbol{\xi}_0$  is a guess solution (which is optional). In zero order regularisation,  $\mathbf{L}$  is proportional to the identity matrix. The diagonal terms of  $\mathbf{L}$  can be set to, for example, some expected form of the solution (not the same as  $\boldsymbol{\xi}_0$ ) or to the minimum values of EM loci curves.

The EM loci curve for a channel can be obtained by dividing the data by the temperature response, giving a curve which gives the maximum possible emission at each temperature (e.g. Schmelz et al. 2011). For an isothermal source, the EM loci curve from different

### 3.2 Analysis Methods for NuSTAR Quiet Sun Data

channels should all intersect at the same point, giving a single temperature and emission measure. However, when calculating a DEM, these curves give an upper limit on the DEM at each temperature, and therefore can be used as a constraint. In all of the DEMs shown in this thesis, the EM loci curves of the six AIA channels, as well as for NuSTAR and XRT, are used to constrain the DEM solution. This is demonstrated for the first DEM analysis in this thesis (see Figure 4.7 in Section 4.8).

A solution for Equation 3.5,  $\xi_\lambda(T)$  can now be found as a function of the regularisation parameter  $\lambda$  using Generalised Singular Value Decomposition (GSVD) (Hansen 1992). The value of  $\lambda$  is determined using Morozov’s discrepancy principle (Morozov 1967), wherein the  $\chi^2$  of the solution is effectively controlled in observable space. The best value of  $\lambda$  is the one which results in a solution that satisfies<sup>4</sup>:

$$\|K\xi_\lambda(T) - g\|^2 - \rho\|\delta g\|^2 = \min \quad (3.6)$$

where  $\delta g$  is the uncertainty in the observable, and  $\rho$  is the regularisation “tweak” parameter, which should have a value of 1. The left-hand term in the above equation is obtained using GSVD, and the DEM solution is the one that has the optimal  $\lambda$  and the desired  $\rho$ .

In this thesis, DEMs are reconstructed using EUV data from the six optically thin coronal temperature channels of AIA and X-ray data from XRT and NuSTAR. We use the Python code<sup>5</sup> based on Hannah & Kontar (2012). We calculate the DEMs for quiet Sun features like bright points by choosing a region in AIA and XRT that covers the entire feature. The data values are averaged over the entire area for each channel. In addition, when finding the DEM for a time range during which there are multiple images, the data values are also averaged over time. The temperature responses for AIA and XRT are calculated using the standard routines in SolarSoft from the instrument teams: `aia_get_response.pro` for AIA and `xrt_temp_resp.pro` for XRT (with the responses plotted in Figures 2.8 and 2.9). The NuSTAR temperature response (Figure 2.6) is calculated in Python, using the same spectral files (ARF, RMF, and PHA; see Section 2.1.2) that were used for the spectral fitting.

To account for uncertainties in the temperature responses of the three instruments, we assign a 20% systematic uncertainty to each of the data values. As the AIA and XRT data values are averaged over many pixels, the photon noise for these instruments is insignificant compared to the systematic uncertainty. However, for NuSTAR photon noise

---

<sup>4</sup>[https://github.com/ianan/demreg/blob/master/notes/demreg\\_maths.pdf](https://github.com/ianan/demreg/blob/master/notes/demreg_maths.pdf)

<sup>5</sup><https://github.com/ianan/demreg/tree/master/python>

### 3.2 Analysis Methods for NuSTAR Quiet Sun Data

is larger, and so we add it in quadrature to the 20% error. The NuSTAR data can be split into multiple energy bands (for example, 2.2–4 keV, and 4–6 keV) if desired.

A previous microflare analysis by [Wright et al. \(2017\)](#) calculated DEMs using data from AIA, XRT, and NuSTAR. This study, following several works that had found discrepancies in the XRT data ([Testa et al. 2011](#); [Schmelz et al. 2015](#); [Cheung et al. 2015](#)), multiplied the XRT temperature responses by a factor of 2. This was found to produce a more consistent DEM with smaller residuals. Including this factor of 2 in the DEM analysis of the quiet Sun features investigated here was, in general, found to similarly improve the DEM solutions, and is therefore included in all analysis (unless otherwise stated).

We calculate DEMs using the above approach for a number of quiet Sun X-ray sources throughout Chapters 4, 5, and 6. The first DEM analysis in this thesis is for the emerging flux region from the 28 September 2018 mosaics, and can be found in Section 4.1.2. In this section, we illustrate the need to include X-ray data in a DEM calculation to constrain the solution at high temperatures.

Note that the inverse regularisation approach of [Hannah & Kontar \(2012\)](#) is only one of a number of techniques which have been used to reconstruct DEMs. Other methods have involved forward fitting of chosen models, for example splines ([Weber et al. 2004](#); [Golub et al. 2004](#)) or multiple gaussians ([Aschwanden & Boerner 2011](#)), finding a minimum  $\chi^2$  statistic. The drawbacks of forward fitting approaches are that they require the assumption of models (which may not be correct), and they can be computationally slow when calculating uncertainties on the DEM solutions (which is generally done using Monte Carlo methods). The above regularised inversion technique used by [Hannah & Kontar \(2012\)](#) is computationally fast, does not require model assumptions, and determines both the DEM and its associated uncertainties. This approach has also proven successful in past DEM analyses using AIA, XRT, and NuSTAR data, as demonstrated in [Wright et al. \(2017\)](#). The regularised inversion method can produce erroneous high temperature components when calculating DEMs using AIA data alone ([Paterson et al. 2023](#)), though this can be avoided by including X-ray data from XRT and/or NuSTAR to constrain the solution (see Section 4.1.2 for further discussion on this).

#### 3.2.4 Non-Thermal Upper Limits

For the features that NuSTAR observes in the quiet Sun, their HXR spectra are often adequately fitted with a thermal model, and no non-thermal component is directly observed.

### 3.2 Analysis Methods for NuSTAR Quiet Sun Data

However, as their spectra are often noisy with few counts at energies above a few keV, a weak non-thermal component could be present but remain undetectable. NuSTAR can be used to put a constraint on this component. Upper limits on the non-thermal emission that could be present, yet remain consistent with a null detection, are obtained in this thesis following the approach of Wright et al. (2017) and Cooper et al. (2020).

This analysis is done using the thermal and thick-target non-thermal models (see Sections 1.5.3 and 1.5.4) from the new X-ray spectral fitting package, Sunxspex<sup>6</sup>. As discussed in Section 1.5.4, XSPEC could not be used for this analysis as it does not have a thick-target model. We begin by using Sunxspex to recreate the thermal model that was fitted to the observed NuSTAR spectrum in units of photons  $\text{s}^{-1} \text{keV}^{-1}$ . This model can then be converted from photon to counts space by folding it through NuSTAR's spectral response matrix, returning a count rate model,  $M$ , in units of counts  $\text{s}^{-1} \text{keV}^{-1}$ . The total number of counts,  $N$ , in the overall model is then calculated from  $M$  via:

$$N = \text{round}\left(\sum_i M_i \times \delta E_i \times \delta t \times l\right) \quad [\text{counts}] \quad (3.7)$$

where  $\delta E_i$  is the width of the  $i^{\text{th}}$  energy bin,  $\delta t$  is the exposure time of the observation, and  $l$  is the livetime fraction (with the product of the latter two giving the effective exposure time). NuSTAR's energy bins have a width of 0.04 keV.

The total number of counts,  $N$ , in the model is rounded to the closest integer. A cumulative sum of the counts spectrum is taken and normalised such that it produces a probability distribution ranging between 0 and 1. This distribution is then sampled  $N$  times to create a discretised synthetic NuSTAR spectrum of the event. An example of a spectrum simulated from a thermal model is shown in Figure 3.10.

The shown simulated spectrum is purely thermal, based on the spectral fitting results. A second spectrum is simulated, this time including a non-thermal component, which is added to the thermal model at the start of the process. This non-thermal thick-target model is dependent on three parameters (see Section 1.5.4): the power law index  $\delta$ , the low energy cutoff  $E_C$ , and the total electron flux  $N_{TOT}$ . Examples of spectra simulated, both including and not including a non-thermal component, are shown in Fig. 3.10. There are two examples, highlighting the effect of changing the parameters of the non-thermal model.

---

<sup>6</sup><https://github.com/sunpy/sunxspex>

### 3.2 Analysis Methods for NuSTAR Quiet Sun Data

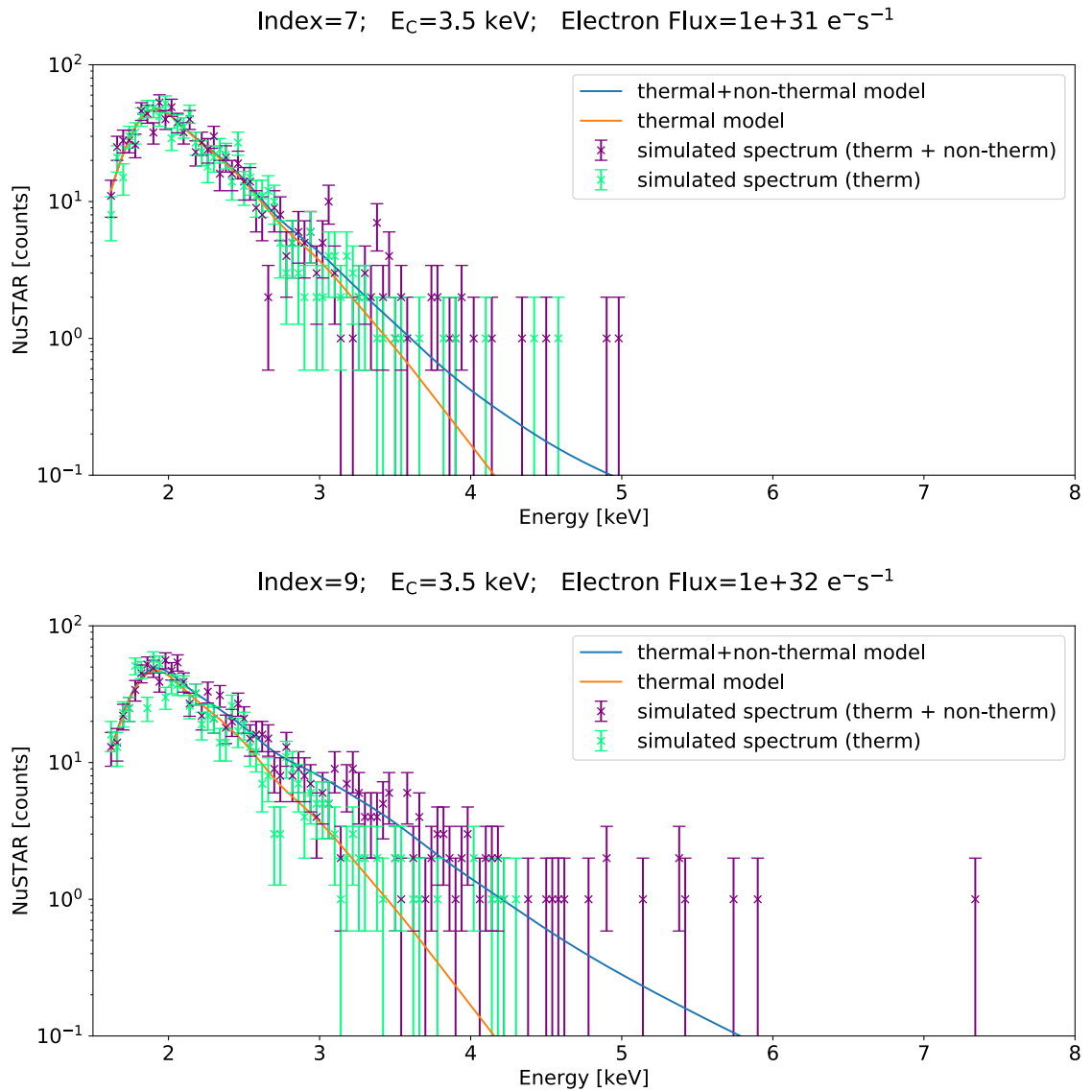


**Figure 3.10:** Examples of spectra simulated using Sunxspex models, using two different non-thermal models. All spectra use the same thermal model (orange) with a temperature of 3.2 MK and an emission measure of  $2.3 \times 10^{43}$   $cm^{-3}$ . The model with the additional non-thermal component, with the parameters shown in the plot titles, is also shown (blue). The simulated spectra are from the thermal model (green) and the thermal + non-thermal model (purple).

### 3.2 Analysis Methods for NuSTAR Quiet Sun Data

These simulated spectra can then be used to determine whether the added non-thermal component could remain undetected over the statistical noise. For this to be possible we set the following requirements:

1. At energies where the purely thermal spectrum produces counts (between 2 and 4 keV in the example in Fig. 3.10), the non-thermal component must not contribute more counts than the Poisson noise in the thermal spectrum, given by the square root of the sum of the thermal model over these energies.
2. At energies higher than this ( $> 4$  keV in this example), the non-thermal model must contribute no more than 4 counts, which is consistent with a null detection (Gehrels 1986).

Any non-thermal component that satisfies these requirements could remain undetected in the noise of the NuSTAR spectrum. In some cases, for example the flaring X-ray bright point discussed in Section 5.2.1, there is an excess in the observed spectrum of  $N_{\text{ex}}$  counts in the higher energy range compared to the isothermal model which fits it. This is not a null detection in NuSTAR, but there are still not enough counts to obtain a reliable fit with an additional non-thermal component. For spectra like this, the second condition instead becomes that there are no more than  $N_{\text{ex}} \pm \sqrt{N_{\text{ex}}}$  counts in the higher energy range, rather than the 4 counts which is consistent with a null detection.

Upper limits on the non-thermal component can be obtained by performing this test for a range of values of parameters for the non-thermal model. We simulate non-thermal models for several values of  $\delta$  (5, 7, and 9, as well as a mono-energetic beam of electrons, all with energy  $E_C$ ) and  $E_C$  between 3–6 keV. For each of these combinations, we reduce the electron flux iteratively until the non-thermal component satisfies the above conditions. We can repeat this calculation many times, taking the mean value to be the upper limit and the standard deviation gives an indication of the spread of the values. This results in a distribution of upper limits on the electron flux for a range of  $\delta$  and  $E_C$  values.

These upper limits on the electron flux can then be converted to upper limits on the power in the non-thermal distribution (see Equation 1.11, derived in Section 1.5.4) using:

$$P(> E_C) = 1.6 \times 10^{-9} \frac{\delta - 1}{\delta - 2} N_{TOT} E_C \quad [\text{erg s}^{-1}] \quad (3.8)$$

where  $E_C$  is in units of keV and the numerical factor that does not appear in Equation 1.11 accounts for the conversion from keV into erg. These powers can then be compared to

### 3.2 Analysis Methods for NuSTAR Quiet Sun Data

the heating power required by the thermal energy of the source in order to determine whether the heating could have been produced by accelerated electrons.

#### Comparison With Thermal Energy

The thermal energy,  $E_{th}$  of a source is given by:

$$E_{th} = \frac{3}{2} \sum_{\alpha} \int n_{\alpha} k_B T_{\alpha} dV \quad [\text{erg}] \quad (3.9)$$

where  $\alpha$  indicates the plasma species,  $k_B$  is the Boltzmann constant, and  $n$  and  $T$  are number density and temperature, respectively (Benz 2017). Assuming that the source is homogeneous and has equal electron and ion temperatures, as well as approximately equal electron and ion densities, the above equation becomes:

$$E_{th} = 3k_B T \sqrt{EM \times V} \quad [\text{erg}] \quad (3.10)$$

where  $T$  and  $EM$  are the temperature and emission measure of the emitting plasma from the spectral fitting, and  $V$  is the volume of the emitting plasma. We assume that this volume is approximately equal to  $A^{\frac{3}{2}}$ , where  $A$  is the area of the source in AIA. However, this volume estimate can be an overestimate by some filling factor between  $1-10^{-4}$  (Cargill & Klimchuk 1997; Takahashi & Watanabe 2000). Therefore, as we assume that the filling factor is 1, the obtained thermal energy is an upper limit.

When divided by the duration of the observation, a required heating power can be determined from the thermal energy. This can then be compared with the upper limits on the non-thermal power. If the power in a non-thermal distribution is greater than the heating requirement, then the observed heating could be provided by accelerated electrons (as in larger flares).

The analysis method discussed in the section is used several times throughout Chapters 4, 5, and 6, with the first example—for an emerging flux region observed in the 28 September 2018 NuSTAR quiet Sun mosaics—detailed in Section 4.1.3.

## 3.3 Summary

In this Chapter, we gave a brief overview of the six NuSTAR quiet Sun observing campaigns conducted between 2018–2020, during the minimum of the solar activity cycle. These have provided many orbits worth of data, including observations in both dwell mode (allowing rigorous investigation of the HXR time evolution of regions of interest) and full-disk mosaic mode (allowing all of the various types of HXR sources on the disk at the same time to be studied).

NuSTAR's use of focusing optics has allowed the quiet Sun to be observed at HXR energies with a much greater sensitivity compared to observations with other instruments. This allows the unique opportunity to study the HXR emission from these sources, and to search for high temperature and non-thermal components in these emission. These observations are the first to capture features such as X-ray bright points, small jets, mini-filament eruptions, and quiet Sun flares at HXR energies in the quiet Sun.

In the following chapters, we will present a more in-depth study of some of the NuSTAR quiet Sun observing campaigns. In Chapter 4, we analyse the two orbits of full-disk mosaics from 18 September 2018. This was the first of the NuSTAR quiet Sun observations, and several different types of features were captured in these mosaics, including an emerging flux region. In Chapter 5, we investigate two X-ray bright points from the 21 February and 12–13 September 2020 dwell observations. As both of these were the longest campaigns, with 9 and 10 dwell orbits, respectively, this provides an opportunity to study the time evolution of the bright points in HXRs over many hours. Finally, in Chapter 6, we study small-scale transient events also captured in the 21 February and 12–13 September 2020 observing campaigns. The Sun was very quiet during both of these observations, and the many hours of dwells increased the chances of detecting short-lived transients. Therefore, these datasets are the best of the six campaigns for this analysis.

# 4

## A Survey of Quiet Sun Features Captured in NuSTAR Full-Disk Mosaics

*The work in this Chapter is based on the research published in Paterson et al. (2023).*

In this chapter, we present analysis of the features observed on 28 September 2018, during the first of the NuSTAR quiet Sun observing campaigns from solar minimum (previously summarised in Section 3.1.1). NuSTAR observed the quiet Sun in mosaic mode for two orbits, the first from 18:24–19:24 UT, the second from 20:01–21:01 UT. The resulting mosaics are shown in Figure 4.1. XRT data was available for this time, and the corresponding XRT Be-thin and AIA 211 Å images are also shown in this figure.

It can be seen that there are a number of HXR sources which were captured in both mosaics, with EUV and SXR counterparts also being observed with XRT and AIA. One of the most interesting features is an emerging flux region, which went on to become an active region (NOAA 12723  $\beta$ ) a few days after this observation (full analysis presented in Section 4.1). In addition, three X-ray bright points (which we label BP1–3) were also identified in the NuSTAR mosaics, all appearing in both orbits (see Section 4.2). A small pair of quiet Sun loops, lying close to BP3, were also captured by NuSTAR in both orbits. There is a HXR source which appears in the first NuSTAR mosaic but not the second, suggesting that it is transient (unlike any of the other features captured in these mosaics). AIA images confirm that this source is a small jet (see Section 4.3). The largest and brightest source in both mosaics, located on the East limb, lies at the site where an active region was located two solar rotations previous to this observation. This feature is therefore a decayed active region (see Section 4.4). There are also regions of diffuse HXR emission in both mosaics.

Throughout Sections 4.1–4.4, we investigate each of the sources present using data from NuSTAR, AIA, and XRT. We fit their NuSTAR HXR spectra, searching for high temperature (>

## 4.1 Emerging Flux Region

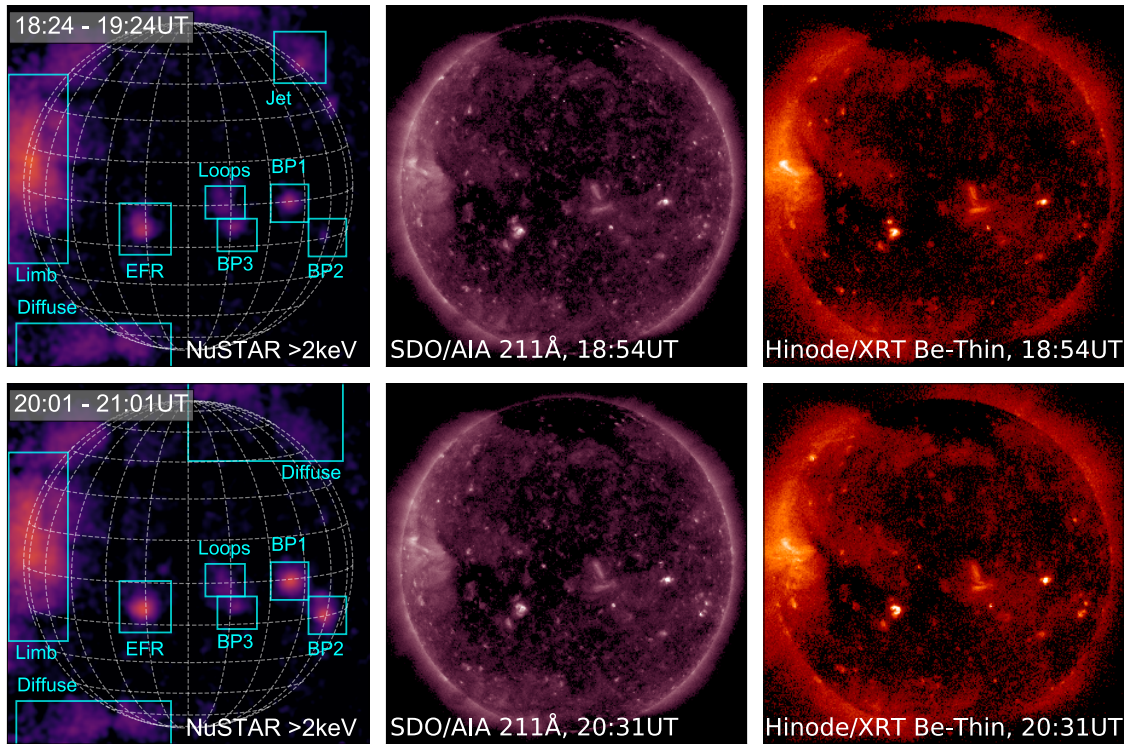


**Figure 4.1:** An overview of the NuSTAR QS observation on 28 September 2018, where NuSTAR observed in mosaic mode for two orbits. Full-disk images are from NuSTAR (left), AIA 211 Å (middle), and XRT Be-thin (right), with the images of the top row being from Orbit 1, and those on the bottom from Orbit 2. The boxes marked on the NuSTAR images highlight the different features observed, and the AIA and XRT images are from the mid-time of the two NuSTAR orbits. This figure is from Paterson et al. (2023).

5 MK) and non-thermal emission, and investigate their multi-thermal properties through DEM analysis. In the penultimate section of the chapter, Section 4.5, we compare the results found for the different types of quiet Sun phenomena.

### 4.1 Emerging Flux Region

AIA images show that the emerging flux region (EFR) captured in these mosaics first began to form shortly after 00:00 UT on 28 September 2018. This can be seen in the leftmost panels of Figure 4.2, which contains AIA 211 Å images and HMI magnetograms showing the evolution of the EFR between 28–29 September. There was then some flux cancellation between opposite polarities, after which the positive and negative polarities spread apart. This was the stage of the EFR’s lifetime which NuSTAR captured, shown on the third panel

#### 4.1 Emerging Flux Region

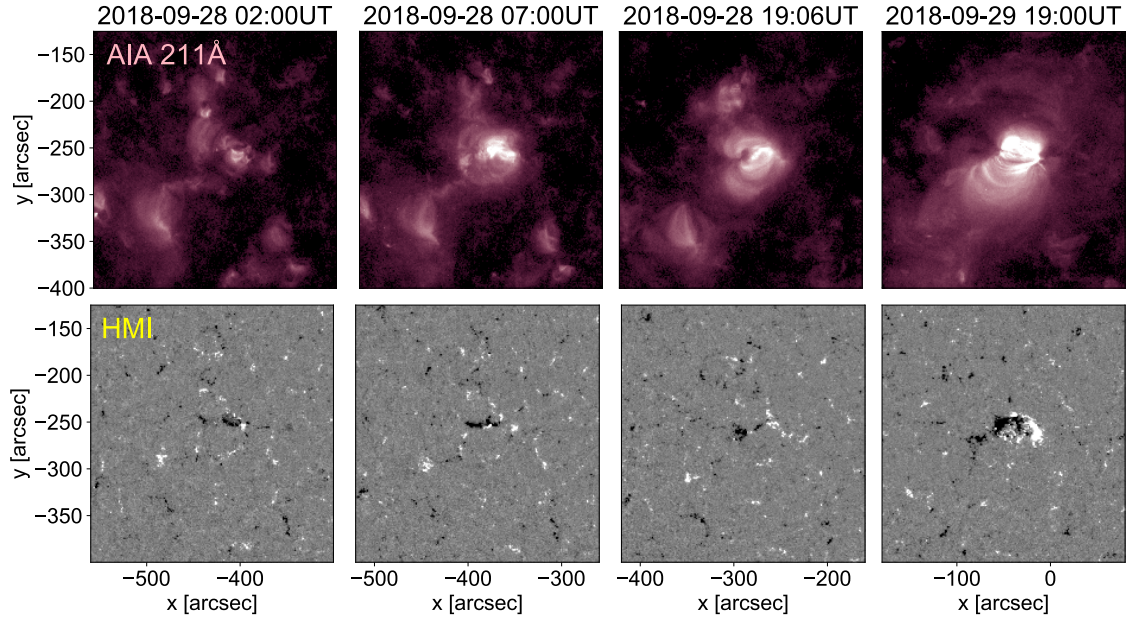


**Figure 4.2:** AIA 211 Å images (top row) and HMI magnetograms (bottom row) showing the evolution of the EFR from around the time of the first flux emergence (leftmost two panels), to when NuSTAR captured it in the mosaics (third panel from left), until this feature became an active region (rightmost panels).

from the left in each row in Figure 4.2. The following day, more intense flux emergence at this region occurred, which ultimately resulted in the formation of an active region. This is illustrated in the rightmost panels of Figure 4.2.

The full-disk mosaic observing mode is not ideal for tracking a feature over time but, fortunately, the overlapping mosaic tiles do provide the opportunity to investigate the temporal evolution of this EFR. This feature was captured in four pointings in each orbit (totalling 8 over the whole observation): 12, 13, 18, and 19.

AIA 211 Å and XRT Be-thin images of this feature, over-plotted with NuSTAR (2.2–4.0 keV) contours are shown in Figure 4.3. The NuSTAR image was shifted so that it was aligned with AIA. It can be seen from these images that the EFR is comprised of three separate regions of enhanced EUV and SXR emission: a bright central region ( $-250''$ ,  $-250''$ ), an upper region above this ( $-300''$ ,  $-200''$ ), and a lower region beneath ( $-350''$ ,  $-350''$ ). The NuSTAR contours confirm that the HXR emission originates primarily from the central region, as it does in EUV and SXR. However, during P12 of the first NuSTAR orbit, when the X-ray emission from this source is fainter, the NuSTAR contours indicate that there is some contribution from the upper region to the HXR emission. The lower region does not

#### 4.1 Emerging Flux Region

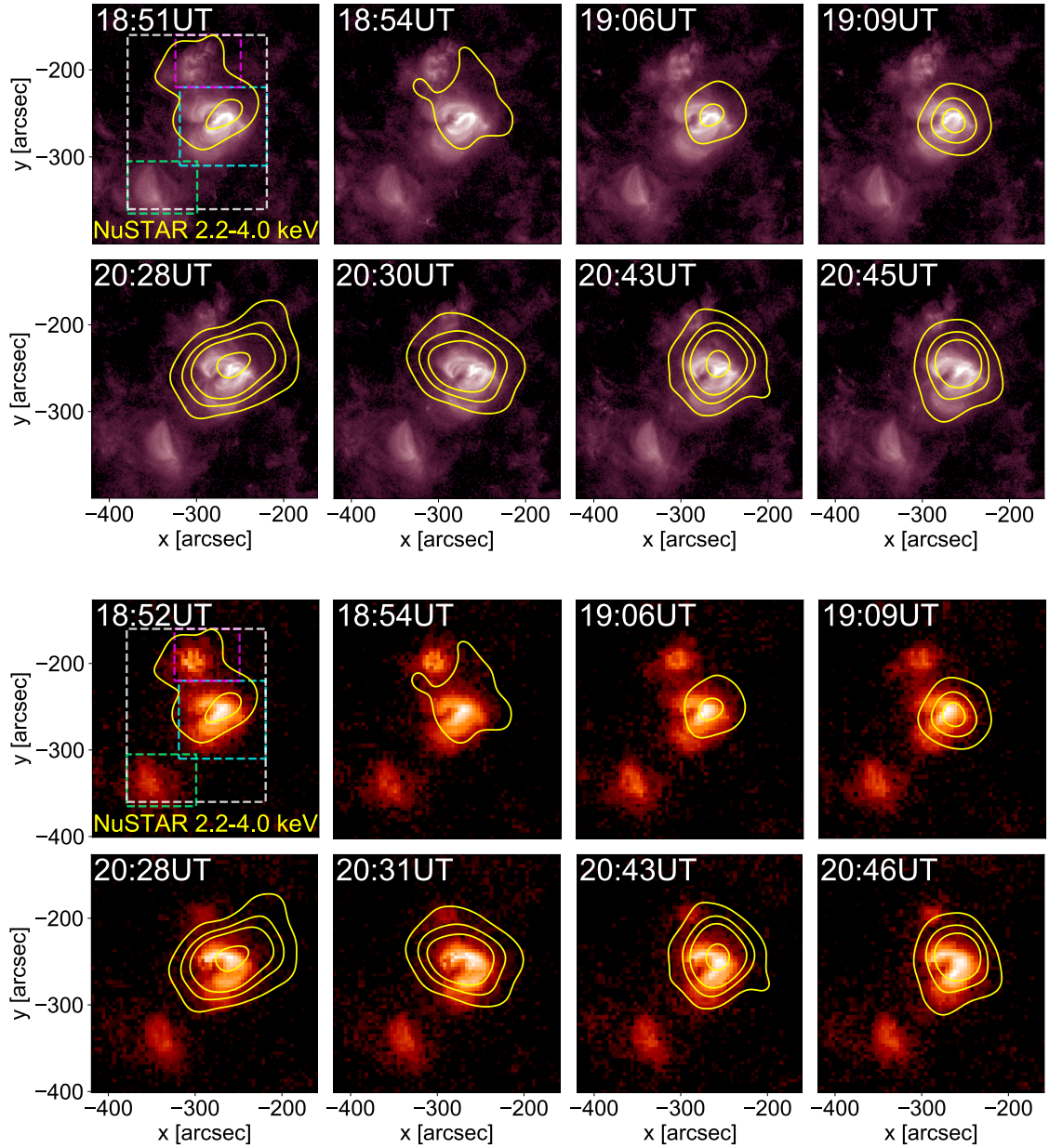


**Figure 4.3:** AIA 211 Å (top two rows) and XRT Be-thin images (bottom two rows) showing the EFR at the mid-times of the eight NuSTAR pointings in which this feature was captured. For both AIA and XRT, the top row shows the pointings from Orbit 1, with pointings 12, 13, 18, and 19 arranged from left to right. The bottom row shows the same for Orbit 2. The yellow contours represent NuSTAR FPMA+B 2.2–4.0 keV, aligned with AIA and plotted at 5, 10, 15, and  $30 \times 10^{-4}$  counts  $s^{-1}$ . This figure is from Paterson et al. (2023).

## 4.1 Emerging Flux Region

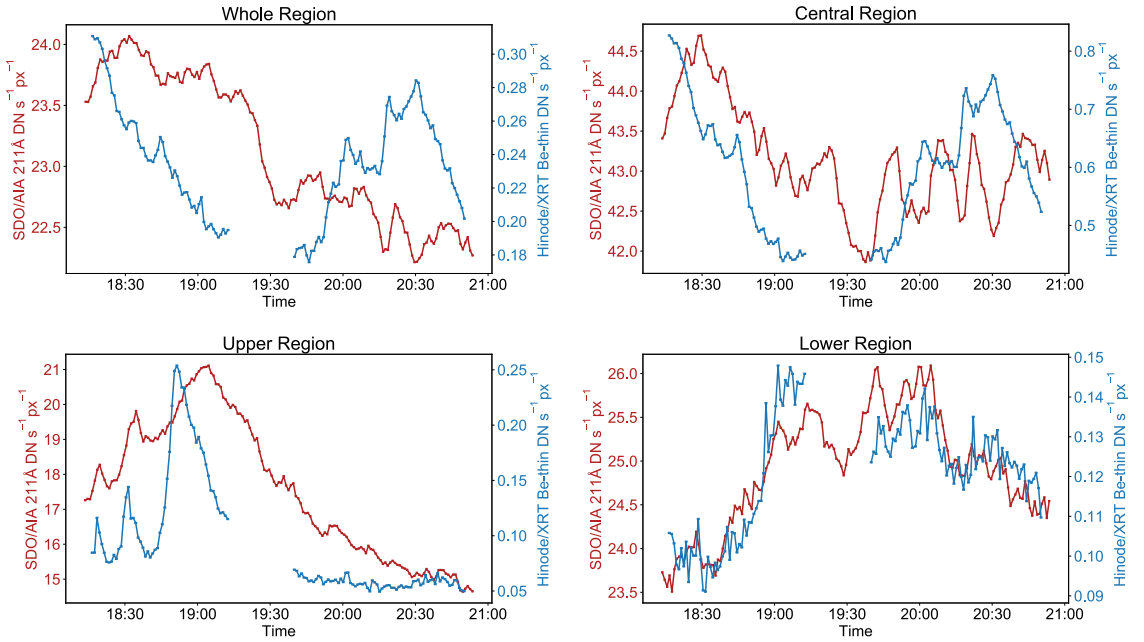


**Figure 4.4:** AIA 211 Å (red) and XRT Be-thin (blue) lightcurves for the three separate regions, as well as for the whole source, over the time period of the NuSTAR observation. These were calculated over the regions indicated in Figure 4.3. The green shaded areas indicate the times when NuSTAR was pointed at the EFR (P12, 13, 18, and 19 in both orbits).

significantly contribute to the NuSTAR emission at any point. However, this region would be positioned near the NuSTAR detector gaps (see Section 2.1) in some of these pointings and outside the FOV in others, which could explain the lack of detection.

The XRT and AIA 211 Å time profiles for this source over the two orbits of the NuSTAR observation are plotted in Figure 4.4. These are for the EFR as a whole, as well as for the separate regions discussed above (with the boxes that these time profiles were calculated over shown in the top left panel of Figure 4.3). It can immediately be seen that the central region dominates the SXR emission. Between NuSTAR P12 and 13 and P18 and 19 in the first orbit (these times are highlighted in green in Figure 4.4), both the AIA and XRT time profiles decrease. However, in the second orbit their behaviour differs. The XRT lightcurve reaches a peak during P12 and 13, and decreases through to P18 and 19. Conversely, the AIA 211 Å lightcurve is at a minimum during the earlier pointings, and increases until the later ones. It should be noted, however, that the change in 211 Å is very small in comparison to the change in XRT. This opposing behaviour in the AIA and XRT lightcurves will be further investigated through DEM analysis in Section 4.1.2.

For the upper region, the XRT lightcurve exhibits a sharp peak at the time of P12 in Orbit 1.

## 4.1 Emerging Flux Region

This is in agreement with the NuSTAR contours at this time (shown in Figure 4.3, top left panel), which indicate that this region contributes significantly to the NuSTAR emission at this time. The AIA 211 Å time profile reaches a peak later just before P18 and 19 of Orbit 1. This delay between the peaks in SXR and EUV suggest that the plasma is heated and then cools out of the range of XRT's sensitivity before that of 211 Å. The time profile for the lower region confirms that this source is very faint in X-rays compared to the central region at all times, and would therefore be unlikely to contribute in a significant way to the NuSTAR emission even if it were suitably located on the detector.

### 4.1.1 NuSTAR Spectral Analysis

The NuSTAR HXR spectra for the EFR were fitted in XSPEC for several times over the observation using the method detailed in Section 3.2.2. In order to improve the signal-to-noise while still retaining information about how the source evolves over time, the spectra from the consecutive pairs of pointings, P12 and 13 and P18 and 19, from each orbit were fitted simultaneously. The results obtained from fitting these spectra with XSPEC's APEC isothermal models are displayed in Figure 4.5, and are also summarised (along with all of the spectral fitting results from these mosaics) in Table 4.1. Also, Figure 4.6 summarises the results of the spectral analysis by plotting the fit temperatures and emission measures against time.

All four of these spectra are adequately fitted with isothermal models, and show no evidence of any hotter or non-thermal component. These spectra indicate that the temperature of this EFR stays almost constant throughout the NuSTAR observation, though it does increase slightly from 2.54 MK in Orbit 1 P12 and 13 to 2.63 MK in Orbit 2 P18 and 19. The corresponding emission measure ranges between  $1.93\text{--}6.10 \times 10^{44} \text{ cm}^{-3}$ . The emission measure decreases from 3.42 to  $1.93 \times 10^{44} \text{ cm}^{-3}$  between P12 and 13 and P18 and 19 in Orbit 1, when XRT also sees a decrease in emission (see Figure 4.4). The emission measure is highest, at  $6.10 \times 10^{44} \text{ cm}^{-3}$ , during Orbit 2 P12 and 13, at which time the XRT time profile peaks. Following the trend of the XRT lightcurve, it then falls off to  $2.40 \times 10^{44} \text{ cm}^{-3}$  later in this orbit during P18 and 19.

Note that, as seen previously in Equation 1.6, the emission measure of a source is related to both the volume and the electron number density. However, due to NuSTAR's poor spatial resolution, it is not easy to accurately determine what sub-region within the central region of the source seen in AIA that the HXR emission originated from. It is therefore difficult to say whether the changes in emission measure indicated from the spectral fitting are

### 4.1 Emerging Flux Region

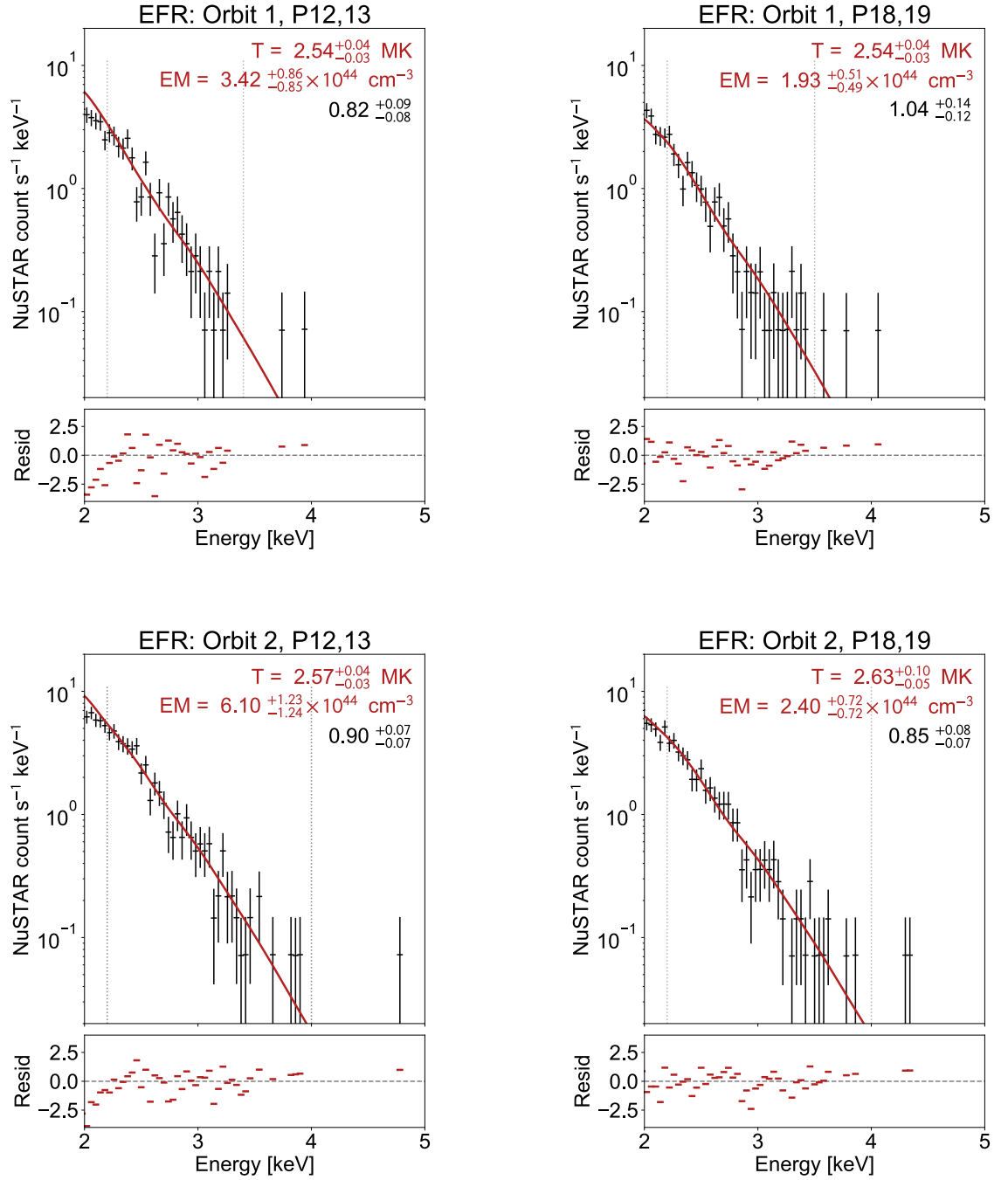


**Figure 4.5:** NuSTAR spectra for the EFR from Orbit 1 (top row) and Orbit 2 (bottom row), P12 and 13 (left) and P18 and 19 (right). These spectra are fitted with isothermal models (red), with the fit temperatures, emission measures, and constant multiplicative factors marked on the plot. The fitting range is indicated by vertical dotted lines.

## 4.1 Emerging Flux Region

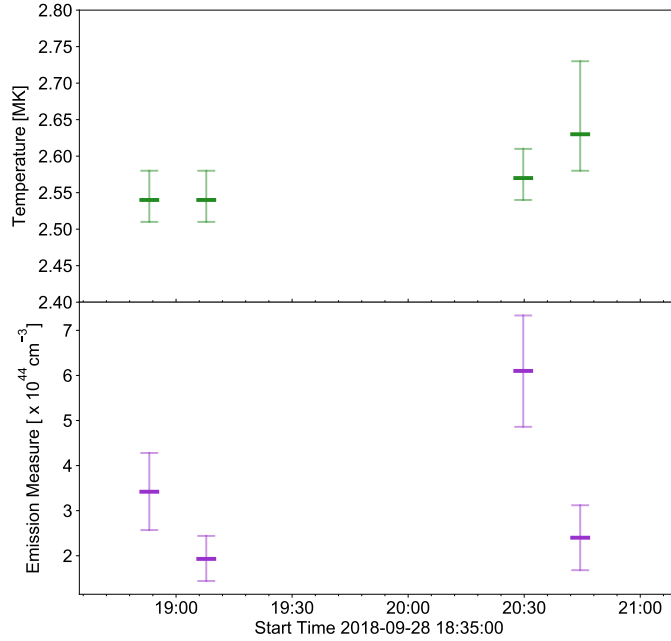


**Figure 4.6:** A summary of the NuSTAR spectral fitting results shown in Figure 4.5 for the EFR. The fit temperatures (top) and emission measures (bottom) are plotted against time.

due to a change in the volume of the source and/or in the number density of emitting electrons.

### 4.1.2 Differential Emission Measures

The AIA 211 Å and XRT Be-thin lightcurves for the EFR (Figure 4.4) were found to show different behaviours. In Orbit 2, the XRT time profile decreases between P12 and 13 (20:30 UT) and P18 and 19 (20:45 UT), at the same time as the AIA 211 Å lightcurve increases. As XRT is sensitive to hotter material than AIA 211 Å, this indicates the presence of hotter material at the earlier time, which then cools, resulting in the increased 211 Å emission at the later time. This can be confirmed by comparing the DEM of the EFR from these times. In order to investigate the discrepancy between AIA and XRT, we therefore reconstructed DEMs for the EFR using the method explained in Section 3.2.3. We jointly considered consecutive pointings (P12 and 13, and P18 and 19 from each orbit) as was done with the NuSTAR spectral fitting in the previous section.

When calculating these DEMs, the inclusion of X-ray data from NuSTAR and XRT is important in constraining the solution at high temperatures. Figure 4.7 is an example of an

#### 4.1 Emerging Flux Region

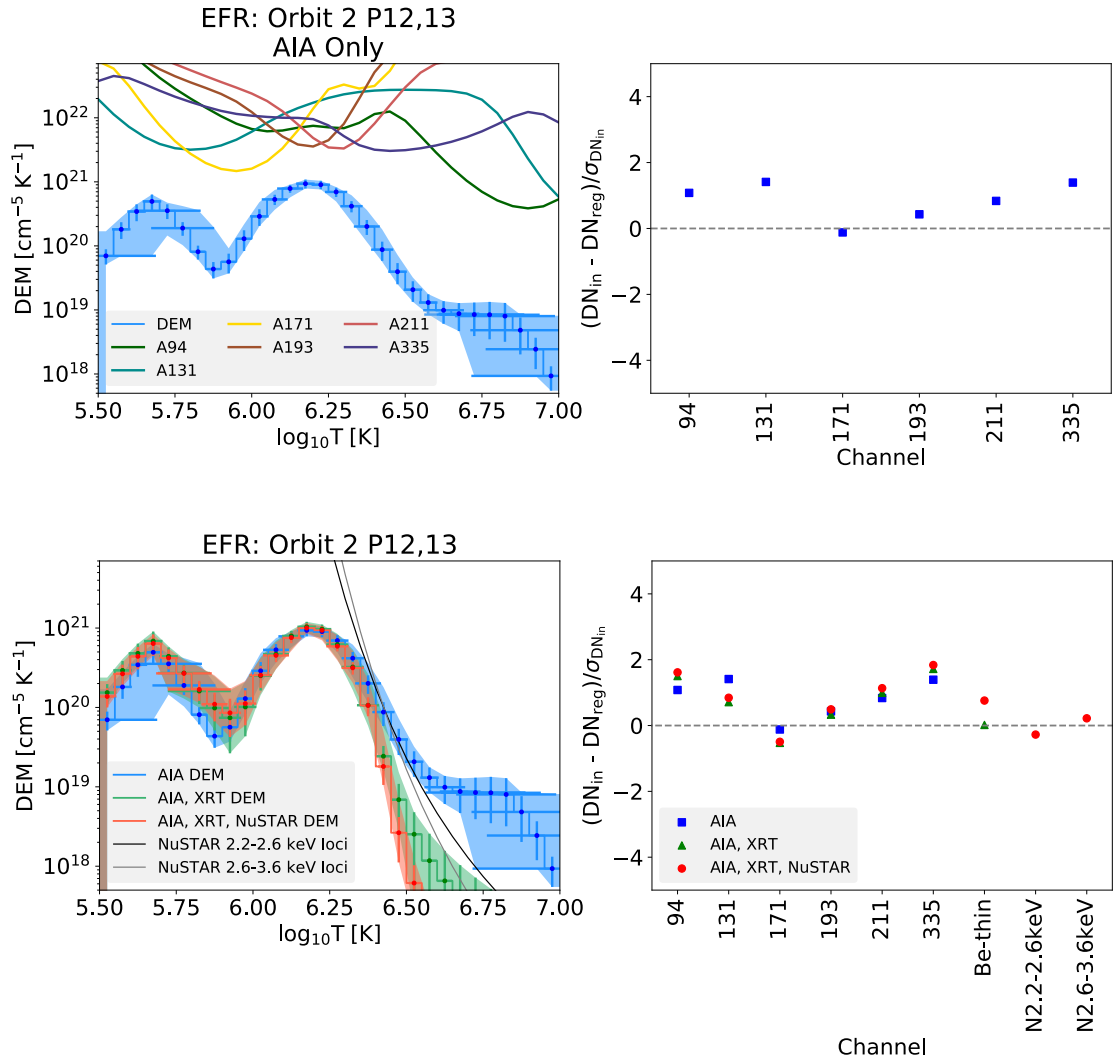


**Figure 4.7:** An example of an EFR DEM (from Orbit 2 P12 and 13) calculated with and without X-ray data. (Top row) The DEM calculated using only EUV data from AIA. The EM loci curves for each of the channels, which constrain the DEM solution, are also plotted. (Bottom row) These DEMs were calculated using data from AIA only (blue, same as the DEM in the top row), AIA and XRT (green), and AIA, XRT, and NuSTAR (red). The NuSTAR EM loci curves are also plotted in black and grey. The corresponding normalised residuals are shown on the right.

#### 4.1 Emerging Flux Region

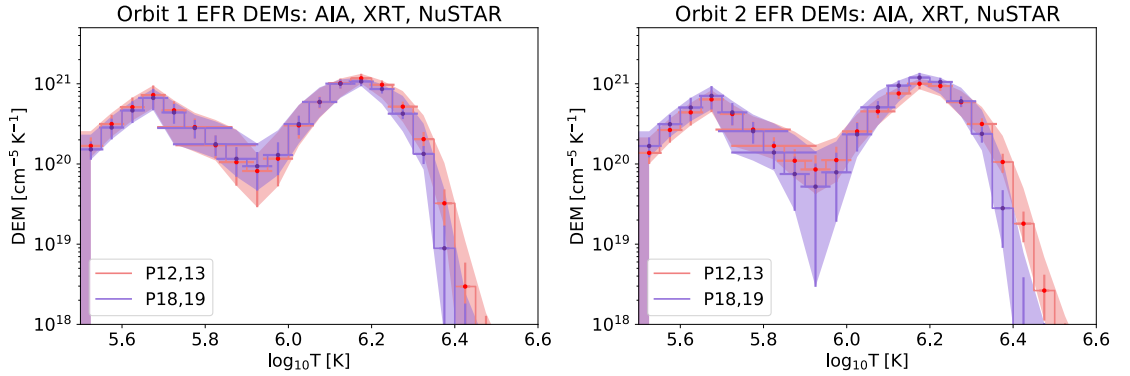


**Figure 4.8:** DEMs calculated for the EFR using AIA and NuSTAR data for Orbits 1 (left) and 2 (right), P12 and 13 (red) and P18 and 19 (blue). This figure is from Paterson et al. (2023).

EFR DEM from Orbit 2 P12 and 13 which illustrates the benefits of including X-ray data in a DEM calculation. This plot shows DEMs calculated using data from AIA only, AIA and XRT, and AIA, XRT, and NuSTAR. The EM loci curves (the data divided by the temperature response, which give the maximum possible emission at each temperature and are used to constrain the DEM solution—see Section 3.2.3) for AIA and NuSTAR are also plotted. It can be seen that all three DEM solutions are in agreement up to  $\log(T) \sim 6.4$ . Above this temperature, calculating the DEM with only AIA data introduces an erroneous high temperature component, as shown in the top row of Figure 4.7. Figure 4.7 demonstrates that DEMs calculated using only EUV data are unconstrained at high temperatures. Including X-ray data in the calculation helps to solve this problem.

There have been past studies that have calculated DEMs for non-flaring active regions, and also found the result (using different methods for DEM recovery) that using only AIA data produces erroneous DEM components at high temperatures (Reale et al. 2009; Schmelz et al. 2015). In these cases, including HXR data (from RHESSI) to constrain the DEM at these temperatures was found to remove these components. The DEMs found in a previous EFR study by Kontogiannis et al. (2020) were not well constrained at higher temperatures as only EUV data from Hinode/EIS was included.

The DEMs recovered for the EFR, using data from AIA, XRT, and NuSTAR, are compared in Figure 4.8. It can immediately be seen that the DEMs from all four times show a similar two-peak structure, with peaks at  $\log(T) \sim 5.7$  and 6.15. This is in line with a previous study of an EFR in the quiet Sun by Kontogiannis et al. (2020), which reconstructed DEMs using EUV data from Hinode/EIS. They also found a peak in their DEM at  $\log(T) \sim 6.1$  at a similar magnitude to those found for this EFR.

#### 4.1 Emerging Flux Region

The DEMs from the four times can be compared to investigate the evolution of the EFR. The EFR DEMs for the first orbit are shown in Figure 4.8 (left panel). In this orbit, the AIA 211 Å and XRT lightcurves both decrease between P12 and 13 and P18 and 19, though the changes in each are less than the 20% uncertainties that were assigned to the data values for the DEM calculation. The DEM for P12 and 13 the higher of the two for  $\log(T) > 6.2$ , though the difference between them is not significant when the uncertainties are considered, agreeing with the small decreases in the time profiles.

The EFR DEMs for the second orbit are shown in Figure 4.8 (right panel). In this orbit, the XRT time profile decreases between P12 and 13 and P18 and 19 by more than the 20% systematic uncertainty, while the AIA 211 Å emission increases by a small amount. The DEMs show more emission at  $\log(T) > 6.3$  (2 MK) at the earlier time, confirming that there is more hot material at the time of the peak in the XRT lightcurve. The DEM from P18 and 19 is the higher of the two at  $\log(T) \sim 6.1$ – $6.3$ , though they are not significantly different at this temperature range when the error bars are considered. It is likely that material at these temperatures produced the increase in the AIA 211 Å lightcurve between these times.

##### 4.1.3 Non-Thermal Upper Limits

The NuSTAR spectra for the EFR (shown in Figure 4.5) were all adequately fitted with isothermal models. So, we determined upper limits on the non-thermal emission consistent with a null detection in NuSTAR, and compared them to the thermal energy of the EFR using the method outlined in Section 3.2.4. This was done for the time of the peak in the XRT time profile shown in Figure 4.4, corresponding to P12 and 13 in the second NuSTAR orbit.

We assumed that the NuSTAR emission primarily originates from the bright central region in AIA, which we took to have an area of  $\sim 35'' \times 35''$ . This is demonstrated in the left-hand panel of Figure 4.9. Using  $V \sim A^{\frac{3}{2}}$ , this means that the emitting volume is  $1.65 \times 10^{28} \text{ cm}^3$ . The resulting thermal energy (from Equation 3.7, and using  $T = 2.57 \text{ MK}$  and  $EM = 6.10 \times 10^{44} \text{ cm}^{-3}$  from the NuSTAR spectral fit) was found to be  $3.37 \times 10^{27} \text{ erg}$ . This can be divided by the observation time (the time from the start of P12 until the end of P13) of 246 s to obtain a heating power of  $1.37 \times 10^{25} \text{ erg s}^{-1}$ .

The calculated non-thermal upper limits for the EFR, along with the thermal heating power needed, are plotted in Figure 4.9. It can be seen that none of the non-thermal

## 4.2 X-ray Bright Points

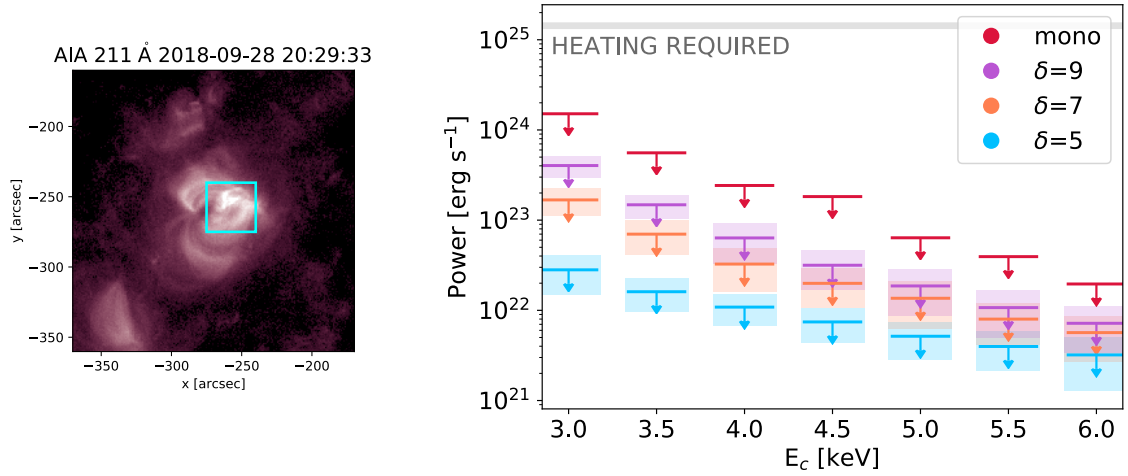


**Figure 4.9:** (Left) AIA 211 Å image of the EFR, with the blue box indicating the area used for calculating its thermal energy. (Right) Non-thermal upper limits for the EFR for a range of low energy cutoffs and power law indices (including a mono-energetic beam of electrons at  $E = E_C$ ). The shaded boxes indicate the  $\pm 1\sigma$  range, and the grey line indicates the heating requirement dictated by the thermal energy.

upper limits satisfy this requirement; they are all at least an order of magnitude too small. The heating requirement could be reduced if the area used were an over-estimate and a smaller area was chosen. However, with the difference between the required heating power and the non-thermal upper limits being so large, it can be concluded that it is unlikely that this source is heated by a non-thermal component.

## 4.2 X-ray Bright Points

In the 28 September 2018 NuSTAR mosaics, NuSTAR captured three X-ray bright points, as shown in the full disk images in Figure 4.1 (labelled BP1–3). AIA 211 Å and XRT Be-thin images of these bright points are shown in Figure 4.10.

BP1 and BP2 lie close to each other, in a region which was captured in P14, 15, 16, and 17 in both orbits. BP1 was observed by NuSTAR in all eight of these pointings. However, BP2 was extremely faint in HXRs in the first orbit, and was positioned near the edge of the NuSTAR detector in P14 and 15 of the second orbit. Therefore, the only usable pointings for spectroscopy for BP2 are Orbit 2 P16 and 17. BP3 is the faintest of the bright points in NuSTAR, AIA, and XRT. NuSTAR also detected emission from a pair of quiet Sun loops

## 4.2 X-ray Bright Points

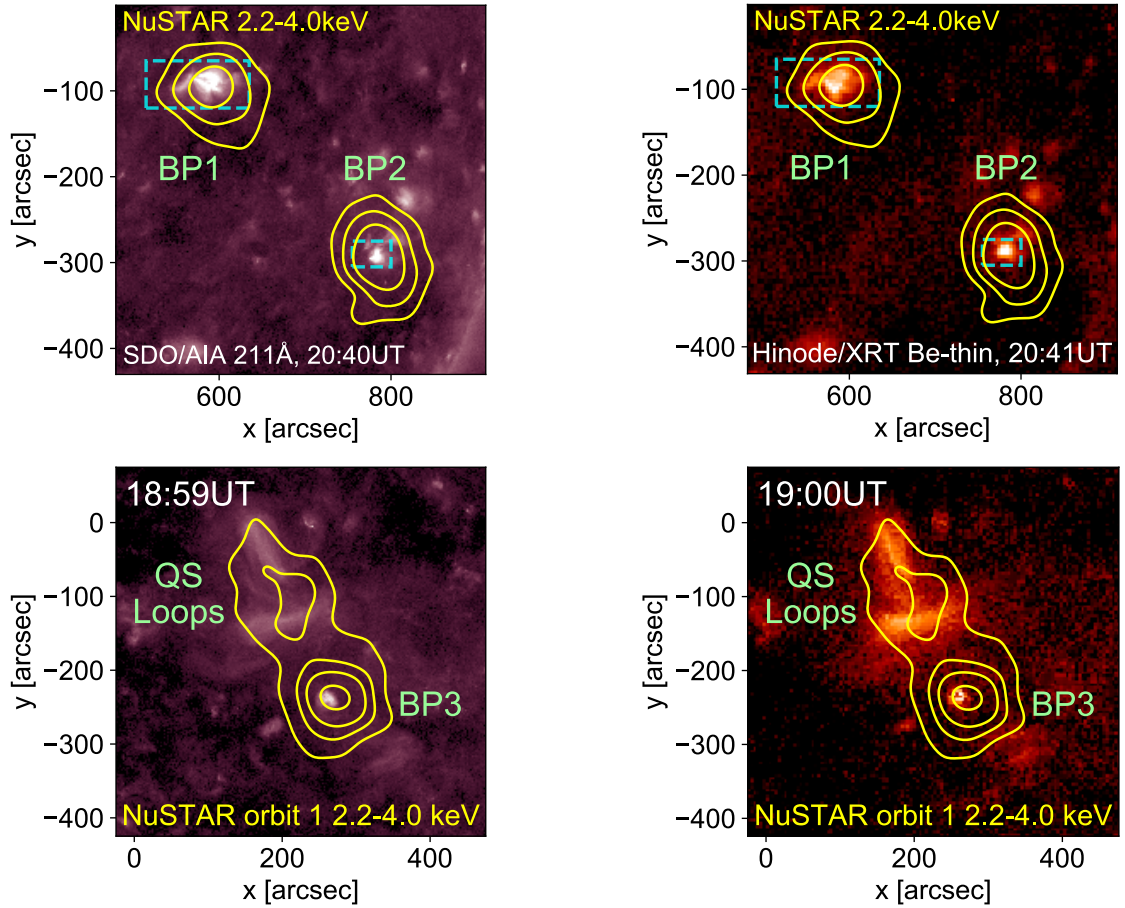


**Figure 4.10:** (Top) AIA 211 Å and XRT Be-thin images of BP1 and BP2 at the time of Orbit 2 P17. The NuSTAR emission is represented by the yellow contours which are plotted at  $5$ ,  $10$ , and  $20 \times 10^{-4}$  counts  $s^{-1}$ . The boxes indicate the regions used for calculating lightcurves. (Bottom) AIA 211 Å and XRT Be-thin images of BP3 and the nearby quiet Sun loops from NuSTAR Orbit 1. The NuSTAR contours, which are summed over all of the pointings which captured BP3 in this orbit (13, 14, 16, and 17), are plotted at  $4$ ,  $5$ ,  $10$ , and  $15 \times 10^{-4}$  counts  $s^{-1}$ . This figure is from Paterson et al. (2023).

## 4.2 X-ray Bright Points

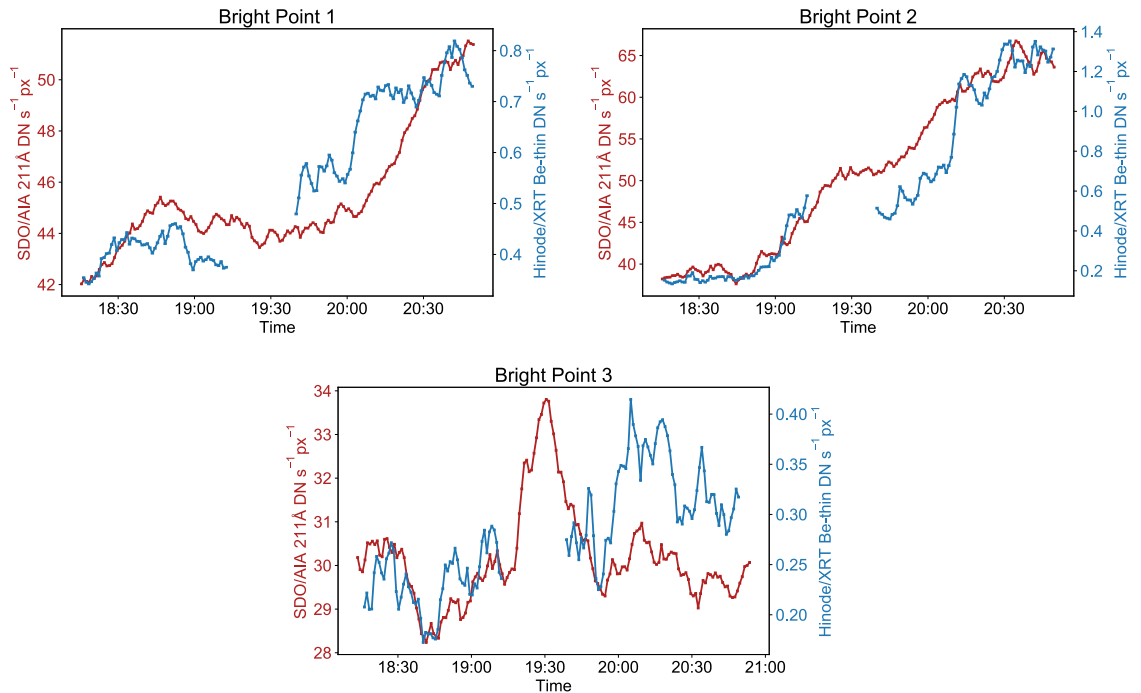


**Figure 4.11:** AIA 211 Å (red) and XRT Be-thin (blue) lightcurves for BP1 (top left), BP2 (top right), and BP3 (bottom). The shaded green areas indicate the times where NuSTAR was pointed at the bright points, and each bright point was observed suitably well for performing NuSTAR spectroscopy (P14, 15, 16, and 17 in both orbits for BP1; P16 and 17 in Orbit 2 for BP2; and P13, 14, 17, and 18 in both orbits for BP3)

that lay close to BP3. Both of these features were captured in P13, 14, 17, and 18 in both orbits.

The AIA 211 Å and XRT time profiles for all three of the bright points are plotted in Figure 4.11. It can be seen that both BP1 and BP2 brighten in EUV and SXR over the two NuSTAR orbits. In both AIA and XRT, BP1 reaches a peak in brightness just before the NuSTAR pointings in Orbit 1, and then continues to brighten through to Orbit 2. BP2 is not well observed by NuSTAR in Orbit 1, but is captured in Orbit 2, indicating an increase in HXR emission. This is in agreement with the increase in SXR (and EUV) emission between the NuSTAR pointings in the two orbits observed with XRT (and AIA).

The AIA 211 Å lightcurve for BP3 does not change significantly between the pointings in which NuSTAR captured it. There is a spike in this lightcurve at around 19:30 UT, but neither NuSTAR nor XRT were observing this feature at this time. The XRT Be-thin time profile for BP3 also does not show as large a relative change between the two orbits as was

## 4.2 X-ray Bright Points

seen for the other two bright points.

### 4.2.1 NuSTAR Spectral Analysis

The NuSTAR HXR spectra were fitted for all three bright points, as well as the QS loops, for the two orbits. For BP1, since the four NuSTAR pointings from each orbit which captured this feature were consecutive, all of them could be combined for the spectral fitting to obtain the best signal-to-noise. BP2 was sufficiently well observed to perform spectroscopy in Orbit 2 P16 and 17, and so the spectra from these pointings only were fitted simultaneously. BP3, the faintest of the bright points, was captured in P13, 14, 17, and 18, and all four of these pointings were fitted simultaneously for both orbits. The results of fitting these spectra with APEC isothermal models, following the approach explained in Section 3.2.2, are shown in Figure 4.12.

For BP1, the NuSTAR fit temperature does not change between the two orbits, remaining at  $\sim 2.5$  MK. However, the emission measure does change, increasing from  $1.12$  to  $4.07 \times 10^{44} \text{ cm}^{-3}$ . This is in agreement with the steady increase in brightness in both SXR and EUV shown in the lightcurves for this feature in Figure 4.11. The relative increases in all of the instruments are different, however. NuSTAR sees the emission measure increase by a factor of  $\sim 4$ , whereas the XRT Be-thin and AIA 211 Å lightcurves only increase by factors of  $\sim 2$  and  $1.2$ , respectively. This is because NuSTAR is only sensitive to the hottest emission (at  $\sim 2.5$  MK) in this bright point. AIA 211 Å (and to a lesser extent, XRT) also has sensitivity to material at lower temperatures. Therefore, the brightening at 2.5 MK is less significant to the overall emission than it is in NuSTAR.

The spectral fit for BP2 indicates a slightly hotter temperature compared to BP1 of 3.22 MK, with an emission measure of  $5.98 \times 10^{43} \text{ cm}^{-3}$ . Previous studies have found coronal bright points do not typically reach temperatures higher than 2–3 MK (Golub et al. 1974; Doschek et al. 2010; Alexander et al. 2011), though Kariyappa et al. (2011) investigated a bright point which was heated to temperatures of  $\sim 3.4$  MK. BP2 therefore contains hotter material than would be expected for a typical X-ray bright point.

For the faintest of the bright points, BP3, the NuSTAR spectral fit gives a temperature and emission measure of 3.22 MK and  $1.33 \times 10^{43} \text{ cm}^{-3}$  in the first orbit, and of 2.56 MK and  $5.10 \times 10^{43} \text{ cm}^{-3}$  in the second. However, this feature is very faint, particularly in Orbit 2. Therefore, the fits may not be entirely reliable.

## 4.2 X-ray Bright Points

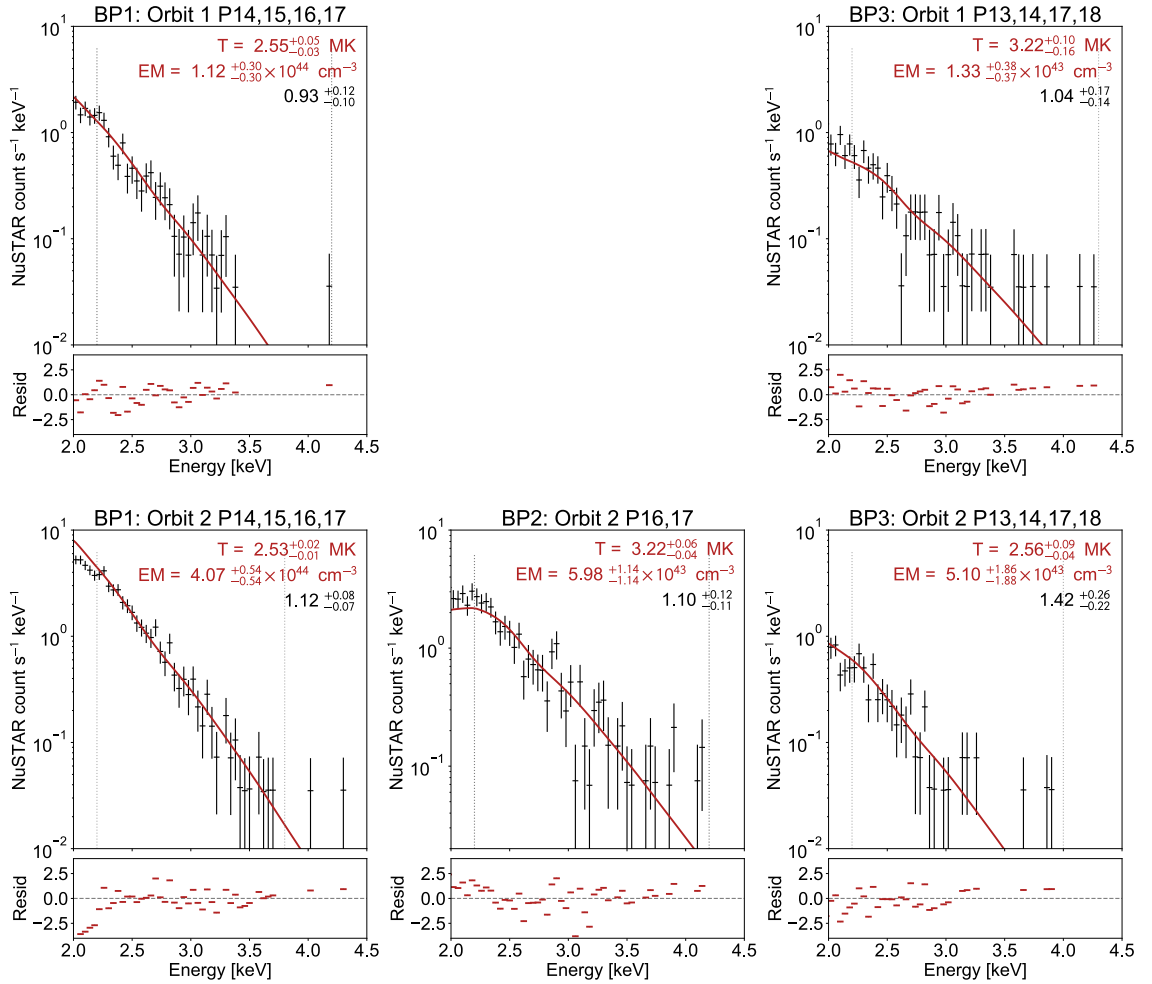


**Figure 4.12:** NuSTAR spectra for the three X-ray bright points observed on 28 September 2018, with the spectra from Orbit 1 plotted in the top row, and those from Orbit 2 on the bottom. Spectra for BP1 (left) combine P14, 15, 16, and 17. The BP2 spectrum (bottom row, middle panel) combines P16 and 17. The BP3 spectra (right) combine P13, 14, 17, and 18 from both orbits. These spectra are fitted with isothermal models (red), with the fit temperatures, emission measures, and constant multiplicative factors marked on the plot. The fitting range is indicated by vertical dotted lines.

## 4.2 X-ray Bright Points

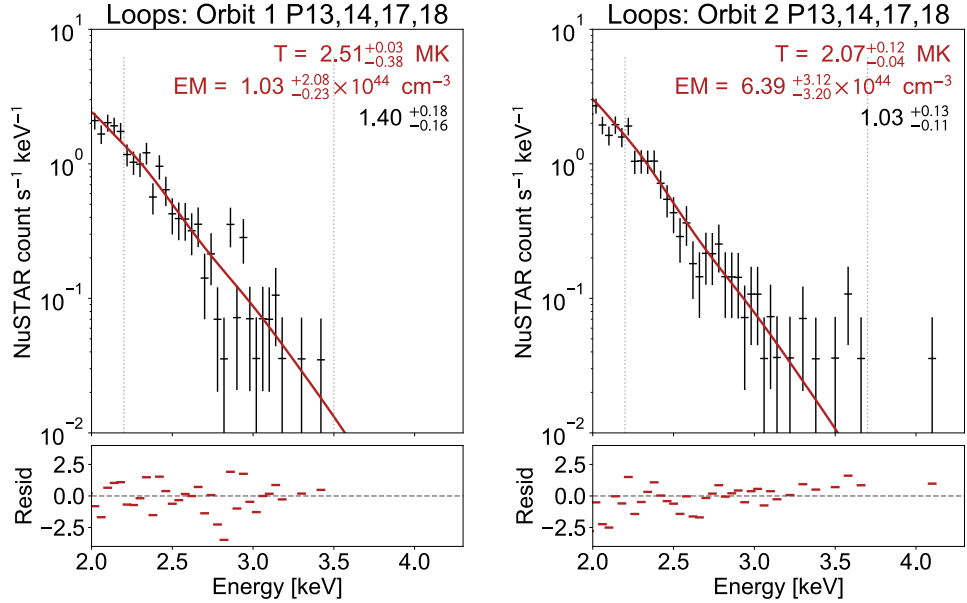


**Figure 4.13:** NuSTAR spectra for the quiet Sun loops observed on 28 September 2018, for Orbits 1 (left) and 2 (right). The NuSTAR spectra for P13, 14, 17, and 18 were fitted simultaneously for both orbits. These spectra are fitted with isothermal models (red), with the fit temperatures, emission measures, and constant multiplicative factors marked on the plot. The fitting range is indicated by vertical dotted lines.

We also fitted the NuSTAR spectrum from each orbit for the QS loops that were situated near BP3 (using the same pointings as for BP3—P13, 14, 17, and 18—for simultaneous fitting). The results of fitting these spectra with an isothermal model are shown in Figure 4.13. These fits returned slightly cooler temperatures ranging from 2.1–2.5 MK (with emission measures between  $1.03\text{--}6.39 \times 10^{44} \text{ cm}^{-3}$ ).

The spectra for all of the X-ray bright points (and for the quiet Sun loops) are all adequately fitted by isothermal models, with no suggestion of a higher temperature or non-thermal component.

### 4.2.2 Differential Emission Measures

As seen in Section 4.2.1, the spectral fitting for BP2 returned a higher temperature of 3.2 MK compared to BP1. DEM analysis was performed in order to confirm that BP2 does contain more material heated to higher temperatures compared to BP1, which has a more typical bright point temperature. We reconstructed the DEMs for all three of the bright points using the method outlined in Section 3.2.3. We calculated the DEMs for BP1 for both

## 4.2 X-ray Bright Points

orbits and for BP2 during Orbit 2, using the same pointings used in the spectral fitting in the previous section. The DEMs for BP1 were recovered using data from AIA, XRT, and NuSTAR, whereas only AIA and NuSTAR were used for BP2. This is because several of the XRT pixels covering BP2 were saturated during Orbit 2 (though performing the DEM calculation including the XRT data was not found to significantly change the resulting DEM).

The DEMs for BP1 and BP2 are plotted in the top row of Figure 4.14. The increase in brightness in X-rays and EUV between the two orbits that is observed in the lightcurves (in Figure 4.11) for BP1 is reflected in the DEMs. For this bright point, the DEM from Orbit 2 is greater than in Orbit 1 for  $\log(T) > 6.2$ . BP2 is the brightest of the two features in NuSTAR and XRT, and this is in agreement with the DEM for BP2 being higher than the BP1 DEM (even in the second orbit, when BP1 is at its brightest) at  $\log(T) > 6.2$ . The flatter tail of the BP2 DEM at high temperatures is consistent with the hotter NuSTAR spectral fit temperature compared to BP1.

The bottom row of Figure 4.14 shows DEMs for all three bright points, including BP3 during Orbit 1, when the NuSTAR spectral fits indicated that this feature was hottest (with a temperature of  $\sim 3.2$  MK, similar to BP2 during Orbit 2). BP3 is the faintest of the three bright points, and this is reflected in its DEM, which lower than the other two across all temperatures. However, its DEM does exhibit a similarly shaped tail to BP2 (which had a similar NuSTAR fit temperature) at  $\log(T) > 6.2$ .

The DEMs for all three bright points have a two-peak structure, peaking at  $\sim 5.7$  and  $6.15$ . Peaks around these temperatures have also been found in previous analyses including DEMs (Brosius et al. 2008; Doschek et al. 2010). Past studies have attributed the lower temperature peak to the background corona, and the higher temperature one to the bright point itself. HXR data from NuSTAR helps to constrain the DEM solutions found here at higher temperatures. This confirms that none of the bright points studied here constrain any significant emission  $> 4$  MK.

### 4.2.3 Non-Thermal Upper Limits

We calculated non-thermal upper limits (using the approach from Section 3.2.4) for the two strongest bright points, BP1 and BP2. For both bright points, the upper limits were calculated for Orbit 2, when these features were producing the brightest HXR emission. The NuSTAR spectra used for this analysis are shown in the bottom row of Figure 4.12,

## 4.2 X-ray Bright Points

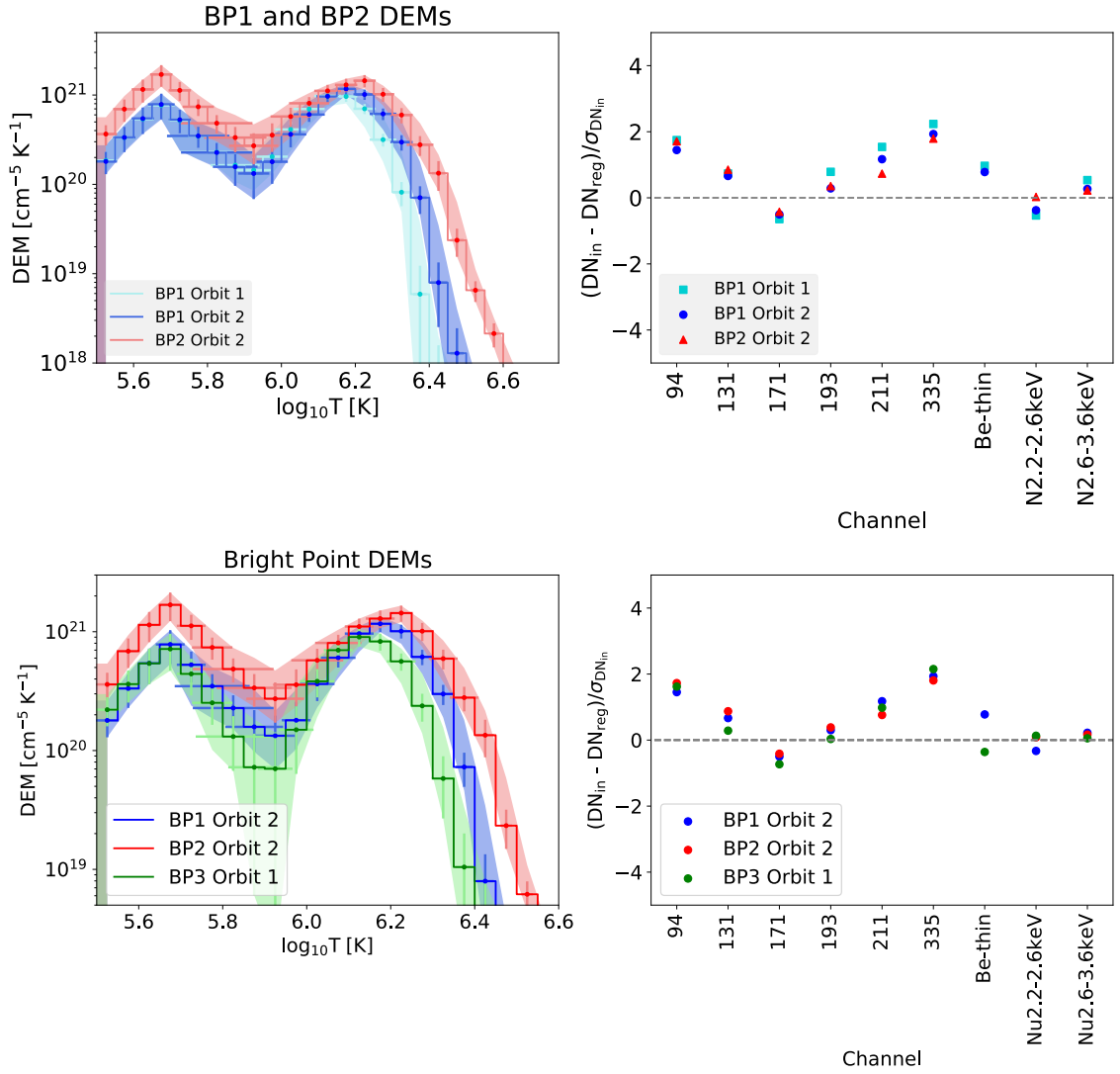


**Figure 4.14:** (Top row) DEMs for the best observed bright points: BP1, during Orbits 1 (light blue) and 2 (dark blue) and BP2 during Orbit 2 (red). (Bottom row) DEMs for all three bright points: BP1 (blue) and BP2 (red) from Orbit 2, and BP3 (green) from Orbit 1, when this bright point had the highest spectral fit temperature. This figure is from Paterson et al. (2023).

### 4.3 Jet

with the fit temperatures and emission measures used to calculate the thermal energy marked on these plots.

AIA images show that BP1 has an area of  $\sim 35'' \times 35''$  (as demonstrated in the top left panel of Figure 4.15), which corresponds to a volume of  $1.65 \times 10^{28} \text{ cm}^3$ . Therefore, using the fit parameters, the thermal energy of this bright point is  $2.71 \times 10^{27} \text{ erg}$ . This can be divided by the observation time (between the start of P14 and the end of P17) of 540 s to find a thermal heating requirement of  $5.02 \times 10^{24} \text{ erg s}^{-1}$ .

The non-thermal upper limits for BP1 are shown in the top right panel of Figure 4.15. It can be seen that most of the upper limits are at least an order of magnitude below the heating required. This requirement could be reduced by using a filling factor  $< 1$  or by using a smaller area estimate. However, as was the case with the EFR, this source is not likely to be powered by a non-thermal component.

From the AIA image in the bottom left panel of Figure 4.15, it can be seen that BP2 covers an area of  $\sim 15'' \times 15''$ , giving a volume of  $1.30 \times 10^{27} \text{ cm}^3$ . Using this volume and the temperature and emission measure from the NuSTAR spectral fit, the thermal energy of BP2 is  $3.71 \times 10^{26} \text{ erg}$ . Dividing this by observation duration (from the start of P16 to the end of P17) of 245 s gives a heating power of  $1.52 \times 10^{24} \text{ erg s}^{-1}$ .

This heating requirement is higher than any of the non-thermal upper limits, as shown in the bottom right panel of Figure 4.15. However, this difference is only small for a very steep (basically mono-energetic) non-thermal distribution at  $\sim 3 \text{ keV}$ . Again, the heating requirement could be lowered by introducing a filling factor or reducing the area, which could make it less than some of the upper limits. However, while it is therefore possible that this source could be heated by a non-thermal component, this is a marginal result.

### 4.3 Jet

While most of the sources that NuSTAR detected in the 18 September 2018 mosaics were steady sources that were present in both orbits, there is a feature that appears in the top right corner of the first mosaic but not the second. AIA images of this source confirm that it is a compact jet, which NuSTAR was fortunate to capture as it rastered across the disk. This source appears in P4–7 in the first mosaic. AIA and XRT images from the times of these pointings showing the evolution of this transient event can be found in Figure 4.16. The AIA 211 Å images show that the material is ejected almost perpendicularly to the right

### 4.3 Jet

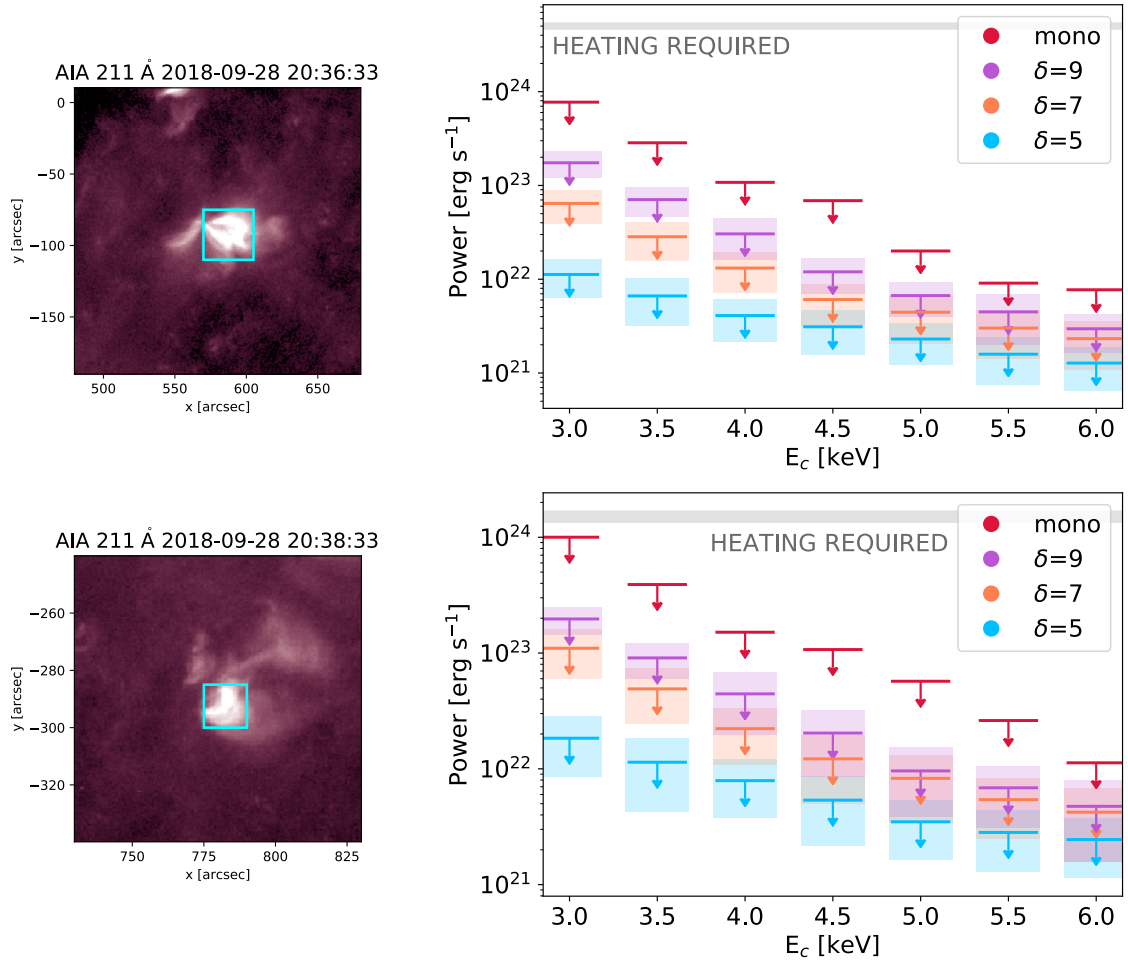


**Figure 4.15:** Non-thermal upper limits for BP1 (top row) and BP2 (bottom row). (Left) AIA 211 Å image of the bright point, with the blue box indicating the area used for calculating its thermal energy. (Right) Non-thermal upper limits for the bright point for a range of low energy cutoffs and power law indices (including a mono-energetic beam of electrons at  $E = E_c$ ). The shaded boxes indicate the  $\pm 1\sigma$  range, and the grey line indicates the heating requirement dictated by the thermal energy.

### 4.3 Jet

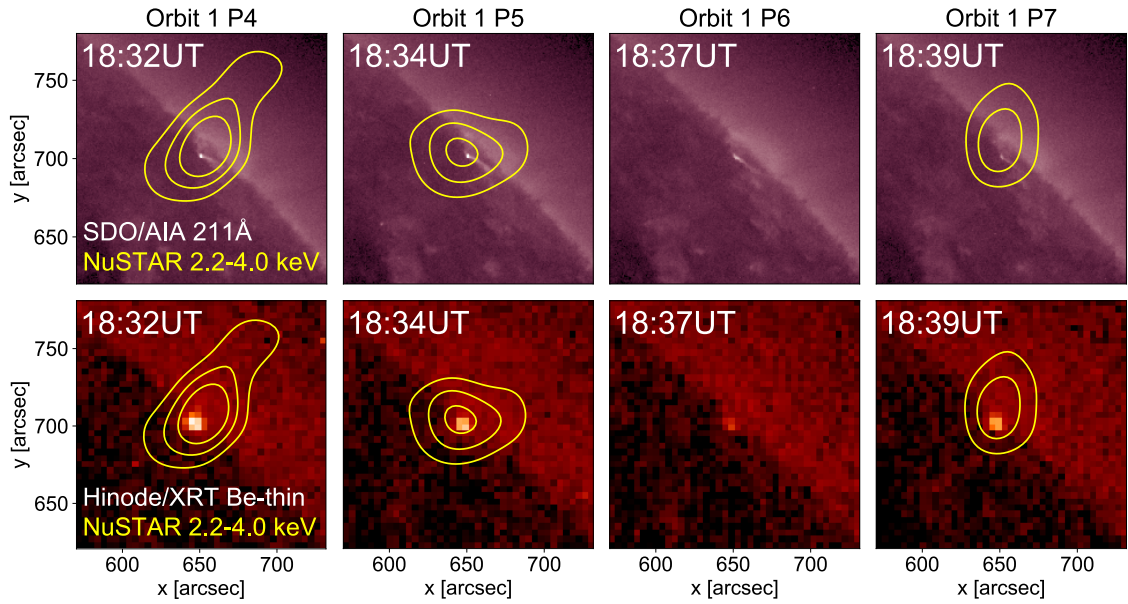


**Figure 4.16:** AIA 211 Å (top row) and XRT Be-thin (bottom row) images of the jet that NuSTAR captured in the 28 September 2018 mosaics, from the mid-times of the four NuSTAR pointings in which it was captured. The yellow contours show the evolution of this event in NuSTAR (FPMA+B, 2.2–4.0 keV, aligned with AIA, plotted at  $5, 7, 9 \times 10^{-4}$  counts  $s^{-1}$ ). There are no NuSTAR contours for P6 (the third column) because the HXR emission from the jet was very faint at this time, making the source barely detectable over the background. This figure is from [Paterson et al. \(2023\)](#).

in this event, compared to the radially, as is typical for solar jets (e.g. [Shen 2021](#)). This implies that the outflowing material was pushed to the side by the overlying magnetic field. The NuSTAR contours plotted in Figure 4.16 were aligned with AIA using the same x and y shifts for each pointing, as the CHU combination used to determine the pointing (see Section 2.1) did not change over these four tiles.

The lightcurves for this jet are plotted in Figure 4.17. The X-ray and EUV time profiles for this event are not in agreement. Both AIA and XRT see a peak in emission at  $\sim 18:30$  UT, at which time NuSTAR also detects the strongest HXR emission during P4. During P5, the HXR emission has decreased, as well as the SXR emission detected by XRT. However, the 211 Å time profile rises to another peak, at a similar brightness to the first, at this time. Again in agreement, the XRT and NuSTAR lightcurves both decrease further afterwards, reaching a minimum during P6, before increasing to another (smaller) peak at the time of P7. This source is not positioned close to a detector gap, meaning that the variation in the NuSTAR emission is real. During P6, the feature is so faint in NuSTAR that it is practically undetectable compared to the background (therefore making this pointing unusable for

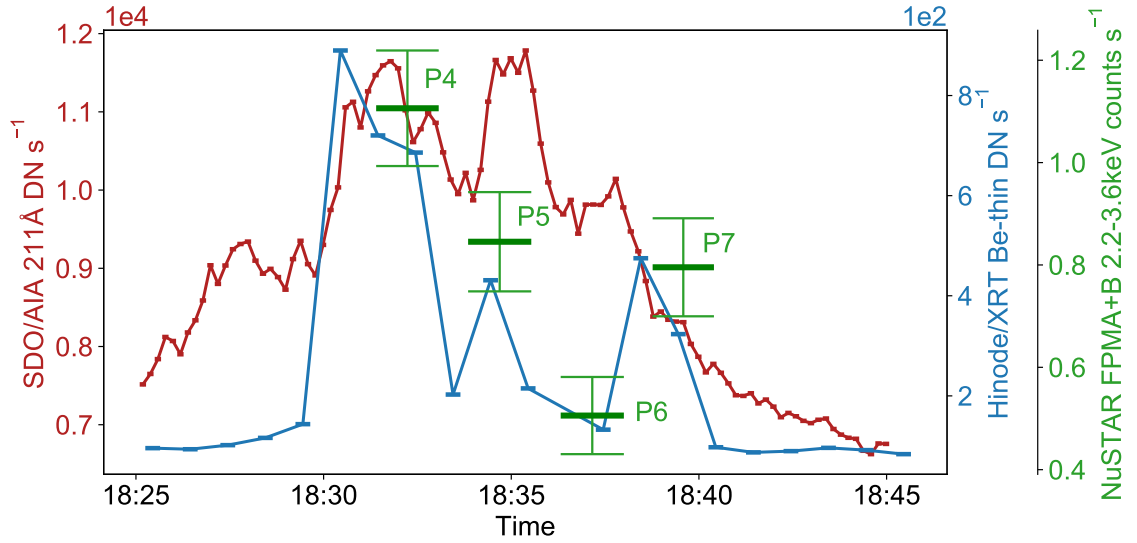


**Figure 4.17:** AIA 211 Å (red), XRT Be-thin (blue), and NuSTAR (green) time profiles for the jet that NuSTAR captured in the 28 September 2018 mosaics. The NuSTAR counts rates, for pointings 4, 5, 6, and 7, are summed over FPMA and FPMB and are corrected for livetime. This figure is from [Paterson et al. \(2023\)](#).

spectroscopy). This is also observed in the XRT images, in which the jet is faintest during P6.

### 4.3.1 NuSTAR Spectral Analysis

The spectrum for the jet was fitted simultaneously over P4, 5, and 7. As the HXR emission from this source was too faint to be easily distinguished from the background in P6, this pointing was not used in the spectral fitting. From the AIA 211 Å and XRT Be-thin time profile and images, it is clear that this source is evolving over the course of these NuSTAR pointings. However, we fitted the NuSTAR spectra for each of these pointings individually, and found that the fit temperatures and emission measures did not vary significantly over the three pointings. This may seem surprising given the variation in the lightcurves shown in Figure 4.17. However, the NuSTAR spectra from individual pointings contained few counts at energies  $> 2.2$  keV, resulting in poor fits with large uncertainties on the temperatures and emission measures (which overlapped for the three pointings). Therefore, the spectra were fitted simultaneously to get the best signal-to-noise.

The results of fitting the jet's spectrum with an isothermal model are shown in Figure 4.18. This model has a temperature of 2.6 MK and an emission measure of  $8.86 \times 10^{43} \text{ cm}^{-3}$ .

### 4.3 Jet

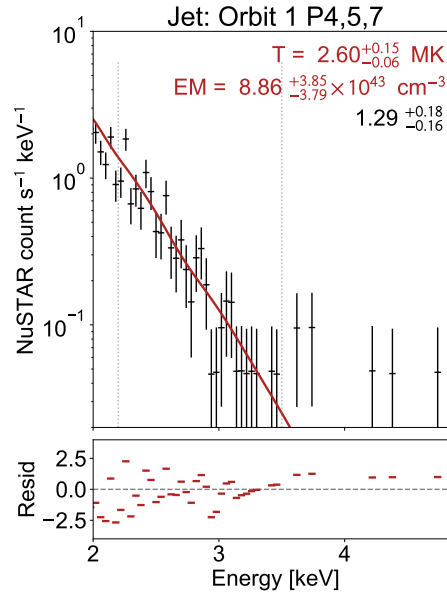


**Figure 4.18:** NuSTAR spectrum for the jet, simultaneously fitted over P4, 5, and 7 from the first orbit. The red line shows the isothermal model, with the parameters marked on the plot. The fitting range is indicated by vertical dotted lines. This figure is from Paterson et al. (2023).

The NuSTAR and AIA 211 Å lightcurves in Figure 4.17 show different behaviours (though NuSTAR agrees with XRT). The fit temperature of 2.6 MK is slightly above the peak in the temperature sensitivity of the 211 Å channel (though still lies within the range of its sensitivity). Therefore, this suggests that NuSTAR and XRT are observing emission at different temperatures to 211 Å, with this AIA channel observing emission dominated by slightly cooler temperatures.

#### 4.3.2 Non-Thermal Upper Limits

As for the EFR and bright points, upper limits on the non-thermal emission that could be present and still be consistent with the lack of detection in the NuSTAR spectrum (as shown in Figure 4.18) were determined using the method explained in Section 3.2.4. From the AIA image, we use the area of the bright footpoint of the jet, which has an area of  $\sim 3'' \times 3''$ , corresponding to a volume of  $1.04 \times 10^{25} \text{ cm}^3$ . Using the temperature and emission values for the NuSTAR spectral fit, the thermal energy of this jet is  $3.26 \times 10^{25} \text{ erg}$ . Dividing this by the event duration (from the start of P4 to the end of P7) of 528 s gives a heating requirement of  $6.18 \times 10^{24} \text{ erg s}^{-1}$ .

#### 4.4 Decayed Active Region

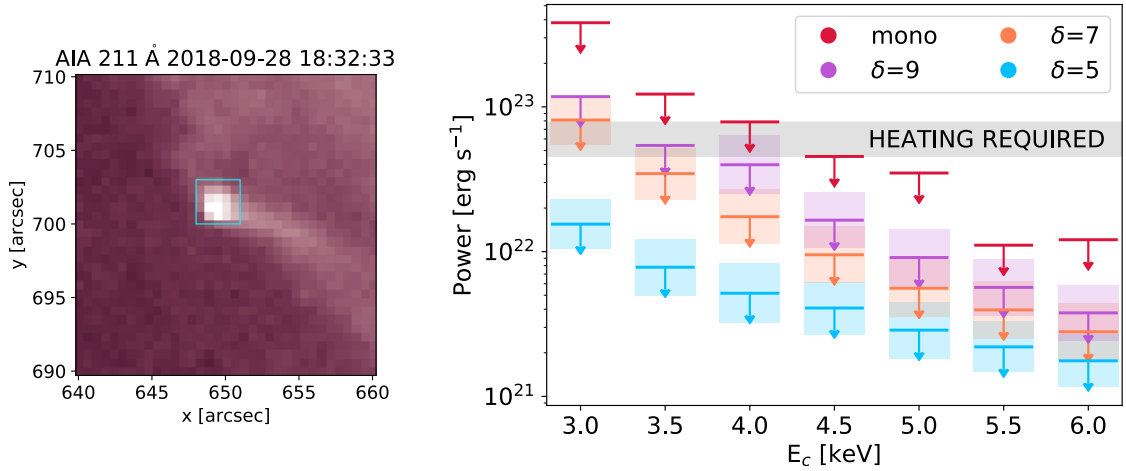


**Figure 4.19:** (Left) AIA 211 Å image of the jet, with the blue box indicating the area used for calculating its thermal energy. (Right) Non-thermal upper limits for the jet for a range of low energy cutoffs and power law indices (including a mono-energetic beam of electrons at  $E = E_C$ ). The shaded boxes indicate the  $\pm 1\sigma$  range, and the grey line indicates the heating requirement dictated by the thermal energy.

Figure 4.19 shows the calculated non-thermal upper limits in comparison to this heating requirement. It can be seen that the upper limits satisfy this requirement (by producing a non-thermal power greater than it) when the non-thermal distribution is very steep (with  $\delta \geq 7$ , practically mono-energetic), with a low energy cutoff between 3–4 keV. We can therefore conclude that accelerated electrons could have produced the required heating only if their non-thermal distribution satisfied these conditions.

#### 4.4 Decayed Active Region

The largest and brightest source in the 28 September 2018 mosaics lies on the East limb, as seen in the full-disk images shown in Figure 4.1. The AIA and XRT images from this time show that this bright feature in NuSTAR is composed of HXR emission from two distinct sources: a bright loop, and some surrounding diffuse emission. This can be seen clearly in the zoomed-in XRT images of this region shown in the bottom row of Figure 4.20. One solar rotation before this observation, this feature was an active region which, though too faint to be identified by NOAA, was detected with the Spatial Possibilistic Clustering Algorithm (SpOCA, Verbeeck et al. (2014)) and given the identification number 22053. Therefore, the source that NuSTAR detected in these mosaics is in fact the decaying remnants of an active

## 4.5 A Comparison of the Thermal Properties

region (and so we label it DAR loop). This source was captured fully in P11 of both orbits, as shown in Figure 4.20. It was also captured partially in P10 and 20.

### 4.4.1 NuSTAR Spectral Analysis

While this source is very bright in comparison to the other mosaic features, meaning that its spectrum has a lot more counts and therefore better signal-to-noise, the fact that the NuSTAR emission comes from a combination of the bright loop and the surrounding diffuse emission complicates the fitting. Also, the diffuse emission is very extended, spread over all four detector quadrants, which all have different responses. Therefore, we fitted the spectrum for the bright loop only by selecting just the brightest region in NuSTAR.

Even though the limb source is present in three pointings in each orbit, it is not ideally positioned in all of these for fitting the spectrum of the bright loop. This bright source lies either on the edge of a detector or outside the FOV completely in P20 in both orbits and in P10 and 11 in Orbit 2. However, it was well observed in P10 and 11 in the first orbit (though it was observed more clearly in FPMA than FPMB). Therefore, we simultaneously fitted the spectra from these pointings from FPMA only, as shown in Figure 4.21. The resulting isothermal model fitted to this feature's spectrum has a temperature and emission measure of 2.53 MK and  $9.62 \times 10^{44} \text{ cm}^{-3}$ . Unfortunately, as a spectrum for this source could not be fitted for any other times, no information could be obtained about how the region evolved over time in HXR.

## 4.5 A Comparison of the Thermal Properties

Many different types of quiet Sun phenomena were observed in the 28 September 2018 mosaics. This is the first time that these types of features could be observed with a HXR imaging spectrometer, and the results of fitting all of their NuSTAR spectra (with isothermal models) are summarised in Table 4.1.

The first point to note is that all of these quiet Sun features have very similar fit temperatures, lying in a small range between 2.0–3.2 MK, with none of the spectra showing any hotter components. The DEMs of the quiet Sun features peak in the 1–2 MK range, after which they fall off sharply. This results in the NuSTAR emission being dominated by an isothermal component in this temperature range. In order to detect higher temperatures

#### 4.5 A Comparison of the Thermal Properties

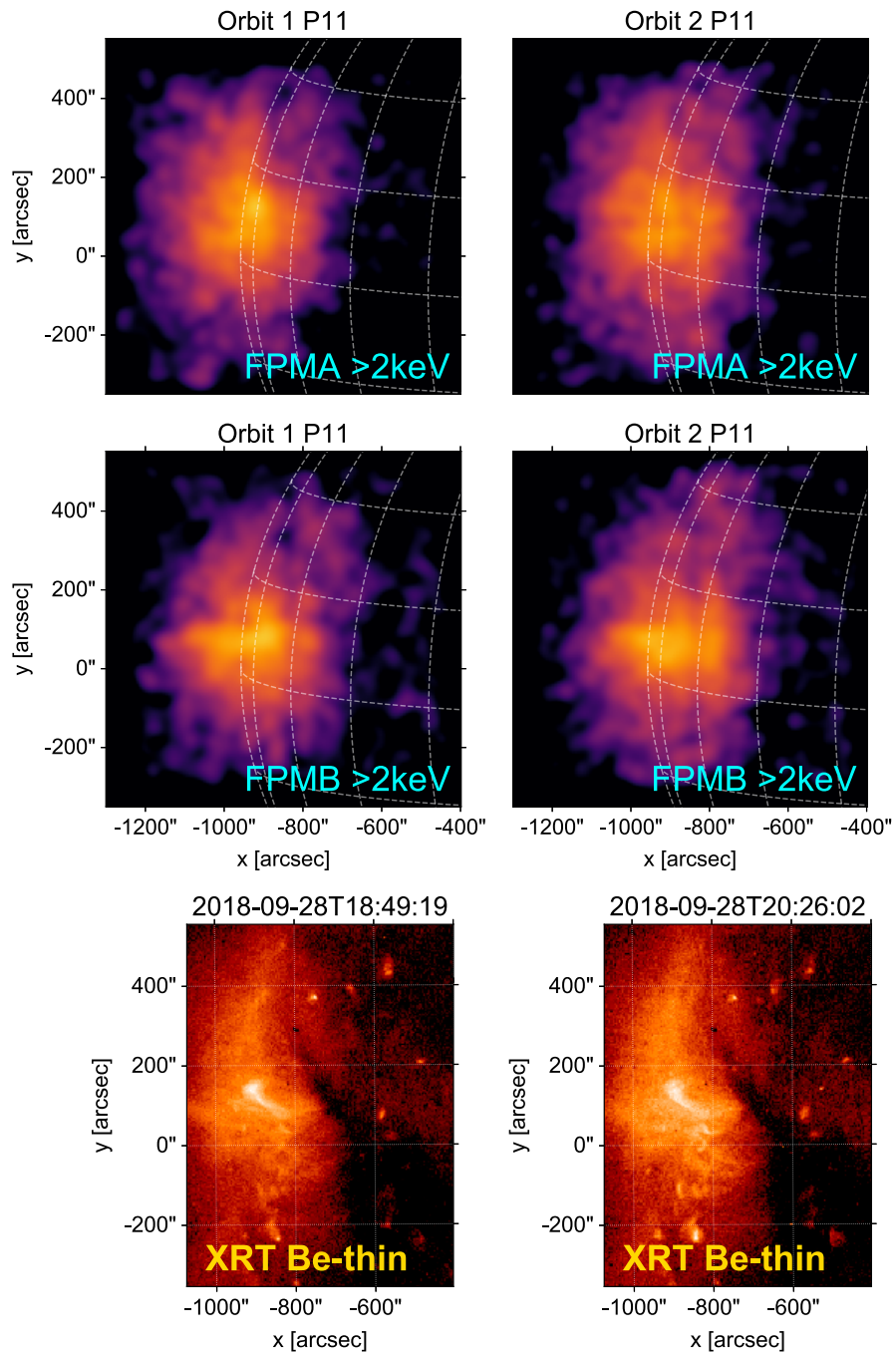


**Figure 4.20:** (Top two rows) NuSTAR ( $> 2$  keV) images of the decayed active region on the East limb, shown for FPMA (top row) and FPMB separately (middle row). The panels on the left are for Orbit 1, and those on the right are for Orbit 2. The XRT images from these two times are shown on the bottom row for context.

#### 4.5 A Comparison of the Thermal Properties

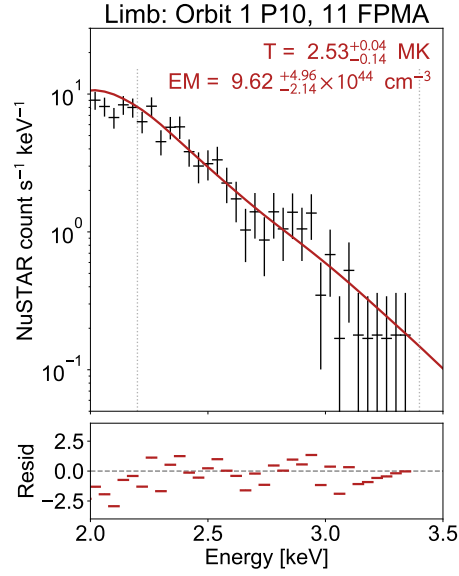


**Figure 4.21:** NuSTAR spectrum for the bright loop in the decayed active region, simultaneously fitted over P10 and 11 from the first orbit, FPMA only. The red line shows the isothermal model, with the parameters marked on the plot. The fitting range is indicated by vertical dotted lines.

**Table 4.1:** A summary of the isothermal models fitted to the NuSTAR spectra for all of the features. Results from different times throughout the NuSTAR observation are given, in the appropriate cases.

Feature	Orbit/Pointing	Temperature	Emission Measure
		MK	$\times 10^{43} \text{ cm}^{-3}$
EFR (Section 4.1)	Orbit 1 P12,13	$2.54^{+0.04}_{-0.03}$	$34.2^{+8.6}_{-8.5}$
	Orbit 1 P18,19	$2.54^{+0.04}_{-0.03}$	$19.3^{+5.1}_{-4.9}$
	Orbit 2 P12,13	$2.57^{+0.04}_{-0.03}$	$61.0^{+12.3}_{-12.4}$
	Orbit 2 P18,19	$2.63^{+0.10}_{-0.05}$	$24.0^{+7.2}_{-7.2}$
BP1 (Section 4.2)	Orbit 1 P14,15,16,17	$2.55^{+0.05}_{-0.03}$	$11.2^{+3.0}_{-3.0}$
	Orbit 2 P14,15,16,17	$2.53^{+0.02}_{-0.01}$	$40.7^{+5.4}_{-5.4}$
BP2 (Section 4.2)	Orbit 2 P16,17	$3.22^{+0.06}_{-0.04}$	$5.98^{+1.14}_{-1.14}$
BP3 (Section 4.2)	Orbit 1 P13,14,17,18	$3.22^{+0.10}_{-0.16}$	$1.33^{+0.38}_{-0.37}$
	Orbit 2 P13,14,17,18	$2.56^{+0.09}_{-0.04}$	$5.10^{+1.86}_{-1.88}$
QS Loops (Section 4.2)	Orbit 1 P13,14,17,18	$2.51^{+0.03}_{-0.38}$	$10.3^{+20.8}_{-2.3}$
	Orbit 2 P13,14,17,18	$2.07^{+0.12}_{-0.04}$	$63.9^{+31.2}_{-32.0}$
Jet (Section 4.3)	Orbit 1 P4,5,7	$2.60^{+0.15}_{-0.06}$	$8.86^{+3.85}_{-3.79}$
DAR Loop (Section 4.4)	Orbit 1 P10,11	$2.53^{+0.04}_{-0.14}$	$96.2^{+49.6}_{-21.4}$

#### 4.5 A Comparison of the Thermal Properties

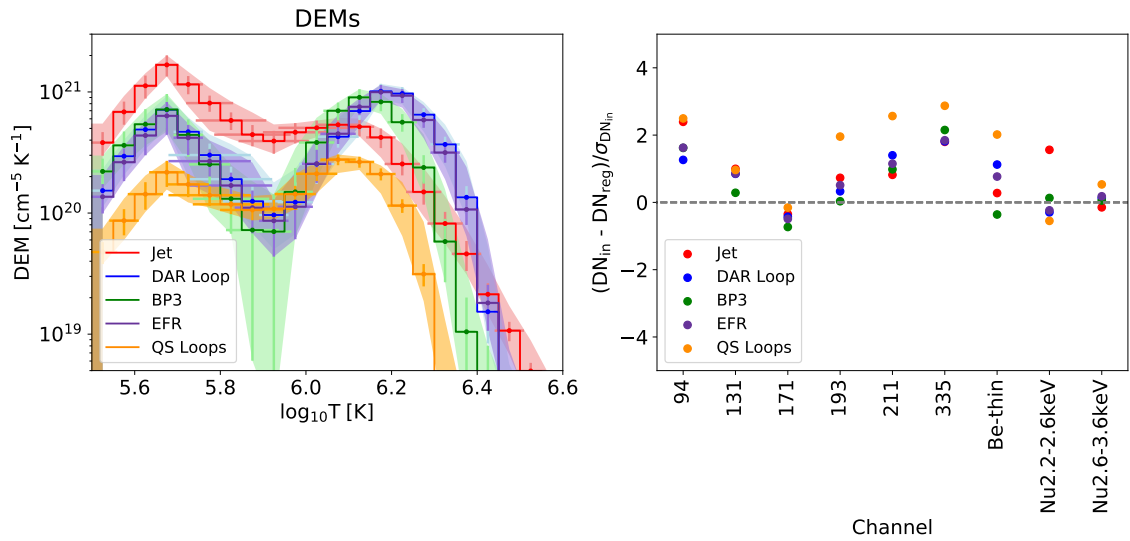


**Figure 4.22:** (Left) DEMs for several of the features present in the 28 September 2018 mosaics. The shaded regions indicate the uncertainties in the calculated DEMs. (Right) The normalised residuals corresponding to the shown DEMs. This figure is from [Paterson et al. \(2023\)](#).

> 3 MK, this hot component would either have to be very bright, or the feature would have to be observed for a longer time. The latter is not possible in mosaic mode due to the short 100 s pointings.

Previous studies of bright points using EUV and SXR data ([Doschek et al. 2010](#); [Alexander et al. 2011](#); [Kariyappa et al. 2011](#)) have found that they generally have temperatures < 3 MK, with some reaching temperatures just above this. This is in agreement with the temperatures found here for the bright points (and other quiet Sun phenomena) studied. BP2 and BP3 do reach temperatures slightly above 3 MK, slightly hotter than previous results for typical bright points.

For comparison, Figure 4.22 plots the DEMs for several of the quiet Sun phenomena captured in these mosaics. It can be seen that all of the DEMs for the different features are similar in that they have two peaks, one at  $\log(T) \sim 5.7$  and a higher temperature one at  $\log(T) \sim 6.1\text{--}6.2$ . The lower temperature peak has been found before in bright point DEM analyses using EUV data ([Doschek et al. 2010](#); [Brosius et al. 2008](#)), and for the DEMs calculated here is dominated by emission observed in the AIA 131 Å channel. It was found that changing the temperature range that these DEMs were calculated over by increasing the lower boundary towards  $\log(T) = 5.9$  resulted in no significant change in the DEMs at higher temperatures of  $\log(T) > 6.1$  (and produced a discrepancy when compared to the observed AIA 131 Å flux).

## 4.6 Summary and Conclusions

The second peak in the DEM occurs at slightly lower temperatures for the jet, the QS loops, and BP3, all peaking at  $\log(T) \sim 6.1$ . The DEMs for the EFR and the DAR loop on the East limb all peak at  $\log(T) \sim 6.2$ . In fact, the DEMs for the EFR and the DAR loop are very similar, lying almost on top of one another. This similarity in the DEMs is interesting given that one is for an active region at the very start of its lifetime, and the other for one at the end, though this maybe only a coincidence.

The features for all five of these DEMs are similar in that they all fall off sharply at temperatures above the second peak, indicating that there is very little hotter material in these sources. This result was achieved by using X-ray data from NuSTAR and XRT to constrain the DEM solution at high temperatures. This fall-off is less rapid for the jet, for which the DEM tail is more flat. This indicates that there may be some hotter emission for this event, though this was not detected in the NuSTAR spectral fit. However, this event was very faint which, combined with the short duration of the event and NuSTAR's limited throughput, could explain this lack of detection.

The spectral fitting for all of these features indicated that NuSTAR was seeing emission at 2–3 MK. None of the AIA channels have a temperature response that peaks in this temperature range, as demonstrated in Figure 2.8. This can complicate the analysis, with the AIA 211 Å time profiles shown previously in this chapter often not exhibiting good agreement with NuSTAR (and XRT). Analysis of NuSTAR microflares (e.g. Cooper et al. (2020)) has made use of the AIA Fe XVIII proxy channel, which is a linear combination of the 94, 171, and 211 Å channels (as discussed in Section 2.2.1). However, Fe XVIII has sensitivity at temperatures  $> 4$  MK, making these sources too cool to produce a signature in this channel.

## 4.6 Summary and Conclusions

In this chapter, we have presented for the first time a survey of quiet Sun features observed in HXRs during the most recent solar minimum. The 28 September 2018 mosaics were the first of NuSTAR's quiet Sun observing campaigns, and gave the opportunity to observe the types of features present for the first time at HXR energies. As NuSTAR was able to observe over the full disk, all of the sources present could be studied, including steady features like bright points, as well as short-lived events such as the jet.

As was discussed and summarised in Section 4.5 and Table 4.1, fitting the HXR spectra for these features confirmed that NuSTAR is seeing emission at 2–3 MK, at which temperatures

#### 4.6 Summary and Conclusions

their DEMs are sharply falling off. As was seen in Figure 4.7, recovering DEMs using EUV data (especially multi-channel EUV images) alone results in solutions which are not well constrained at high temperatures. Therefore, it is vital to use X-ray data from instruments like NuSTAR and XRT to provide this constraint. Doing so allows us to conclude that there is no significant emission above 4 MK in these quiet Sun features.

Though no non-thermal component was directly observed in any of the features' HXR spectra, we determined upper limits on the non-thermal emission that could be present and remain consistent with a null detection in NuSTAR. This was then compared with heating requirements obtained from the features' thermal energies. It was found that in most cases it was unlikely that a non-thermal component could be responsible for the observed heating. However, for the jet it was determined that a very steep ( $\delta \geq 7$ ), essentially mono-energetic, non-thermal distribution with a low energy cutoff of 3–4 keV could have satisfied the requirement.

We conclude that no non-thermal or high temperature ( $> 5$  MK) sources were detected in this analysis. However, the short duration mosaic pointings and NuSTAR's limited throughput (which is dominated by lower energy X-rays) mean that any such components would have to be relatively strong (or be observed for a sufficiently long duration) to be detectable. Therefore, the lack of detection may be only due to NuSTAR not having the required sensitivity.

However, other NuSTAR quiet Sun campaigns have orbits of data observed in dwell mode (see Table 3.1). As any sources present in these observations are observed for  $\sim$  an hour (compared to the 100 s mosaic pointings), the chances of detecting any hotter or non-thermal emission are increased. The HXR time evolution of any persisting features (like X-ray bright points) can also be investigated in more detail than for this observation. Such analysis is detailed for X-ray bright points observed over multiple orbits in dwell mode (in September and February 2020) in Chapter 5, taking advantage of the longer observation time compared to the mosaics to search for more energetic HXR emission. Dwell observations also increase the chances of detecting transient phenomena, and allow their evolution to be fully tracked without a change in pointing. A number of transient events detected in NuSTAR dwell observations are analysed in Chapter 6.

# 5

## Time Evolution of X-Ray Bright Points from the NuSTAR Quiet Sun Dwell Observations

*The work in this Chapter is based on the research presented in Paterson et al., 2023 (submitted to MNRAS).*

In this Chapter, we present analysis on two X-ray bright points captured with NuSTAR during quiet Sun dwell observations from the recent solar minimum. Both bright points were observed over several hours with NuSTAR, giving the opportunity to study their evolution in HXRs (as well as in EUV and SXR with AIA and XRT) for the first time. Being able to fit their NuSTAR spectra over longer durations also improves the signal-to-noise compared to the 100 s pointings in the mosaics (which complicated the fitting for the 28 September 2018 mosaic features in Chapter 4). This increases the chances of detecting faint hot or non-thermal components.

Section 5.1 gives a brief overview of the two bright points. One of these bright points is the brightest feature captured on 21 February 2020 (whole observation summarised previously in Section 3.1.5), and the other is the bright point that emerged in the final three orbits on 12–13 September 2020 (whole observation summarised in Section 3.1.6). Short-lived impulsive events from both of these observations are analysed later in Chapter 6.

Analysis of the February 2020 bright point, including time profiles, NuSTAR HXR spectroscopy, DEMs, and non-thermal upper limits, can be found in Section 5.2. Similar analysis for the September 2020 bright point is reported on in Section 5.3. Finally, we fit the NuSTAR spectra for both bright points integrated over several hours of observation in Section 5.4.

## 5.1 Overview

An overview of the largest X-ray bright point that NuSTAR captured in the 21 February 2020 observation is shown in Figure 5.1. In this observation, it can be seen that the brightest source is located at  $\sim (-50'', -300'')$ . This bright point began to emerge around the same time that this observation started (shortly after 05:00 UT), and was captured in all of the NuSTAR orbits. This feature was detected by the Spatial Possibilistic Clustering Algorithm (SPoCA; Verbeeck et al. (2014)) as an active region, and was given the identification number SPoCA 23914. However, it was not bright enough to be classified as a NOAA active region. This source persisted on the solar disk for  $\sim 4$  days. While this is longer than the typical lifetime of X-ray bright points ( $< 48$  hours; Golub et al. (1974)), we still consider this source to be an X-ray bright point (as opposed to a small active region). However, its unusually long lifetime does make its nature somewhat ambiguous.

The X-ray time profiles (shown in the bottom panel of Figure 5.1) show this bright point's emergence, with the X-ray emission increasing through the first few dwell orbits until 12:00 UT. Afterwards, the NuSTAR lightcurves exhibit significant variability, including several sharp peaks. The corresponding XRT time profile shows a broadly similar shape to the NuSTAR one. The two largest peaks in the HXR emission were captured in Orbit 6 at 13:55 UT, and in Orbit 9 at 18:15 UT, during which we consider the bright point to have been “flaring”. XRT also observed a peak at the time of the first flare, though a data gap (from 13:35–13:49 UT) unfortunately coincided with the second NuSTAR peak. However, XRT did observe heightened emission just prior to this data gap, and a smaller flux immediately after, following a similar trend to the NuSTAR lightcurve. Analysis of the February 2020 bright point, including on these two events, can be found in Section 5.2.

When pointed at a region near the East limb in the 12–13 September observation, NuSTAR captured mainly small-scale impulsive events. However, a bright point (summarised in Figure 5.2) emerged towards the end of the NuSTAR observation, located at  $\sim (-800'', -50'')$ . This bright point was visible in AIA 211 Å until around 14:00 UT on 14 September, meaning that its lifetime in EUV was  $\sim 40$  hours. The X-ray lightcurves confirm that this bright point emerged at  $\sim 19:30$  UT, and that it was captured in the final three NuSTAR orbits (Orbits 8–10). In Orbits 8 and 10, the NuSTAR time profiles are at around the same level. However, in Orbit 9 the X-ray emission, as observed by both NuSTAR and XRT, is enhanced, with several spikes. In Section 5.3, we analyse this behaviour, investigating the nature of these X-ray spikes. It should be noted that the two large spikes in the NuSTAR time profile

## 5.1 Overview

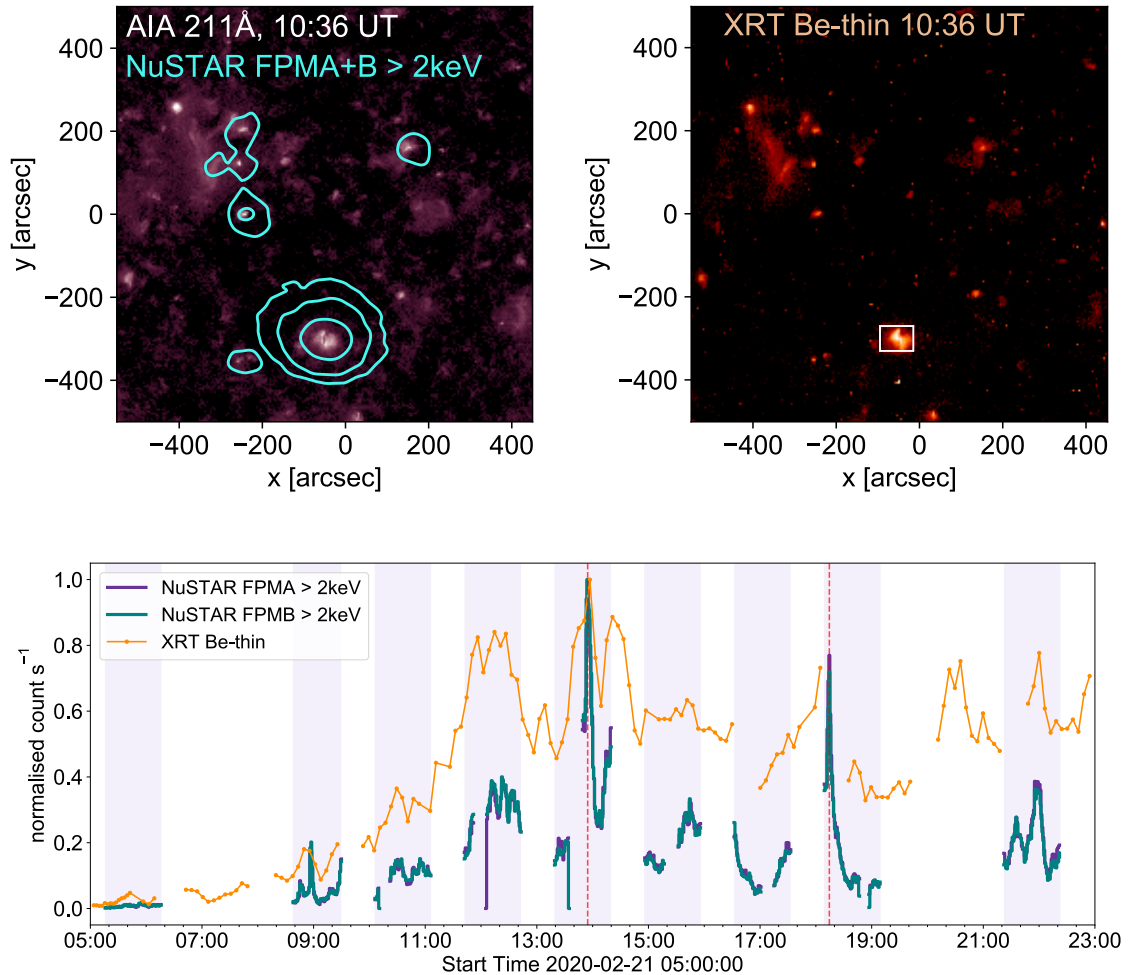


**Figure 5.1:** An overview of the largest bright point captured in the 21 February 2020 NuSTAR quiet Sun observation. AIA 211 Å (top left) and XRT Be-thin (top right) images show the region that NuSTAR captured in the this observation, with NuSTAR FPMA+B contours aligned with AIA 211 Å and over-plotted at  $3$ ,  $8$ , and  $50 \times 10^{-3} \text{ counts s}^{-1}$ . The white box on the XRT image shows the region used for calculating the time profiles for NuSTAR and XRT (bottom panel). Shaded areas indicate when NuSTAR was observing in dwell mode, and the red lines on marked on the time profile plot highlight two times where the bright point was flaring.

## 5.1 Overview

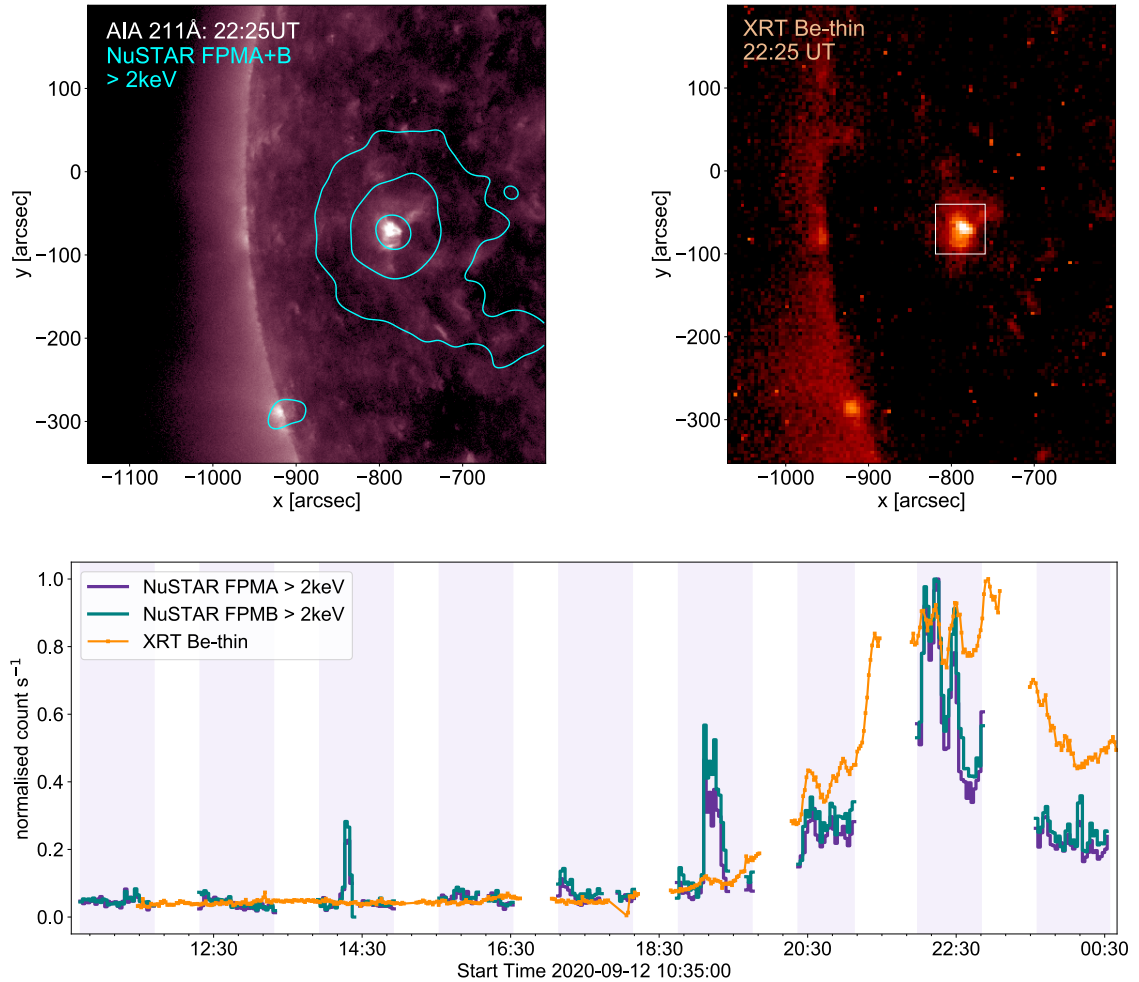


**Figure 5.2:** An overview of the largest bright point captured in the 12–13 September NuSTAR quiet Sun observation. AIA 211 Å (top left) and XRT Be-thin (top right) images show the region that NuSTAR captured in this observation, with NuSTAR FPMA+B contours aligned with AIA 211 Å and overplotted at 1, 5, and  $20 \times 10^{-3}$  counts  $s^{-1}$ . The white box on the XRT image shows the region used for calculating the time profiles for NuSTAR and XRT (bottom panel). Shaded areas indicate when NuSTAR was observing in dwell mode.

## 5.2 A Bright Point in the 21 February 2020 Observation

during the earlier orbits (at around 14:20 and 19:20 UT) are due ghost rays originating from outside the FOV (see Section 2.1), and are not associated with the bright point.

At the time of both of these observations, the Sun was very quiet (there were no active regions on the disk, and the GOES soft X-ray flux was below A-level). This means that the effect of ghost rays originating from outside NuSTAR’s FOV is minimal in both observations. This, in addition to the fact that there are many hours worth of data for the two bright points, makes this dataset ideal for studying their time evolution.

### 5.2 A Bright Point in the 21 February 2020 Observation

As was seen in the X-ray time profiles in Figure 5.1, the bright point from 21 February 2020 showed significant variability over the course of the NuSTAR observation. In this analysis, we focus only on the times of the two largest peaks in the NuSTAR lightcurve, when the bright point was flaring. We label the HXR spike that occurred at 13:55 UT “Flare 1”, and the one from 18:15 UT “Flare 2” (both are indicated by red dashed lines on the lightcurve plot in Figure 5.1). We investigate Flare 1 in Section 5.2.1 and Flare 2 in Section 5.2.2.

#### 5.2.1 Flare 1

The sixth NuSTAR orbit in the 21 February 2020 observation occurred from 13:20–14:20 UT. There is a gap in the NuSTAR data during this orbit, between 13:33–13:49 UT. From the NuSTAR and XRT lightcurves shown in the overview in Figure 5.1, it can be seen that after the data gap, the NuSTAR emission more than doubles compared to the previous level and it continues to rise, peaking just after 13:53 UT. A similar increase in emission was observed with XRT at this time.

An overview of Flare 1 is presented in Figure 5.3, including AIA and XRT images showing the evolution of the event. NuSTAR contours are over-plotted on the AIA images, which were shifted such that NuSTAR was aligned with AIA.

Lightcurves for NuSTAR, XRT, and AIA during the sixth NuSTAR orbit are shown in Figure 5.3. At the time of the peak in NuSTAR ( $\sim 13:54$  UT), there is also increased emission in both XRT Be-thin and Al-poly. From this figure, XRT appears to peak slightly after NuSTAR, at around (13:57 UT). However, this is due to the 6 minute cadence of the XRT images.

## 5.2 A Bright Point in the 21 February 2020 Observation

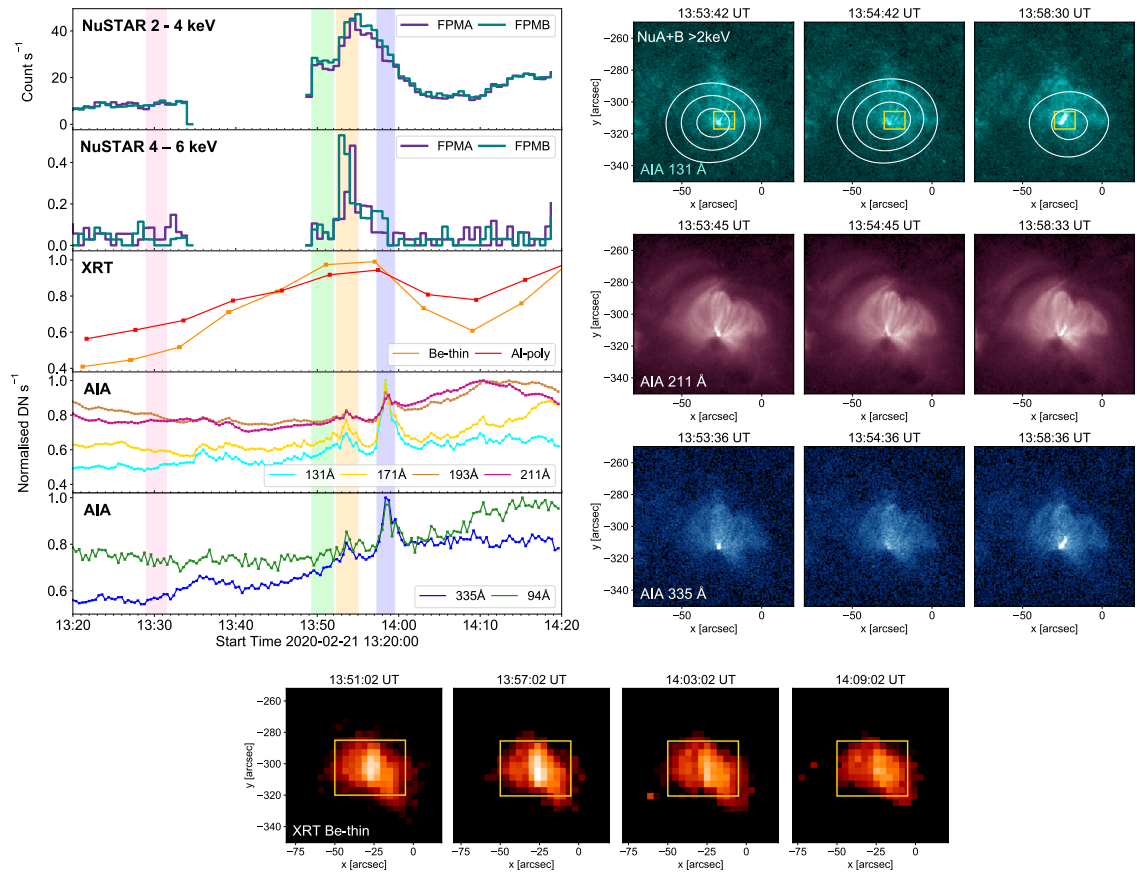


**Figure 5.3:** (Top left) NuSTAR, XRT, and AIA time profiles for Flare 1 from NuSTAR's sixth orbit. The shaded time ranges are used for spectral analysis. (Top right) AIA 131, 211, and 335 Å showing the evolution of this event in EUV. The white contours are NuSTAR FPMA+B > 2 keV (plotted at 0.04, 0.06, and 0.08 counts s<sup>-1</sup>), and the yellow boxes in the top row show the region used to calculate the AIA time profiles. (Bottom) XRT images showing the evolution of this event in SXR, with the yellow boxes showing the region used to calculate the XRT lightcurves.

## 5.2 A Bright Point in the 21 February 2020 Observation

There are no XRT images from between 13:51 and 13:57 UT, meaning that it unfortunately missed the exact time of the NuSTAR peak.

All of the AIA channels see a small increase in brightness at the same time (around 13:54 UT) as the peak in the NuSTAR 4–6 keV channel and the rise in the 2–4 keV channel. However, after a decrease back to the background level by 13:55 UT, the AIA time profiles all rise to a second higher peak at 13:58:30 UT. This behaviour is reflected in the corresponding AIA images, which show that the increase in brightness at the time of the NuSTAR peak comes from a small region near the bottom of the bright point. During the second AIA peak, there is increased brightness extending along a loop originating from the region which originally brightened. The differing behaviour of the AIA and NuSTAR time profiles for this event will be further investigated through DEM analysis in later in this section.

Note that, while a region covering the full bright point had to be used to calculate the time profiles for NuSTAR and XRT, AIA's superior spatial resolution meant that a much smaller area covering only the brightening region could be used to obtain the EUV ones. This helps to emphasise the flaring behaviour in the AIA lightcurves; using the whole bright point region did not change the shape of the time profiles, and only made the peaks less prominent.

### NuSTAR HXR Spectroscopy

Using the approach laid out in Section 3.2.2, we used XSPEC to fit the NuSTAR spectrum of this bright point at several times throughout Orbit 6 to investigate the properties of the flare. For this analysis, we chose four time ranges to perform spectroscopy over, which are highlighted on the lightcurves in Figure 5.3 (top left). These are as follows: a quiescent time from 13:29:00–13:31:30 UT (pink), before the event began; an early flare time from 13:49:20–13:52:00 UT (green), when the NuSTAR time profiles is flat just before the increase in emission (but at a heightened level compared to before the data gap); a flare time from 13:52:20–13:55:00 UT (orange), during which the NuSTAR emission peaks; and 13:57:20–13:59:30 UT (purple), when the AIA emission reaches a second stronger peak, but NuSTAR observes the gradual phase of the flare. The flare time was chosen to be the time range during which NuSTAR observed a peak in the 4–6 keV energy band. By choosing a time when the higher energy HXRs are peaking, the likelihood of detecting a non-thermal or higher temperature component in the flare time spectrum is increased.

The spectra from all four of these time ranges were fitted with isothermal APEC models, the results of which are plotted in Figure 5.4. During the quiescent time before the flare started,

## 5.2 A Bright Point in the 21 February 2020 Observation

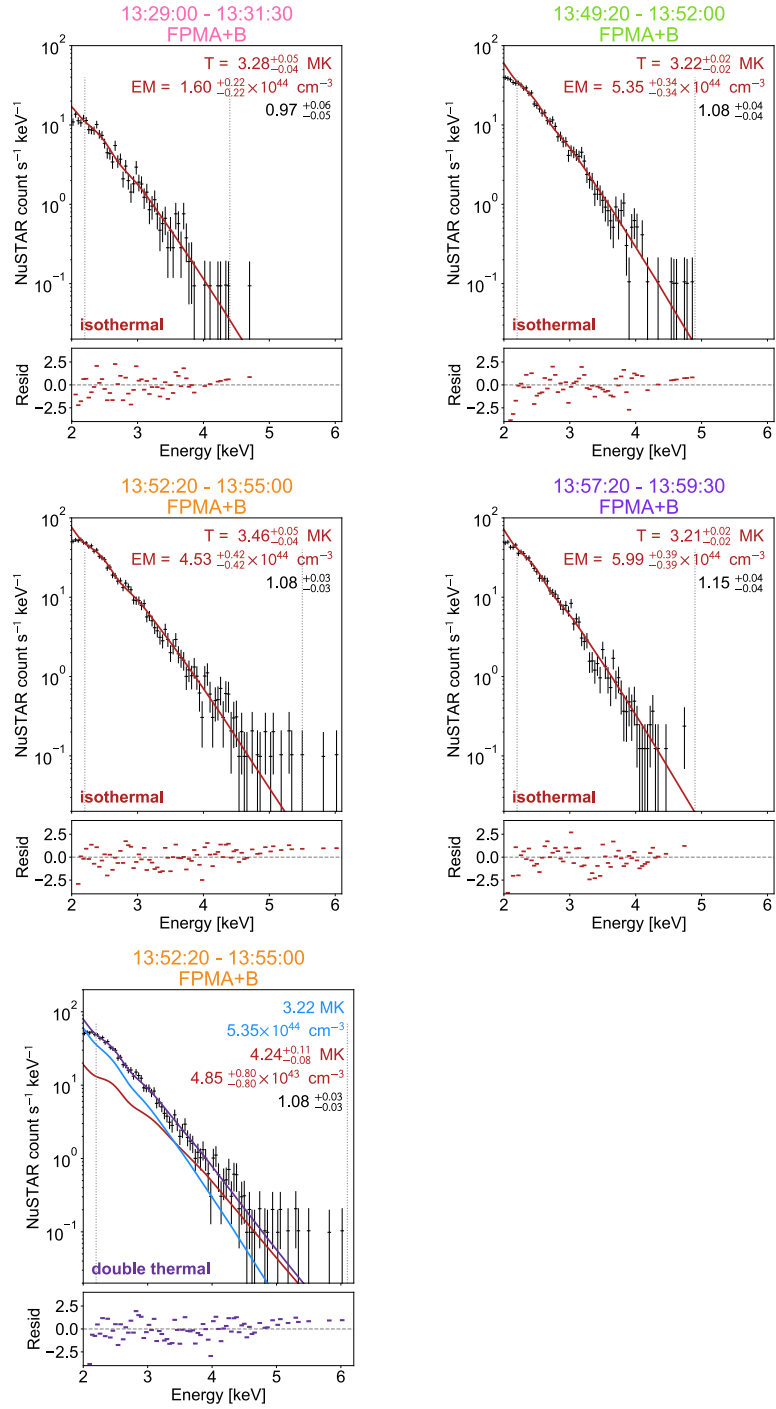


**Figure 5.4:** (Top two rows) NuSTAR spectral fits for Flare 1 for the quiescent time (13:29:00–13:31:30 UT), the early flare time (13:49:20–13:52:00 UT), the flare time (13:52:20–13:55:00 UT), and NuSTAR’s gradual phase (13:57:20–13:59:30 UT). These are fitted with isothermal models (red). (Bottom row) The NuSTAR spectrum from the flare time, fitted with a double thermal model (purple, with the two separate thermal components plotted in red and blue).

## 5.2 A Bright Point in the 21 February 2020 Observation

the NuSTAR spectrum is adequately fitted with an isothermal model with a temperature of 3.28 MK and an emission measure of  $1.60 \times 10^{44} \text{ cm}^{-3}$ . The NuSTAR spectrum for the early flare time has a similar temperature of 3.22 MK, but an increased emission measure of  $5.35 \times 10^{44} \text{ cm}^{-3}$ , reflecting the increase in the NuSTAR lightcurve between these two times.

The NuSTAR spectrum from the flare time was fitted with an isothermal model with a temperature of 3.46 MK and an emission measure of  $4.53 \times 10^{44} \text{ cm}^{-3}$ . However, unlike the spectra from the previous two times, this spectrum exhibits an excess compared to the isothermal model at energies  $> 4 \text{ keV}$ . This suggests that a hotter (or non-thermal) component is required to fit this spectrum. Therefore, we also tried fitting it with a double thermal model. One of the components was fixed as the thermal model that was fit to the early flare time spectrum (just before the NuSTAR emission began to rise), with  $T = 3.22 \text{ MK}$  and  $EM = 5.35 \times 10^{44} \text{ cm}^{-3}$ . By setting this model as a fixed component, we therefore only fitted the excess in the spectrum during the flare time compared to the early flare time, giving an indication of the temperature that material was heated to during the HXR spike. It was determined that the second thermal model required to fit the flare time spectrum (as shown in Figure 5.4, bottom row) had a temperature and emission measure of 4.24 MK and  $4.85 \times 10^{43} \text{ cm}^{-3}$ , respectively. This suggests that the bright point was heated to temperatures  $> 4 \text{ MK}$  during the flare. This result is confirmed via DEM analysis later in this section.

It can be seen that fitting this spectrum with a double thermal model rather than an isothermal one results in the residuals being reduced at higher energies. However, even when fitted with the double thermal model, there remains a small excess compared to the model at higher energies. This will be further investigated later in this section, by calculating upper limits on the non-thermal emission.

The final spectrum, from the time of the largest AIA peak (which occurred during NuSTAR's gradual phase), is well-fitted with an isothermal model with a temperature of 3.21 MK, similar to the early flare time, though the fit indicates a slightly higher emission measure (of  $5.99 \times 10^{44} \text{ cm}^{-3}$ ). This is in agreement with the NuSTAR time profile being higher during this time range than at the early flare time. This spectrum does not show any hints of the hotter emission that was present during the peak of the HXR time profile.

## 5.2 A Bright Point in the 21 February 2020 Observation

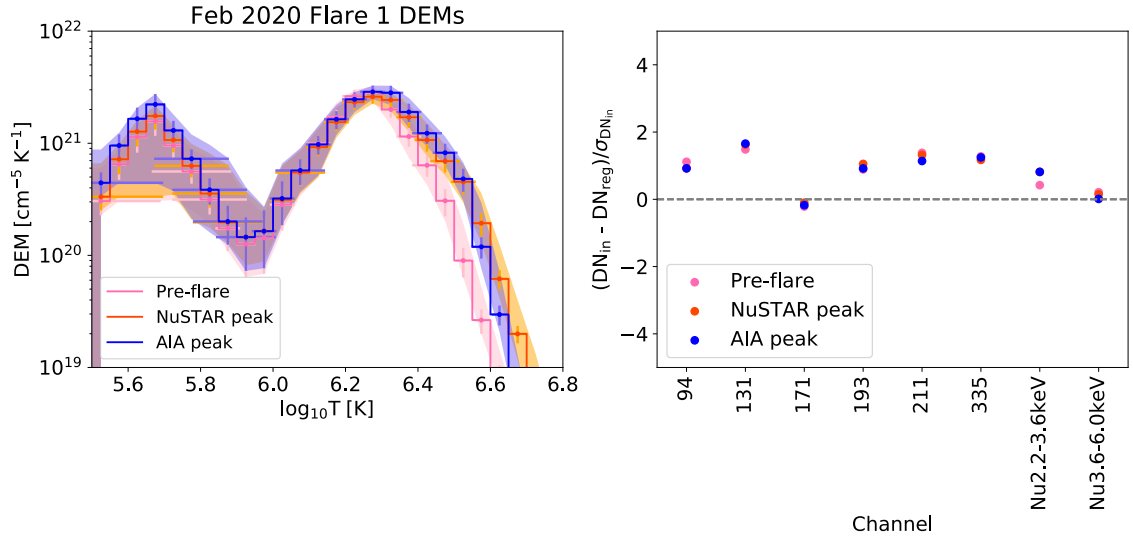


**Figure 5.5:** (Left) DEMs calculated for the brightening region of the February 2020 bright point during Flare 1. These are for the quiescent time (13:29:00–13:31:30 UT, pink), the time of the NuSTAR peak (13:52:20–13:55:00 UT, orange), and the time of the largest AIA peak (13:57:20–13:59:30 UT, purple). (Right) Normalised residuals.

### DEM Analysis

The NuSTAR and AIA time profiles for Flare 1 (Figure 5.3, top left) show different behaviour. The AIA channels observe only a small increase in brightness at the time that NuSTAR observes maximum HXR emission. The AIA time profiles then rise to a second, higher, peak a few minutes later, and this is not observed in NuSTAR at all; at this time, the NuSTAR time profile is decaying. In an effort to understand the differing behaviours of the EUV and X-ray time profiles for this event, we reconstructed DEMs for several of the time ranges which were previously used for spectroscopy. For this analysis, we chose the times where NuSTAR and AIA both peaked (13:52:20–13:55:00 UT), and where AIA peaked more strongly (13:57:20–13:59:30 UT). For comparison, we also calculated the DEM during the quiescent time before the onset of the flare (13:29:00–13:31:30 UT). We calculated all three of the DEMs over the small brightening region used to calculate the AIA lightcurves in Figure 5.3. As this was the brightest region in AIA even before the beginning of the flare, we assume that the NuSTAR emission predominantly originated from this area. The DEMs were recovered using the method detailed in Section 3.2.3, but using only NuSTAR and AIA data, as there were not XRT images from all of the chosen time intervals.

The resulting DEMs are plotted in Figure 5.5. All three of the DEMs show a similar structure, with two peaks at  $\log(T) = 5.7$  and  $6.3$ . This two-peak structure has been found in previous

## 5.2 A Bright Point in the 21 February 2020 Observation

bright point DEM analyses (Brosius et al. 2008; Doschek et al. 2010), which have attributed the lower temperature peak to the background line-of-sight corona, and the higher peak to the bright point itself. However, previous bright point studies have found DEMs peaking at lower temperatures ( $\log(T) \sim 6.15$ ), compared to the February 2020 bright point. At temperatures of  $\log(T) < 6.3$  below the second peak, all of the DEMs shown in Figure 5.5 are identical. However, above the peak, the DEM from the quiet time falls off more sharply than the other two, indicating that more material  $> 2$  MK is present during the flaring times.

The two DEMs from during of the flare, from the time of the NuSTAR peak and of the strongest AIA peak, only begin to show different behaviour from each other for temperatures above  $\log(T) \sim 6.6$  (4 MK). The tail of the DEM from the NuSTAR peak time is slightly flatter at these temperatures, while the one from the AIA peak time falls off more steeply. At the time of the NuSTAR peak, HXR spectroscopy indicated the presence of emission at  $\sim 4.2$  MK. The DEMs shown here are consistent with this result.

The DEM from the time of the AIA peak (which occurs during NuSTAR's gradual phase) does indicate that less material is heated to temperatures  $> 4$  MK than during the time of the NuSTAR peak. However, at temperatures of  $6.3 < \log(T) < 6.5$ , the DEM is higher than the one from the NuSTAR peak time, suggesting increased emission at 2–3 MK. This implies that the second AIA peak is a result of material cooling (from  $T > 4$  MK) into a temperature range to which the AIA channels are more sensitive (as shown in the AIA temperature response plot in Figure 2.8). As NuSTAR has some sensitivity at these temperatures, a gradual phase is observed. However, the two DEMs are not significantly different in this temperature range when their error bars are considered, so a definite conclusion cannot be made here.

### Non-Thermal Upper Limits

When the NuSTAR spectrum for the flare time (13:52:20–13:55:00 UT) was fitted with a double thermal model (shown in Figure 5.4, bottom panel), there is a small excess at energies  $> 5$  keV. When the double thermal model was subtracted from the observed spectrum, it was found that this excess totals to 10 counts. Using the method detailed in Section 3.2.4, we calculated upper limits on the non-thermal component which could be present, and remain consistent with this observed excess.

We could then compare this to the thermal energy of the flare, calculated using Equation 3.10. For the emitting area, we chose a smaller region with dimensions  $5'' \times 5''$

## 5.2 A Bright Point in the 21 February 2020 Observation

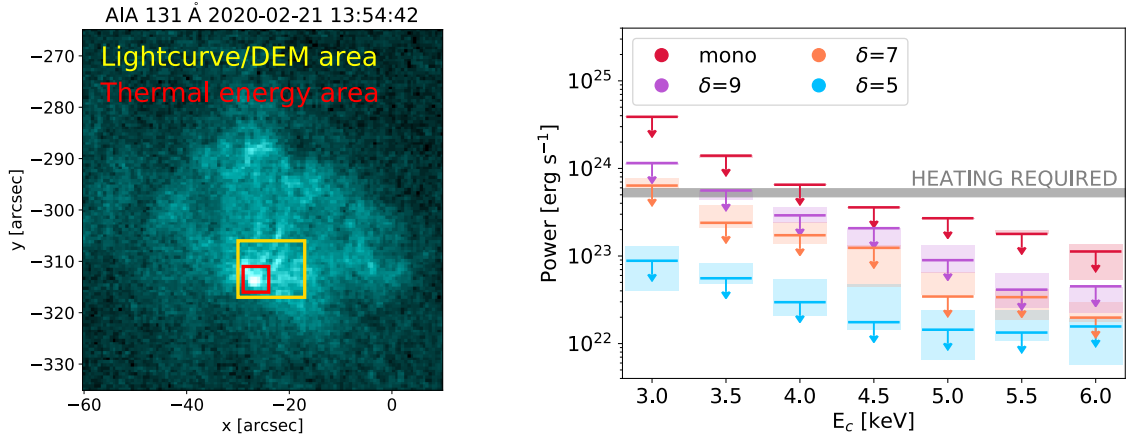


**Figure 5.6:** (Left) An AIA 131 Å image of the February 2020 bright point during the time of Flare 1. The yellow box shows the region used for calculating time profiles and DEMs, while the red box shows the more zoomed in area used to calculate the thermal energy of the event. (Right) Upper limits on the non-thermal emission in Flare 1 for a range of power law indices. The shaded regions indicate the  $\pm 1\sigma$  range, and the grey line indicates the heating requirement dictated by the thermal energy.

compared to the area used for calculating the time profiles and DEMs. The larger region was used for both of these because the brightening later extends along the loop, meaning that a bigger box had to be used. However, as only this small  $5'' \times 5''$  region brightened during the flare time range, we use as small of an area as possible to calculate the heating requirement.

We calculated the thermal energy using the fit temperature and emission measure from the NuSTAR spectroscopy detailed in Section 5.2.1. Taking the cooler component (taken from the early flare time) to be a background, we use the parameters from the hotter component ( $T = 4.24$  MK and  $EM = 4.85 \times 10^{43} \text{ cm}^{-3}$ ) in the calculation. The resulting thermal energy of this event was therefore found to be  $8.47 \times 10^{25}$  erg. The time range that this energy was calculated over had a duration of 360 s. Therefore the required heating power for this flare is  $5.30 \times 10^{23} \text{ erg s}^{-1}$ .

The non-thermal upper limits for this event are plotted in the right-hand panel of Figure 5.6, with the heating requirement dictated by the thermal energy marked on the plot. It can be seen that there are only a few non-thermal upper limits which are in excess of the heating requirement. It can be concluded that only a very steep non-thermal distribution with  $\delta \geq 7$  between 3–4 keV could have provided the necessary heating.

## 5.2 A Bright Point in the 21 February 2020 Observation

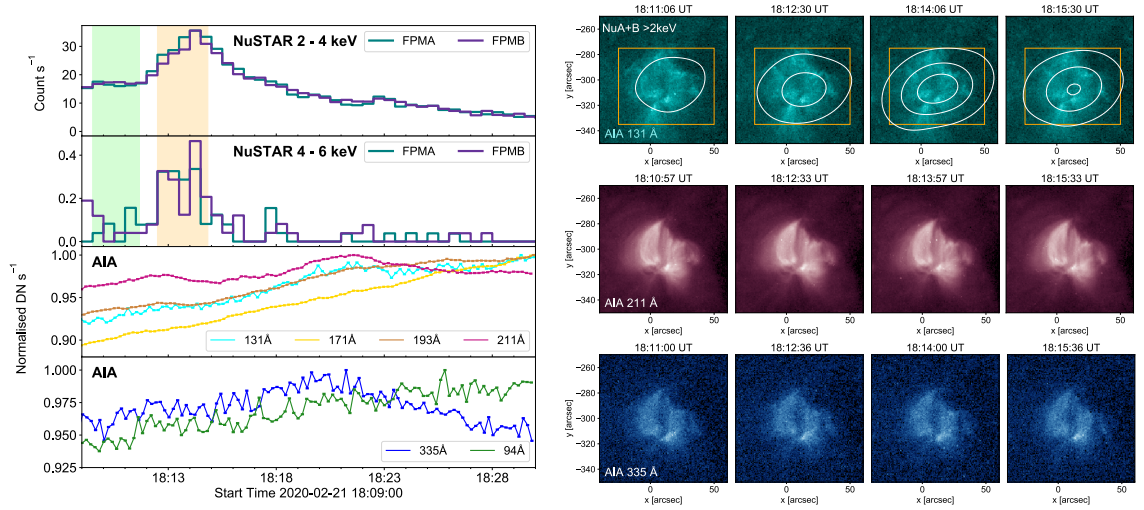


**Figure 5.7:** (Left) NuSTAR and AIA time profiles for Flare 2 from NuSTAR’s ninth orbit. The shaded time ranges are used for spectral analysis. (Right) AIA 131, 211, and 335 Å showing the evolution of this event in EUV. The white contours are NuSTAR FPMA+B > 2 keV (plotted at 0.01, 0.02, and 0.03 counts s<sup>-1</sup>), and the yellow boxes in the top row show the region used to calculate the AIA time profiles.

### 5.2.2 Flare 2

The second biggest peak in the NuSTAR lightcurve for the February 2020 bright point occurs in the ninth NuSTAR orbit, with the HXR emission reaching a peak at around 18:15 UT, as shown in Figure 5.1 (bottom panel). It can be seen that XRT unfortunately misses this event due to a data gap between 18:05–18:35 UT. However, both the NuSTAR and XRT Be-thin time profiles begin to rise at  $\sim 17:00$  UT, with the XRT one reaching a maximum at 18:05 UT, in the final image before the data gap. After the data gap, the XRT lightcurve has fallen to a lower level, reflecting the similar behaviour also seen with NuSTAR.

AIA and NuSTAR time profiles for the bright point at the time of the event can be found in Figure 5.7. In NuSTAR, there is a plateau immediately after the start of the orbit, beginning at  $\sim 18:10$  UT, where the time profile is very flat. At 18:12 UT, the NuSTAR emission begins to rise, reaching a peak at around 18:14 UT, and then gradually falls off until  $\sim 18:30$  UT, reaching a constant level, lower than at the start of the orbit.

At the time of the NuSTAR peak, the AIA time profiles show no clear indication of flaring behaviour, only a steady increase in emission observed across all channels. Though these

## 5.2 A Bright Point in the 21 February 2020 Observation

lightcurves were calculated over a region which covered the entire bright point, we also plotted AIA time profiles for smaller boxes within the bright point (not shown), and found no significantly increased emission at the time of the NuSTAR event. The AIA images (shown in Figure 5.7) also show no clear evidence of any flaring behaviour at this time.

While this lack of detection in AIA is puzzling, it is likely the result of NuSTAR (due to its high sensitivity) detecting a very small event, which is too faint in EUV to be detectable over the emission at 2–3 MK from the rest of the bright point. This is further investigated in the next section, through NuSTAR spectroscopy. We can assume that the event which NuSTAR detected is real, as the increased HXR emission does not appear to be a result of the bright point moving through detector gaps, nor were there any NuSTAR pointing changes at this time. This event was also not due to ghost rays, as it appears as a distinct imaged source in NuSTAR’s FOV, not showing the recognisable ghost ray pattern (an example of which is shown in Figure 2.3, right panel).

### NuSTAR HXR Spectroscopy

We investigated the properties of Flare 2 (and the lack of detection in AIA) through fitting the NuSTAR spectra from two time ranges, shown as shaded regions on the time profiles in Figure 5.7. We take the time interval from 18:09:30–18:11:40 UT, during which the NuSTAR time profile is flat just before the rise begins, to be the pre-flare time. We took the flare time to be from 18:12:30–18:14:50 UT, again choosing the time interval during which the NuSTAR 4–6 keV emission was strongest.

The NuSTAR spectra from both of these times were first fitted with isothermal models, as shown in the two left-hand panels of Figure 5.8. The spectrum from the pre-flare time was adequately fitted by an isothermal model with a temperature and emission measure of 3.20 MK and  $5.89 \times 10^{44} \text{ cm}^{-3}$ , respectively. During the flare time, the isothermal model fitted to the NuSTAR spectrum has a higher temperature of 4.01 MK, with a corresponding emission measure of  $2.85 \times 10^{44} \text{ cm}^{-3}$ . However, as was the case for Flare 1, there is a small excess in the observed spectrum compared to this model at higher energies ( $> 4.5 \text{ keV}$ ). This indicates that the isothermal model alone may not sufficiently fit this spectrum, and that a hotter or non-thermal component could be present.

We also tried fitting this model with a double thermal model, fixing one of the components to have  $T = 3.20 \text{ MK}$  and  $EM = 5.89 \times 10^{44} \text{ cm}^{-3}$  (the same isothermal model that was fitted to the pre-flare spectrum). The results of this approach are shown in Figure 5.8, right panel. It can be seen that the second thermal component has a temperature of 4.39 MK

## 5.2 A Bright Point in the 21 February 2020 Observation

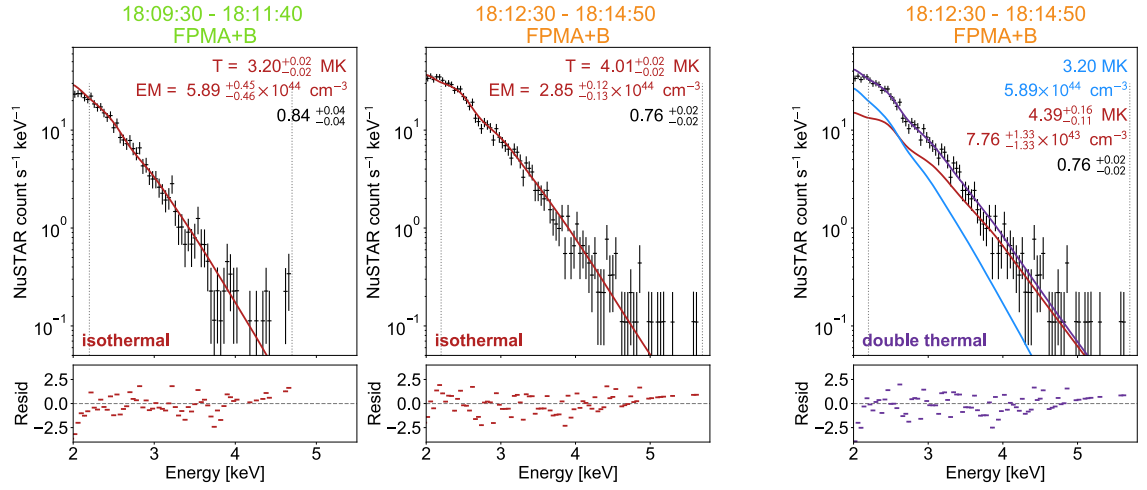


**Figure 5.8:** (Left) NuSTAR spectral fits for Flare 2 during the pre-flare (18:09:30–18:11:40 UT) and flare (18:12:30–18:14:50 UT) times, fitted with isothermal models (red). (Right) The NuSTAR spectrum from the flare time, fitted with a double thermal model (purple, with the two separate thermal components plotted in red and blue).

and an emission measure of  $7.76 \times 10^{43} \text{ cm}^{-3}$ . This temperature lies in a range where the AIA channels have less sensitivity (see Figure 2.8). This explains why AIA did not see enhanced emission at the time of the NuSTAR flare, especially when the EUV emission would be dominated by emission at 2–3 MK from the rest of the (non-flaring) bright point. It would be expected that this material would produce an EUV signature upon cooling, which was not observed. We suggest that the lack of detection is due to this event being very small compared to the dominant background emission from the bright point.

### Non-Thermal Upper Limits

Even when fitted with a double thermal model, the observed NuSTAR spectrum for Flare 2 (Figure 5.8) still shows a slight excess at energies  $> 5 \text{ keV}$ . When the fitted model was subtracted from the observed spectrum, it was found that there is a total number of 5 counts in excess of the model at higher energies. We calculated non-thermal upper limits that would be consistent with this excess using the approach from Section 3.2.4.

Unfortunately, comparing these upper limits to the heating requirement from the thermal energy is complicated for this event. The thermal energy calculation depends on the area of the emitting region, and no clear signature of this event was observed in AIA, making it difficult to select an accurate area for this analysis. However, we did calculate the thermal energy for several different areas for comparison with the non-thermal upper limits.

## 5.2 A Bright Point in the 21 February 2020 Observation

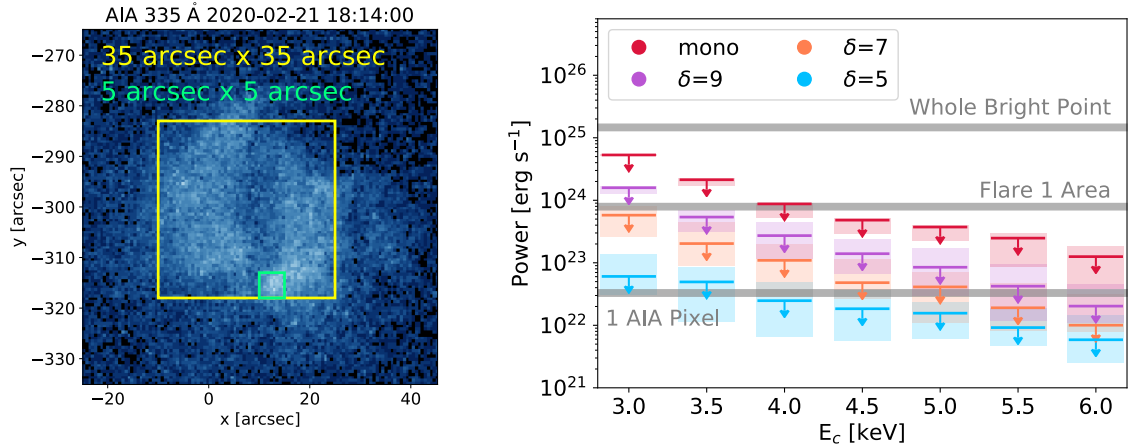


**Figure 5.9:** (Left) An AIA 335 Å image of the February 2020 bright point during the time of Flare 2. The boxes show different areas used for calculating the thermal energy of the flare. The yellow box shows an area covering the whole bright point, whereas the green box shows an area of  $5'' \times 5''$ , the same as what was used for Flare 1. (Right) Upper limits on the non-thermal emission in Flare 2 for a range of power law indices. The shaded regions indicate the  $\pm 1\sigma$  range. The grey lines indicate the heating requirement dictated by the thermal energy, calculated using three different areas.

We chose three different areas:  $0.6'' \times 0.6''$ , a tiny area corresponding to the size of a single AIA pixel;  $5'' \times 5''$ , the area of the brightening region in Flare 1 (see Section 5.2.1); and  $35'' \times 35''$ , an area that covers the entire bright point. These areas (except for the single pixel, which is too small to plot) are indicated on the AIA image in Figure 5.9 (left panel). We calculated the thermal energy of the flare using these areas and the results from the NuSTAR spectral fitting results. The cooler pre-flare component was taken to be the background, and we therefore took the temperature and emission measure from the hot component of the double thermal model ( $T = 4.39$  MK and  $EM = 7.76 \times 10^{43} \text{ cm}^{-3}$ ). The thermal energies were determined to be (in order of increasing area)  $4.61 \times 10^{24}$ ,  $1.12 \times 10^{26}$ , and  $2.05 \times 10^{27}$  erg. Dividing all three by the duration of the flare (140 s) resulted in thermal heating requirements of  $3.29 \times 10^{22}$ ,  $7.93 \times 10^{23}$ , and  $1.47 \times 10^{25}$  erg  $\text{s}^{-1}$ , respectively.

Figure 5.6 displays the non-thermal upper limits for Flare 2, as well as the heating requirements for the three test areas. In this plot, it can be seen the significant effect that changing the area has on the results of this analysis. When a very small area the size of a single AIA pixel is used, many of the non-thermal upper limits satisfy the heating requirement. A non-thermal component with  $\delta \geq 7$  with a low energy cutoff up to  $\sim 5$  keV could provide the observed heating. However, using a much larger area enclosing the full bright point gives a heating requirement greater than any of the non-thermal upper limits,

### 5.3 *A Bright Point in the 12–13 September 2020 Observation*

meaning that the heating could not be non-thermal. Using the more realistic example of  $5'' \times 5''$ , a very steep—practically mono-energetic—non-thermal component between 3–4 keV could provide the necessary heating.

If the X-ray brightening originated from a small sub-region from within the bright point it is therefore possible that a steep non-thermal distribution at low energies could have satisfied the heating requirement. However, a definitive conclusion cannot be made here due to the lack of a clear detection in AIA.

Note that we did not perform DEM analysis for Flare 2. This is because of the area issue that also affects the non-thermal upper limit calculation. The lack of detection in AIA means that the sub-region within the bright point that the flare originated from could not be identified. Selecting an accurate AIA area is important in DEM analysis, so we did not reconstruct DEMs for this event.

## 5.3 A Bright Point in the 12–13 September 2020 Observation

The only bright point strongly observed in the 12–13 September 2020 NuSTAR observation began to emerge (in X-rays as observed by XRT) near the East limb at  $\sim 19:30$  UT, and was therefore only captured in the final three NuSTAR orbits. The NuSTAR, XRT, and AIA time profiles for this bright point over the last three orbits can be found in Figure 5.10, along with AIA and XRT images showing its evolution. From the NuSTAR and XRT time profiles, it can be seen that the bright point is relatively quiet in X-rays in Orbits 8 and 10. However, during Orbit 9, the X-ray emission is stronger, with several spikes observed with both XRT and NuSTAR between 22:00–22:30 UT. These spikes are not observed in EUV. In fact, the AIA time profiles for this source show a very different behaviour to the X-ray ones, with the EUV emission rising steadily in all channels throughout Orbits 8 and 9. At  $\sim 23:00$  UT, the AIA lightcurves level out, and remain relatively flat—at a higher level than at the start of Orbit 8—throughout the tenth NuSTAR orbit. AIA time profiles were calculated for smaller sub-regions within the bright point (not shown), but similar spikes to those found in the X-ray lightcurves could still not be identified.

### 5.3.1 NuSTAR Spectral Analysis

In order to investigate the evolution of this bright point over the three orbits, and in an effort to understand the nature of the X-ray spikes in Orbit 9, we performed NuSTAR HXR

### 5.3 A Bright Point in the 12–13 September 2020 Observation

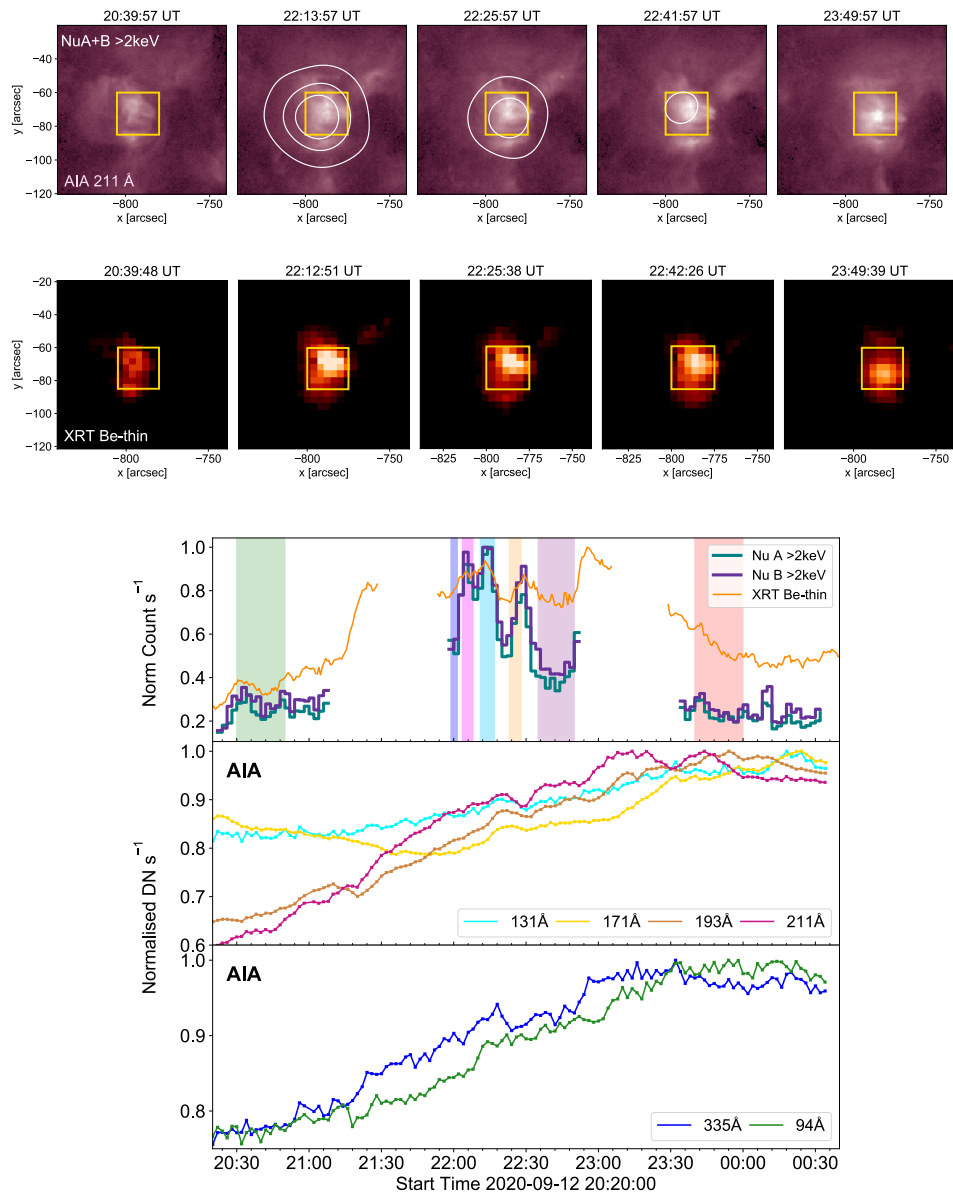


**Figure 5.10:** (Top) AIA 211 Å (top row) and XRT Be-thin (bottom row) images showing the evolution in EUV and SXR of the September 2020 bright point over the final three NuSTAR orbits. The first image for each is from Orbit 8, the next three from Orbit 9, and the final one from Orbit 10. The yellow boxes show the region used for calculating time profiles (which was appropriately shifted to account for the Sun’s rotation), and the white contours are NuSTAR FPMA+B > 2 keV (plotted at  $5, 8, \text{ and } 10 \times 10^{-3}$  counts s<sup>-1</sup>). (Bottom) NuSTAR, XRT, and AIA time profiles of the bright point over the final three NuSTAR orbits. The shaded time ranges are those used for spectral analysis, detailed in Figure 5.11.

### 5.3 A Bright Point in the 12–13 September 2020 Observation

spectroscopy for several time ranges using the approach detailed in Section 3.2.2. All seven of the chosen time ranges are shown as shaded regions on the lightcurves in Figure 5.10.

For the Orbits 8 and 10, where the NuSTAR emission is at an approximately constant level, we chose long time windows in order to obtain a good signal-to-noise ratio. These time ranges are 20:30:00–20:50:00 UT (green) in Orbit 8, and 20:40:00–00:00:00 UT (red) in Orbit 10. From Orbit 9, five separate time intervals were chosen: 21:58:50–22:01:30 (dark blue), when the NuSTAR lightcurve is flat for a short time before rising to the peaks; 22:03:30–22:08:00 UT (pink), the time of the first X-ray spike; 22:11–22:17 UT (light blue), covering the second—and strongest—of the NuSTAR peaks; 22:23:00–22:28:00 UT (yellow), when NuSTAR observes a smaller third peak; and 22:35:00–22:50:00 UT (purple), where the NuSTAR lightcurve reaches a minimum following the three peaks.

The NuSTAR spectra from all of these time intervals, which were fitted with single thermal models using XSPEC and the method explained in Section 3.2.2, are shown in Figure 5.11. The results of this fitting are also summarised in plots of fit temperature and emission measure against time, shown in Figure 5.12. It can be seen that the fit temperature for this bright point stays approximately constant at  $\sim 2.6$  MK. The spectral fits from all of the chosen time ranges resulted in this temperature, except for the spectrum from 22:35:00–22:50:00 UT (during the minimum in the NuSTAR lightcurve in the ninth orbit). The isothermal model which was fitted to the spectrum from this time was a little cooler, with a temperature of 2.44 MK (and a corresponding emission measure of  $3.03 \times 10^{44} \text{ cm}^{-3}$ ). However, the error bars on the temperature and emission measure from this fit are larger than for the other times (as highlighted in the temperature and emission measure versus time plots in Figure 5.12), suggesting that this result is not as reliable.

In Orbits 8 and 10, a similar emission measure of  $\sim 1 \times 10^{44} \text{ cm}^{-3}$  (and a temperature of  $\sim 2.6$  MK) was found. This is lower than the emission measure found at any point in Orbit 9, in agreement with the NuSTAR time profiles being at a lower (and similar) level in Orbits 8 and 10 compared to the middle orbit. In Orbit 9, the NuSTAR fit temperature again stays constant at  $\sim 2.6$  MK while the emission measure changes, following a similar pattern to the NuSTAR time profile in Figure 5.10. At the start of the orbit, it is at an elevated (compared to the other two orbits) level of  $1.97 \times 10^{44} \text{ cm}^{-3}$ . It then increases to  $3.54 \times 10^{44} \text{ cm}^{-3}$  during the first spike, and reaches a maximum value of  $3.66 \times 10^{44} \text{ cm}^{-3}$  during the second, and largest, spike. The emission measure then falls off slightly to  $2.41 \times 10^{44} \text{ cm}^{-3}$  during the smaller third peak.

This spectral analysis found that the fit temperature stayed approximately constant while the emission measure increased during the observed NuSTAR peaks. This suggests that

### 5.3 A Bright Point in the 12–13 September 2020 Observation

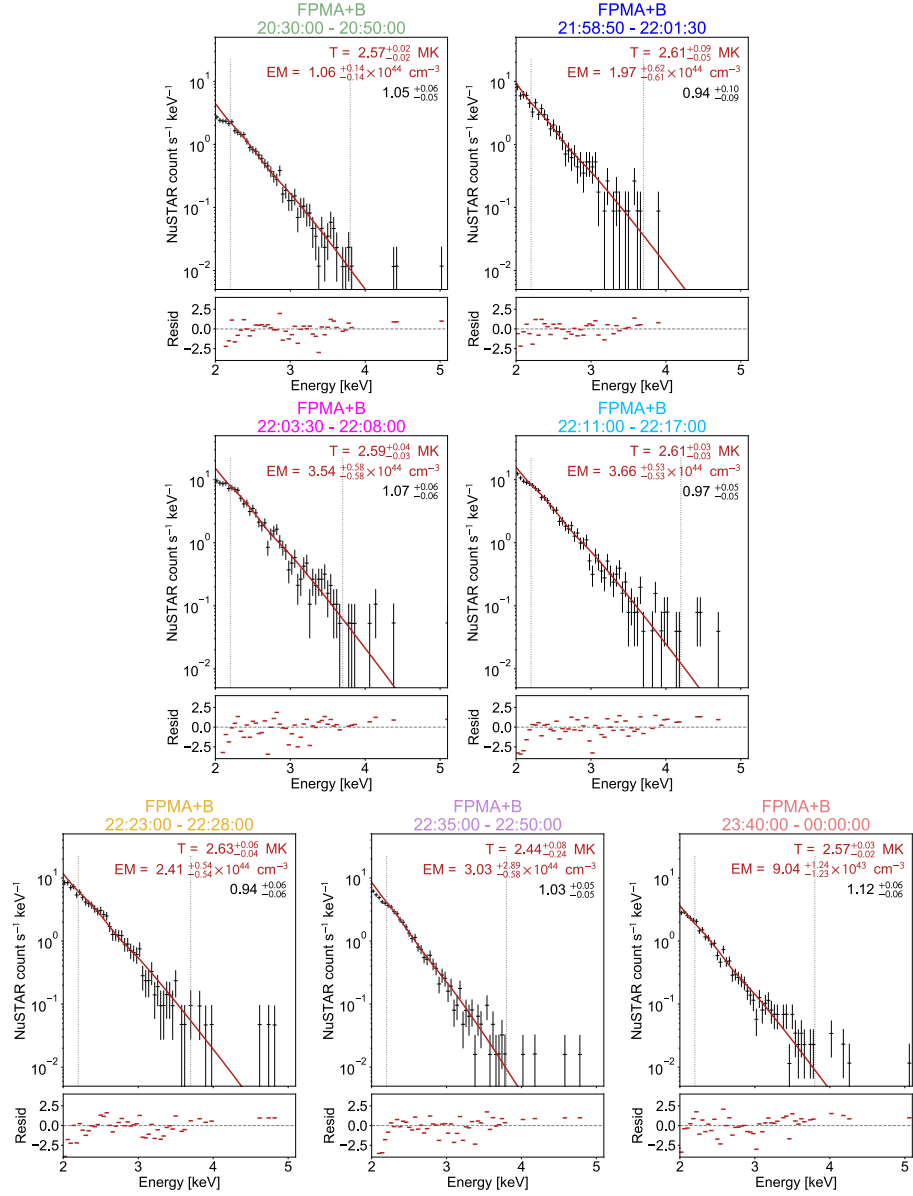


**Figure 5.11:** NuSTAR FPMA+B spectra for the the September 2020 bright point, fit with isothermal models (red). The time ranges that these spectra are from are marked on the NuSTAR lightcurves plotted in Figure 5.10. The top-left spectrum is from Orbit 8, the bottom-right from Orbit 10, and all others from different times throughout Orbit 9 (when the bright point showed the most variability).

### 5.3 A Bright Point in the 12–13 September 2020 Observation

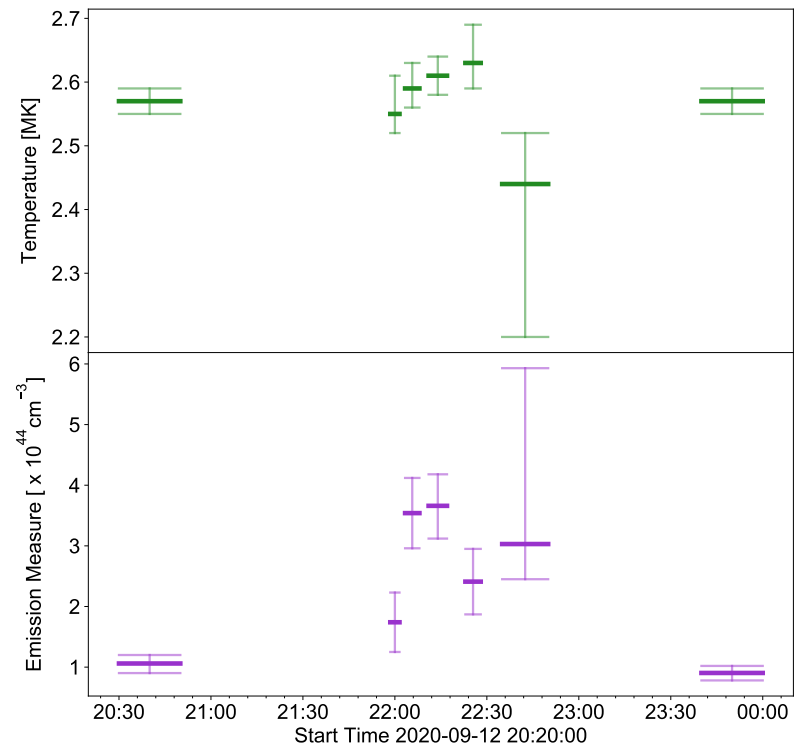


**Figure 5.12:** A summary of the NuSTAR spectral fitting results shown in Figure 5.11 for the September 2020 bright point. The fit temperatures (top) and emission measures (bottom) are plotted against time.

### 5.3 A Bright Point in the 12–13 September 2020 Observation

the HXR spikes are caused by an increase in the amount of material emitting, rather than a significant temperature change. Due to NuSTAR’s poor spatial resolution, it is difficult to say whether these changes are a result of variation in volume and/or electron number density. As will be discussed further in Section 5.3.3, the lack of AIA detection for this event makes it difficult to determine what sub-region within the bright point that the NuSTAR emission is coming from. This makes it difficult to tell whether the volume of the HXR source has changed.

While most of these spectra are well-fitted with the isothermal models and show no evidence of any hot or non-thermal components, there is possibly a slight excess in the two spectra from the times of the strongest NuSTAR peaks. These could indicate the presence of temperatures  $> 2.6$  MK at these times, though the excesses are very small and do not look to be significant. This can be further investigated through DEM analysis.

#### 5.3.2 DEM Analysis

Similarly to the February 2020 bright point, the NuSTAR and AIA time profiles for the September 2020 bright point are not in agreement (see Figure 5.10). The NuSTAR light-curve shows several spikes in the ninth orbit that were not observed in EUV with AIA. The NuSTAR spectroscopy suggests that these spikes are due to an increase in emission measure, but not any significant heating. We performed DEM analysis to further investigate the nature of these HXR spikes, as well as to study the multi-thermal evolution of the September 2020 bright point through the three NuSTAR orbits in which it was captured. The X-ray emission is brightest (and most variable) from this feature in Orbit 9 (as shown in Figure 5.10). However, the AIA time profiles show that the bright point is brightest in EUV during Orbit 10. To investigate this behaviour, we calculated the DEMs for three different times (which were also used for spectral analysis) throughout this source’s evolution.

The time ranges that DEMs were reconstructed for are as follows: 20:30–20:50 UT, the time where the bright point is quiet in X-rays and at its lowest brightness in EUV; 22:11–22:17 UT, the time of the largest X-ray spike in Orbit 9, during which AIA sees only a steady rise; and 23:40–00:00 UT, during Orbit 10 when the X-ray time profiles have returned to background level but maximum brightness has been reached in AIA. All of these time ranges are indicated by the shaded regions on the lightcurve plot in Figure 5.10 (coloured green, light blue, and red, respectively).

The DEMs for this bright point for the three chosen time intervals are plotted in Figure 5.13. The DEMs for all three time ranges have two peaks, with the higher temperature one

### 5.3 A Bright Point in the 12–13 September 2020 Observation

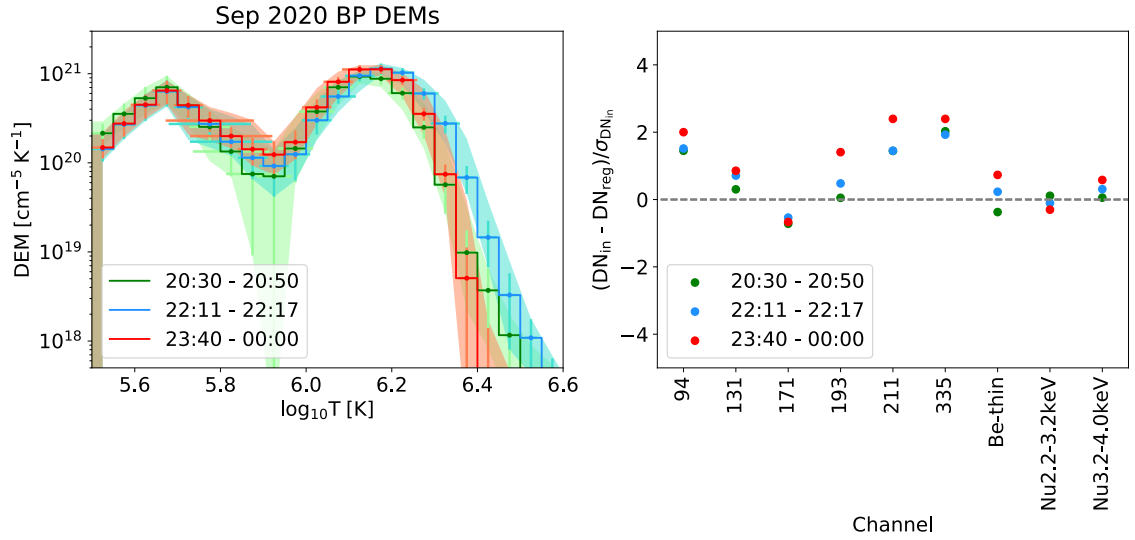


**Figure 5.13:** (Left) DEMs reconstructed for the September 2020 bright point using AIA, XRT, and NuSTAR data. These DEMs are from 20:30–20:50 UT (green), 22:11–22:17 UT (blue), and 23:40–00:00 UT (red). These time ranges are highlighted on the time profiles in Figure 5.10. (Right) Normalised residuals.

occurring at  $\log(T) \sim 6.15$ , as was found for the DEM analysis of the bright points in the 28 September 2018 mosaics in Chapter 4 (see Section 4.2.2). This result is also in line with previous DEM analyses by Brosius et al. (2008) and Doschek et al. (2010). The peak shifts slightly higher (closer to  $\log(T) = 6.2$ ) during the time of the largest X-ray spike in Orbit 9.

The bright point’s DEM is higher during Orbit 10 at temperatures between  $5.8 < \log(T) < 6.3$  than it is during Orbit 8. This suggests that there is more material emitting at temperatures  $< 2$  MK in the final orbit, which is consistent with the increase in EUV emission observed with AIA for this source. At higher temperatures above  $\log(T) \sim 6.2$ , the DEMs from Orbit 8 and 10 are very similar as they decay. This is a reflection of the X-ray time profiles, which are at similar quiescent levels during both of these orbits.

The DEM from Orbit 9 during the highest X-ray spike is very similar to the other two DEMs below the second peak (for  $\log(T) < 6.2$ ). However, at temperatures higher than this, the DEM is slightly higher than the other two, indicating the presence of slightly more hot material. This is consistent with the increased X-ray emission at this time, which suggests the presence of more material  $> 2.5$  MK. However, though the spectrum for this time does seem to show a slight excess when fitted with an isothermal model (see Figure 5.11, middle row, right panel), this DEM confirms that there is not any significant emission above 3 MK.

### 5.3 A Bright Point in the 12–13 September 2020 Observation

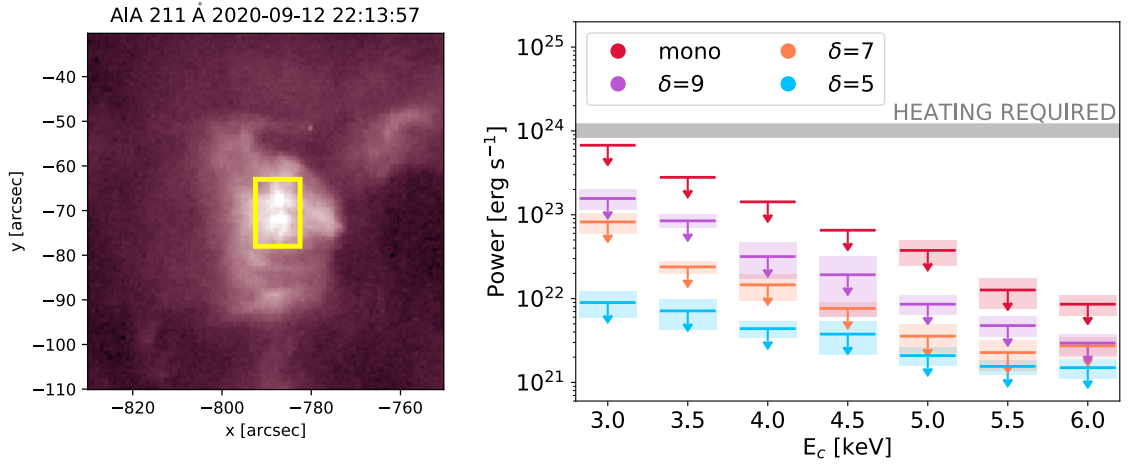


**Figure 5.14:** (Left) An AIA 211 Å image of the September 2020 bright point during the time of the largest X-ray spike. The yellow box shows the area used to calculate the thermal energy of the event. (Right) Upper limits on the non-thermal emission during the X-ray spike for a range of power law indices. The shaded regions indicate the  $\pm 1\sigma$  range, and the grey line indicates the heating requirement dictated by the thermal energy.

All three DEMs fall off very sharply after  $\log(T) \sim 6.3$  (2 MK), which is consistent with the NuSTAR spectra from all three times being well-fitted with isothermal models at 2.6 MK. We can conclude that the enhanced X-ray emission is due to an increase in the amount of material at  $\sim 2.5$  MK, rather than any significant heating to hotter temperatures as was found for the February 2020 bright point (analysed in Section 5.2).

#### 5.3.3 Non-Thermal Upper Limits

As seen in Figure 5.11, during the time of the strongest X-ray spike (22:11:00–22:17:00 UT), there is a small excess above the NuSTAR spectrum compared to the isothermal model. On subtracting the isothermal model from the observed spectrum, it was found that this excess totalled four counts at energies  $> 4$  keV. We calculated upper limits on the non-thermal component consistent with this excess using the method from Section 3.2.4.

We took the area of the emitting region to be  $15'' \times 10''$ , as indicated on the AIA 211 Å image in Figure 5.14. This area was selected from AIA images, choosing the brightest region of EUV emission. However, as no EUV spike was observed at the time of the X-ray one, it is difficult to accurately determine the size of the emitting region.

To calculate the thermal energy of this spike, we used the temperature and emission measure values from the NuSTAR spectral analysis in Section 5.3.1. The temperature

## 5.4 Integrated Spectra

during this time interval is 2.61 MK, with a corresponding emission measure of  $3.66 \times 10^{44} \text{ cm}^{-3}$ . However, the temperature did not change between the short time range at the start of Orbit 9 where the NuSTAR time profile is flat (21:58:50–22:01:30 UT) and the time of the strongest X-ray spike. Therefore, we took this earlier time to be a background component, and subtracted the emission measure at this time ( $1.97 \times 10^{44} \text{ cm}^{-3}$ ) from that during the spike. This gives an emission measure of  $1.69 \times 10^{44} \text{ cm}^{-3}$ , which represents the change in emission between the two times.

Using the above parameters, the thermal energy was calculated to be  $3.73 \times 10^{26} \text{ erg}$ . Dividing this by the duration of the peak (360 s) gives a required heating power of  $1.04 \times 10^{24} \text{ erg s}^{-1}$ . This is marked on the plot showing the calculated non-thermal upper limits, which can be found in Figure 5.14 (right panel).

It can be seen that there are no non-thermal upper limits which could have provided the required heating. However, the highest of the upper limits (for a mono-energetic distribution at 3 keV) is less than a factor of 2 below the requirement. The area used may have been over-estimated, especially since the region producing the X-ray spike could not be clearly identified in AIA. Also, there may have been some filling factor  $< 1$ , which would further reduce the thermal energy. Therefore, we can conclude that, if either of these were the case, the heating requirement would likely be lowered such that some of the non-thermal upper limits would satisfy it.

## 5.4 Integrated Spectra

In Sections 5.2 and 5.3, we studied the time evolution of the February and September 2020 bright points, and the NuSTAR spectral analysis focused on the investigation of how the bright points' properties changed on shorter time scales. However, it is difficult to detect any faint hot or non-thermal components in these short time intervals. If there were some weak steady hot or non-thermal component, it would only be detectable over a long duration observation.

The NuSTAR dwell observations from February and September 2020 provided several hours of data on both of the bright points studied in this chapter. We could therefore combine several orbits (several hours) of data for both bright points, giving an integrated NuSTAR spectrum for each.

## 5.4 Integrated Spectra

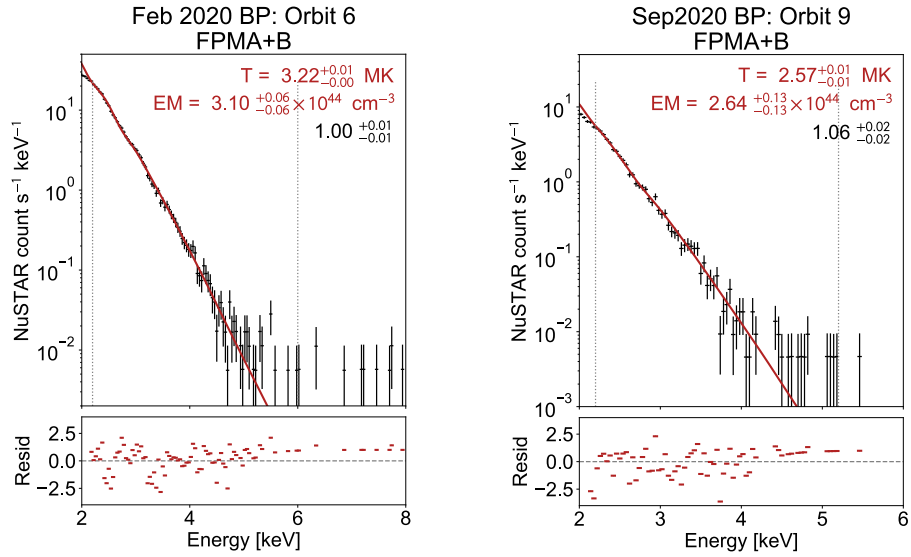


**Figure 5.15:** The NuSTAR FPMA+B spectra for the February 2020 bright point integrated over all of Orbit 6 (left), and for the September 2020 bright point integrated over all of Orbit 9 (right).

We first fitted the NuSTAR spectra of these bright points integrated over a single orbit. We chose the orbits during which these features were brightest in X-rays: Orbit 6 for the February 2020 bright point, Orbit 9 for the September 2020 one (see Figures 5.1 and 5.2). We fitted these spectra in XSPEC, following the approach of Section 3.2.2. The results of this are plotted in Figure 5.15.

It can be seen that the February 2020 spectrum is fitted well at energies  $< \sim 5$  keV by a single thermal model with a temperature of 3.22 MK and an emission measure of  $3.10 \times 10^{44} \text{ cm}^{-3}$ . This is in agreement with the quiescent temperature found previously for this bright point in Section 5.2.1. The thermal component dominates the bright point's spectrum, and there is only a small excess at energies  $> 5$  keV that is indicative of hotter emission. We attempted to fit this with an additional thermal component but could not obtain a reliable fit. The spectrum for the September 2020 bright point was fitted with an isothermal model with a temperature of 2.57 MK and an emission measure of  $2.64 \times 10^{44} \text{ cm}^{-3}$ , agreeing with results from previous spectroscopy in Section 5.3.1. There is a very slight excess at energies  $> 4.5$  keV, but no reliable fit could be obtained with an additional hot component. In both of the single orbit spectra, there are a small number counts at energies  $> 5$  keV. The NuSTAR instrumental background produces counts at these energies (see Figure 2.7), but it is not well-sampled in a single orbit as NuSTAR's throughput is dominated by the bright points.

## 5.4 Integrated Spectra

**Table 5.1:** An overview of the orbits used for the integrated NuSTAR spectra for the February and September 2020 bright points shown in Figures 5.16 and 5.17.

Orbit ID	Date/Time	Ontime (s)	Livetime Corrected Exposure (s)	Livetime (%)
80512220001	2020-02-21 08:38:13–09:29:09	3056	2790	91.3
80512221001	2020-02-21 10:06:12–11:05:47	2833	2530	89.3
80512222001	2020-02-21 11:42:51–12:42:26	2715	2307	85.0
80512224001	2020-02-21 14:56:08–15:55:43	2629	2290	87.1
80512225001	2020-02-21 16:32:47–17:32:22	2677	2371	88.6
80512228001	2020-02-21 21:22:42–22:22:18	3576	3174	88.8
80610208001	2020-09-12 20:22:11–21:07:38	2727	2438	89.4
80610209001	2020-09-12 21:58:49–22:50:20	3091	2724	88.1
80610210001	2020-09-12 23:35:28–00:34:01	3513	3143	89.5

We also tried fitting the NuSTAR spectra for these bright points over multiple orbits. For the September 2020 bright point, we fitted the spectrum over the three orbits in which it was observed in HXR, Orbits 8–10. For the February 2020 bright point, we fitted over only the orbits where the bright point was not flaring (and so did not include Orbits 6 and 9) so that the temperature and emission measure would be more constant. We also discarded Orbit 1, as this feature was not very bright at this time. Information about the orbits used for both bright points can be found in Table 5.1.

Similar to the method used to simultaneously fit mosaic pointings, we fitted the combined spectra by grouping all of the FPMA observations and all of the FPMB ones separately. The scaling factor (see Section 3.2.2) was set to 1 for all of the FPMA spectra and set to the same value (which was determined by the fit) for all of the FPMB spectra. Note that poor fits are not unexpected here as this assumes a constant temperature and emission measure, which is clearly not the case.

The integrated spectra (plotted over three different energy ranges to highlight different spectral features) are shown in Figures 5.16 and 5.17. It can be seen that both of these spectra are dominated by a thermal component at energies  $< 4$  keV. The September 2020

## 5.4 Integrated Spectra

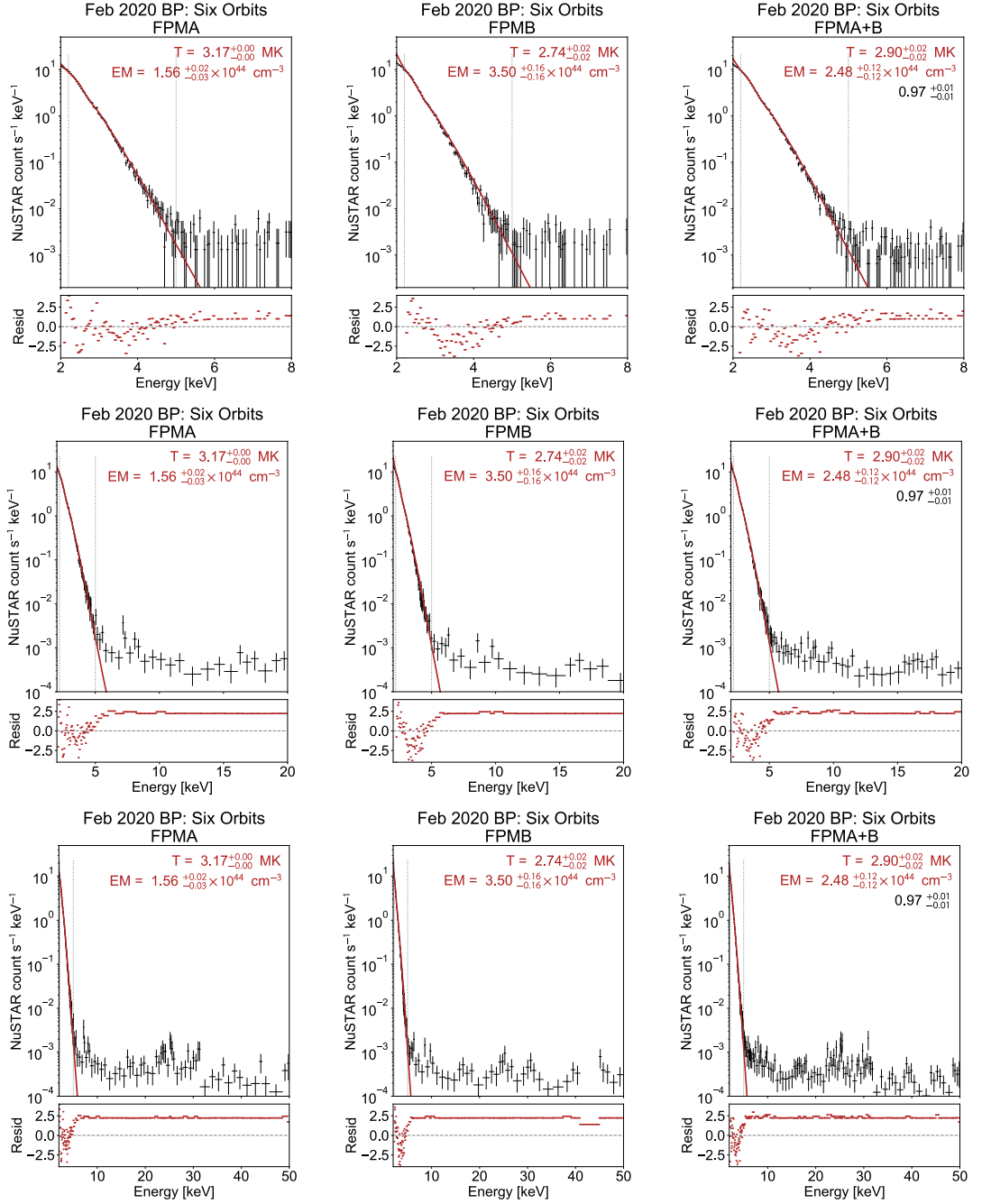


**Figure 5.16:** NuSTAR FPMA (left), FPMB (middle), and FPMA+B (right) spectra for the February 2020 bright point, integrated over the six orbits detailed in Table 5.1. All three rows show the *same* spectra; they are just plotted over different energy ranges: up to 8 keV (top row), up to 20 keV (middle row), and up to 50 keV (bottom row). These are fitted with isothermal models (red), with the fit parameters marked on the plots. The spectra in the bottom two rows have been re-binned so that they have a minimum of 2 counts per bin, but combining a maximum of 100 bins.

## 5.4 Integrated Spectra

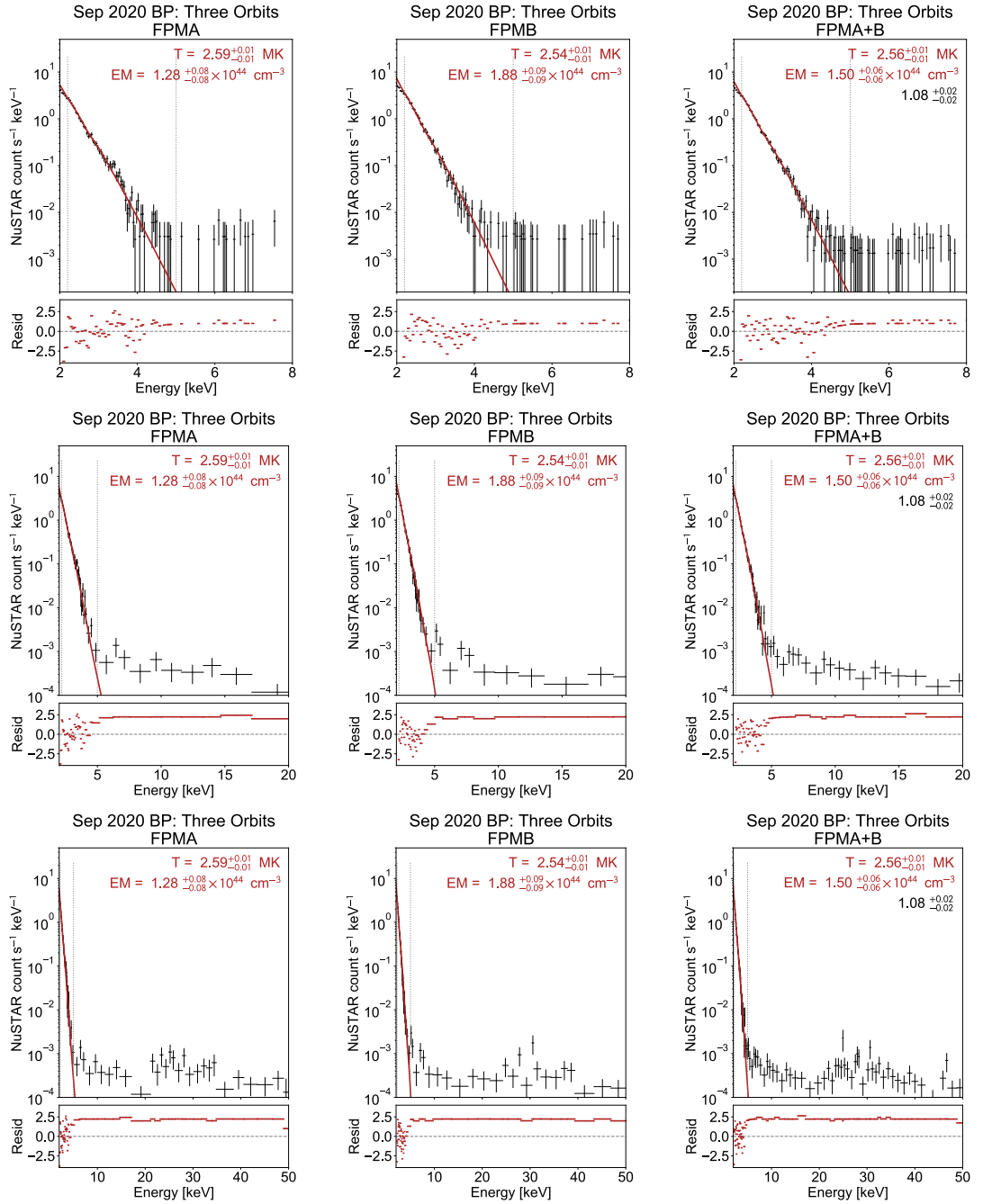


**Figure 5.17:** NuSTAR FPMA (left), FPMB (middle), and FPMA+B (right) spectra for the September 2020 bright point, integrated over the three orbits detailed in Table 5.1. All three rows show the *same* spectra; they are just plotted over different energy ranges: up to 8 keV (top row), up to 20 keV (middle row), and up to 50 keV (bottom row). These are fitted with isothermal models (red), with the fit parameters marked on the plots. The spectra in the bottom two rows have been re-binned so that they have a minimum of 2 counts per bin, but combining a maximum of 100 bins.

## 5.5 Summary and Conclusions

spectrum is fitted with a model with a temperature of 2.6 MK, consistent with previous spectral analysis for this feature. For the February 2020 bright point, there is a slight discrepancy between FPMA and FPMB, which give temperatures of 3.2 and 2.7 MK, respectively. The result for FPMA is in line with previous fits, and this discrepancy—which brings the combined FPMA+B spectrum down to 2.9 MK—is likely a result of the varying temperature and emission measure over the observation. In the integrated spectra for both bright points, there was no hotter or non-thermal component that could be reliably fitted.

In the integrated spectra for both bright points, there are counts detected at energies  $> 4$  keV. The majority of these counts are not attributed to the bright points, but to the instrumental background (Wik et al. 2014), which is plotted in Figure 2.7. As discussed in Section 2.1.5, at energies  $< 20$  keV the dominant background component is the aperture background, and instrumental lines dominate at  $\sim 20$ –30 keV. The background observed in these integrated spectra is consistent with the aperture background. The background level also increases slightly at 20–30 keV, which is consistent with the instrumental lines. The background level in the bright point spectra is lower than that in the plot in Figure 2.1.5, which was taken from Wik et al. (2014). Wik et al. (2014) observed the Bullet Cluster for 266 ks. They developed a background model to apply to their observations from more than 2500 ks of observations, which is the one shown in Figure 2.7. The lower background level found in these bright point spectra is a result of shorter integration times of 15.5 ks (4.3 hours) and 8.3 ks (2.3 hours) compared to the observing time of 2500 ks ( $\sim 700$  hours) of Wik et al. (2014).

There could be counts  $> 4$  keV (where the NuSTAR instrumental background dominates) that could have come from a hotter or non-thermal component in the bright points' HXR emission. Upper limits could be found on the emission that could be present and not attributed to the background. However, this is outside the scope of this thesis. We can however conclude, that there were no hot or non-thermal components directly detected in these integrated bright point spectra.

## 5.5 Summary and Conclusions

In this chapter, we have studied two X-ray bright points observed in the quiet Sun with NuSTAR over multiple orbits during the recent solar minimum, one each on 21 February 2020 and 12–13 September 2020. These are a first observations in HXRs which have captured

## 5.5 Summary and Conclusions

longer term evolution of X-ray bright points. Observing these features for many hours with NuSTAR allowed a much more thorough investigation of their time evolution in HXR (and also in SXR and EUV with XRT and AIA) compared to the X-ray bright points observed in the September 2018 full-disk mosaics, which were analysed in the previous chapter. For the time intervals where the X-ray time profiles showed spikes, we searched for hot ( $> 5$  MK) and/or non-thermal emission in these bright points through NuSTAR spectroscopy and DEM analysis.

We found that both features showed significant variability over the course of the NuSTAR observations, which is a well documented property of X-ray bright points (e.g. [Strong et al. 1992](#); [Alexander et al. 2011](#)). However, for these bright points, the X-ray variability generally did not match that in EUV. In standard models of loop heating ([Cargill 1994](#); [Klimchuk et al. 2008](#); [Reale 2014](#)), there is a cooling pattern in which emission is produced at progressively lower temperatures and emission measures. This means that X-rays (from hotter temperatures) should peak first, with the EUV emission (from cooler temperatures) peaking later. While this was observed in Flare 1 from the February 2020 bright point (see [Figure 5.3](#)), in which the NuSTAR peak was later followed by a peak in the AIA channels, Flare 2 from the same bright point showed no clear EUV signature at all (see [Figure 5.7](#)). The September 2020 bright point also exhibited X-ray spikes with no clear EUV counterpart. We suggest that the lack of any clear EUV signatures for these events, which would indicate cooling material, is likely a result of NuSTAR detecting brightenings that are so small that the EUV emission they produce is undetectable compared to the EUV background from the rest of the bright point.

NuSTAR spectral analysis of both flares studied from the February 2020 bright point confirmed that this source had a quiescent temperature of  $\sim 3$  MK, but indicated the presence of hotter emission at  $> 4$  MK during flaring times. AIA is less sensitive to material at  $\sim 4$  MK, which explains why the AIA time profiles do not closely match NuSTAR during these events. While none of the AIA channels have a strong response at this temperature, these flares should be hot enough to produce a signature in the AIA Fe XVIII proxy channel ([Del Zanna 2013](#)), which has response from 4–10 keV. However, it was found that these events did not in fact produce any detectable Fe XVIII emission. It can be assumed that this is due to these tiny brightenings being so small compared to the background emission from the rest of the bright point.

We fitted the NuSTAR spectra for the September 2020 bright point for several times throughout its evolution, and found that the fit temperature did not vary significantly from 2.6 MK, even during times where the X-ray emission spiked. DEM analysis confirmed that there

## 5.5 Summary and Conclusions

was no significant heating to higher temperatures than this during the peak times. The DEM from the time of the strongest X-ray emission was found to fall off sharply above 2 MK, and indicated that there was no significant emission  $> 3$  MK. AIA did not observe any peaks at the time of the NuSTAR ones, even though these channels should be sensitive to material at 2.6 MK. We suggest that this is due to XRT and NuSTAR detecting emission from 2.5–3.0 MK, whereas AIA observed EUV emission from (slightly) cooler temperatures from the rest of the bright point which dominated over the small events that NuSTAR sees.

During the X-ray spikes in Orbit 9, NuSTAR spectral analysis shows that September 2020 bright point does not get hotter, as only the emission measure changes. This is different to the February 2020 bright point, which was heated to temperatures  $> 4$  MK during flaring times. If flare-like heating were occurring—where a release of energy would accelerate electrons, which would heat and evaporate the cooler lower atmosphere into the corona (as in Reale (2014))—this would cause temperatures to increase from their quiescent levels, as was the case with the February 2020 bright point. For the September 2020 bright point, there may still have been heating to higher temperatures (as models predict), but just not enough to be identified in the observations due to these events being on the edge of NuSTAR’s sensitivity. It is also possible that these X-ray spikes are due to material being heated to the ambient temperature of the bright point ( $\sim 2.6$  MK), which would contradict the impulsive flare scenario. Additionally, compression of a pre-existing flux tube (resulting in an increase in number density) could also increase the emission measure. It remains unclear what the physical origin of these X-ray spikes is.

The temperatures found for the September 2020 bright point (and for the February 2020 one when it is not flaring) are in line with previous bright point work, which has shown that they typically do not reach temperatures  $> 3$  MK (Doschek et al. 2010; Alexander et al. 2011; Kariyappa et al. 2011). This result was also found for the X-ray bright points observed in the September 2018 mosaics, analysed in Chapter 4. However, during flaring times, the February 2020 bright point produced temperatures ranging from 4.2–4.4 MK, with emission measures between  $(4.9\text{--}7.8) \times 10^{43} \text{ cm}^{-3}$ . These temperatures are hotter than those found in previous bright point studies, though it is worth reiterating that this bright point is also unusual in its long lifetime of  $> 4$  days. Previous NuSTAR studies of active region microflares (Duncan et al. 2021; Cooper et al. 2021) have found temperatures hotter than these. These microflares generally exhibited temperatures  $> 5$  MK, with emission measures ranging from  $10^{43}\text{--}10^{46} \text{ cm}^{-3}$ . Later in this thesis, Figure 6.20 puts the spectral fitting results for the February 2020 bright point flares in context compared to NuSTAR microflares.

## 5.5 Summary and Conclusions

In these bright points, we found no significant emission at high temperatures  $> 5$  MK, even during flaring times. We also detected no non-thermal components in their NuSTAR spectra, though we did calculate upper limits on the non-thermal emission for times during which the bright points flared. We found that, for most of the events, the non-thermal distribution would have to be essentially mono-energetic at energies of 3–4 keV to power to observed heating (determined from the thermal energy). However, this analysis was complicated by it being difficult to accurately determine the area from which the NuSTAR emission originated from due to the lack of detection in AIA.

We obtained NuSTAR spectra integrated over several hours of observation for the February and September 2020 bright points. We found that these spectra were dominated by strong thermal components at 3.2 and 2.6 MK at energies  $< 4$  keV. At energies higher than this, the NuSTAR spectra of these bright points were dominated by the instrumental background. Upper limits could be found on the hot or non-thermal components that could produce counts at energies  $> 4$  keV above NuSTAR's aperture background. However, this lies outside the scope of this thesis, and is therefore discussed as future work in Section 7.2.

The NuSTAR quiet Sun dwell observations from February and September 2020 are ideal studying the HXR evolution of steady features like X-ray bright points. However, during both of these campaigns, a number of transient impulsive events were also captured. The analysis of several such events is detailed in Chapter 6.

# 6

## Impulsive Events Observed in the NuSTAR Quiet Sun Dwell Observations

The two previous chapters have largely focused on steady features like X-ray bright points, present for many hours on the disk. However, NuSTAR has also captured a number of impulsive events in the quiet Sun, such as the jet captured in the 28 September 2018 mosaics (detailed in Section 4.3). While the NuSTAR quiet Sun dwell observations from February and September 2020 gave an excellent opportunity to study the HXR time evolution of X-ray bright points (as in Chapter 5), they also improved the chances of capturing quiet Sun impulsive transients. In these NuSTAR observations, in addition to several X-ray bright points, NuSTAR also captured a number of small-scale brightenings and eruptions.

A similar analysis of NuSTAR quiet Sun flares has been done previously by [Kuhar et al. \(2018\)](#). However, this study used NuSTAR observations from 2016–2017, not from the solar minimum. As the Sun was quieter during the February and September 2020 observations, the lower background level presented an opportunity for NuSTAR to detect even fainter events compared to those detailed in [Kuhar et al. \(2018\)](#).

In this chapter, we investigate the thermal properties and the X-ray and EUV evolution of seven small-scale impulsive events, three of which were captured in the disk centre dwells from 21 February 2020, the other four from the limb dwells from 12–13 September 2020. While most of these events are characterised only by enhanced EUV and X-ray brightness, one of them is a mini-filament eruption, captured in the February 2020 dwells.

In Section 6.2, we study the time evolution of the impulsive events in HXRs with NuSTAR, and well as in SXR and EUV with XRT and AIA. We also search for high temperatures and/or non-thermal components through NuSTAR spectroscopy (in Section 6.3) and DEM analysis (in Section 6.4). In Section 6.5, we investigate the correlation between the strengths

## 6.1 Overview of Events

**Table 6.1:** A summary of seven impulsive events captured in the quiet Sun in the NuSTAR dwell observations from 21 February 2020 and 12–13 September 2020. The event durations are the time between the start of the rise and the return to background level in NuSTAR. No duration is given for Event 7, during which a ghost ray event was also detected by NuSTAR, making it difficult to tell when this impulsive event ended (see Section 6.2.7).

Event	Date	Orbit	Start Time	Location	Duration (s)
1	21 Feb 2020	5	11:50 UT	(240'', 200'')	90
2*	21 Feb 2020	8	16:44 UT	(−270'', 185'')	100
3	21 Feb 2020	11	22:00 UT	(−145'', 210'')	450
4	12 Sep 2020	3	12:40 UT	(−810'', 310'')	810
5	12 Sep 2020	6	17:16 UT	(−580'', 60'')	120
6	12 Sep 2020	8	20:37 UT	(−880'', 220'')	480
7	13 Sep 2020	10	00:00 UT	(−830'', 190'')	–

\* = mini-filament eruption

of the events in X-rays (observed with NuSTAR) and EUV (with AIA), and we determine non-thermal upper limits for all of the events in Section 6.6.

## 6.1 Overview of Events

In the dwell observations from 21 February and 12–13 September 2020, NuSTAR observed a number of transient brightenings in the quiet Sun. The seven events analysed in this chapter are summarised in Table 6.1. The events captured on 21 February 2020 were located near disk centre, whereas those from 12–13 September 2020 occurred near the East limb.

These events were all short-lived (with durations on the timescale of minutes). At the times of the NuSTAR events, enhanced emission was also detected with AIA. AIA images confirm that one of the seven events was a mini-filament eruption (which is highlighted in Table 6.1), captured in the eighth NuSTAR orbit on 21 February 2020. We label the other events “quiet Sun flares”, following the example of [Kuhar et al. \(2018\)](#), who previously investigated transient brightenings in the quiet Sun observed with NuSTAR. Early work in EUV and SXR referred to these small-scale brightenings as “nanoflares” ([Aschwanden et al. 2000](#); [Parnell & Jupp 2000](#)).

## 6.2 Event Summaries

In the following section, we investigate the evolution of these events in X-rays with XRT and NuSTAR and in EUV with AIA. Unfortunately, during the times of all three flares on 21 February 2020, high cadence XRT data was not available (XRT observed at a 6 minute cadence, which is shorter than the duration of most of the events). This means that the SXR evolution of these events could not be studied. However, there is XRT data available for all four of the events captured on 12–13 September 2020.

## 6.2 Event Summaries

### 6.2.1 Event 1

The first of the impulsive events occurred in the fifth orbit of the 21 February 2020 observation. This was detected by NuSTAR as a small brightening starting at around 11:50 UT at (240'', 200''). Images of the EUV evolution for this event can be seen in the top panel of Figure 6.1, as well as the corresponding HMI magnetograms. The magnetograms show that this event originates from a bipolar loop system. In the AIA images, this appears as an S-shaped structure with the brightening happening in the middle of the loops.

The time profiles of this event are shown in the bottom panel of Figure 6.1. In NuSTAR, this brightening begins at around 11:50 UT with a sharp increase in brightness. This is followed by a slower decay until 11:52 UT, where a gap begins in the NuSTAR data due to a SAA passage. The time profiles for all of the AIA channels shown exhibit a peak at around 11:51 UT, a minute later than the time of peak NuSTAR emission. This behaviour, the X-ray peak followed by the EUV peak, is indicative of cooling plasma. As the plasma cools, it moves out of the temperature sensitivity range of NuSTAR into a temperature range to which AIA is more sensitive.

### 6.2.2 Event 2

As the lightcurve for the whole FOV plotted in the observation overview in Section 3.1.5, Figure 3.6, is dominated by the behaviour of the large bright point that is present in all orbits, most of the small-scale impulsive events do not stand out in this plot. However, Event 2 produces a strong spike that can be seen clearly even in the full FOV time profile. This event is characterised in NuSTAR by a short-lived brightening at 16:45 UT, located

## 6.2 Event Summaries

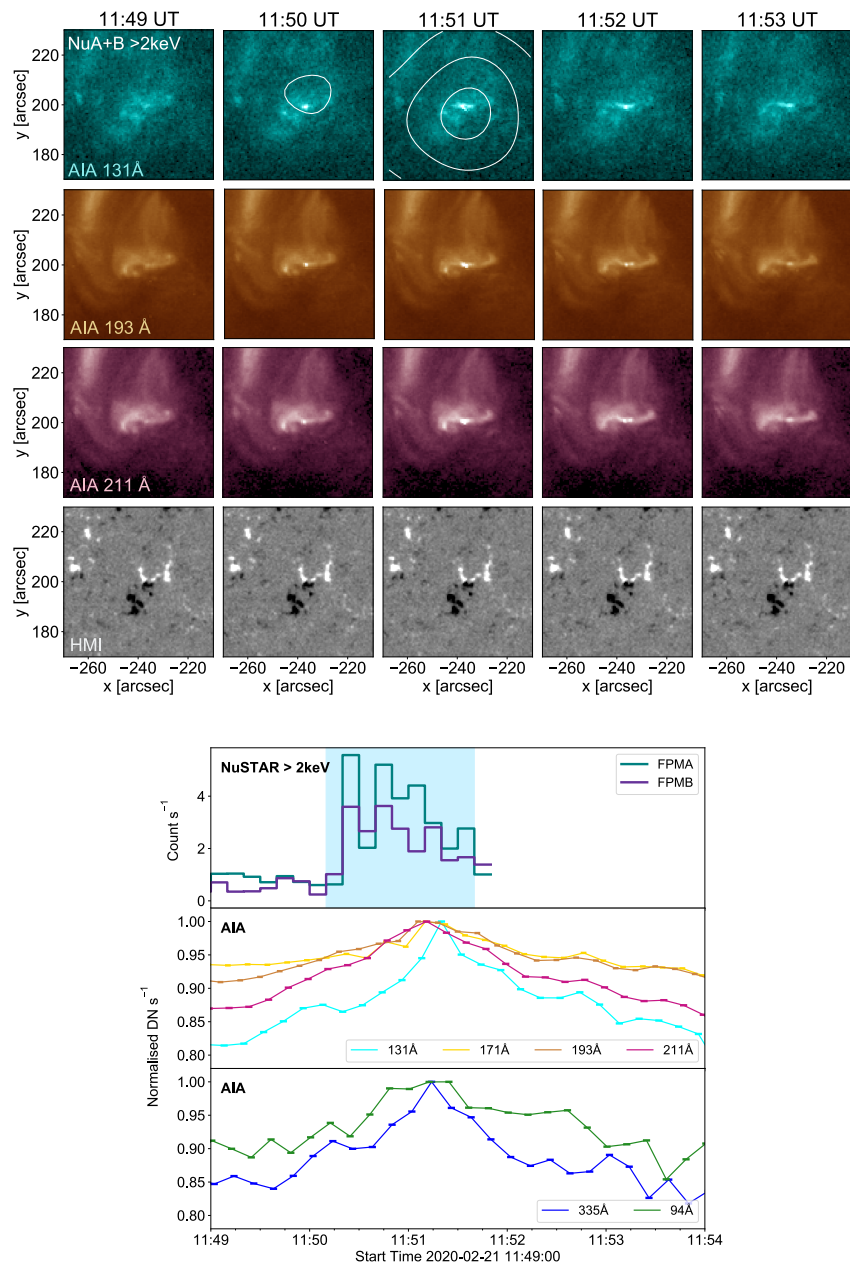


**Figure 6.1:** A summary of Event 1. Top panel: (Top three rows) AIA panels showing the EUV evolution of Event 1. The NuSTAR contours are from 2 minute intervals centred on the time of the AIA images, and are plotted at 0.0015, 0.003, and 0.005 counts/s. (Bottom row) HMI images of the event. Bottom panel: (top) NuSTAR FPMA and FPMB, and AIA (bottom two rows), time profiles for Event 1. The blue shaded region indicates the time range chosen for spectral analysis in Section 6.3.1.

## 6.2 Event Summaries

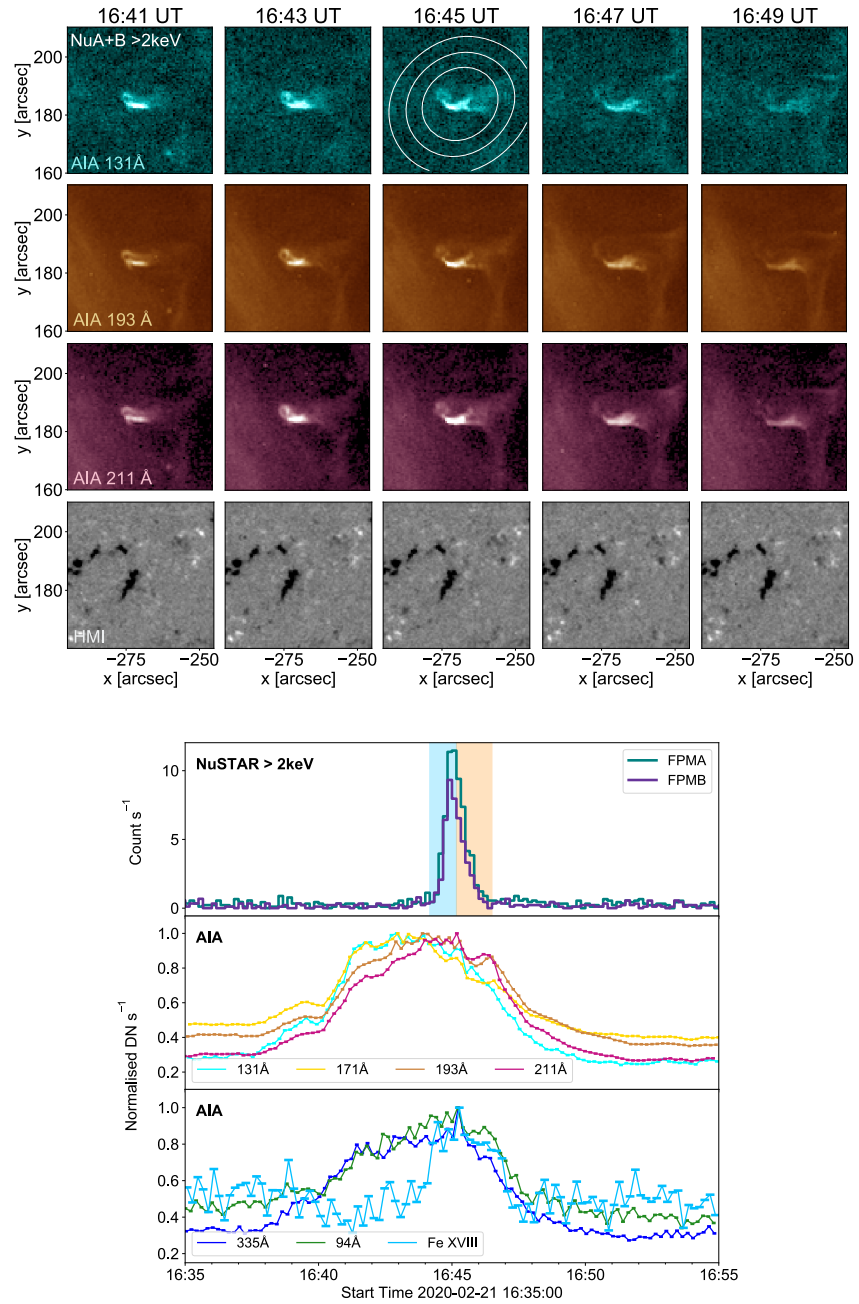


**Figure 6.2:** A summary of Event 2. Top panel: (Top three rows) AIA panels showing the EUV evolution of Event 2 (which was a mini-filament eruption). The NuSTAR contours are from 2 minute intervals centred on the time of the AIA images, and are plotted at 0.006, 0.008, and 0.010 counts/s. (Bottom row) HMI images of the event. Bottom panel: (top) NuSTAR FPMA and FPMB, and AIA (bottom two rows), time profiles for Event 2. The shaded regions indicate the time ranges chosen for spectral analysis in Section 6.3.2.

## 6.2 Event Summaries

at  $(-270'', 185'')$ . AIA images show that the increased HXR emission is a result of a mini-filament eruption.

AIA images showing the EUV evolution of this event can be found in the top panel of Figure 6.2 and the corresponding time profiles for AIA and NuSTAR are plotted in the bottom panel. The AIA images and lightcurves show a slow rise in EUV emission starting at around 16:40 UT. This is then followed by an ejection of material at 16:45 UT, at which point there is a short, sharp spike in HXR emission as observed with NuSTAR. It appears that this HXR emission comes from the heated post-flare loops beneath the eruption. The NuSTAR lightcurve returns to background level rapidly, with the event having a total duration of less than two minutes. This is followed by a slower decay in the AIA lightcurves, which return to background level by 16:50 UT.

It can also be seen from the AIA time profiles that this mini-filament eruption produces a signature in the AIA Fe XVIII channel (see Section 2.2.1). The lightcurve for this channel, which is sensitive to material at 4–10 MK, follows a similar pattern to the NuSTAR one, with the increase in brightness only beginning at around 16:45 UT. The presence of Fe XVIII emission in this event indicates that NuSTAR is observing material at temperatures  $> 4$  MK.

### 6.2.3 Event 3

A third transient brightening was captured in the February 2020 dwells at  $\sim (-145'', 210'')$ , starting in NuSTAR at around 22:00 UT. AIA and HMI images of this event are shown in Figure 6.3 (top panel). The magnetograms show that this region has a bipolar structure. The AIA images show that different regions within the structure brighten over the course of the NuSTAR event. The three strongest peaks in the 211 Å channel occur in regions to the left (at 22:00:30 UT), in the middle (at 22:05:00 UT), and to the right (at 22:08:30 UT) of the structure.

The NuSTAR time profile for this event (as seen in Figure 6.3, bottom panel) shows three distinct peaks after the brightening begins at 22:00:00 UT. These peaks occur at around 22:02:00 UT, 22:04:00 UT, and 22:06:00 UT. However, the timing of these peaks is not well-matched to the three peaks observed in AIA 211Å. The earliest peak in 211 Å precedes the earliest NuSTAR one, indicating that this increase in EUV emission occurred at temperatures below NuSTAR's sensitivity. Though not well observed in the 211 Å channel, a small peak was observed in the 131, 171, and 335 Å channels at the time of the first NuSTAR

## 6.2 Event Summaries

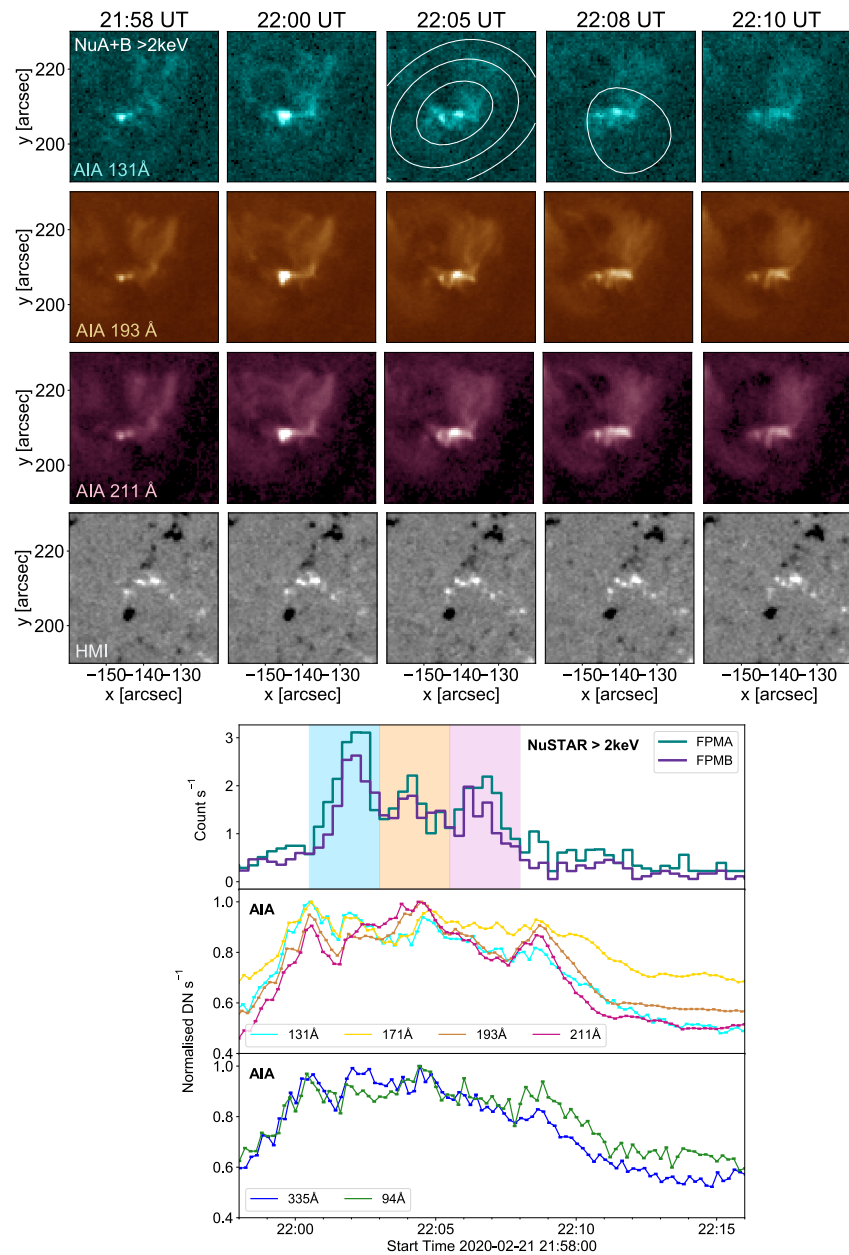


**Figure 6.3:** A summary of Event 3. Top panel: (Top three rows) AIA panels showing the EUV evolution of Event 3. (Bottom row) HMI images of the event. The NuSTAR contours are from 2 minute intervals centred on the time of the AIA images, and are plotted at 0.001, 0.002, and 0.003 counts s<sup>-1</sup>. (Bottom row) HMI images of the event. Bottom panel: (top) NuSTAR FPMA and FPMB, and AIA (bottom two rows), time profiles for Event 3. The shaded regions indicate the time ranges chosen for spectral analysis in Section 6.3.3.

## 6.2 Event Summaries

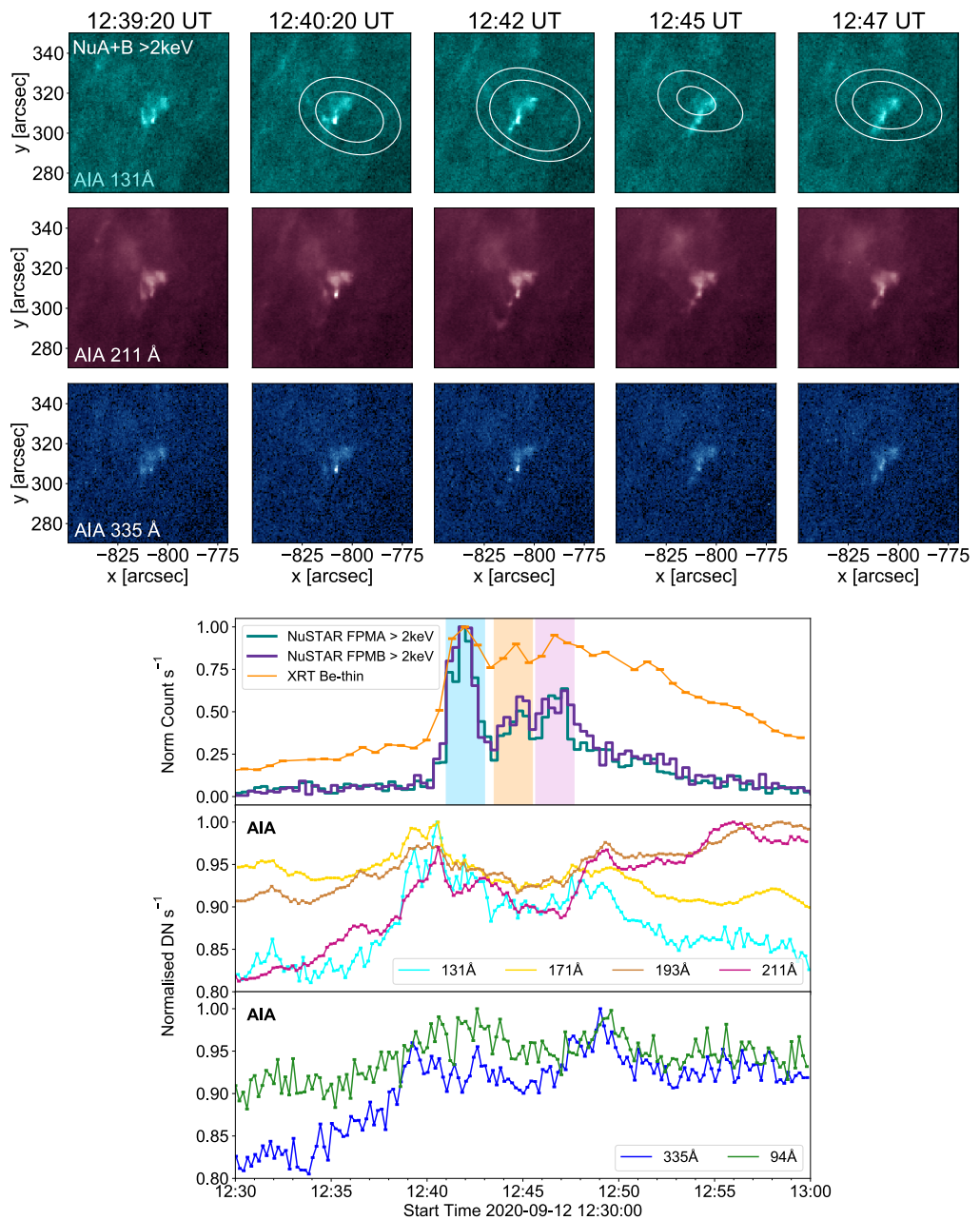


**Figure 6.4:** A summary of Event 4. Top panel: AIA panels showing the EUV evolution of Event 4. The NuSTAR contours are from 2 minute intervals centred on the time of the AIA images, and are plotted at 0.075, 0.010, and 0.020 counts  $s^{-1}$ . Bottom panel: (top) NuSTAR (FPMA and FPMB) and XRT, and AIA (bottom two rows), time profiles for Event 4. The shaded regions indicate the time ranges chosen for spectral analysis in Section 6.3.4.

## 6.2 Event Summaries

peak. The middle AIA 211 Å peak occurs only slightly later than the middle NuSTAR peak, indicating plasma cooling. The final NuSTAR peak is followed  $\sim 2.5$  minutes later by the third 211 Å peak, again suggesting that the plasma is cooling out of the range of NuSTAR's sensitivity.

### 6.2.4 Event 4

Event 4 is the first of the events analysed which was observed in the 12–13 September 2020 observation. NuSTAR detected a brightening source close to the edge of its FOV at  $(-810'', 310'')$  beginning around 12:40 UT. This event was also observed in EUV with AIA, and images showing the evolution of the event can be found in Figure 6.4 (top panel).

The bottom panel of Figure 6.4 plots the NuSTAR, XRT, and AIA lightcurves for this event. This event begins to show enhanced EUV emission at around 12:38 UT. The rise in EUV is most strongly observed in the time profiles for the 131 and 211 Å channels. This is then followed by a strong X-ray spike at 12:42 UT, as observed with both XRT and NuSTAR. Two weaker X-ray peaks occur at 12:45 and 12:47 UT. Later, several of the AIA channels rise to a second peak at 12:49 UT. The fact that the EUV and X-ray lightcurves show different behaviour, with the peaks not occurring at the same time in all channels, indicates that they are observing material at different temperatures.

### 6.2.5 Event 5

NuSTAR observed another brightening on 12 September 2020, which was located at  $(-580'', 60'')$  and began around 17:17 UT. AIA images and HMI magnetograms for this event are shown in Figure 6.5 (top panel). These show that this event originates from a complex loop structure, with two regions within it brightening at different times. However, the brightest region in AIA is the one on the right, which dominates the EUV time profile. In NuSTAR, this event was captured on the very edge of the FOV.

X-ray and EUV time profiles for this event are shown in the bottom panel of Figure 6.5. NuSTAR begins to see increased HXR emission beginning at 17:16 UT, reaching a peak at around 17:18 UT. XRT also captured this event, and the resulting SXR time profile shown in this figure also shows increased emission, though the brightening begins earlier at around 17:14 UT. The time of peak emission is also earlier in XRT than in NuSTAR, with the time of maximum emission falling somewhere between 17:16:34 and 17:18:00 UT (during which

## 6.2 Event Summaries

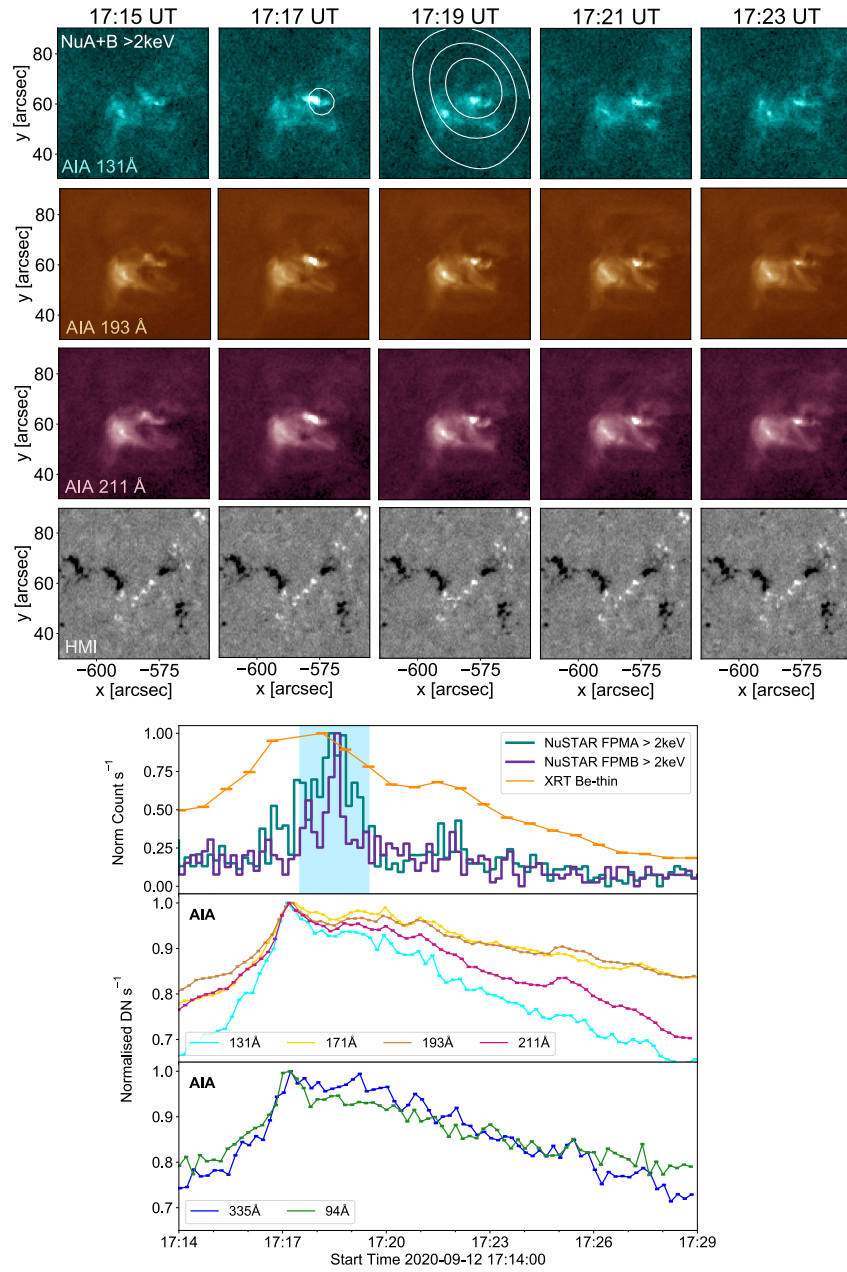


**Figure 6.5:** A summary of Event 5. Top panel: (Top three rows) AIA panels showing the EUV evolution of Event 5. The NuSTAR contours are from 2 minute intervals centred on the time of the AIA images, and are plotted at 0.003, 0.004, and 0.005 counts  $s^{-1}$ . (Bottom row) HMI images of the event. Bottom panel: (top) NuSTAR (FPMA and FPMB) and XRT, and AIA (bottom two rows), time profiles for Event 5. The blue shaded region indicates the time range chosen for spectral analysis in Section 6.3.5.

## 6.2 Event Summaries

time range there is no XRT data). The EUV lightcurves from AIA all show very similar behaviour, with increased emission starting at 17:14 UT, reaching a peak at 17:17 UT, one minute earlier than the NuSTAR peak.

The AIA time profiles have a similar shape to the XRT one, excluding the time of the actual peak, where there is a gap in XRT data. The peak occurring in XRT and AIA before in NuSTAR could be explained by the position of this source on NuSTAR's detectors. As this event was captured close to the edge of NuSTAR's FOV (more-so in FPMB than FPMA), NuSTAR may have lost some of the counts from the beginning of this event. This loss of data could be the cause of the later peak in NuSTAR.

### 6.2.6 Event 6

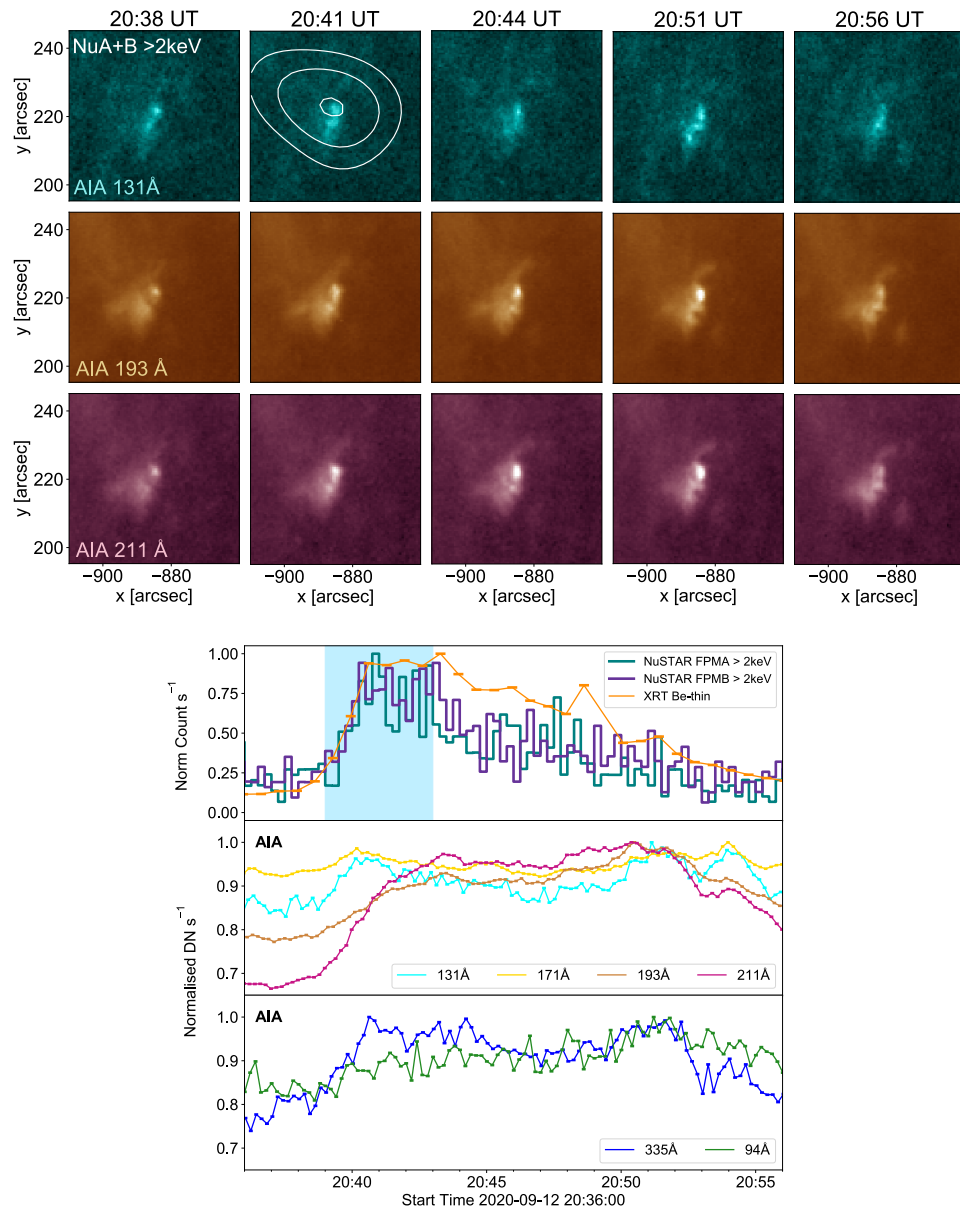
Later in the 12–13 September 2020 observation, another brightening was captured by NuSTAR in Orbit 8, at around 20:40 UT. AIA images showing the EUV evolution of this event, located at  $(-880'', 220'')$ , can be found in Figure 6.6. From these, it can be seen that the brightening region has a dot-like structure, which exhibits heightened EUV emission for an extended period of time between 20:40 and 20:50 UT, particularly in the 193 and 211 Å channels.

Figure 6.6 also displays the time profiles of this event. From these, it can be seen that increased HXR emission was detected by NuSTAR starting just after 20:35 UT, reaching a peak at 20:40 UT. This peak is followed by a slower decay until around 20:55 UT. The SXR lightcurve from XRT shows a very similar profile to NuSTAR, with the emission rising, peaking, and decaying concurrently in both instruments. Out of the AIA channels, this event was observed most clearly in the 193, 211, and 335 Å channels. In these channels, the lightcurves begin to rise at the same time as the X-ray ones, reaching peaks slightly later at around 20:43 UT. The time profiles then flatten out, only beginning to fall off just after 20:50 UT. Again, the X-ray peak preceding the EUV peak is indicative of cooling plasma.

### 6.2.7 Event 7

The weakest of the impulsive events occurred in Orbit 10 of the 12–13 September 2020 observation, with NuSTAR detecting a faint brightening at  $(-830'', 190'')$  just after 00:00 UT. AIA images showing the evolution of this event in EUV can be found in Figure 6.7. From these, it can be seen that this event is extremely small in scale, even when compared to the other six events.

## 6.2 Event Summaries



**Figure 6.6:** A summary of Event 6. Top panel: AIA panels showing the EUV evolution of Event 6. The NuSTAR contours are from 2 minute intervals centred on the time of the AIA images, and are plotted at 0.0020, 0.0025, and 0.0030 counts  $s^{-1}$ . Bottom panel: (top) NuSTAR (FPMA and FPMB) and XRT, and AIA (bottom two rows), time profiles for Event 6. The blue shaded region indicates the time range chosen for spectral analysis in Section 6.3.6.

## 6.2 Event Summaries

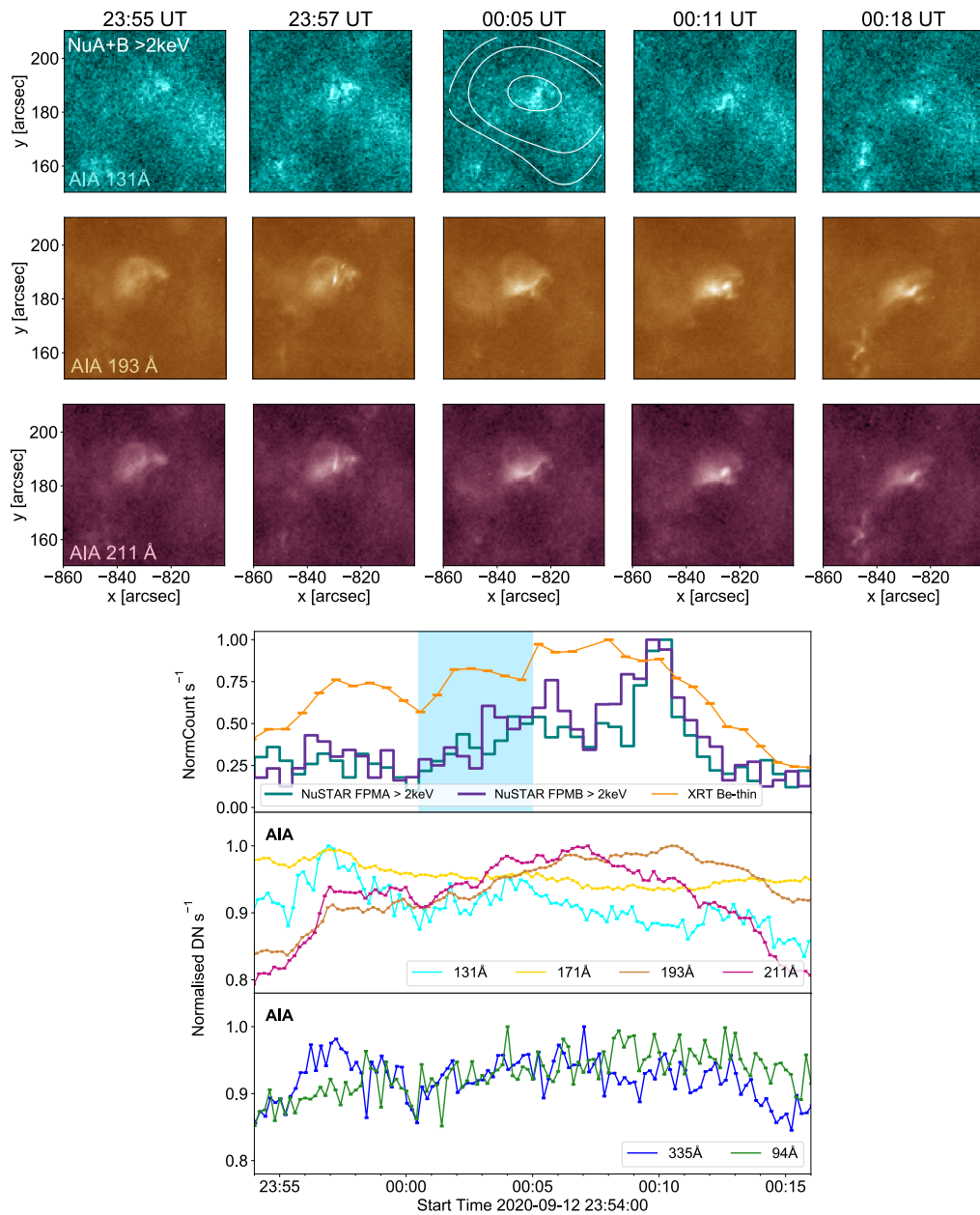


**Figure 6.7:** A summary of Event 7. Top panel: AIA panels showing the EUV evolution of Event 7. The NuSTAR contours are from 2 minute intervals centred on the time of the AIA images, and are plotted at 0.0008, 0.0010, and 0.0015 counts s<sup>-1</sup>. Bottom panel: (top) NuSTAR (FPMA and FPMB) and XRT, and AIA (bottom two rows), time profiles for Event 7. The blue shaded region indicates the time range chosen for spectral analysis in Section 6.3.7.

### 6.3 NuSTAR Spectral Analysis

The time profiles for this event are also shown in Figure 6.7. In NuSTAR and XRT, there is heightened emission between 00:00 UT and 00:15 UT. In AIA, this event is only really obvious in the 193 and 211 Å channels, the time profiles of which show a similar shape as XRT. The NuSTAR lightcurve peaks most strongly at 00:10 UT. However, this peak is the result of a ghost ray flash due to activity from outside NuSTAR’s FOV. This peak was observed across all of the detectors and is therefore not associated with this event.

## 6.3 NuSTAR Spectral Analysis

In order to investigate the thermal properties of these events, we performed NuSTAR spectral analysis using XSPEC, following the method detailed in Section 3.2.2. The time intervals that the NuSTAR spectra were fitted over are highlighted in the lightcurve plots for all of the events in Section 6.2. Table 6.2 gives a summary of the results of the spectral fitting for these events.

### 6.3.1 Event 1

For Event 1, summarised in Section 6.2.1, a single time range from 11:50:10–11:51:40 UT was chosen to fit the NuSTAR spectrum over. This time range, highlighted on the time profile plot in Figure 6.1, covers the NuSTAR rise, and most of the decay until the data gap. This time range was not split into separate intervals for the rise and decay because the chosen time interval is already very short (shorter than a 100 s mosaic pointing), and this event is faint in NuSTAR. Shortening the time range would only produce noisy spectra that would be tricky to fit.

The result of fitting the NuSTAR spectrum for Event 1 is shown in Figure 6.8. It can be seen that this spectrum is adequately fit with an isothermal model with a temperature of 3.91 MK and an emission measure of  $2.25 \times 10^{43} \text{ cm}^{-3}$ . There is not any evidence of any hotter or non-thermal component here.

### 6.3.2 Event 2

For the mini-filament eruption captured on 21 February 2020, we fitted the NuSTAR spectrum over several different time ranges. Firstly, we fitted the spectrum over a time range which covered the entire HXR spike, from 16:44:20–16:46:00 UT, with an isothermal model.

### 6.3 NuSTAR Spectral Analysis

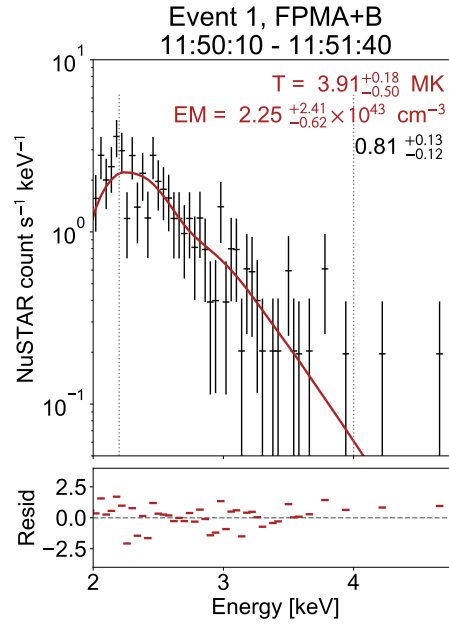


**Figure 6.8:** NuSTAR FPMA+B spectrum for Event 1, fitted over 11:50:10–11:51:40 UT (shown in Figure 6.1, bottom panel), with an isothermal model (red; parameters marked on plot). Dashed lines indicate fitting range, and residuals are shown in the bottom panel.

The resulting fit can be found in Figure 6.9 (top left panel). The fit parameters for this model are  $T = 4.03$  MK and  $EM = 3.96 \times 10^{43} \text{ cm}^{-3}$ . However, there does appear to be a small excess at energies  $> 4$  keV, indicating the presence of hotter and/or non-thermal emission. This isothermal temperature, as well as the excess indicating potentially even higher temperatures in this event, is consistent with the detection in the AIA Fe XVIII channel (as seen in Figure 6.2), which is sensitive to material at 4–10 MK.

We therefore also tried fitting this spectrum with a double thermal model. For this, both components were free to vary. To start, only the lower temperature component was fitted over lower energies from 2.2–2.9 keV. This component was then fixed, and the higher temperature component was fitted over 2.2–5.0 keV. The resulting fit is also shown in Figure 6.9 (bottom panel). It can be seen that the cooler component has a temperature and emission measure of 3.4 MK and  $7.2 \times 10^{43} \text{ cm}^{-3}$ , respectively. The second thermal component has a higher temperature of 5.1 MK, and a corresponding emission measure of  $2.9 \times 10^{42} \text{ cm}^{-3}$ . This result indicates the presence of emission  $> 5$  MK during the mini-filament eruption, consistent with the detection of this event in AIA Fe XVIII.

We also tried splitting the event into two separate phases: impulsive and decay. We took the impulsive phase to be from 16:44:10–16:45:10 UT (shaded blue in Figure 6.2) and the

### 6.3 NuSTAR Spectral Analysis

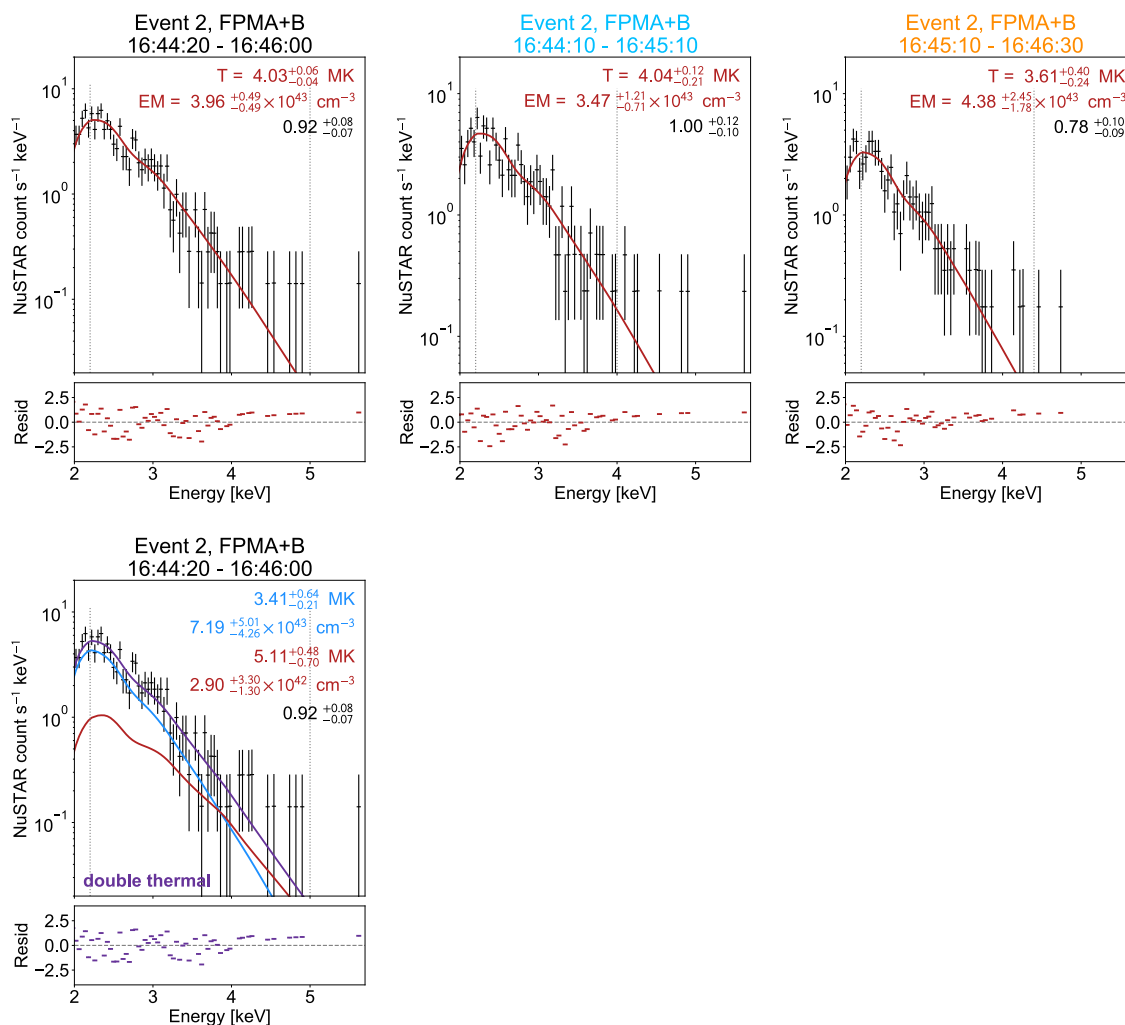


**Figure 6.9:** (Top row) NuSTAR FPMA+B spectra for Event 2, fitted over the whole NuSTAR spike (left) and the impulsive and decay phases (middle and right, respectively), with isothermal models (red; parameters marked on plot). (Bottom) NuSTAR spectrum from the whole flaring time, fitted with a double thermal model. For all spectra, dashed lines indicate fitting range, and residuals are shown in the bottom panel.

### 6.3 NuSTAR Spectral Analysis

decay phase to be from 16:45:10–16:46:30 UT (shaded orange). The NuSTAR FPMA + FPMB spectra from both of these time intervals were fitted with isothermal models, as shown in Figure 6.9 (top middle and right). During the impulsive phase, the temperature is 4.04 MK (with a corresponding emission measure of  $3.47 \times 10^{43} \text{ cm}^{-3}$ ). The temperature is lower during the decay, lying at 3.61 MK, but the emission measure is slightly higher at  $4.38 \times 10^{43} \text{ cm}^{-3}$ . This indicates that hotter material is present during the initial HXR rise compared to when the NuSTAR time profile falls off. However, it should be noted that neither the temperature nor the emission measure change significantly between the two phases when uncertainties are taken into account.

As was the case in the spectrum for the full time range, the spectrum for only the impulsive phase does show a small excess at energies  $> 4$  keV. However, due to the faintness and short duration of this phase, a reliable fit could not be obtained to the spectrum with a double thermal model.

#### 6.3.3 Event 3

For Event 3, the NuSTAR emission exhibits a complex time profile with three distinct peaks. For this flare, we fitted the NuSTAR spectrum separately for all three of the peaks in order to investigate its time evolution. The time ranges chosen, which are marked on the lightcurve plot in Figure 6.3 and are all 150 s long, are as follows: 22:00:30–22:03:00 UT (blue), 22:03:00–22:05:30 UT (orange), and 22:05:30–22:08:00 UT (pink). The spectra from all three of these time intervals were fitted with isothermal models, with the results shown in Figure 6.10.

Throughout this flare, the NuSTAR spectra indicate that progressively lower temperatures are present. During the first (and largest) HXR peak, the isothermal model fitted to the NuSTAR spectrum has a temperature of 3.60 MK. During the following two peaks, the fit temperature drops to 3.37 MK, and then to 3.05 MK. This is accompanied by an increase in emission measure from  $1.98 \times 10^{43} \text{ cm}^{-3}$  during the initial peak, and then to 2.40 and  $5.23 \times 10^{43} \text{ cm}^{-3}$  during the second and third peaks, respectively.

However, it should be noted that the temperature and emission measure do not change significantly between the first and second NuSTAR peaks when the error bars are taken into consideration. Only during the third peak do these move outside the error ranges from the other two times. We can therefore conclude that the hottest material is present at the beginning of the flare, during the initial HXR spike. The NuSTAR spectral analysis

### 6.3 NuSTAR Spectral Analysis

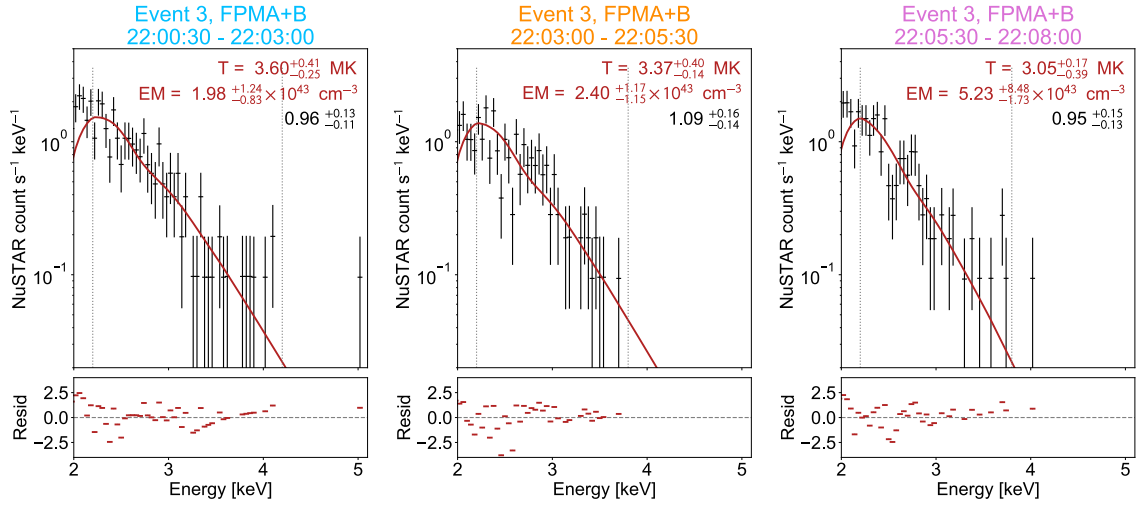


**Figure 6.10:** NuSTAR FPMA+B spectra for Event 3, fitted over three separate time intervals for the three X-ray peaks (shown in Figure 6.3, bottom panel). These are fitted with isothermal models (red; parameters marked on plot). Dashed lines indicate fitting range, and residuals are shown in the bottom panel.

suggests that, during the subsequent peaks, there is less material heated to temperatures  $> 3$  MK.

It can also be seen that the spectra from all three times are fitted well by the isothermal models. There are no significant excesses indicating the presence of hotter or non-thermal emission.

#### 6.3.4 Event 4

The NuSTAR and XRT lightcurves for Event 4 (see Figure 6.4) show three distinct spikes. Therefore, we fitted the NuSTAR HXR spectra for three time intervals covering these peaks. These time ranges, indicated on the time profiles in Figure 6.4, are as follows: 12:41:00–12:43:00 UT (blue; the time of the initial largest NuSTAR peak), 12:43:30–12:45:30 UT (orange), and 12:45:40–12:47:40 UT (pink). The spectra from these times, fitted with isothermal models, are shown in Figure 6.11.

It can be seen that an isothermal model fits all three spectra adequately, with no evidence of any hot or non-thermal component. The fit temperature varies throughout this event, beginning at 3.34 MK during the first peak and dropping to 3.22 MK for the second. The fit temperature then increases to 3.52 MK during the third peak. However, the uncertainties on these three temperatures overlap such that there is not any clear temperature

### 6.3 NuSTAR Spectral Analysis

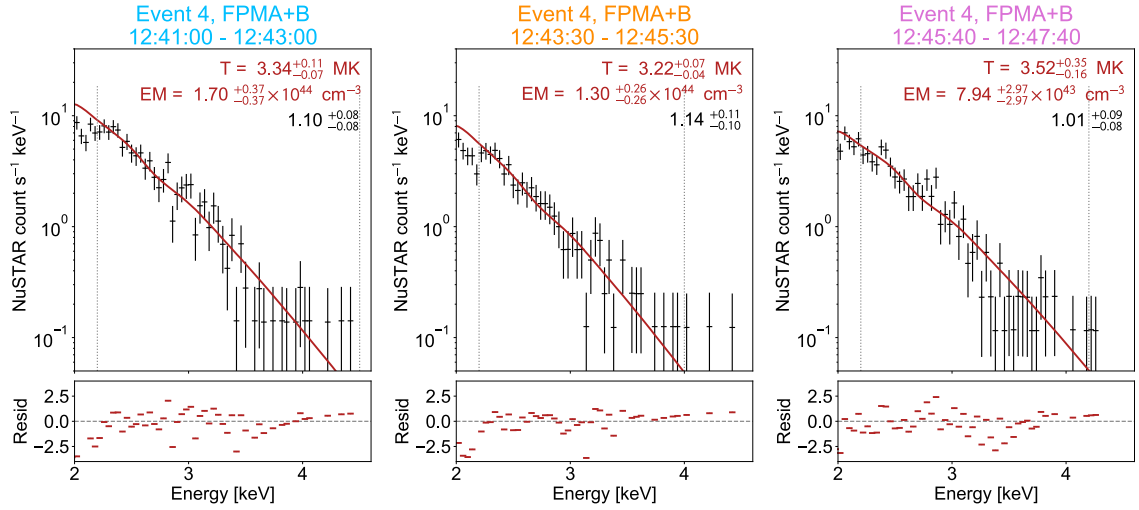


**Figure 6.11:** NuSTAR FPMA+B spectra for Event 4, fitted over three separate time intervals for the three X-ray peaks (shown in Figure 6.4, bottom panel). These are fitted with isothermal models (red; parameters marked on plot). Dashed lines indicate fitting range, and residuals are shown in the bottom panel.

change between the largest initial peak and the other two. The emission measure drops throughout from  $1.70 \times 10^{44} \text{ cm}^{-3}$  between the first two peaks, and then to  $7.94 \times 10^{43} \text{ cm}^{-3}$  during the third. This is consistent with the initial spike being the brightest in NuSTAR and XRT. The emission measure at this time is higher than for any of the other events investigated in this chapter.

#### 6.3.5 Event 5

Event 5 was captured on the very edge of NuSTAR's FOV, meaning that some of the counts were lost. This problem is more severe in FPMB, and so we only considered FPMA for the NuSTAR spectroscopy of this flare. We fitted the NuSTAR spectrum over 17:17:30–17:19:30 UT (shaded in blue on the time profile plot in Figure 6.5), covering the time of the NuSTAR peak. Figure 6.12 shows the results of fitting this spectrum with an isothermal model.

The NuSTAR spectral fitting for Event 5 indicates that this flare has a temperature of 3.41 MK, with an emission measure of  $7.80 \times 10^{43} \text{ cm}^{-3}$ . There is no evidence of any hot or non-thermal components in this spectrum.

### 6.3 NuSTAR Spectral Analysis

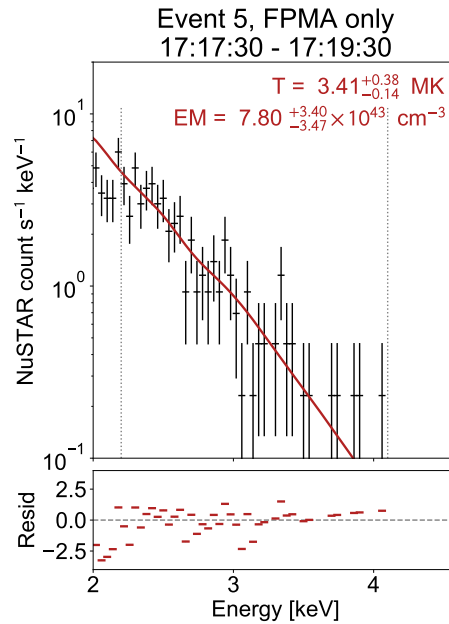


**Figure 6.12:** NuSTAR FPMA spectrum for Event 5, fitted over 17:17:30–17:19:30 UT (shown in Figure 6.5, bottom panel), with an isothermal model (red; parameters marked on plot). Dashed lines indicate fitting range, and residuals are shown in the bottom panel.

#### 6.3.6 Event 6

For Event 6, a single time interval around the NuSTAR peak, from 20:39:00–20:43:00 UT was used for the spectral fitting. The NuSTAR spectrum from this time, fitted with an isothermal model, is shown in Figure 6.13. It can be seen that the resulting model has a temperature of 3.26 MK and an emission measure of  $2.15 \times 10^{43} \text{ cm}^{-3}$ . As for most of the previous events, there are no clear hot or non-thermal components present in this spectrum. We also tried fitting this spectrum over shorter time intervals (from 20:39:00–20:41:00 UT and 20:41:00–20:43:00 UT, covering the impulsive phase and the beginning of the decay). However, the fit temperature and emission measure were not found to change significantly between these two times, so we used the longer time range in order to obtain a spectrum with more counts that could be more reliably fit.

#### 6.3.7 Event 7

Event 7 is the faintest of the NuSTAR quiet Sun flares investigated here. This results in a noisy NuSTAR spectrum which is difficult to fit. This event is further complicated by the ghost ray spike which NuSTAR detected across all detector quadrants at  $\sim 00:10:00$  UT.

## 6.4 DEM Analysis

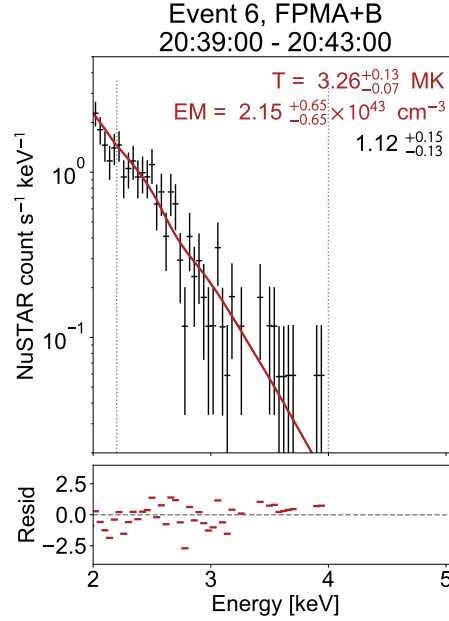


**Figure 6.13:** NuSTAR FPMA+B spectrum for Event 6, fitted over 20:39:00–20:43:00 UT (shown in Figure 6.6, bottom panel), with an isothermal model (red; parameters marked on plot). Dashed lines indicate fitting range, and residuals are shown in the bottom panel.

Therefore, we fitted the HXR spectrum from 00:00:30 (when the NuSTAR emission began to increase) to 00:05:00 UT (just before the ghost ray event began).

The fitted NuSTAR spectrum for Event 7 is shown in Figure 6.14. The spectrum was fitted with an isothermal model with a temperature and emission measure of 3.35 MK and  $7.78 \times 10^{42} \text{ cm}^{-3}$ . This emission measure is very small, even in comparison to the previous events analysed in this chapter, reflecting the faintness of this flare.

## 6.4 DEM Analysis

NuSTAR spectroscopy for the mini-filament eruption (Event 2, see Section 6.3.2) suggests the presence of emission at temperatures  $> 4$  MK. DEM analysis can be used to confirm whether material was heated to these temperatures during this event.

In order to compare the multi-thermal properties of all of the impulsive events and to see if the DEM of the mini-filament eruption differed from the others, we reconstructed their DEMs using the approach detailed in Section 3.2.3. We did this over the time ranges shaded in blue in each of the lightcurve plots in Section 6.2. These are the same times

## 6.4 DEM Analysis

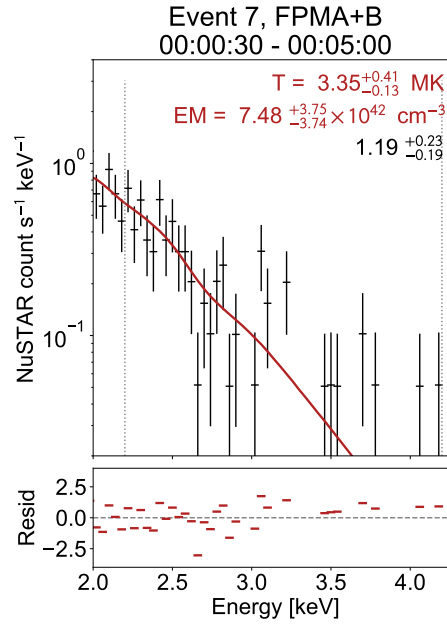


**Figure 6.14:** NuSTAR FPMA+B spectrum for Event 7, fitted over 00:00:30–00:05:00 UT (shown in Figure 6.7, bottom panel), with an isothermal model (red; parameters marked on plot). Dashed lines indicate fitting range, and residuals are shown in the bottom panel.

used for the spectral fitting in Section 6.3. In the cases where the spectra were fitted for multiple time intervals (Events 2, 3, and 4), we calculated the DEM for the time of strongest NuSTAR emission. XRT data was available for the events observed on 12–13 September 2020, but not for those observed on 21 February 2020. Therefore, while the September 2020 events’ DEMs were calculated using data from AIA, XRT, and NuSTAR, the February 2020 ones were calculated with only AIA and NuSTAR data.

The resulting DEMs are plotted together in Figure 6.15, allowing comparison between the events. It is immediately apparent that the DEMs for all seven events have similar shapes, all peaking at similar magnitudes at temperatures between  $\log(T) \sim 6.2$ – $6.3$ . Out of all of the events, the DEM for Event 2 (the mini-filament eruption) peaks at the highest temperature at  $\log(T) \sim 6.3$ . This is consistent with its NuSTAR spectrum being the only one indicating the presence of temperatures  $> 4$  MK. The DEM for the smallest of the flares, Event 7, peaks at the lowest temperature, just below  $\log(T) \sim 6.2$ . These quiet Sun flare DEMs peak at higher temperatures than those of typical X-ray bright points observed with NuSTAR (for examples, see Sections 4.2.2 and 5.3.2), which peak closer to  $\log(T) \sim 6.15$ .

In comparison with the other two events observed on 21 February 2020 (and with the

## 6.4 DEM Analysis

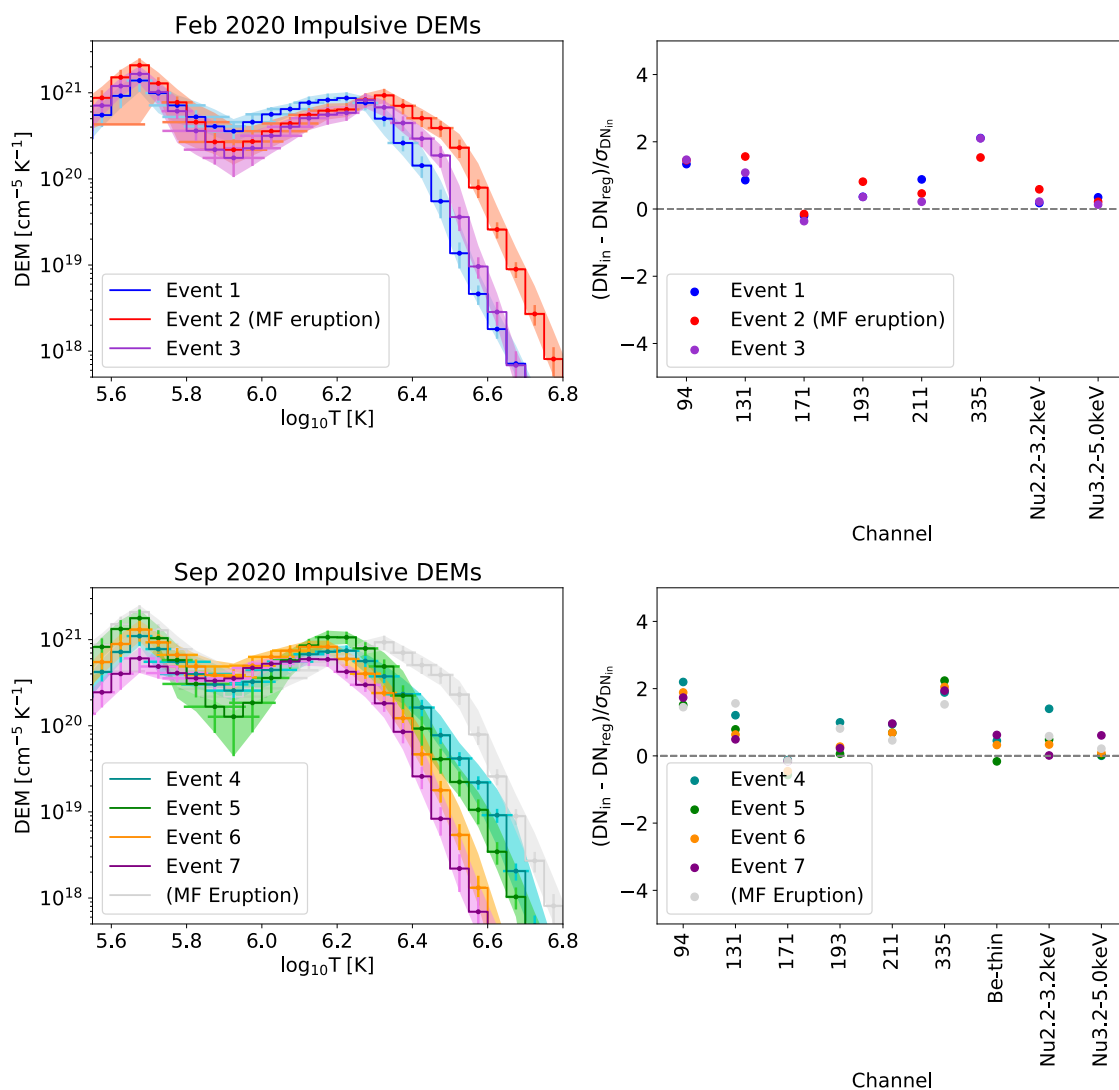


**Figure 6.15:** DEMs reconstructed for the impulsive events observed in February 2020 (top) and September 2020 (bottom). These were calculated using AIA and NuSTAR data only for the February 2020 ones, and AIA, NuSTAR, and XRT for the September 2020 ones. The February 2020 mini-filament eruption DEM is shown on the September 2020 plot for comparison. The plots on the right show the normalised residuals.

## 6.5 Correlation Between AIA and NuSTAR

events from September 2020), it is clear that the mini-filament eruption has more material at  $\log(T) > 6.3$ . The initial fall-off from the peak between  $\log(T) = 6.3$ – $6.55$  is flatter than for the other DEMs. The temperature of the cooler component in the NuSTAR double thermal spectral fit (3.5 MK; see Figure 6.9, bottom panel) lies in this range. At hotter temperatures, the DEM begins to fall off more sharply. The DEM does confirm the presence up material heated to  $\sim 5$  MK, as expected from the spectral analysis. At  $\log(T) = 6.7$  (5 MK), the DEM for the mini-filament eruption is more than an order of magnitude greater than for the other two February 2020 flares, demonstrating that this high temperature component is much stronger for the eruption.

The NuSTAR spectroscopy for Events 1 and 3 gave similar results (see Figures 6.8 and 6.10;  $T = 3.9$  MK for Event 1 and  $T = 3.6$  MK for Event 3, and  $EM \sim 2 \times 10^{43} \text{ cm}^{-3}$  for both). This is reflected in the DEMs for the two flares being very similar. The DEM for Event 1 peaks at a marginally lower temperature and exhibits a slightly flatter decay. This is consistent with the fit temperature for this event being a little higher.

The DEMs for the small flares observed on 12–13 September are plotted in the bottom row of Figure 6.15. The NuSTAR spectral fits for these flares (see Figures 6.11, 6.12, 6.13, and 6.14) all gave temperatures lying in the narrow range 3.2–3.4 MK. All four DEMs fall off at similar rates, reflecting this. Event 4 had the highest emission measure ( $1.7 \times 10^{44} \text{ cm}^{-3}$ ), and its DEM is higher than the other three for  $\log(T) > 6.3$ . The DEM for Event 7, the faintest of the quiet Sun flares (with an emission measure of  $7.5 \times 10^{42} \text{ cm}^{-3}$ ), is the lowest of all of the events for  $\log(T) > 6.0$ . This DEM is similar to the one for Event 6, which had only a slightly higher emission measure of  $2.2 \times 10^{43} \text{ cm}^{-3}$ . The DEMs for both Events 6 and 7 also fall off at lower temperatures than any of the February 2020 events.

It is worth noting that for all of the events from 12–13 September 2020, the DEM solutions had smaller residuals when the XRT response was used without multiplying it by a factor of two. This behaviour is opposite to what was found for all of the other DEM analysis in this thesis.

## 6.5 Correlation Between AIA and NuSTAR

It is interesting to compare the AIA and NuSTAR fluxes for this event to determine whether the EUV and X-ray emission from the seven events is correlated, which would indicate consistent patterns of heating. For each of the AIA channels, Figure 6.16 plots the AIA flux from the flaring regions against the flux in the NuSTAR 2.2–3.2 keV band. Similar plots

## 6.6 Non-Thermal Upper Limits

are also shown in Figure 6.17, only for a higher NuSTAR energy band, 3.2–5.0 keV. The plotted data values are the same ones that were used in the DEM calculations detailed in Section 6.4.

For the lower energy band (2.2–3.2 keV), none of the AIA channels are perfectly correlated with NuSTAR. The channel that is least correlated with NuSTAR is 171 Å, for which there is no clear relation between the two. This suggests that the 171 Å channel is dominated by plasma at different (lower) temperatures to NuSTAR for these events. There is a slight correlation between NuSTAR and the 131 Å channel, as well as the 335 Å channel, which has a broad temperature response. The AIA channels that show the strongest correlation with NuSTAR are 94 and 211 Å.

The same plots for the higher NuSTAR energy band (Figure 6.17), reveal that most of the AIA channels are not strongly correlated with the higher energy X-rays. Again, the strongest correlation with NuSTAR is seen in the 94 and 211 Å channels. However, there are outlying points for each (Event 6 for 94 Å and Event 4 for 211 Å). As was the case with the lower energy band, the weakest correlation is with the 171 Å channel. Again, the remaining three channels exhibit a slight correlation with NuSTAR. For both energy bands, the 193 Å channel is weakly correlated with NuSTAR for the faintest four NuSTAR events, after which the correlation plot plateaus.

Event 7 is the faintest event in NuSTAR in both energy bands, and it is also the faintest event in five of the six AIA channels. The exception is 171 Å, which in general showed no correlation with NuSTAR, suggesting that this channel is observing material at different temperatures to NuSTAR. The mini-filament eruption (Event 2) is not the strongest event in the low energy NuSTAR band (it is weaker only than Event 4). However, this event did produce the greatest flux in the higher energy band, which is consistent with more high temperature emission being present for this event. It can be seen that the mini-filament eruption produced a stronger flux in the 131 Å channel compared to the other events. This implies that the 131 Å channel must be observing the hotter material that was present in this event.

## 6.6 Non-Thermal Upper Limits

None of the events produced NuSTAR spectra which showed evidence of a non-thermal component. However, we calculated upper limits on the non-thermal emission that could be present and remain consistent with a null detection (or with the observed excess in the

## 6.6 Non-Thermal Upper Limits

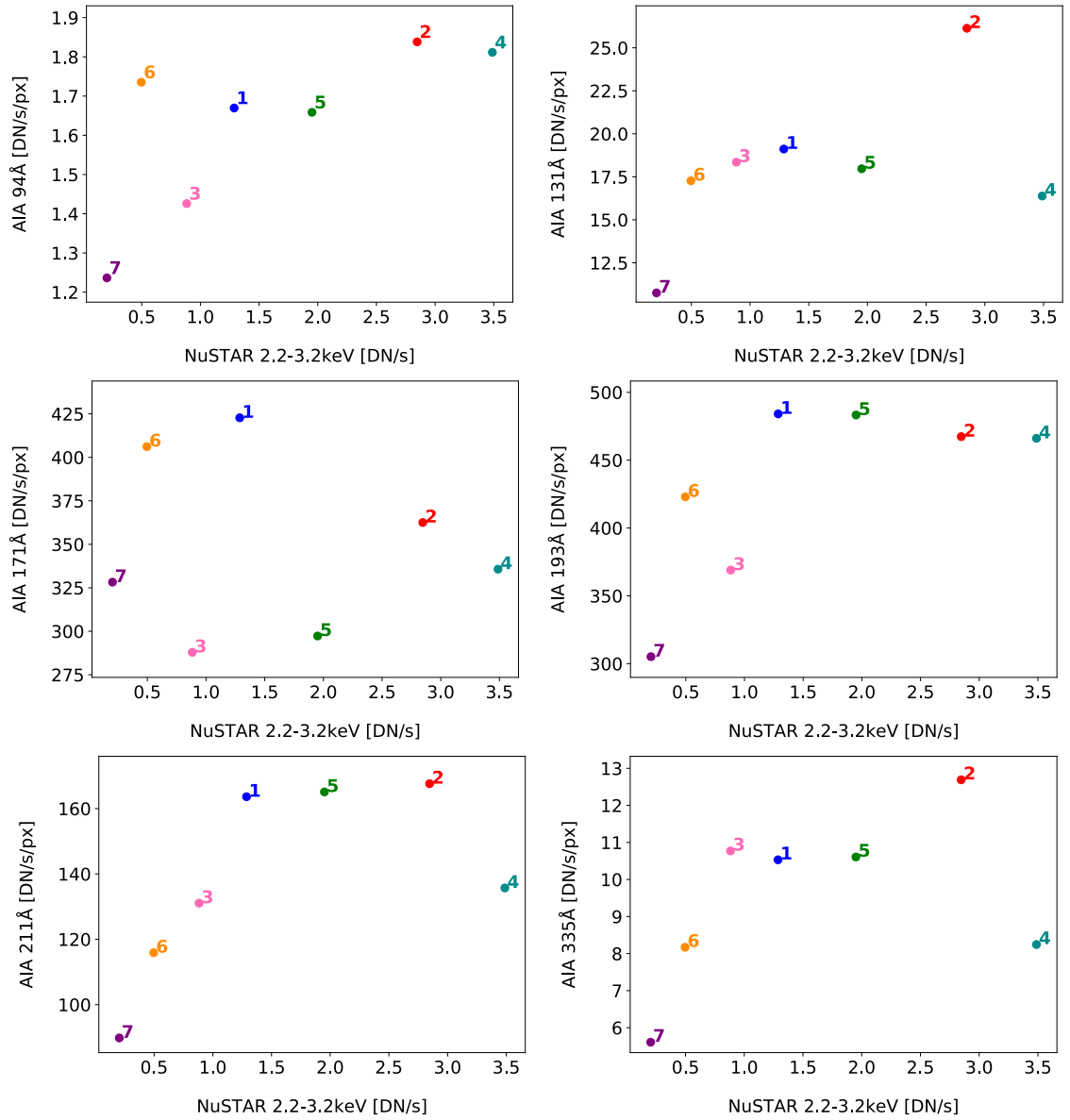


**Figure 6.16:** Plots of the flux in each of the AIA channels against the flux in the NuSTAR 2.2–3.2 keV energy band for the seven impulsive events. These are the same values used to calculate the DEMs in Section 6.4.

## 6.6 Non-Thermal Upper Limits

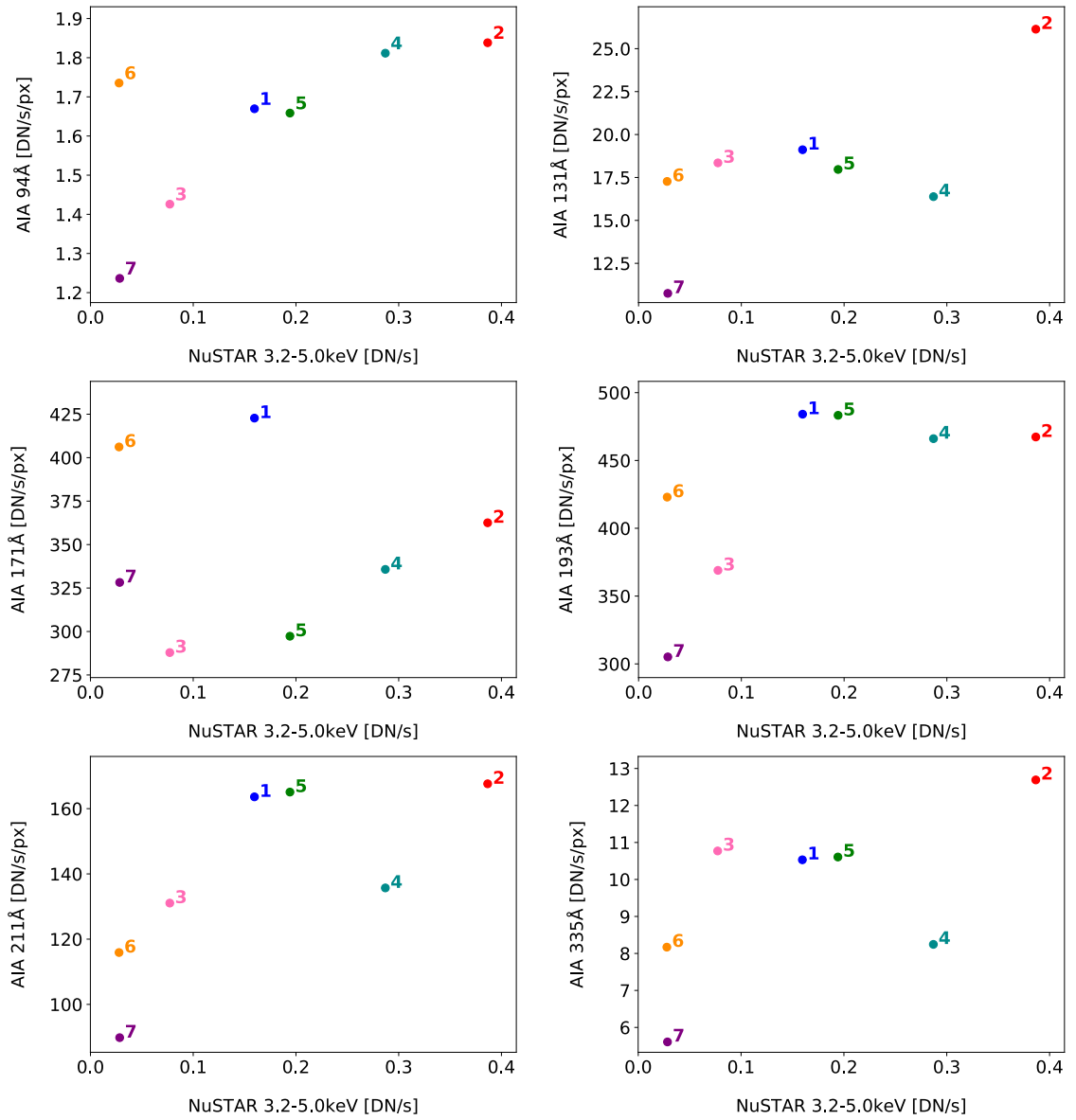


**Figure 6.17:** Plots of the flux in each of the AIA channels against the flux in the NuSTAR 3.2–5.0 keV energy band for the seven impulsive events. These are the same values used to calculate the DEMs in Section 6.4.

## 6.6 Non-Thermal Upper Limits

**Table 6.2:** A summary of the properties of all of the quiet Sun flares, including the temperatures and emission measures found from the spectral fitting in Section 6.3, as well as the thermal energies calculated from these fit parameters. The heating requirements were calculated by dividing the thermal energy by the duration of the event. All values are for the time ranges shaded blue in the lightcurve plots in Section 6.2.

Event	Area	Temperature (MK)	Emission Measure ( $\times 10^{43} \text{ cm}^{-3}$ )	Thermal Energy ( $\times 10^{25} \text{ erg}$ )	Heating Requirement ( $\times 10^{23} \text{ erg s}^{-1}$ )
1	4" $\times$ 3"	3.91 <sup>+0.18</sup> <sub>-0.50</sub>	2.25 <sup>+2.41</sup> <sub>-0.62</sub>	3.07 <sup>+2.42</sup> <sub>-2.09</sub>	3.41 <sup>+2.02</sup> <sub>-1.74</sub>
2	8" $\times$ 3"	4.04 <sup>+0.12</sup> <sub>-0.21</sub>	3.47 <sup>+1.21</sup> <sub>-0.71</sub>	6.62 <sup>+1.30</sup> <sub>-1.02</sub>	11.0 <sup>+2.16</sup> <sub>-1.71</sub>
3	7" $\times$ 4"	3.60 <sup>+0.41</sup> <sub>-0.25</sub>	1.98 <sup>+1.24</sup> <sub>-0.83</sub>	5.00 <sup>+0.90</sup> <sub>-1.46</sub>	3.34 <sup>+0.60</sup> <sub>-0.97</sub>
4	4" $\times$ 4"	3.34 <sup>+0.11</sup> <sub>-0.07</sub>	17.0 <sup>+3.70</sup> <sub>-3.70</sub>	8.94 <sup>+1.25</sup> <sub>-0.91</sub>	7.45 <sup>+1.04</sup> <sub>-0.76</sub>
5	5" $\times$ 4"	3.41 <sup>+0.38</sup> <sub>-0.14</sub>	7.80 <sup>+3.40</sup> <sub>-3.47</sub>	7.31 <sup>+2.43</sup> <sub>-2.09</sub>	6.09 <sup>+2.02</sup> <sub>-1.74</sub>
6	3" $\times$ 4"	3.26 <sup>+0.13</sup> <sub>-0.07</sub>	2.15 <sup>+0.65</sup> <sub>-0.65</sub>	2.50 <sup>+0.47</sup> <sub>-0.46</sub>	1.04 <sup>+0.19</sup> <sub>-0.19</sub>
7	8" $\times$ 5"	3.35 <sup>+0.41</sup> <sub>-0.13</sub>	0.75 <sup>+0.38</sup> <sub>-0.37</sub>	3.74 <sup>+1.42</sup> <sub>-1.20</sub>	1.39 <sup>+0.53</sup> <sub>-0.44</sub>

case of the mini-filament eruption) in NuSTAR. This was done for each event following the approach of Section 3.2.4, and the resulting upper limits were then compared to the thermal energy of the event. The time ranges used for this analysis are the same as those used to calculate the DEMs, and are shaded blue in all of the time profile plots in Section 6.2.

For all of the events, the area was chosen from AIA images such that only the small brightening region was enclosed. The thermal energy was then calculated using the fit temperature and emission measure and the volume ( $A^{\frac{3}{2}}$ ) using Equation 3.10. The results of this calculation for all of the events are summarised in Table 6.2. The areas were chosen from the AIA images such that only the brightest region was enclosed. These chosen areas are highlighted on the AIA 211 Å images on the left-hand panel of all rows in Figures 6.18 and 6.19. Selecting the areas was straightforward in all cases except for Event 5, in which two separate regions brightened in AIA (as demonstrated in Figure 6.19, second row, left panel). However, as both the NuSTAR and XRT lightcurves agree with the behaviour of the brightest of the two regions in AIA (the one on the right), then this part was taken to be the origin of the HXR emission.

## 6.6 Non-Thermal Upper Limits

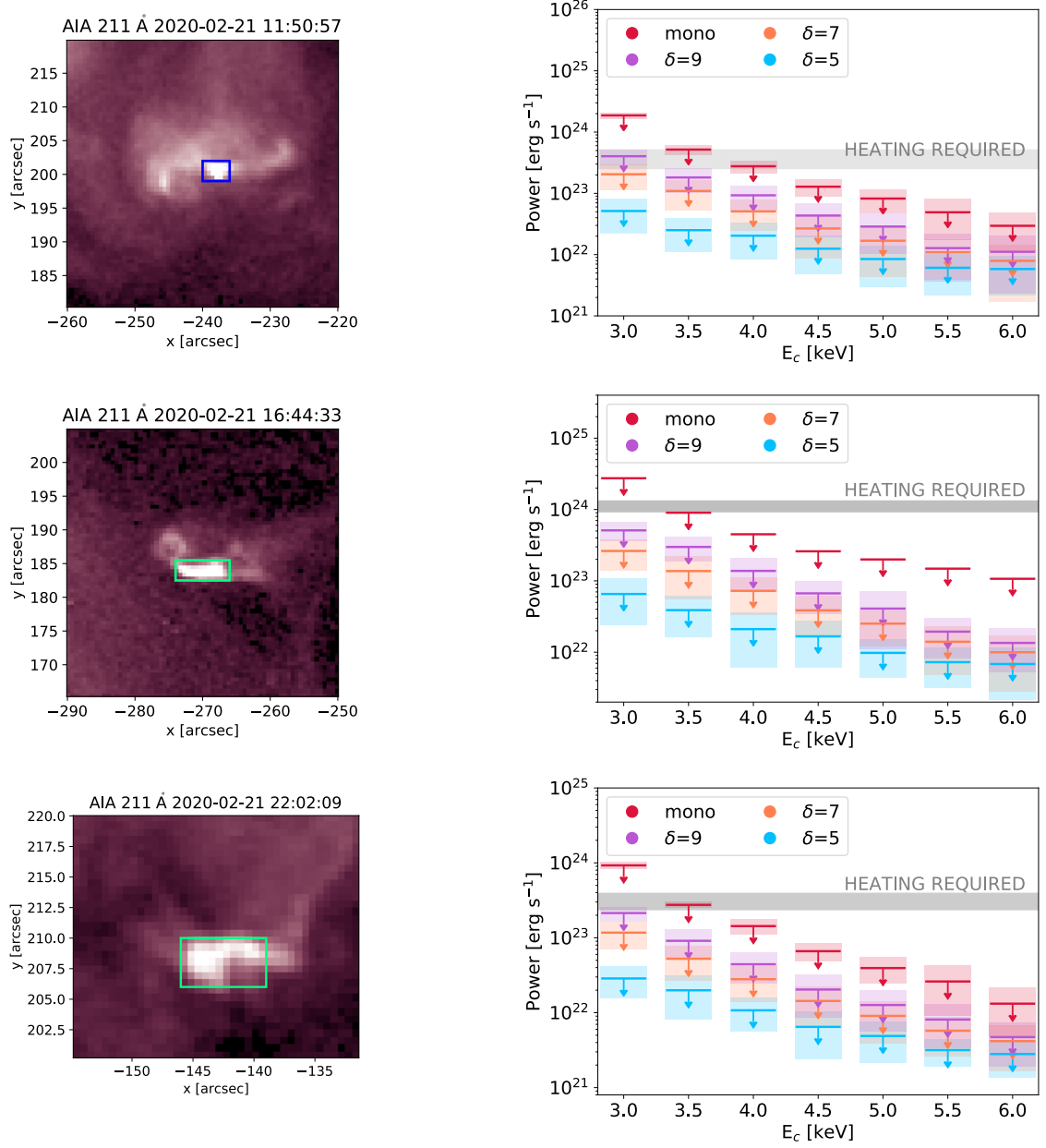


**Figure 6.18:** Non-thermal upper limits for Events 1–3 (from top to bottom row). (Left) AIA images showing the area used for calculating the thermal energy. (Right) Upper limits on the non-thermal emission for the event for a range of power law indices. The shaded regions indicate the  $\pm 1\sigma$  range, and the grey line indicates the heating requirement dictated by the thermal energy.

## 6.6 Non-Thermal Upper Limits

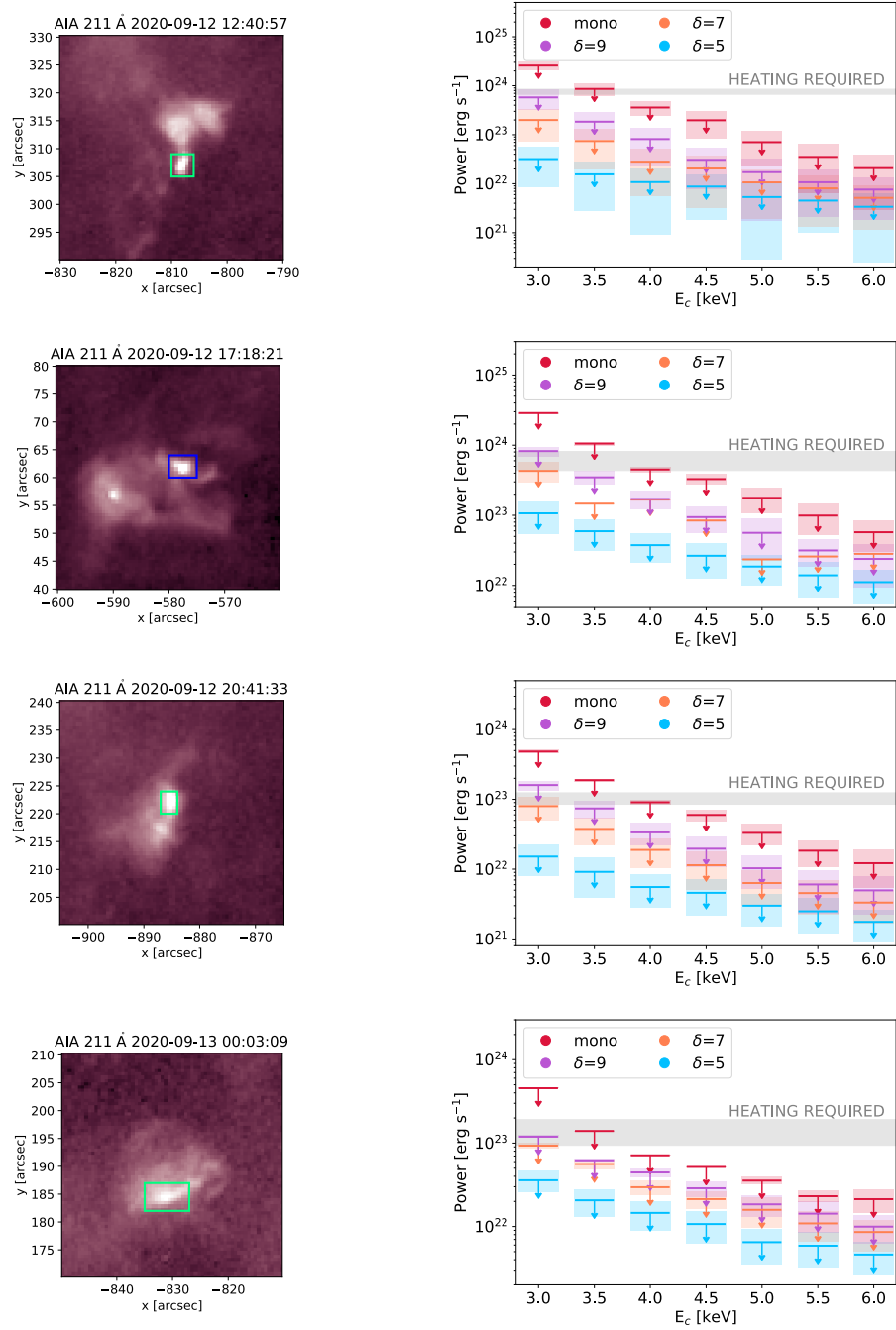


**Figure 6.19:** Non-thermal upper limits for Events 4–7 (from top to bottom row). (Left) AIA images showing the area used for calculating the thermal energy. (Right) Upper limits on the non-thermal emission for the event for a range of power law indices. The shaded regions indicate the  $\pm 1\sigma$  range, and the grey line indicates the heating requirement dictated by the thermal energy.

## 6.7 Summary and Conclusions

As was seen in Figure 6.9, the NuSTAR spectrum of the mini-filament eruption from a time range covering the whole peak (16:44:20–16:46:00 UT) could be fitted with a double thermal model with a hot component at  $\sim 5$  MK. However, during the impulsive phase (from 16:44:10–16:45:10 UT), the spectrum was too noisy to obtain a reliable fit with two thermal models, and was instead fitted with an isothermal model. Therefore, in this analysis, we use the result from the impulsive phase with the isothermal fit, and find non-thermal upper limits consistent with the observed excess. This excess in the observed spectrum compared to the model was found to be 6 counts between 4–6 keV.

The calculated thermal energies (summarised in Table 6.2) ranged from  $(3\text{--}9) \times 10^{25}$  erg. When divided by the event durations, the required heating power was of the order  $10^{23}\text{--}10^{24}$  erg s $^{-1}$ . These were compared to the calculated non-thermal upper limits, as shown in the right-hand panel for each event in Figures 6.18 and 6.19. It can be seen that, while the heating requirements and the values of the non-thermal upper limits vary, the conclusion as to whether the heating could have been produced by the non-thermal component is consistent across the events. For all seven, a mono-energetic non-thermal distribution between 3–3.5 keV could provide the observed heating. In the case of the mini-filament eruption (Event 2; shown in Figure 6.18, middle row), these are the only combinations that satisfy the requirement. For some of the other events (1, 5, 6, and 7), there are more non-thermal upper limits (for  $\delta \geq 7$  and  $E_C \sim 3$  keV) that are greater than the heating requirement.

In general, it can be concluded that, while a non-thermal component could have powered the heating for all of these events, this component would have to be practically mono-energetic between 3–4 keV. This is similar to the result that was found for the jet observed in the 28 September 2018 mosaics, as shown in Section 4.3.

## 6.7 Summary and Conclusions

In this chapter, we investigated the evolution and multi-thermal properties of seven small brightenings in the quiet Sun observed in the NuSTAR dwell observations from 21 February and 12–13 September 2020. These events were also all observed with AIA, allowing us to study their evolution in EUV in addition to HXRs. While XRT was observing at too low cadence to capture the evolution of the events observed in February 2020, it observed the September 2020 ones well, and the XRT and NuSTAR time profiles were well-matched.

## 6.7 Summary and Conclusions

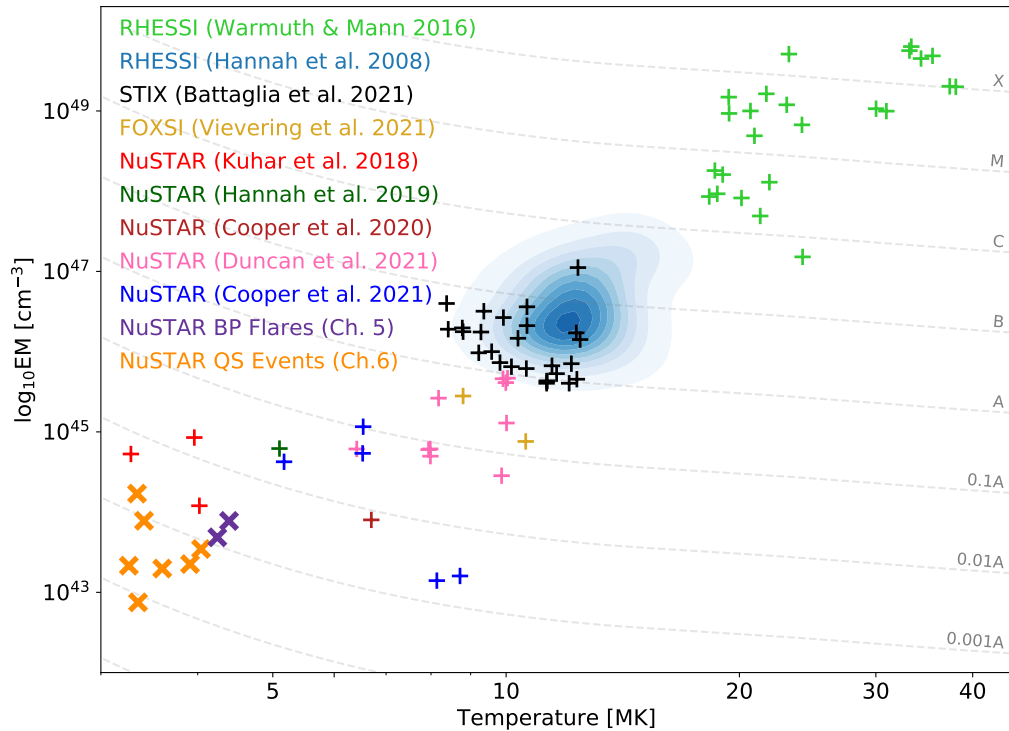


**Figure 6.20:** Plot of isothermal temperature against emission measure for flares/microflares observed in X-rays with RHESSI, STIX, FOXSI, and NuSTAR (Warmuth & Mann 2016; Hannah et al. 2008; Battaglia et al. 2021; Vievering et al. 2021; Kuhar et al. 2018; Hannah et al. 2019; Cooper et al. 2020; Duncan et al. 2021; Cooper et al. 2021), compared to the results found here for the quiet Sun impulsive events from this chapter, and the flaring X-ray bright point (observed on 21 February 2020) from Chapter 5. The GOES classes, from X down to A and below, are shown as grey dashed lines. This figure is adapted from Figure 6 in Battaglia et al. (2021).

One of the events observed in February 2020 exhibited an ejection of material, and AIA images confirm that this was a mini-filament eruption.

We fitted the NuSTAR spectra for the seven brightenings, and found that most were well-fitted with isothermal models with temperatures ranging from 3.3–4.0 MK and emission measures between  $(0.75\text{--}17) \times 10^{43} \text{ cm}^{-3}$ . The full results of the spectral fitting can be found in Table 6.2. A similar study to this one has been performed previously by Kuhar et al. (2018), who looked at three small flares observed in the quiet Sun with NuSTAR between 2016–2017, a few years before the solar minimum. As was generally the case here, this previous work found that the flares’ spectra were adequately fitted with isothermal models, with no high temperature or non-thermal components. They found comparable temperatures, between 3.2–4.1 MK, to the seven events investigated here, with emission

## 6.7 Summary and Conclusions

measures ranging from  $(0.6\text{--}15) \times 10^{44} \text{ cm}^{-3}$ . The emission measures for these flares were generally higher than those observed in 2020 as the Sun was more active at this time, and the higher background emission meant that fainter events would not have been detectable. The majority of the events observed in February 2020 and September 2020 are weaker than those investigated previously. The spectral fit temperatures for the impulsive events are generally higher than for steady features like X-ray bright points (analysed in Chapters 4 and 5), which had fit temperatures between 2.5–3.2 MK during non-flaring times.

The isothermal fit results for these quiet Sun impulsive events are compared with those from past analyses of flares and microflares using data from RHESSI, Solar Orbiter/STIX, FOXSI, and NuSTAR in Figure 6.20. This plot also includes the results for the flaring bright point from 21 February 2020 reported on in Chapter 5, and for the NuSTAR quiet Sun flares studied by [Kuhar et al. \(2018\)](#). It can be seen that the quiet Sun events occur at lower temperatures compared to the NuSTAR active region microflares, which all reach temperatures  $> 5$  MK ([Hannah et al. 2019](#); [Cooper et al. 2020](#); [Duncan et al. 2021](#); [Cooper et al. 2021](#)). They also generally produce lower emission measures, with the faintest one having the lowest emission measure of any NuSTAR impulsive event. This figure emphasises how small in scale these quiet Sun phenomena are, even in comparison with sub-A class NuSTAR microflares.

Small-scale brightenings, known as “campfires”, have recently been observed with the Extreme Ultraviolet Imager on board Solar Orbiter ([Berghmans et al. 2021](#)). These campfires are smaller but have only been observed at cooler temperatures of  $\leq 1$  MK, compared to the 3–4 MK temperatures of the impulsive events studied here.

Though most of seven events’ NuSTAR spectra were adequately fitted with isothermal models, the spectrum for the February 2020 mini-filament eruption (when fitted over a time range covering the whole HXR spike; see Figure 6.9) contained an excess compared to the isothermal model (with  $T \sim 4$  MK) at energies  $> 4$  keV. We therefore also tried fitting this with a double thermal model (Figure 6.9, bottom panel), and found that two thermal models with  $T = 3.4$  MK and  $5.1$  MK were consistent with the observed spectrum. This event did produce a signature in the AIA Fe XVIII channel (which matched the NuSTAR HXR profile well). As this channel is sensitive to material between 4–10 MK, this is consistent with there being material heating to  $> 4$  MK in this mini-filament eruption, as the NuSTAR HXR spectroscopy suggests.

DEMs were calculated for the seven events, and it was found that all showed similar shapes, including a peak at  $\log(T) \sim 6.2\text{--}6.3$ . The DEMs of the fainter events (in particular Events 6 and 7) were found to peak at slightly lower temperatures and fall off more sharply than

## 6.7 Summary and Conclusions

for the brighter ones. The DEM for the mini-filament eruption was found to exhibit more material at temperatures of  $\log(T) > 6.3$  (2 MK) compared to any of the other events. This is consistent with the NuSTAR spectroscopy indicating the presence of hotter temperatures in this event.

Finally, though no non-thermal component was directly observed in any of the events' spectra, we calculated upper limits on the non-thermal emission that could be present and remain undetected. For comparison, the thermal energies of the events were calculated and were found to range from  $(3-9) \times 10^{25}$  erg. These energies were divided by the duration of the flares and compared to the upper limits on the non-thermal heating power. It was found that there were possible non-thermal components that could have been present and provided the required heating. However, these would have had to be very steep (practically mono-energetic) between 3–4 keV.

# 7

## Conclusions and Future Work

In this thesis, we studied a number of quiet Sun phenomena from the recent solar minimum which, due to NuSTAR's high sensitivity, could be observed for the first time with a HXR imaging spectrometer. We studied steady HXR sources, such as X-ray bright points and an emerging flux region, as well as short-lived impulsive brightenings. In order to investigate their contribution to heating the corona, we searched for high temperature ( $> 5$  MK) and non-thermal components in their HXR emission. In this final chapter, we summarise the key results found throughout all of the work in Section 7.1, and we then go on to discuss the future steps for this analysis in Section 7.2.

### 7.1 Conclusions

In Chapter 1, we introduced the coronal heating problem, and the popular theory that small-scale reconnection events may provide the solution. We discussed the types of phenomena that are typically found in the quiet Sun, when there are no active regions present on the disk. These included steady features (with lifetimes of several hours) like X-ray bright points, as well as transient events such as quiet Sun flares, jets, and eruptions. All of these phenomena have been extensively studied in EUV and SXR previously. However, the lack of a HXR instrument with the required sensitivity to detect the faint emission from these sources means that there has not been an opportunity to observe them in HXR. Observing quiet Sun phenomena at HXR energies is vital in investigating how they heat the corona, through searching for hotter temperatures and non-thermal components in their emission.

NuSTAR (a brief overview of which was given in Chapter 2) has provided the first opportunity for sensitive observations of quiet Sun features and transient events with a HXR

## 7.1 Conclusions

imaging spectrometer. Chapter 3 gave a summary of the six NuSTAR quiet Sun observing campaigns from the recent solar minimum between 2018–2020. These observations were done in either mosaic mode (giving the opportunity to capture multiple features on the disk at the same time), or dwell mode (providing several hours of data for persisting sources, and increasing the chances of capturing transient events). In this thesis, we focused on the first of the NuSTAR quiet Sun observing campaigns, from 28 September 2018, as well as the longest and most quiet of the dwell observations, from 21 February 2020 and 12–13 September 2020.

Analysis of two orbits of NuSTAR full-disk mosaics from 18 September 2018 (which has been published in [Paterson et al. \(2023\)](#)) was detailed in Chapter 4. In this observation, NuSTAR captured a variety of quiet Sun phenomena. These included three X-ray bright points, as well as an emerging flux region that went on to become an active region (with NOAA ID 12723 $\beta$ ) in the days following the NuSTAR observation. A short-lived jet was also captured, in the first orbit. NuSTAR provided the opportunity to perform HXR spectroscopy for these types of quiet Sun phenomena for the first time. We found that the NuSTAR spectra for all of the quiet Sun features from these mosaics were adequately fitted with isothermal models with temperatures lying in the narrow range from 2.0–3.2 MK (with corresponding emission measures between  $(0.9\text{--}6.4) \times 10^{44} \text{cm}^{-3}$ ). This agreed with previous SXR and EUV work on bright points, which has found that they do not typically reach temperatures higher than 2–3 MK ([Doschek et al. 2010](#); [Kariyappa et al. 2011](#); [Alexander et al. 2011](#)).

We recovered DEMs for each of the mosaic features to investigate their multi-thermal emission. Using X-ray data from NuSTAR (as well as XRT) allowed the solutions to be constrained at high temperatures, unlike DEMs calculated using EUV data alone (e.g. [Reale et al. 2009](#); [Schmelz et al. 2015](#); [Kontogiannis et al. 2020](#)). The recovered DEMs confirmed the lack of any significant heating to temperatures  $> 4$  MK in these features. Also, while no non-thermal component was detected through NuSTAR spectroscopy, it was found that, in the case of the jet, there were some non-thermal components (all very steep between 3–4 keV) which could have provided the observed heating.

While useful in allowing multiple sources on the disk at the same time to be investigated, NuSTAR’s full-Sun mosaic observing mode is not ideal for studying time evolution of long-lived sources. In addition, any weak hot or non-thermal components would be difficult to detect in the 100 s pointings.

Fortunately, the quiet Sun dwell observations from February and September 2020 allowed for a more thorough investigation of the time evolution of two X-ray bright points, one from 21 February 2020 and the other from 12–13 September 2020, analyses of which (which

## 7.1 Conclusions

have been written-up in Paterson et al. 2023, submitted to MNRAS) were presented in Chapter 5. Both bright points showed significant X-ray variability (in NuSTAR and XRT) throughout the multiple hours of observation. The February 2020 bright point flared twice, and NuSTAR spectral analysis suggested that the bright point was heated from its quiescent temperature of  $\sim 3.2$  MK to  $> 4$  MK during flaring times. This is the first time that emission  $> 4$  MK has been observed in “flaring” X-ray bright points using HXRs. Previous bright point studies have found temperatures  $\leq 3.4$  MK (Dosc hek et al. 2010; Kariyappa et al. 2011; Alexander et al. 2011). The AIA time profiles for both of these flares did not show good agreement with NuSTAR, likely due to AIA being less sensitive to material at these temperatures.

While the February 2020 bright point showed evidence of increased temperatures during the times of X-ray spikes, NuSTAR spectral analysis for the September 2020 bright point told a different story. The NuSTAR time profile for this bright point also showed significant variability, including several spikes during one of the orbits. When the NuSTAR spectra for the times of these spikes were fitted, we found that the fit temperature stayed approximately constant at  $\sim 2.6$  MK, with no evidence of any hotter temperature emission being present. Flare-like heating (e.g. Reale 2014) would result in heating to temperatures higher than the quiescent value, which is not consistent with the constant temperature (with only changes in emission measure) observed in the September 2020 bright point. It is unclear whether this is due to NuSTAR not having the required sensitivity to detect any faint hotter emission, or to some physical process not accounted for by standard models.

As was the case for the September 2018 mosaic features, no non-thermal components were directly detected in the February or September 2020 bright points. However, when non-thermal upper limits were determined and compared to thermal energy estimates, it was found that steep non-thermal components at  $\sim 3\text{--}4$  keV could provide the observed heating during flaring times in some cases. However, not being able to tell from AIA images the exact area that the NuSTAR emission originated from complicated this analysis, making it difficult to make a definite conclusion.

The NuSTAR quiet Sun dwell observations allowed a rigorous investigation of the time evolution of X-ray bright points in HXRs. However, observing the Sun in this mode also increased the chances of detecting more short-lived sources, such as quiet Sun flares, eruptions and jets. The analysis of seven transient events detected on 21 February and 12–13 September 2020 was presented in Chapter 6. Six of these were quiet Sun flares, while AIA images confirmed that one event (from February 2020) was a mini-filament eruption.

## 7.1 Conclusions

When performing NuSTAR spectral analysis for the seven transient events, we found that their spectra were generally well-fitted with isothermal models with temperatures lying in the narrow range from 3.3–4.0 MK (with corresponding emission measures between  $(0.75\text{--}17) \times 10^{43} \text{ cm}^{-3}$ ). These temperatures are similar to those found in a previous study of NuSTAR quiet Sun flares by [Kuhar et al. \(2018\)](#), which found temperatures between 3.2–4.1 MK and emission measures from  $(0.6\text{--}15) \times 10^{44} \text{ cm}^{-3}$ . However, as the February and September 2020 events were observed during solar minimum (when the background emission was lower), most of the emission measures found in this work were lower than those found previously. These events were also found to be considerably cooler and generally fainter than NuSTAR active region microflares (which have  $T > 5 \text{ MK}$ ,  $EM \sim 10^{43}\text{--}10^{46} \text{ cm}^{-3}$ ; [Duncan et al. \(2021\)](#); [Cooper et al. \(2021\)](#)).

Of the seven events, only one showed the potential presence of even hotter ( $> 5 \text{ MK}$ ) emission. The NuSTAR spectrum of the mini-filament eruption, though reasonably well-fitted with an isothermal model at 4 MK, showed a small excess at high temperatures. We found that this spectrum could also be fitted with two thermal models with temperatures of 3.4 and 5.1 MK. This event did produce a signature (with a similar time profile to NuSTAR) in the AIA Fe XVIII channel, confirming the heating of material to temperatures  $> 4 \text{ MK}$ . Further, the DEM for this event indicated that more material was present at temperatures of  $\log(T) > 6.3$  (2 MK) compared to any of the six quiet Sun flares.

No non-thermal component was detected through NuSTAR spectral analysis for any of the events. However, we found that non-thermal upper limits (which were steep between 3–4 keV) were comparable to thermal energy estimates. This means that there remains a possibility that the observed heating in these events could have been produced by accelerated electrons.

In general, we found no direct evidence of temperatures  $> 5 \text{ MK}$  (except for in the February 2020 mini-filament eruption) or non-thermal emission in any of the quiet Sun HXR sources studied in this work. However, this may be due to NuSTAR not being sensitive enough to detect such components if they were very weak. The spectra of the NuSTAR mosaic features were noisy due to short pointing times, meaning that a hot or non-thermal component would have to be relatively strong to be detectable. This was also an issue with the spectra of short-lived (generally only a few minutes) impulsive events. A more sensitive dedicated HXR solar instrument would be required to determine whether any faint hot or non-thermal emission is present in such quiet Sun sources.

## 7.2 Future Work

While the research presented in this thesis was the most detailed study so far of quiet Sun phenomena at HXR energies, there is still much work that could be done to further these results.

For the two bright points from the February and September 2020 dwells discussed in Chapter 5, the AIA and NuSTAR time profiles were generally mismatched. We proposed that this was due to X-ray spikes occurring at temperatures that AIA had less sensitivity to and the AIA channels being dominated by emission at 2–3 MK from the rest of the (non-flaring) bright points. However, it would be useful to confirm that the AIA observations are indeed consistent with the results from the NuSTAR spectral fitting. This could be done using modelling codes, such as HYDRAD (Bradshaw & Cargill 2010; Bradshaw & Cargill 2013) or the Enthalpy-Based Thermal Evolution of Loops (EBTEL; Klimchuk et al. (2008); Cargill et al. (2012)). Using these modelling codes with the fit temperatures and emission measures from the NuSTAR spectral fits would allow confirmation that AIA should not have showed a similar behaviour to NuSTAR for these bright points.

In Section 5.4, we combined multiple orbits of data to create integrated NuSTAR spectra for the February and September 2020 bright points. These spectra were dominated by single thermal components at 2.6–3.2 MK at energies  $< 4$  keV. As these spectra combined data over several hours, this allowed the instrumental background to be sampled (as shown in Figures 5.16 and 5.17). We found that the background in these spectra, which dominated at energies  $> 4$  keV, was approximately consistent with the NuSTAR aperture background (Wik et al. 2014). Future analysis will involve finding upper limits on the emission at energies  $> 4$  keV that could be present and not attributed to the background. This could be tricky, as it would require identifying the possible cosmic X-ray background sources that were components of the aperture background.

The work on the bright point integrated spectra could also be extended to creating a full quiet Sun spectrum by combining data from all of the full-disk mosaics (summarised in Table 3.1). While this spectrum will likely be dominated by the 2–3 MK thermal emission from X-ray bright points, combining many mosaic tiles will allow the search for additional components. Full Sun HXR spectra have been produced before using data from other X-ray instruments (for example, RHESSI in Hannah et al. (2010), FOXSI in (Buitrago-Casas et al. 2022) and XSM in Mondal et al. (2023)—see Section 1.4). The NuSTAR full Sun spectrum could then be compared to these previous works, and also compared to predictions of

## 7.2 Future Work

quiet Sun emission from other sources, like synchrotron emission from galactic cosmic rays (Orlando et al. 2023; Petrosian et al. 2023).

When fitting some of the NuSTAR spectra, such as for the mini-filament eruption (see Section 6.3.2), it is unclear which model best describes them. For this event, the residuals for the isothermal model and for the double thermal model were similar, making it unclear which was the correct physical interpretation. Future work should include using more robust methods of model comparison. One approach being considered as part of the `Sunxspex` package<sup>1</sup> is nested sampling and bayesian evidence (Cooper et al. 2023, in prep).

In this thesis, we presented analysis on data from the 28 September 2018, and 21 February and 12–13 September 2020 observations. However, as summarised in Section 3.1, there were six quiet Sun observing campaigns from the solar minimum between 2018–2020. The dwells and mosaics from 12 January 2020 captured several bright points over multiple orbits, presenting another opportunity to investigate X-ray bright point time evolution. While the Sun was rather bright during the 02 July 2019 mosaics, the four mosaics from 25–26 April 2020 were very quiet, with several steady sources that were present for multiple orbits.

Even within the datasets analysed in this thesis, there are several HXR sources—for example, more X-ray bright points captured in the February 2020 dwells—which were not studied. In fact, additional work could also be done on some of the features which have already been analysed. For example, the NuSTAR time profile for the February 2020 bright point (Figure 5.1) showed significant variability, with a number of HXR spikes. Here, we focused only on the two largest spikes, but more future work could include investigating other times of interesting behaviour for this bright point.

NuSTAR has provided the unique opportunity to observe quiet Sun HXR sources with unprecedented sensitivity. However, NuSTAR still has some limitations in this work that could be improved on with a future mission. A HXR instrument designed with the objective of studying faint HXR quiet Sun sources would need to be highly sensitive. Like NuSTAR, any mission with this purpose would have to use focusing optics. This results in a decrease in background of several orders of magnitude (Grefenstette et al. 2016) compared to using indirect optics (as in RHESSI), and therefore a drastic increase in sensitivity. However, a solar dedicated focusing HXR telescope would ideally have a higher maximum throughput than NuSTAR's 400 counts s<sup>-1</sup>. Even in the quiet Sun, NuSTAR's livetime can fall to below

---

<sup>1</sup><https://github.com/sunpy/sunxspex>

## 7.2 Future Work

50 % (as was discussed in Section 3.1), with the brightest sources in the FOV dominating the throughput and reducing NuSTAR's sensitivity to any fainter sources present as a consequence. A larger effective area compared to NuSTAR's ( $800 \text{ cm}^2$ ) would also increase the sensitivity. Another drawback of NuSTAR is its poor spatial resolution (of  $18''$  FWHM). As quiet Sun HXR sources are generally small in scale, a higher spatial resolution would help to put these phenomena into a better spatial context than is possible with NuSTAR. A mission with these improvements compared to NuSTAR would allow the detection of even fainter events than those analysed in this thesis.

However, the NuSTAR observing campaigns from solar minimum are currently the most sensitive HXR observations of the quiet Sun. Unfortunately, it is not known if NuSTAR will still be operating at the time of the next solar minimum, and there are presently no dedicated solar HXR instruments with the same capabilities. The future of quiet Sun HXR analysis will rely on proposed missions such as Solar Particle Acceleration Radiation and Kinetics (SPARK; [Matthews et al. \(2012\)](#)) which uses the FOXSI concept for a solar dedicated HXR focusing optics telescope ([Christe et al. 2023](#); [Glesener et al. 2023](#)). Another promising prospect is the Marshall Grazing Incidence X-ray Spectrometer (MaGIXS; [Savage et al. \(2023\)](#)) sounding rocket, a soft X-ray imaging spectrometer. MaGIXS is sensitive to emission lines which form at temperatures  $> 5 \text{ MK}$ , and its observations will provide further insight into the coronal heating problem.

## Bibliography

- Adams, M., Sterling, A. C., Moore, R. L., & Gary, G. A. 2014, *The Astrophysical Journal*, 783, 11, doi: [10.1088/0004-637X/783/1/11](https://doi.org/10.1088/0004-637X/783/1/11) 16
- Alexander, C. E., Del Zanna, G., & Maclean, R. C. 2011, *Astronomy and Astrophysics*, 526, A134, doi: [10.1051/0004-6361/201014045](https://doi.org/10.1051/0004-6361/201014045) 9, 85, 99, 132, 133, 170, 171
- Alipour, N., & Safari, H. 2015, *The Astrophysical Journal*, 807, 175, doi: [10.1088/0004-637X/807/2/175](https://doi.org/10.1088/0004-637X/807/2/175) 8, 9
- Arnaud, K., Dorman, B., & Gordon, C. 1999, *Astrophysics Source Code Library*, record ascl:9910.005, ascl:9910.005 22, 24
- Arnaud, K. A. 1996, in *Astronomical Society of the Pacific Conference Series*, Vol. 101, *Astronomical Data Analysis Software and Systems V*, ed. G. H. Jacoby & J. Barnes, 17, <https://ui.adsabs.harvard.edu/abs/1996ASPC..101...17A> 60
- Aschwanden, M. J., & Boerner, P. 2011, *The Astrophysical Journal*, 732, 81, doi: [10.1088/0004-637X/732/2/81](https://doi.org/10.1088/0004-637X/732/2/81) 65
- Aschwanden, M. J., Tarbell, T. D., Nightingale, R. W., et al. 2000, *The Astrophysical Journal*, 535, 1047, doi: [10.1086/308867](https://doi.org/10.1086/308867) 13, 14, 136
- Athiray, P. S., Vievering, J., Glesener, L., et al. 2020, *The Astrophysical Journal*, 891, 78, doi: [10.3847/1538-4357/ab7200](https://doi.org/10.3847/1538-4357/ab7200) 18
- Battaglia, A. F., Saqri, J., Massa, P., et al. 2021, *Astronomy and Astrophysics*, 656, A4, doi: [10.1051/0004-6361/202140524](https://doi.org/10.1051/0004-6361/202140524) 166
- Benz, A. O. 2017, *Living Reviews in Solar Physics*, 14, 2, doi: [10.1007/s41116-016-0004-3](https://doi.org/10.1007/s41116-016-0004-3) ix, 2, 3, 4, 69
- Benz, A. O., & Krucker, S. 2002, *The Astrophysical Journal*, 568, 413, doi: [10.1086/338807](https://doi.org/10.1086/338807) 13
- Berghmans, D., Auchère, F., Long, D. M., et al. 2021, *Astronomy and Astrophysics*, 656, L4, doi: [10.1051/0004-6361/202140380](https://doi.org/10.1051/0004-6361/202140380) 167

## Bibliography

- Boerner, P., Edwards, C., Lemen, J., et al. 2012, *Solar Physics*, 275, 41, doi: [10.1007/s11207-011-9804-8](https://doi.org/10.1007/s11207-011-9804-8) 39
- Boerner, P. F., Testa, P., Warren, H., Weber, M. A., & Schrijver, C. J. 2014, *Solar Physics*, 289, 2377, doi: [10.1007/s11207-013-0452-z](https://doi.org/10.1007/s11207-013-0452-z) 39
- Bradshaw, S. J., & Cargill, P. J. 2010, *The Astrophysical Journal Letters*, 710, L39, doi: [10.1088/2041-8205/710/1/L39](https://doi.org/10.1088/2041-8205/710/1/L39) 173
- Bradshaw, S. J., & Cargill, P. J. 2013, *The Astrophysical Journal*, 770, 12, doi: [10.1088/0004-637X/770/1/12](https://doi.org/10.1088/0004-637X/770/1/12) 173
- Brosius, J. W., Rabin, D. M., Thomas, R. J., & Landi, E. 2008, *The Astrophysical Journal*, 677, 781, doi: [10.1086/528930](https://doi.org/10.1086/528930) 9, 10, 13, 88, 99, 112, 124
- Brown, J. C., & Emslie, A. G. 1988, *The Astrophysical Journal*, 331, 554, doi: [10.1086/166581](https://doi.org/10.1086/166581) 21
- Buitrago-Casas, J. C., Glesener, L., Christe, S., et al. 2022, *Astronomy and Astrophysics*, 665, A103, doi: [10.1051/0004-6361/202243272](https://doi.org/10.1051/0004-6361/202243272) ix, 18, 173
- Cargill, P. J. 1994, *The Astrophysical Journal*, 422, 381, doi: [10.1086/173733](https://doi.org/10.1086/173733) 16, 132
- Cargill, P. J., Bradshaw, S. J., & Klimchuk, J. A. 2012, *The Astrophysical Journal*, 752, 161, doi: [10.1088/0004-637X/752/2/161](https://doi.org/10.1088/0004-637X/752/2/161) 5, 173
- Cargill, P. J., & Klimchuk, J. A. 1997, *The Astrophysical Journal*, 478, 799, doi: [10.1086/303816](https://doi.org/10.1086/303816) 69
- Carroll, B. W., & Ostlie, D. A. 2007, *An Introduction to Modern Astrophysics*, 2nd edn., ed. S. F. P. Addison-Wesley 1
- Cash, W. 1979, *The Astrophysical Journal*, 228, 939, doi: [10.1086/156922](https://doi.org/10.1086/156922) 60
- Chen, P. F., & Shibata, K. 2000, *The Astrophysical Journal*, 545, 524, doi: [10.1086/317803](https://doi.org/10.1086/317803) 15
- Cheung, M. C. M., Boerner, P., Schrijver, C. J., et al. 2015, *The Astrophysical Journal*, 807, 143, doi: [10.1088/0004-637X/807/2/143](https://doi.org/10.1088/0004-637X/807/2/143) 65
- Chitta, L. P., Kariyappa, R., van Ballegoijen, A. A., et al. 2013, *The Astrophysical Journal*, 768, 32, doi: [10.1088/0004-637X/768/1/32](https://doi.org/10.1088/0004-637X/768/1/32) 10
- Christe, S., Alaoui, M., Allred, J., et al. 2023, in *Bulletin of the American Astronomical Society*, Vol. 55, 065, doi: [10.3847/25c2cfcb.bd82b0a5](https://doi.org/10.3847/25c2cfcb.bd82b0a5) 175
- Cooper, K., Hannah, I. G., Grefenstette, B. W., et al. 2020, *The Astrophysical Journal Letters*, 893, L40, doi: [10.3847/2041-8213/ab873e](https://doi.org/10.3847/2041-8213/ab873e) 40, 66, 100, 166, 167
- Cooper, K., Hannah, I. G., Grefenstette, B. W., et al. 2021, *Monthly Notices of the Royal Astronomical Society*, 507, 3936, doi: [10.1093/mnras/stab2283](https://doi.org/10.1093/mnras/stab2283) 40, 133, 166, 167, 172

## Bibliography

- Craig, I. J. D., & Brown, J. E. 1977, *Nature*, 267, 411, doi: [10.1038/267411a0](https://doi.org/10.1038/267411a0) 23, 63
- Del Zanna, G. 2013, *Astronomy and Astrophysics*, 558, A73, doi: [10.1051/0004-6361/201321653](https://doi.org/10.1051/0004-6361/201321653) 40, 132
- Del Zanna, G., Dere, K. P., Young, P. R., & Landi, E. 2021, *The Astrophysical Journal*, 909, 38. <https://ui.adsabs.harvard.edu/abs/2021ApJ...909...38D> 36
- Del Zanna, G., & Mason, H. E. 2018, *Living Reviews in Solar Physics*, 15, 5, doi: [10.1007/s41116-018-0015-3](https://doi.org/10.1007/s41116-018-0015-3) 20
- Dere, K. P., Del Zanna, G., Young, P. R., Landi, E., & Sutherland, R. S. 2019, *The Astrophysical Journal Supplement Series*, 241, 22, doi: [10.3847/1538-4365/ab05cf](https://doi.org/10.3847/1538-4365/ab05cf) 36
- Dere, K. P., Landi, E., Mason, H. E., Monsignori Fossi, B. C., & Young, P. R. 1997, *Astronomy and Astrophysics Supplement Series*, 125, 149, doi: [10.1051/aas:1997368](https://doi.org/10.1051/aas:1997368) 20, 36
- Doschek, G. A., Landi, E., Warren, H. P., & Harra, L. K. 2010, *The Astrophysical Journal*, 710, 1806, doi: [10.1088/0004-637X/710/2/1806](https://doi.org/10.1088/0004-637X/710/2/1806) ix, 8, 10, 11, 13, 85, 88, 99, 112, 124, 133, 170, 171
- Duncan, J., Glesener, L., Grefenstette, B. W., et al. 2021, *The Astrophysical Journal*, 908, 29, doi: [10.3847/1538-4357/abca3d](https://doi.org/10.3847/1538-4357/abca3d) 20, 40, 133, 166, 167, 172
- Feldman, U. 1992, *Physica Scripta*, 46, 202, doi: [10.1088/0031-8949/46/3/002](https://doi.org/10.1088/0031-8949/46/3/002) 20, 36, 39, 41, 60
- Gehrels, N. 1986, *The Astrophysical Journal*, 303, 336, doi: [10.1086/164079](https://doi.org/10.1086/164079) 68
- Glesener, L., Krucker, S., Hannah, I. G., et al. 2017, *The Astrophysical Journal*, 845, 122, doi: [10.3847/1538-4357/aa80e9](https://doi.org/10.3847/1538-4357/aa80e9) 28
- Glesener, L., Krucker, S., Christe, S., et al. 2016, in *Society of Photo-Optical Instrumentation Engineers (SPIE) Conference Series*, Vol. 9905, *Space Telescopes and Instrumentation 2016: Ultraviolet to Gamma Ray*, ed. J.-W. A. den Herder, T. Takahashi, & M. Bautz, 99050E, doi: [10.1117/12.2232262](https://doi.org/10.1117/12.2232262) 18
- Glesener, L., Krucker, S., Duncan, J., et al. 2020, *The Astrophysical Journal Letters*, 891, L34, doi: [10.3847/2041-8213/ab7341](https://doi.org/10.3847/2041-8213/ab7341) 28, 44
- Glesener, L., Shih, A. Y., Caspi, A., et al. 2023, in *Bulletin of the American Astronomical Society*, Vol. 55, 129, doi: [10.3847/25c2cfeb.78fa7c49](https://doi.org/10.3847/25c2cfeb.78fa7c49) 175
- Golub, L., Davis, J. M., & Krieger, A. S. 1979, *The Astrophysical Journal*, 229, L145, doi: [10.1086/182949](https://doi.org/10.1086/182949) 8
- Golub, L., Deluca, E. E., Sette, A., & Weber, M. 2004, in *Astronomical Society of the Pacific Conference Series*, Vol. 325, *The Solar-B Mission and the Forefront of Solar Physics*, ed. T. Sakurai & T. Sekii, 217. <https://ui.adsabs.harvard.edu/abs/2004ASPC...325..217G> 65

## Bibliography

- Golub, L., Krieger, A. S., Silk, J. K., Timothy, A. F., & Vaiana, G. S. 1974, *The Astrophysical Journal*, 189, L93, doi: [10.1086/181472](https://doi.org/10.1086/181472) 8, 9, 10, 85, 103
- Golub, L., DeLuca, E., Austin, G., et al. 2007, *Solar Physics*, 243, 63, doi: [10.1007/s11207-007-0182-1](https://doi.org/10.1007/s11207-007-0182-1) 41
- Grefenstette, B. W., Glesener, L., Krucker, S., et al. 2016, *The Astrophysical Journal*, 826, 20, doi: [10.3847/0004-637X/826/1/20](https://doi.org/10.3847/0004-637X/826/1/20) 19, 25, 26, 27, 28, 29, 30, 31, 32, 36, 60, 174
- Habbal, S. R., & Withbroe, G. L. 1981, *Solar Physics*, 69, 77, doi: [10.1007/BF00151257](https://doi.org/10.1007/BF00151257) 9
- Hannah, I. G., Christe, S., Krucker, S., et al. 2008, *The Astrophysical Journal*, 677, 704, doi: [10.1086/529012](https://doi.org/10.1086/529012) ix, 14, 166
- Hannah, I. G., Christe, S., Krucker, S., et al. 2008, *The Astrophysical Journal*, 677, 704, doi: [10.1086/529012](https://doi.org/10.1086/529012) 13
- Hannah, I. G., Hudson, H. S., Hurford, G. J., & Lin, R. P. 2010, *The Astrophysical Journal*, 724, 487, doi: [10.1088/0004-637X/724/1/487](https://doi.org/10.1088/0004-637X/724/1/487) ix, 17, 18, 19, 173
- Hannah, I. G., Hurford, G. J., Hudson, H. S., Lin, R. P., & van Bibber, K. 2007, *The Astrophysical Journal Letters*, 659, L77, doi: [10.1086/516750](https://doi.org/10.1086/516750) 17
- Hannah, I. G., Kleint, L., Krucker, S., et al. 2019, *The Astrophysical Journal*, 881, 109, doi: [10.3847/1538-4357/ab2dfa](https://doi.org/10.3847/1538-4357/ab2dfa) 166, 167
- Hannah, I. G., & Kontar, E. P. 2012, *Astronomy and Astrophysics*, 539, A146, doi: [10.1051/0004-6361/201117576](https://doi.org/10.1051/0004-6361/201117576) 23, 62, 63, 64, 65
- Hansen, P. C. 1992, *Inverse Problems*, 8, 849, doi: [10.1088/0266-5611/8/6/005](https://doi.org/10.1088/0266-5611/8/6/005) 64
- Harrison, F. A., Craig, W. W., Christensen, F. E., et al. 2013, *The Astrophysical Journal*, 770, 103, doi: [10.1088/0004-637X/770/2/103](https://doi.org/10.1088/0004-637X/770/2/103) ix, 6, 19, 25, 26, 27, 28
- Harvey, K. L., Strong, K. T., Nitta, N., & Tsuneta, S. 1993, *Advances in Space Research*, 13, 27, doi: [10.1016/0273-1177\(93\)90453-I](https://doi.org/10.1016/0273-1177(93)90453-I) 8, 12
- Hermans, L. M., & Martin, S. F. 1986, in *NASA Conference Publication*, Vol. 2442, NASA Conference Publication, 369–375. <https://ui.adsabs.harvard.edu/abs/1986NASCP2442.369H> 15
- Holman, G. D., Aschwanden, M. J., Aurass, H., et al. 2011, *Space Science Reviews*, 159, 107, doi: [10.1007/s11214-010-9680-9](https://doi.org/10.1007/s11214-010-9680-9) 20
- Hong, J., Jiang, Y., Yang, J., et al. 2014, *The Astrophysical Journal*, 796, 73, doi: [10.1088/0004-637X/796/2/73](https://doi.org/10.1088/0004-637X/796/2/73) 15
- Hong, J., Jiang, Y., Yang, J., et al. 2016, *The Astrophysical Journal*, 830, 60, doi: [10.3847/0004-637X/830/2/60](https://doi.org/10.3847/0004-637X/830/2/60) 16

## Bibliography

- Hudson, H. S. 1991, *Solar Physics*, 133, 357, doi: [10.1007/BF00149894](https://doi.org/10.1007/BF00149894) 3
- Jefferies, J. T., Orrall, F. Q., & Zirker, J. B. 1972, *Solar Physics*, 22, 307, doi: [10.1007/BF00148698](https://doi.org/10.1007/BF00148698) 23, 63
- Kamio, S., Curdt, W., Teriaca, L., & Innes, D. E. 2011, *Astronomy and Astrophysics*, 529, A21, doi: [10.1051/0004-6361/201015715](https://doi.org/10.1051/0004-6361/201015715) 12
- Kariyappa, R., Deluca, E. E., Saar, S. H., et al. 2011, *Astronomy and Astrophysics*, 526, A78, doi: [10.1051/0004-6361/201014878](https://doi.org/10.1051/0004-6361/201014878) 9, 85, 99, 133, 170, 171
- Klimchuk, J. A. 2006, *Solar Physics*, 234, 41, doi: [10.1007/s11207-006-0055-z](https://doi.org/10.1007/s11207-006-0055-z) 4
- Klimchuk, J. A. 2015, *Philosophical Transactions of the Royal Society of London Series A*, 373, 20140256, doi: [10.1098/rsta.2014.0256](https://doi.org/10.1098/rsta.2014.0256) ix, 5
- Klimchuk, J. A. 2017, arXiv e-prints, arXiv:1709.07320, doi: [10.48550/arXiv.1709.07320](https://doi.org/10.48550/arXiv.1709.07320) 6
- Klimchuk, J. A., Patsourakos, S., & Cargill, P. J. 2008, *The Astrophysical Journal*, 682, 1351, doi: [10.1086/589426](https://doi.org/10.1086/589426) 5, 18, 132, 173
- Kontar, E. P., Brown, J. C., Emslie, A. G., et al. 2011, *Space Science Reviews*, 159, 301, doi: [10.1007/s11214-011-9804-x](https://doi.org/10.1007/s11214-011-9804-x) 23
- Kontogiannis, I., Tsiropoula, G., Tziotziou, K., et al. 2020, *Astronomy and Astrophysics*, 633, A67, doi: [10.1051/0004-6361/201936778](https://doi.org/10.1051/0004-6361/201936778) 12, 80, 170
- Kosugi, T., Matsuzaki, K., Sakao, T., et al. 2007, *Solar Physics*, 243, 3, doi: [10.1007/s11207-007-9014-6](https://doi.org/10.1007/s11207-007-9014-6) 41
- Krucker, S., & Benz, A. O. 1998, *The Astrophysical Journal Letters*, 501, L213, doi: [10.1086/311474](https://doi.org/10.1086/311474) 13, 14
- Krucker, S., Benz, A. O., Bastian, T. S., & Acton, L. W. 1997, *The Astrophysical Journal*, 488, 499, doi: [10.1086/304686](https://doi.org/10.1086/304686) 13
- Kuhar, M., Krucker, S., Glesener, L., et al. 2018, *The Astrophysical Journal Letters*, 856, L32, doi: [10.3847/2041-8213/aab889](https://doi.org/10.3847/2041-8213/aab889) 14, 15, 135, 136, 166, 167, 172
- Kwon, R.-Y., Chae, J., Davila, J. M., et al. 2012, *The Astrophysical Journal*, 757, 167, doi: [10.1088/0004-637X/757/2/167](https://doi.org/10.1088/0004-637X/757/2/167) 8
- Lemen, J. R., Title, A. M., Akin, D. J., et al. 2012, *Solar Physics*, 275, 17, doi: [10.1007/s11207-011-9776-8](https://doi.org/10.1007/s11207-011-9776-8) 38
- Lin, R. P., Schwartz, R. A., Kane, S. R., Pelling, R. M., & Hurley, K. C. 1984, *The Astrophysical Journal*, 283, 421, doi: [10.1086/162321](https://doi.org/10.1086/162321) 4
- Lin, R. P., Dennis, B. R., Hurford, G. J., et al. 2002, *Solar Physics*, 210, 3, doi: [10.1023/A:1022428818870](https://doi.org/10.1023/A:1022428818870) 17, 27, 36

## Bibliography

- Madjarska, M. S. 2019, *Living Reviews in Solar Physics*, 16, 2, doi: [10.1007/s41116-019-0018-8](https://doi.org/10.1007/s41116-019-0018-8) 7
- Madsen, K. K., Forster, K., Grefenstette, B. W., Harrison, F. A., & Miyasaka, H. 2021, arXiv e-prints, arXiv:2110.11522 26, 60
- Madsen, K. K., Harrison, F. A., Markwardt, C. B., et al. 2015, *The Astrophysical Journal Supplement Series*, 220, 8, doi: [10.1088/0067-0049/220/1/8](https://doi.org/10.1088/0067-0049/220/1/8) 26, 29, 62
- Matthews, S. A., Williams, D. R., Klein, K.-L., et al. 2012, *Experimental Astronomy*, 33, 237, doi: [10.1007/s10686-011-9260-3](https://doi.org/10.1007/s10686-011-9260-3) 175
- McIntosh, S. W., de Pontieu, B., Carlsson, M., et al. 2011, *Nature*, 475, 477, doi: [10.1038/nature10235](https://doi.org/10.1038/nature10235) 4
- Mondal, B., Klimchuk, J. A., Vadawale, S. V., et al. 2023, *The Astrophysical Journal*, 945, 37, doi: [10.3847/1538-4357/acb8bb](https://doi.org/10.3847/1538-4357/acb8bb) 17, 173
- Moore, R. L., Tang, F., Bohlin, J. D., & Golub, L. 1977, *The Astrophysical Journal*, 218, 286, doi: [10.1086/155681](https://doi.org/10.1086/155681) 16
- Morozov, V. A. 1967, *Dokl. Akad. Nauk SSSR*, 175, 1225 64
- Mou, C., Madjarska, M. S., Galsgaard, K., & Xia, L. 2018, *Astronomy and Astrophysics*, 619, A55, doi: [10.1051/0004-6361/201833243](https://doi.org/10.1051/0004-6361/201833243) 8
- Mulay, S. M., Del Zanna, G., & Mason, H. 2017, *Astronomy and Astrophysics*, 606, A4, doi: [10.1051/0004-6361/201730429](https://doi.org/10.1051/0004-6361/201730429) 16
- Munro, R. H., Gosling, J. T., Hildner, E., et al. 1979, *Solar Physics*, 61, 201, doi: [10.1007/BF00155456](https://doi.org/10.1007/BF00155456) 15
- Nakakubo, K., & Hara, H. 2000, *Advances in Space Research*, 25, 1905, doi: [10.1016/S0273-1177\(99\)00621-3](https://doi.org/10.1016/S0273-1177(99)00621-3) 8
- Narukage, N., Sakao, T., Kano, R., et al. 2014, *Solar Physics*, 289, 1029, doi: [10.1007/s11207-013-0368-7](https://doi.org/10.1007/s11207-013-0368-7) 41
- Narukage, N., Sakao, T., Kano, R., et al. 2011, *Solar Physics*, 269, 169, doi: [10.1007/s11207-010-9685-2](https://doi.org/10.1007/s11207-010-9685-2) 41
- Orlando, E., Petrosian, V., & Strong, A. 2023, *The Astrophysical Journal*, 943, 173, doi: [10.3847/1538-4357/acad75](https://doi.org/10.3847/1538-4357/acad75) 174
- Panesar, N. K., Sterling, A. C., & Moore, R. L. 2018, *The Astrophysical Journal*, 853, 189, doi: [10.3847/1538-4357/aaa3e9](https://doi.org/10.3847/1538-4357/aaa3e9) 15
- Panesar, N. K., Sterling, A. C., Moore, R. L., & Chakrapani, P. 2016, *The Astrophysical Journal Letters*, 832, L7, doi: [10.3847/2041-8205/832/1/L7](https://doi.org/10.3847/2041-8205/832/1/L7) 15

## Bibliography

- Parker, E. N. 1988, *The Astrophysical Journal*, 330, 474, doi: [10.1086/166485](https://doi.org/10.1086/166485) 4, 13
- Parnell, C. E., & Jupp, P. E. 2000, *The Astrophysical Journal*, 529, 554, doi: [10.1086/308271](https://doi.org/10.1086/308271) 13, 14, 136
- Paterson, S., Hannah, I. G., Grefenstette, B. W., et al. 2023, *Solar Physics*, 298, 47, doi: [10.1007/s11207-023-02135-4](https://doi.org/10.1007/s11207-023-02135-4) 45, 46, 65, 71, 72, 74, 80, 83, 89, 92, 93, 94, 99, 170
- Pesnell, W. D., Thompson, B. J., & Chamberlin, P. C. 2012, *Solar Physics*, 275, 3, doi: [10.1007/s11207-011-9841-3](https://doi.org/10.1007/s11207-011-9841-3) 38
- Petrosian, V., Orlando, E., & Strong, A. 2023, *The Astrophysical Journal*, 943, 21, doi: [10.3847/1538-4357/aca474](https://doi.org/10.3847/1538-4357/aca474) 174
- Phillips, K. J. H. 2004, *The Astrophysical Journal*, 605, 921, doi: [10.1086/382523](https://doi.org/10.1086/382523) 20
- Phillips, K. J. H., Feldman, U., & Landi, E. 2008, *Ultraviolet and X-ray Spectroscopy of the Solar Atmosphere*. <https://ui.adsabs.harvard.edu/abs/2008uxss.book.....P> 22
- Reale, F. 2014, *Living Reviews in Solar Physics*, 11, 4, doi: [10.12942/lrsp-2014-4](https://doi.org/10.12942/lrsp-2014-4) 132, 133, 171
- Reale, F., McTiernan, J. M., & Testa, P. 2009, *The Astrophysical Journal Letters*, 704, L58, doi: [10.1088/0004-637X/704/1/L58](https://doi.org/10.1088/0004-637X/704/1/L58) 80, 170
- Savage, S. L., Winebarger, A. R., Kobayashi, K., et al. 2023, *The Astrophysical Journal*, 945, 105, doi: [10.3847/1538-4357/acbb58](https://doi.org/10.3847/1538-4357/acbb58) 175
- Schmelz, J. T., Asgari-Targhi, M., Christian, G. M., Dhaliwal, R. S., & Pathak, S. 2015, *The Astrophysical Journal*, 806, 232, doi: [10.1088/0004-637X/806/2/232](https://doi.org/10.1088/0004-637X/806/2/232) 42, 65, 80, 170
- Schmelz, J. T., Jenkins, B. S., Worley, B. T., et al. 2011, *The Astrophysical Journal*, 731, 49, doi: [10.1088/0004-637X/731/1/49](https://doi.org/10.1088/0004-637X/731/1/49) 63
- Schou, J., Scherrer, P. H., Bush, R. I., et al. 2012, *Solar Physics*, 275, 229, doi: [10.1007/s11207-011-9842-2](https://doi.org/10.1007/s11207-011-9842-2) 38, 41
- Shen, Y. 2021, *Proceedings of the Royal Society of London Series A*, 477, 217, doi: [10.1098/rspa.2020.0217](https://doi.org/10.1098/rspa.2020.0217) 15, 92
- Shibata, K., Nitta, N., Strong, K. T., et al. 1994, *The Astrophysical Journal Letters*, 431, L51, doi: [10.1086/187470](https://doi.org/10.1086/187470) 16
- Strong, K. T., Harvey, K., Hirayama, T., et al. 1992, *Publications of the Astronomical Society of Japan*, 44, L161. <https://ui.adsabs.harvard.edu/abs/1992PASJ...44L.161S> 10, 132
- Sylwester, B., Sylwester, J., Siarkowski, M., et al. 2019, *Solar Physics*, 294, 176, doi: [10.1007/s11207-019-1565-9](https://doi.org/10.1007/s11207-019-1565-9) 16
- Sylwester, J., Kowalinski, M., Gburek, S., et al. 2012, *The Astrophysical Journal*, 751, 111,

## Bibliography

- doi: [10.1088/0004-637X/751/2/111](https://doi.org/10.1088/0004-637X/751/2/111) 16, 17
- Takahashi, M., & Watanabe, T. 2000, *Advances in Space Research*, 25, 1833, doi: [10.1016/S0273-1177\(99\)00628-6](https://doi.org/10.1016/S0273-1177(99)00628-6) 69
- Testa, P., Reale, F., Landi, E., DeLuca, E. E., & Kashyap, V. 2011, *The Astrophysical Journal*, 728, 30, doi: [10.1088/0004-637X/728/1/30](https://doi.org/10.1088/0004-637X/728/1/30) 65
- Tian, H., Tu, C. Y., He, J. S., & Marsch, E. 2007, *Advances in Space Research*, 39, 1853, doi: [10.1016/j.asr.2007.03.065](https://doi.org/10.1016/j.asr.2007.03.065) 8
- Tomczyk, S., McIntosh, S. W., Keil, S. L., et al. 2007, *Science*, 317, 1192, doi: [10.1126/science.1143304](https://doi.org/10.1126/science.1143304) 4
- Török, T., & Kliem, B. 2005, *The Astrophysical Journal Letters*, 630, L97, doi: [10.1086/462412](https://doi.org/10.1086/462412) 15
- Vadawale, S. V., Shanmugam, M., Acharya, Y. B., et al. 2014, *Advances in Space Research*, 54, 2021, doi: [10.1016/j.asr.2013.06.002](https://doi.org/10.1016/j.asr.2013.06.002) 16
- Vadawale, S. V., Mithun, N. P. S., Mondal, B., et al. 2021, *The Astrophysical Journal Letters*, 912, L13 17
- Vaiana, G. S., Krieger, A. S., & Timothy, A. F. 1973, *Solar Physics*, 32, 81, doi: [10.1007/BF00152731](https://doi.org/10.1007/BF00152731) 7
- van Driel-Gesztelyi, L., & Green, L. M. 2015, *Living Reviews in Solar Physics*, 12, 1, doi: [10.1007/lrsp-2015-1](https://doi.org/10.1007/lrsp-2015-1) 12
- Verbeeck, C., Delouille, V., Mampaey, B., & De Visscher, R. 2014, *Astronomy and Astrophysics*, 561, A29, doi: [10.1051/0004-6361/201321243](https://doi.org/10.1051/0004-6361/201321243) 53, 95, 103
- Vievering, J. T., Glesener, L., Athiray, P. S., et al. 2021, *The Astrophysical Journal*, 913, 15, doi: [10.3847/1538-4357/abf145](https://doi.org/10.3847/1538-4357/abf145) 166
- Warmuth, A., & Mann, G. 2016, *Astronomy and Astrophysics*, 588, A115, doi: [10.1051/0004-6361/201527474](https://doi.org/10.1051/0004-6361/201527474) 166
- Weber, M. A., DeLuca, E. E., Golub, L., & Sette, A. L. 2004, in *Multi-Wavelength Investigations of Solar Activity*, ed. A. V. Stepanov, E. E. Benevolenskaya, & A. G. Kosovichev, Vol. 223, 321–328, doi: [10.1017/S1743921304006088](https://doi.org/10.1017/S1743921304006088) 65
- Wik, D. R., Hornstrup, A., Molendi, S., et al. 2014, *The Astrophysical Journal*, 792, 48, doi: [10.1088/0004-637X/792/1/48](https://doi.org/10.1088/0004-637X/792/1/48) ix, 36, 37, 131, 173
- Withbroe, G. L., & Noyes, R. W. 1977, *Annual Review of Astronomy and Astrophysics*, 15, 363, doi: [10.1146/annurev.aa.15.090177.002051](https://doi.org/10.1146/annurev.aa.15.090177.002051) 4
- Woods, T. N., Eparvier, F. G., Hock, R., et al. 2012, *Solar Physics*, 275, 115, doi: [10.1007/](https://doi.org/10.1007/)

## *Bibliography*

[s11207-009-9487-6](#) 38

Wright, P. J., Hannah, I. G., Grefenstette, B. W., et al. 2017, *The Astrophysical Journal*, 844, 132, doi: [10.3847/1538-4357/aa7a59](#) 65, 66

Zhang, J., Wang, J., Deng, Y., & Wu, D. 2001, *The Astrophysical Journal Letters*, 548, L99, doi: [10.1086/318934](#) 15